Insights into Dioxygen Activation by Biomimetic Alkyl Thiolate-Ligated Iron Complexes

Maike N Blakely

A dissertation

submitted in partial fulfillment of the

requirements for the degree of

Doctor of Philosophy

University of Washington

2019

Reading Committee:

Julie A. Kovacs, Chair

Brandi M. Cossairt

Daniel R. Gamelin

Program Authorized to Offer Degree:

Chemistry

University of Washington

Abstract

Insights into Dioxygen Activation by Biomimetic Alkyl Thiolate-Ligated Iron Complexes

Maike N Blakely

Chair of the Supervisory Committee:
Professor Julie A. Kovacs
Department of Chemistry

Dioxygen activation by non-heme thiolate-ligated Fe-enzymes, such as isopenicillin N synthase (IPNS) and cysteine dioxygenase (CDO) are believed to proceed through several intermediates, including an Fe-superoxo, -hydroperoxo, and high-valent oxo. Thiolate (RS-) ligands are predicted lower the activation barrier to O_2 binding, facilitate peroxo O-O bond cleavage via the formation of highly covalent Fe^{III}–SR bonds, and H-atom abstraction reactions. There are few reported examples of well-characterized RS-Fe-superoxo, or -hydroperoxo intermediates. This dissertation describes a new structurally characterized alkyl thiolate-ligated Fe^{II} complex, $[Fe^{II}(S_2{}^{Me2}N_3(Pr,Pr)]$, which reacts with dioxygen (O_2) to form an unprecedented example of a reactive RS-Fe^{III}-superoxo intermediate The kinetics of formation of the thiolate ligated Fe^{III}-superoxo intermediate $[Fe^{III}(S_2{}^{Me2}N_3(Pr,Pr)(O_2)]$ formed via the addition of O_2 to $[Fe^{II}(S_2{}^{Me2}N_3(Pr,Pr)]$, and the addition of potassium superoxide (KO_2) to $[Fe^{III}(S_2{}^{Me2}N_3(Pr,Pr)]^+$,

are presented. This RS-Fe^{III}-superoxo intermediate goes on to cleave strong C-H bonds converting to a second observable intermediate, proposed to be an Fe^{III}-hydroperoxo, *en route* to a rare example of a crystallographically characterized η^2-coordinated sulfenate (RSO-) complex. A look into the mechanism of the formation of the rare stable sulfenate was carried out using oxo atom donors added to the oxidized $[Fe^{III}(S_2{}^{Me2}N_3(Pr,Pr)]^+$. The formation of oxo atom donor adducts is observed in these reactions at low temperatures, which then convert to the singly oxygenated sulfenate. This implicates a metal-mediated pathway for sulfur oxygenation, as opposed to direct attack at the sulfur, and possibly an unobservable Fe^V-oxo as the active oxidant. Finally, synthetic routes to new alkyl-thiolate ligated Fe complexes are discussed due to their potential to expand our understanding of how thiolates influence reactivity.

TABLE OF CONTENTS

LIST OF FIGURES

LIST OF TABLES

LIST OF NUMBERED COMPLEXES

1 $[Fe^{II}(S_2{}^{Me2}N_3(Pr,Pr)]$

2 $[Fe^{III}(S_2{}^{Me2}N_3(Pr,Pr)]^{+}$

3 $[Fe^{III}(S_2{}^{Me2}N_3(Pr,Pr)(N_3)]$

4 $[(Fe^{II}(S_2{}^{Me2}N_3(Pr,Pr))\text{-}\mu\text{-}(Fe^{II})]^{2+}$

5 $[Fe^{III}(\eta^2\text{-}S^{Me2}O)(S^{Me2}N_3(Pr,Pr))]^{+}$

6 $[Fe^{III}(S_2{}^{Me2}N_3(Pr,Pr))(O_2)]$

7 $[Fe^{III}(S_2{}^{Me2}N_3(Pr,Pr))(OOH)]$

8 $[Fe^{III}(S_2{}^{Me2}N^{Me}N_2{}^{amide}(Pr,Pr)]^{1-}$

9 $[Fe^{III}(S_2{}^{Me2}N^{Me}N_2(Pr,Pr))]^{+}$

10 $[Fe^{III}(S_2{}^{Me2}N_3(Pr,Pr)(PNO)]^{+}$

11 $[Fe^{III}(S_2{}^{Me2}N^{H}N_2{}^{amide}(Pr,Pr)]^{1-}$

12 *N*-(2,6-diisopropylphenyl)-*N*-[2-(2,6-diisopropylphenyl)amino]ethyl]-*N*-[2-thioethyl]-1,2-ethanediamine (BDAT)

13 $[Fe^{II}(BDAT)]^{1-}$

14 $[Fe^{II}(S^{Me2}N_4(tren\text{-}dipp_{amide})]^{1-}$

15 *N*-(2-thiol-2-methylpropanone)-*N*-[3-(2-thiol-2-methylpropanone)propyl]-1,3-propanediamine hydrochloride $((HS^{Me2})_2NH(HN^{amide})_2(Pr,Pr)\bullet HCl)$

16 ethyl 2-bromo-2-methyl propionate

17 benzyl mercaptan

18 2-benzyl-2-methyl propionic acid

19 *tert*-butyl bis(3-aminopropyl)carbamate

20 *N*-(2-benzylthiol-2-methylpropanone)-*N*-[3-(2-benzylthiol-2-methylpropanone)propyl]-*N*-[3-(*tert*-butyloxycarbonyl)]-1,3-propanediamine ($Bn_2S_2^{Me2}NBoc(HN)_2^{amide}(Pr,Pr)$)

21 *N*-(2-thiol-2-methylpropanone)-*N*-[3-(2-thiol-2-methylpropanone)propyl]-*N*-[3-(*tert*-butyloxycarbonyl)]-1,3-propanediamine ($((HS^{Me2})_2NBoc(HN)_2^{amide}(Pr,Pr)$)

22 2-iodoethanol

23 2,6-diisopropylaniline

24 2-(2,6-diisopropylphenylamino)ethanol

25 *N*-(2-iodoethyl)-2,6-diisopropylbenzenaminium chloride

26 *S*-benzylcysteamine

27 *N*-(2,6-diisopropylphenyl)-*N*-[2-(2,6-diisopropylphenyl)amino]ethyl]-*N*-[2-(phenylthio)ethyl]-1,2-ethanediamine (Bn-BDAT)

28 *N*-(2,6-diisopropylphenyl)-*N*-[2-(2,6-diisopropylphenyl)amino]ethyl]-*N*-[2-ethylamino]-1,2-ethanediamine (N_4(tren-$dipp_{amine}$))

29 1-(*tert*-butyloxycarbonyl)ethyldiamine (NNBoc)

30 *N*-(2,6-diisopropylphenyl)-*N*-[2-(2,6-diisopropylphenyl)amino]ethyl]-*N*-[2-ethylamino-Boc]-1,2-ethanediamine **(**N_4(tren-$dipp_{amine}$)-Boc)

31 3-methyl-3-mercapto-2-butanone

32 $[Fe^{II}(S^{Me2}N_4(tren\text{-}dipp_{amide})]^{1+}$

GLOSSARY

δ	Isomer shift
τ	5-coordinate geometry index
⊥-mode	perpendicular-mode
Å	Ångström
ACV	*δ*(L-α-aminoadipoyl)-L-cysteinyl-D-valine
AZADOL	2-hydroxy-2-azaadamantane
BDE	Bond dissociation energy
Cys	Cysteine
CDO	Cysteine dioxygenase
CD_2Cl_2	Deuterated methylene chloride
CHD	1,4-cyclohexadiene
CN^-	Cyanide anion
CSA	Cysteine sulfinic acid
CysOEt	L-Cysteine ethyl ester
DCM	Methylene chloride
DFT	Density functional theory
DHA	Dihydroanthracene
E_a	Activation energy
EAS	Electronic absorption spectrum
EDG	Electron donating group
EPR	Electron paramagnetic resonance
ΔE_Q	Quadrupole splitting
ESI-MS	Electrospray-ionization mass spectroscopy
Et_2O	Diethyl ether
EWG	Electron withdrawing group
EXAFS	Extended X-ray absorption fine structure
G	Gauss
Gln	Glutamine

ΔH	Enthalpy
$\Delta H^{\ddagger}$	Enthalpy of activation
HAT	Hydrogen atom transfer
H_2O_2	Hydrogen peroxide
His	Histidine
HOTf	Triflic acid
Hz	Hertz
IAr	Iodoarene
$IArF_5$	Pentafluoroiodobenzene
IBX-ester	Iodoxybenzoate
IPN	Isopenicillin N
IPNS	Isopenicillin N synthase
KO_2	Potassium superoxide
*m*CPBA	3-chloroperoxybenzoic acid
MeCN	Acetonitrile
Me-THF	2-Methyltetrahydrofuran
MCD	Magnetic circular dichroism
N_3^-	Azide anion
$NBu_4(PF_6)$	Tetrabutylammonium hexafluorophosphate
NHase	Nitrile hydratase
NMR	Nuclear magnetic resonance
NO	Nitric oxide
$O_2^{\bullet-}$	Superoxide
OX	Oxo atom donor
PDB	Protein data bank
ppm	Parts per million
PhIO	Iodosylbenzene
PNO	Pyridine-*N*-oxide
$PhIO_2$	Iodoxybenzene
PFIB	Pentafluoro-iodosylbenzene

QM/MM	Quantum mechanics/molecular mechanics
rR	Resonance Raman
ΔS	Entropy
$\Delta S^{\ddagger}_{THF}$	Entropy of activation
SCE	Saturated calomel electrode
Sec	Selenocysteine
Ser	Serine
T	Calculated overlap parameter
TD-DFT	Time-dependent density functional theory
TEMPOH	1-hydroxy-2,2,6,6-tetramethyl-piperidine
THF	Tetrahydrofuran
TMS	Tetramethylsilane
Tyr	Tyrosine
XAS	X-ray absorption spectroscopy
Val	Valine

ACKNOWLEDGEMENTS

I am so grateful to have been part of Professor Julie Kovacs research group for the last five years. Julie Kovacs's enthusiasm for our science and her students is huge part of what has made her a wonderful advisor and role model for me. The senior group members, Dr. Ben Leipzig, Dr. Julian Rees and Audra Johansen graciously gave me their time and taught me so much in my first few years. The current group has grown quite a bit and I would like to thank them for their friendship and support. My lab sibling, Maksym Dedushko, has kept me caffeinated and been lively companion whom I have learned so much from. I am excited to see the current group, Maksym Dedushko Penny Poon, Dylan Rogers, Alex Downing, Maria Greiner, Julian Smith-Jones, Bennet Karel and Paige Gannon, continue to produce interesting results and the careers they will pursue following their time in the Kovacs group.

The University of Washington's department of chemistry has been a wonderful community in which to learn, discuss and perform science. I would like to acknowledge the many committee members, Professors Karen Goldberg, Daniel Gamelin, Tomikazu Sasaki, AJ Boydston, Brandi Cossairt, Ron Stenkamp, Munira Khalil, and Jerry Seidler, that have given me advice and encouragement over the past few years. The inorganic division has been supportive group and I have made many friends on the 3rd floor of the Chemistry Building.

Quite of few of those friends have gone on numerous hikes with me and I am especially grateful to have had the company of my close friends, Adrianna Simonelli, Emily Dieter, Elizabeth and Michael Enright. In addition to hiking, I have enjoyed playing for the Isotopes men's beer league ice hockey team. A lot of these guys have become like a second family. The best part of playing for this team was meeting Walter, my fiancé. I cannot thank him enough for his support and love

throughout my graduate school career. I look forward to our next adventure in Bozeman, MT. Finally, I want to thank my soon-to-be family, Walter, Peggy, Brian and Megan Lundahl, and my family. My mom, dad and sisters, Lauren and Natalie, have all been there for me throughout this exciting period of my life. Thank you!

DEDICATION

To Walt

Chapter 1. Introduction to Iron Thiolate Metalloenzymes and Biomimetic Models

1.1 Bioinorganic Chemistry

First row transition metal ions such as: manganese, iron, cobalt, nickel, copper and zinc are employed by nature to carry out a wide variety of functions essential to life.[1] The specific activity of the metal is due to the unique environments of the metal within the metalloenzymes.[2] These functions include, but are not limited to, cell replication, O_2 transport, water oxidation, tumor suppression, biosynthesis of neurotransmitters, photosynthesis and the degradation of toxic radicals.[3,4] Thus, metalloenzymes play important roles in our health, the development of sustainable energy and green chemistry. Our understanding of the roles of metalloenzymes in biology is of great importance and the focus of bioinorganic chemistry field.

Bioinorganic chemistry encompasses, but is not limited to, enzymology, biochemistry, coordination chemistry and spectroscopy. This multifaceted approach is used to elucidate the functions and mechanisms of metalloenzymes, which can be challenging to study directly since critical biological intermediates in catalytic cycles are short-lived and highly reactive. In addition to life-time constraints of intermediates, the large size, complexity, temperature and solubility constraints of proteins provides additional difficulties when examining intermediates. Catalysis often occurs at the metal ion, which, along with the nearby amino-acids in the primary and secondary coordination sphere, is referred to as the "active site".

To augment the study of proteins, small molecule models of the active sites can be powerful in identifying remarkable reactions occurring in the biological systems. Models have the capacity

to mimic the coordination sphere of the active site and can be tuned to observe reactive intermediates within key fundamental steps in the metalloenzymes reactivity. The knowledge of chemical and physical properties of biomimetic models provides insights into biological pathways and can inspire the design of earth-abundant catalysts.

1.2 Iron Metalloenzymes with Mixed Nitrogen/Sulfur Ligation

Iron is commonly incorporated into many metalloenzymes for O_2 activation due to its accessibility of multiple redox states and the availability of the metal within the earth's crust. These enzymes containing iron can be classified as heme or non-heme. The term heme comes from hemoglobin and describes an Fe ion in a redox active porphyrin ligand environment. Hemoglobin transport of O_2 through the body has been well studied. Cytochrome P450, which breaks down ~70% of pharmaceuticals in the body, contains a heme and a coordinated cysteine (Cys) as well.[5] The cysteine has been shown to increase reactivity and allow for the cleavage of strong C-H bonds in hydrocarbons.

Non-heme iron enzymes typically contain a 2-His-1-carboxylate triad coordination environment.[6] However, there are several examples that break from this trend and contain Cys in the coordination sphere, and/or a tris-His triad. Cysteine plays a significant role in the activation of dioxygen by lowering the activation barrier of O_2 binding and stabilizing a subsequent the Fe^{III}-superoxo intermediate.[7] This is due to the covalent Fe-S bond formed between the cysteinate and Fe^{III} ion. Modeling these types of specific active sites present challenges since thiolates are difficult to manipulate and coordinate to Fe. Thiolates are prone to oligomerization or auto-reduction forming a disulfide therefore fewer cysteinate ligated Fe biomimetic models exist. Yet this dearth of models limits the understanding of many enzymes which would impart significant importance to the fields of health care and industry. The focus of this thesis will be on understanding the

complexities of reactive intermediates with small molecule iron complexes that contain thiolates in the coordination environment.

1.3 Nitrile Hydratase

1.3.1 *Background*

The metalloenzyme, nitrile hydratase (NHase), is one of the first biocatalysts successfully used by industry due to the catalyzation of nitriles to high-value amides (Figure 1.1).[8,9] Currently, NHase produces more than 95 kilotons of acrylonitrile amide per year making up 25% of worldwide output, while nicotinamide, 5-cyanovaleramide and several more high-value amides can be produced by NHase from the corresponding nitriles.[10] The NHase-mediated hydration of amides occurs in neutral aqueous environments at ambient temperatures. These mild conditions coupled with efficient product purification and high reaction yields contrasts traditional methods requiring high temperatures and pressures, and strongly acidic/basic solutions. The applications of NHase goes beyond the commercial production of amides and has shown potential in the bioremediation of toxic nitriles from pharmaceutical and industrial waste water, shale oil, and contaminated soils. [8,10,11] Many nitriles including acrylonitrile are neurotoxic, carcinogenic, and mutagenic compounds. [12–14] The utilization of NHase by industry to carry out important organic reactions under mild conditions and the potential application for environmental clean-up has made it the focus of intense study.

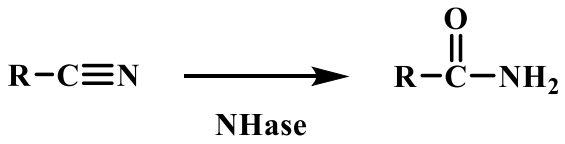

Figure 1.1. Conversion of nitriles to amides by NHase. A protein-derived oxygen is the source of the amide oxygen.[15]

1.3.2 *Structure of Nitrile Hydratase*

The structure of the NHase active site plays a large role in its catalysis. NHase has an unusual active site that contains a low-spin metal ion (Fe^{III} S =1/2 or Co^{III} S = 0) coordinated to three cysteine residues, and the peptide backbone, via two amide-type nitrogen atoms from Ser113 and Cys114 residues. The active form of nitrile hydratase is generated by post-translational modification through the oxidation of two cysteine residues to a Cys-sulfinate (RSO_2^-) and Cys-sulfenate (RSO^-) acids but significantly leaves the third axial cysteine unmodified (Figure 1.2).[16] The selective oxidation of two equatorial cysteine residues is critical for hydratase activity and over oxygenation of Cys–SO^- results in loss of function.[17,18] The reasons proposed for these modified thiolates include modulation of Lewis acidity of the Fe-ion,[19–21] facilitation of reversible nitric oxide (NO) bonding[22,23] and activation of H_2O by the more basic RSO^-.[24–26] The exact role of the Cys-SO^- sulfenate has been greatly debated, and new experimental and computational work is beginning to elucidate its critical role in the hydrolysis of nitriles.

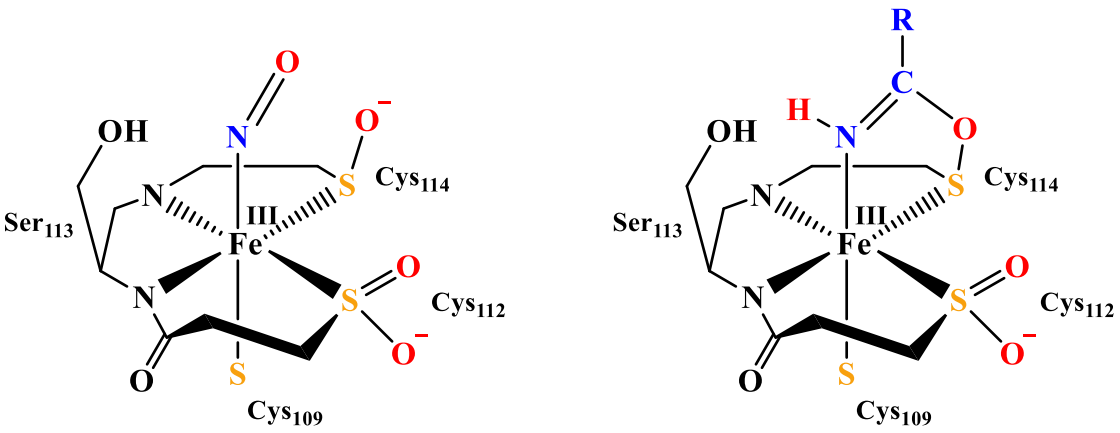

Figure 1.2. Depictions of the active site of NO bound NHase based off the crystallographically determined structure (PDB ID: 2AHJ)[16] and *tert*-butylisonitrile NHase intermediate from time resolved X-ray crystallography.[27]

1.3.3 *Mechanism of Nitrile Hydratase*

Recent experimental and theoretical calculations support an inner-sphere mechanism where Cys-SO^- functions as a nucleophile attacking the metal-coordinated nitrile.[28,29] Heinrich et al. first proposed that the sulfenate acts as a nucleophile from the study of biomimetic Co-complexes however, it was through an outer-sphere mechanism.[30] This was supported by direct evidence involving the enzyme, which showed that the source of the carboxamido oxygen in the amide product comes from the protein-based nucleophilic Cys-SO^- oxygen.[15] More recently, an inner-sphere mechanism was proposed (Figure 1.3).[28] This mechanism requires the nitrile to bind to the Fe ion which is in agreement with competitive inhibition studies using butyric acid.[31] The first step after nitrile coordination is the nucleophilic attack by the oxygen atom from Cys-SO^- forming the cyclic intermediate (A_{NHase}). Recently, the time-resolved crystal structure of a cyclic intermediate supports the initial step in the reaction is *tert*-butylisonitrile binding of to the Fe-ion

(Figure 1.2).[27] Cleavage of the cyclic intermediate occurs through attack of the Cys109 on the sulfur atom resulting in the cleavage of the S-O bond and the formation of a disulfide bond (B_{NHase}). Protonation of the nitrogen generates the amide bound intermediate (C_{NHase}). The amide product is released (D_{NHase}). There is little experimental evidence to support the later steps covering the reformation of the active site (C_{NHase} through E_{NHase}). Additional hybrid quantum mechanics/molecular mechanics (QM/MM) studies supports a cyclic intermediate and a disulfide switch in the mechanism but regenerate the sulfenate concurrent to the amide formation.[29] The combined work of enzymatic, biomimetic and computational studies has begun to elucidate the structure function relationship in this unique protein environment allowing for the catalysis of amides. However, how this unusual active site is initially formed and the subsequent reaction steps following nucleophilic attack are still ambiguous. Further work is needed to understand the structure and function of NHase to advance the use of this metalloenzyme and bio-inspired catalysts capable of economical and eco-friendly synthesis of amides.

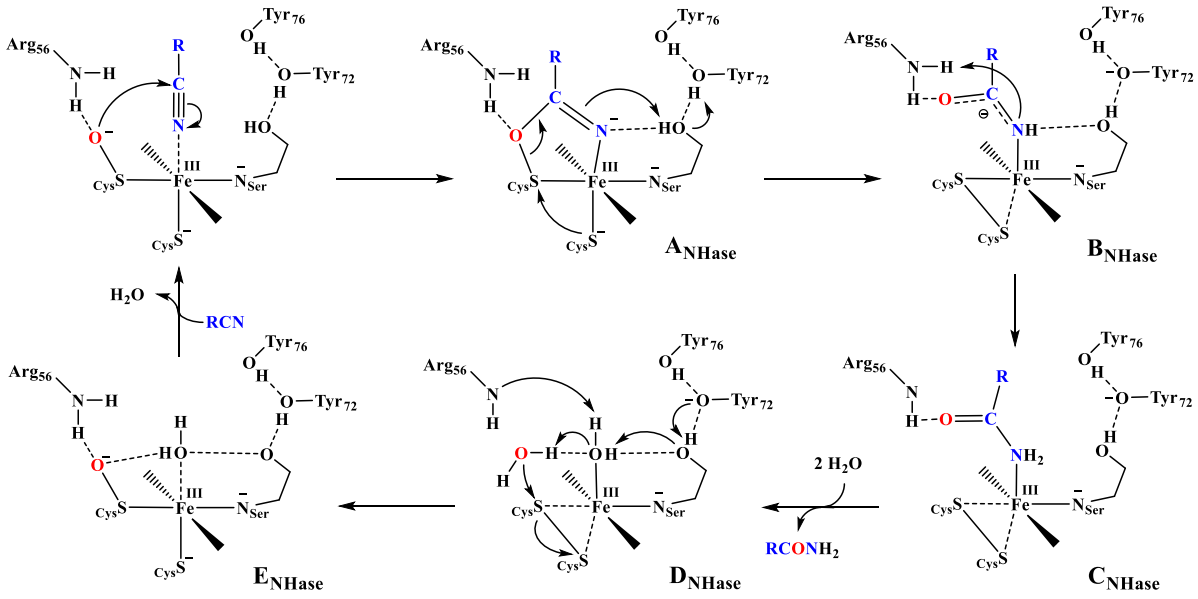

Figure 1.3. Proposed catalytic mechanism of NHase and active-site regeneration by Hopmann.[28] The doubly oxygenated sulfinate is out of plane to the back and was not labeled for clarity.

1.3.4 *Model Chemistry*

The void of experimental evidence regarding both the mechanism of formation of the active site and nitrile hydrolysis by NHase enzymes has greatly motivated studies involving biomimetic, transition metal-thiolate complexes and O_2 or other oxo atom transfer agents, which yield sulfur oxygenates.[32] The majority of reported small molecule enzyme analogues form doubly oxygenated (sulfinate) or triply oxygenated (sulfonate) products; only a few singly oxygenated (sulfenate) complexes have been reported.[32,33] Selective S-oxygenation is synthetically challenging therefore only a handful of mixed sulfinate/sulfenate complexes have been reported.[34–38] Of these only a ruthenium complex had an open coordination site and was capable of activating nitriles but had low catalytic activity.[37] There has yet to be a functional iron model complex reported. Despite this, studies on Fe containing mimics have provided insights into the structure and function of NHase.

Notable mixed N/S ligated Fe complexes that have contributed to the understanding of the unique active site of NHase are herein described. Mascharak reported a square pyramidal complex with two aromatic thiolates that readily binds NO at -40 °C (Figure 1.4).[39] Non-selective oxygenation of the thiolates using (1*S*)-(+)-(10-camphorsulfonyl)oxaziridine produces the bis-sulfinate (Figure 1.4).[39] After this modification the NO photoreleases replicating the photoactivation of NO-bound NHase observed by enzymatic studies.[17] This suggests S-oxygenation is essential for the photoregulation using NO of NHase activity.

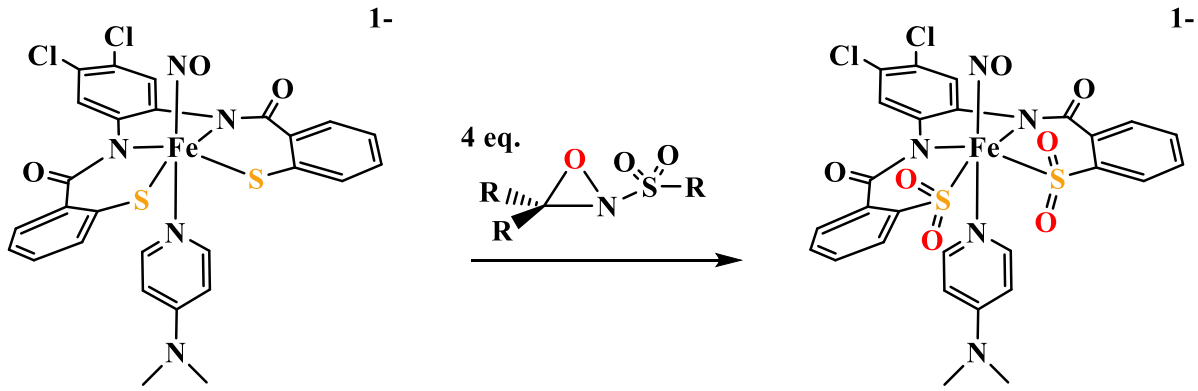

Figure 1.4. Thiolate S-oxygenation of NO-bound synthetic Fe-NHase model using (1*S*)-(+)-(10-camphorsulfonyl)oxaziridine at -40 °C.[39]

The key role of regulating the electronic properties of the metal ions within metalloenzymes is often allocated the atoms ligating the metal. The Kovacs group has demonstrated the key role of thiolates in the modulating the spin state in many first-row transition metals.[20,36,40–43] One extremely relevant example is a series of modifications to a six-coordinate bis-thiolate Fe^{III} complex that establishes the importance on the effect of oxygenation of the thiolates and the impact it will produce on the electronics of the iron. The starting Fe^{III} complex,

$[Fe^{III}(ADIT)_2)]^+$, was synthesized without an available coordination site allowing for the selective oxygenation of only one of the thiolate ligands provided electronic insights into the compensatory effect of the unmodified thiolate. First $[Fe^{III}(ADIT)_2)]^+$ underwent S-oxygenation using tert-butyl N-sulfonyloxaziridine (Figure 1.5). The singly oxygenated $[Fe^{III}(ADIT)(ADIT\text{-}O)]^+$ was the first isolated and characterized Fe^{III}-sulfenate complex.[20] Spectroscopic studies including sulfur K-edge X-ray absorption spectroscopy (XAS) revealed that the bond between the unmodified thiolate and Fe ion increased in covalency upon single oxygen atom addition. Addition of a strong acid at low temperatures results in the protonation of the sulfenate further weakening the Fe-SOH π-bond since SOH is a poorer ligand. The unmodified thiolate increases its electron donation to the Fe ion compensating for this modification as well. Whether the sulfenate of NHase is protonated or not has not been unambiguously determined.[44] However, the unmodified thiolate is capable of tuning the electronic properties of the Fe ion thus stabilizing the 3+ oxidation state and the low spin-state Fe-NHase requires for catalytic activity.

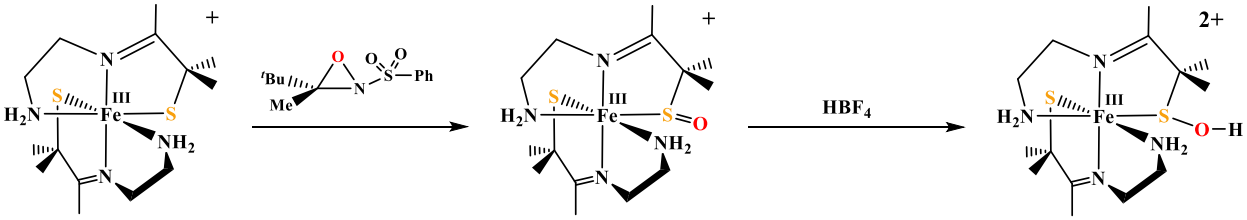

Figure 1.5. Formation of the singly oxygenated $[Fe^{III}(ADIT)(ADIT\text{-}O)]^+$ and subsequent protonation of the sulfenate.[20]

While the two examples above demonstrate important aspects of thiolate oxidation, they do not contain the N_2S_3 ligand environment which is critical and observed in NHase. Two systems that better represent the active site are structural isomers reported by Chottard and Kovacs readily

react with dioxygen (Figure 1.6).[42,45] Chottard's model was the first to undergo S-oxygenation from O_2 which is the likely oxidant that NHase uses for its post translational modification.[45] For both complexes the apical thiolate was oxygenated by O_2 and the equatorial thiolate donors were left unmodified. In the latter case the Fe^{III} starting material was isolated and revealed a long Fe-S bond for the apical thiolate.[42] The regioselectivity for O_2 addition is likely due to the susceptibility of the apical thiolate. Neither of the monosulfinate complexes bind an additional ligand trans to the O-bound sulfinate thus do not display catalytic activity. Very little is known about the sequence of thiolate oxidation needed to create the active site of NHase.[46] These examples show there is still much to learn from small molecule models where synthetic tuning of the ligands is possible to probe the effects on reactivity.

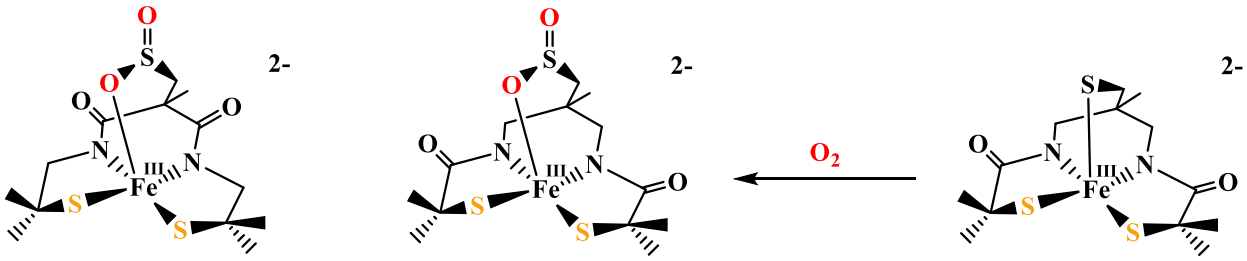

Figure 1.6. Chottard's first example of a Fe-sulfinate derived from O_2 (left).[41] Sulfinate complex $[Fe^{III}(tame\text{-}N_2SO_2)S_2{}^{Me2})]^{2-}$ produced from the oxygenation of $[Fe^{III}(tame\text{-}N_2S)S_2{}^{Me2})]^{2-}$ (right). [42]

1.4 Cysteine dioxygenase

1.4.1 *Background*

Cysteine dioxygenase (CDO) is a non-heme mononuclear iron(II) enzyme that regulates the concentration of Cys by utilizing dioxygen to oxidize Cys to cysteine sulfinic acid (CSA) and

initiates the cysteine catabolism pathway in mammals (Figure 1.7).[47] A decrease in CDO activity, leading to the accumulation of cysteine, has been linked to neurological disorders, including Parkinson's, Alzheimer's diseases as well as autoimmune disorders.[48] Recently, a genetic mutation of CDO has been linked to ~60 % of breast cancers and has an influence on the progression of the disease and outcome.[49] Despite its medical importance, CDO's atypical active site structure and the mechanism of sulfur-oxidation are not well understood.

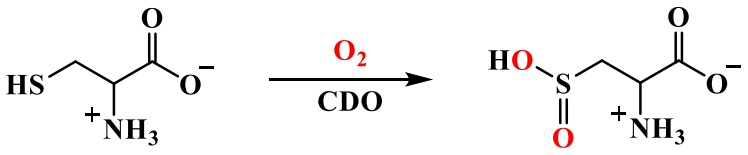

Figure 1.7. CDO catalyzed conversion of cysteine to sulfinic acid (CSA).

1.4.2 *Structure of Cysteine Dioxygenase*

Similar to NHase, CDO is one of a small group of non-heme iron oxygenases whose active sites differ from the 2-His-1-carboxylate triad coordination environment and does not follow either of the two major reactivity pathways by dioxygenases.[50] An extensive study with an X-ray crystallography structure revealed an Fe^{II} center bound to three neutral histidine residues and a rare cysteinyltyrosine intermolecular cross-link (Figure 1.8).[51] Human CDO was crystallized under high concentration of cysteine with lower resolution (2.7 Å) and showed the binding of cysteine to the Fe ion (Figure 1.8). [52] However, doubt was initially cast on if Cys-bound Fe^{II}-CDO is an active species by extended X-ray absorption fine structures (EXAFS) spectroscopy study that found no evidence of sulfur in the primary coordination sphere.[53] Cysteine bound Fe^{II}-CDO

complex does not have a feature in the visible absorbance spectrum thus cannot be tracked by electronic absorbance spectroscopy.[54] Brunold and co-workers reported resonance Raman and magnetic circular dichroism (MCD) spectra of CDO with features characteristic of thiolate ligation to Fe ions. [54] Jameson and co-workers utilizing Mössbauer spectroscopy showed the emergence of a quadrupole doublet upon cysteine binding to Fe^{II} ion with a considerable decrease in the isomer shift from 1.2 to 0.80 mm s^{-1} consistent with covalent Fe-S bonds.[55] Additionally, other cysteines are critical to enzyme activity as site-directed mutagenesis studies showed the cysteinyltyrosine (Tyr157-Cys93) cross-link in the secondary coordination sphere is important to catalytic activity.[52,56,57] Collectively, these experimental findings provide support for cysteine binding being the initial step in CDO's catalytic cycle and the involvement of the Tyr157-Cys93 residues.

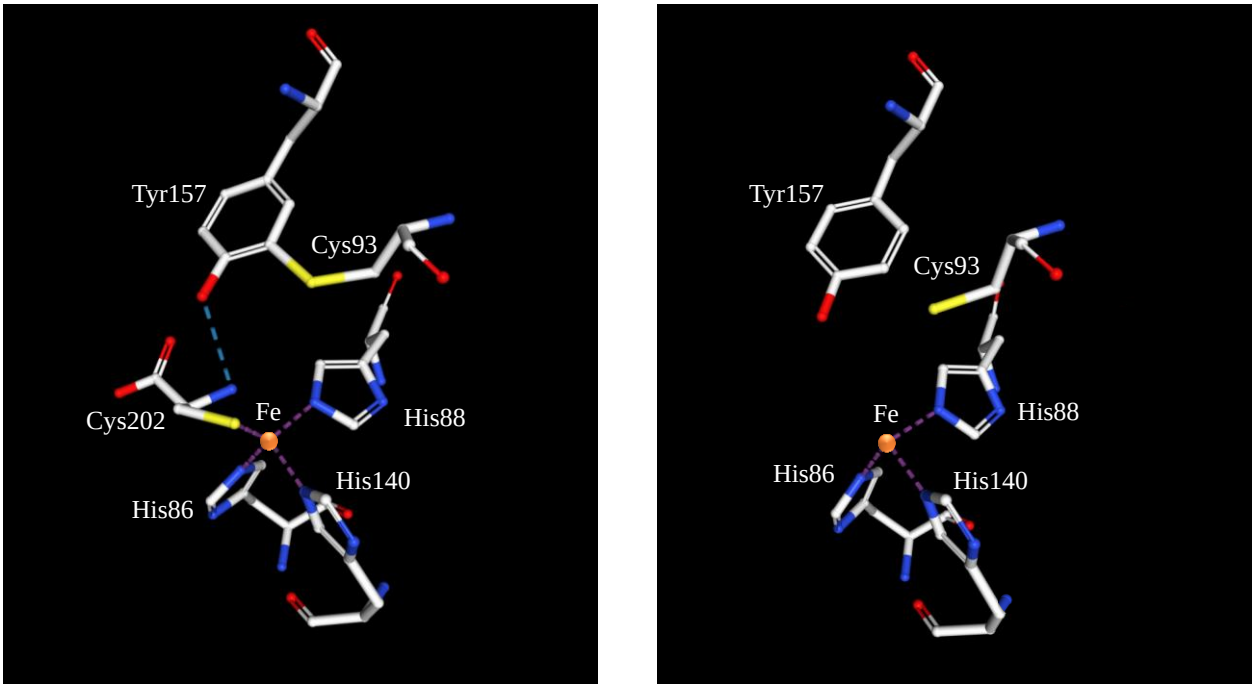

Figure 1.8. The active site of rat CDO with cross link (PDB ID: 2B5H)[51] (left) and human CDO-Cys (PDB ID: 2IC1)[52] (right).

1.4.3 *Mechanism of Cysteine Dioxygenase*

For CDO, there are several competing potential mechanisms with limited supporting experimental evidence. Theoretical calculations have shown that the direct involvement of the metal ion provides a lower energy pathway to sulfur oxygenation.[58,59] In proposed pathways, a cysteine binds to an Fe^{II} ion, which then binds O_2 *cis* to the $^{cys}S^-$, to generate an Fe^{III}-superoxo intermediate. Pierce et al. performed a single turnover using CDO-Fe^{III} and a superoxide anion to support the first step of the mechanism is the formation of a Fe^{III}-superoxo.[60] After this step the proposed mechanisms diverge. Several purely computational studies from the Visser group using quantum mechanics/molecular mechanics (QM/MM) calculations modeling CDO and density functional theory (DFT) on model complexes set out to elucidate if a peroxythiolate bound Fe-CDO species that has been crystallographically isolated[61] is a catalytically active species (Figure 1.9).[59,62–64] The predicted pathway does not include this species but it can be found on a higher energy pathway. The QM/MM study predicted mechanism[59] begins with an Fe^{III}-superoxo (**A**) with $S = 0$ spin state (Figure 1.10). Then the distal oxygen attacks the thiolate forming a four-membered ring, RS-Fe^{II}-O-O (**B**). Heterolytic cleavage of the O-O bond is proposed to yield a singly oxygenated $^{cys}SO^-$ sulfenate and an Fe^{IV}-oxo (**C**). A S=O rotation (**D**) followed by *cis*-migration of the oxo affords a doubly oxygenated cysteine sulfinate (**E**). Thus, the Visser mechanism proposes a high valent Fe^{IV} species for the second oxidation, which differs from other proposed mechanisms.[59,62–64]

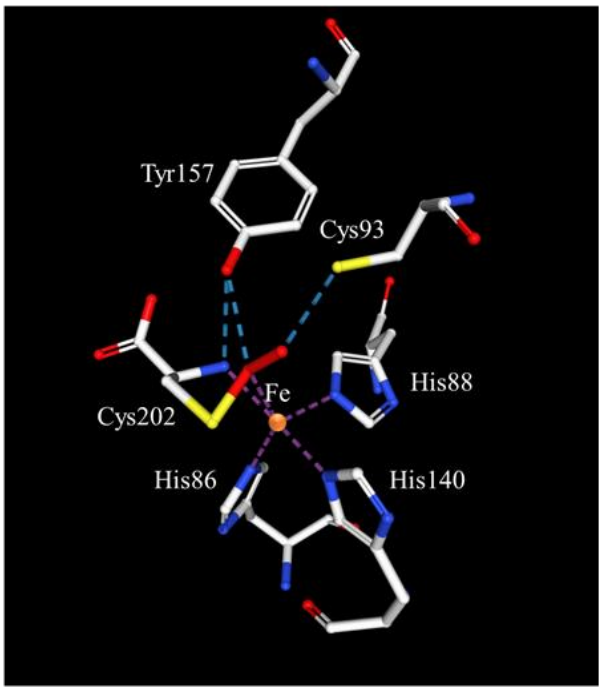

Figure 1.9. Trapped persulfenate bound to Fe-CDO that has been crystallographically isolated (PDB: 3ELN).[61]

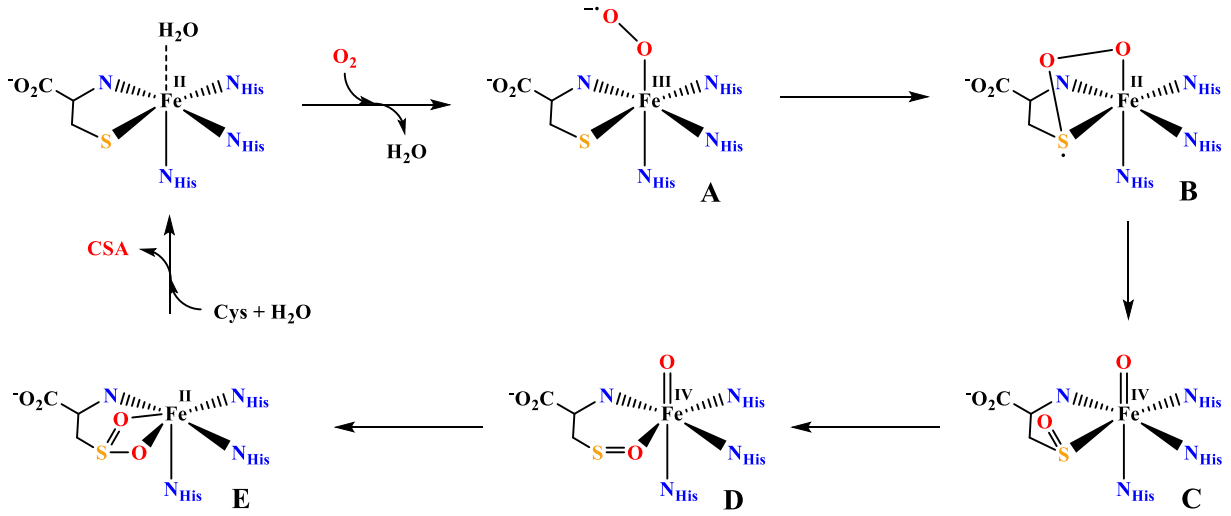

Figure 1.10. Proposed CDO mechanism calculated by Visser et al. [59,62–64]

Another mechanism was developed using nitric oxide (NO) and azide (N_3^-) as analogues for O_2 to mimic the early reaction intermediates of CDO, collecting MCD, electron paramagnetic resonance (EPR) and electronic absorption spectra of these species to validate computational methods used. [65,66] They performed a computational study focusing on the differences in reactivity between Cys- and selenocysteine (Sec)-bound CDO with O_2. The former is the natural substrate that is oxidized to CSA and the latter is not oxidized by CDO.[54] They replaced the NO in the computational models with O_2 to determine the nature of catalytically relevant intermediates and investigated several spin states for each. Their proposed mechanism begins with a high spin Fe^{II}-CDO that binds O_2 forming an intermediate spin Fe^{III}-superoxo (**F**) that is ferromagnetically coupled with the superoxide racial (Figure 1.11). They believe a resonance form (**'F**) with substantial radical character on the sulfur is essential for directing the formation of the first S-O bond. However, their own computational investigations show little unpaired spin density on the sulfur atom thus it's a relatively minor contributor. The cysteinyl sulfur's lone pair attacks the distal oxygen and the superoxide transfers an electron back to the Fe^{III} center. This intermediate (**G**) possess a high spin Fe^{II} bound to a persulfenate moiety. Next, a spin-crossover occurs by a homolytic O-O bond cleavage forms an intermediate spin Fe^{III}-oxyl species (**H**) and sulfur radical that could recombine to form the second S-O bond. However, this last step was not investigated. The same mechanism but for the substrate analogue Sec was compared and found the major differences in optimized geometries for the Fe^{III}-superoxo species. For the Sec-bound Fe-CDO the dioxygen adduct is above the Fe-Se bond to a geometry that is nearly identical to the crystal structure of the persulfenate-bound CDO. Therefore, they suggest the persulfenate-CDO is an off-reaction-pathway species and formation of a dioxygen adduct is thermodynamically unfavorable. This hypothesis is consistent with the observation of the same Sec-CDO samples independent of

an aerobic or anerobic preparation. Brunold's proposed mechanism favors a step-wise addition of O_2 to cysteine rather than a concerted mechanism that a persulfenate species would support.

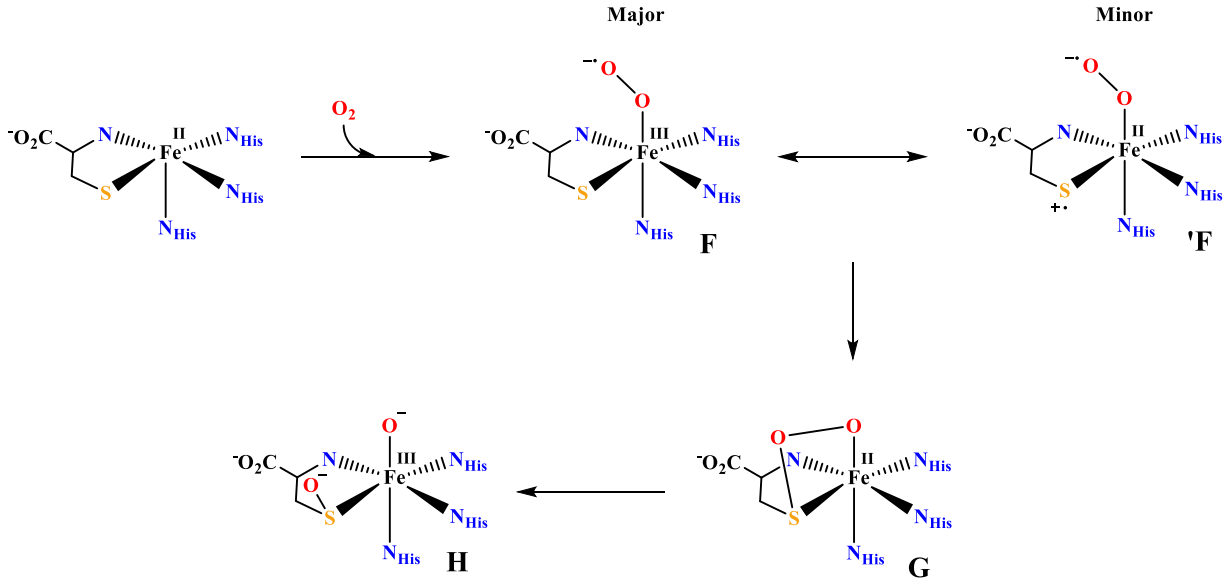

Figure 1.11. Proposed CDO mechanism calculated by Brunold et al.[65,66]

Recently obtained X-ray crystal structures of CDO have led to the first proposed mechanism for the formation of the Tyr157-Cys93 crosslink where the Cys93 is oxidized first and influenced new computational studies that support a concerted mechanism. Computational studies based off a crystal structures of NO-bound Fe^{II}-CDO with and without the Tyr157-Cys93 cross-link.[67] The latter structure was isolated by incorporating 3,5-difluoro-$_L$-tryosine at the active site. In the uncross-linked NO-bound Fe^{II}-CDO structure, Cys93 is positioned only 3.1 Å away from the NO ligand closer than assumed from the previous structures that contained the cross-link (Figure 1.12). In addition, they calibrated their DFT methods to the *g*-tensor and ^{14}N hyperfine

tensor values from the EPR spectra of the NO-Fe^{II}-CDO complexes. The proximity of Cys93 to the Fe center suggests the more reactive cysteine could be oxidized first instead of the Tyr which has been proposed previously.[68,69] Cysteine has nearly same one-electron oxidation potential as Tyr (~0.9 V) but a higher nucleophilic property.[70] Upon Cys binding to the Fe center and addition of O_2 then an Fe^{III}-superoxo (**I**) forms that abstracts a hydrogen atom from Cys93 forming an Fe^{III}-OOH (**J**) species (Figure 1.13). The generated thiyl racial then oxidatively attacks Tyr157 forming a thioether bond and a tyrosyl-like radical (**K**). This promotes the protonation of the proximal oxygen in the Fe^{III}-OOH (**K**) resulting in the creation and release of hydrogen peroxide. The ketone species (**L**) then abstracts a cleaves the C-H bond forming the active site of CDO. Now the Tyr157 residue is positioned to enhance the catalytic conversion of cysteine to sulfinic acid.

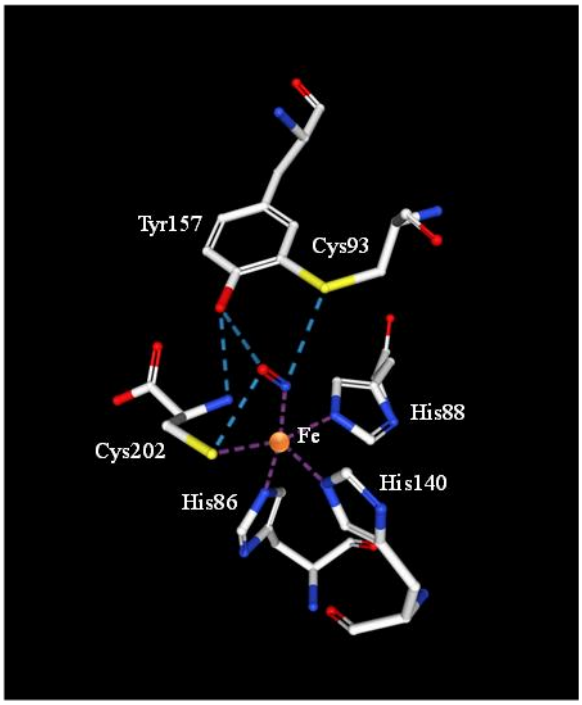

Figure 1.12. Depiction of the active site of cysteine, nitric oxide-bound ferrous form of the crosslinked human cysteine dioxygenase in the anaerobic condition (PDB ID: 6N43)[71]

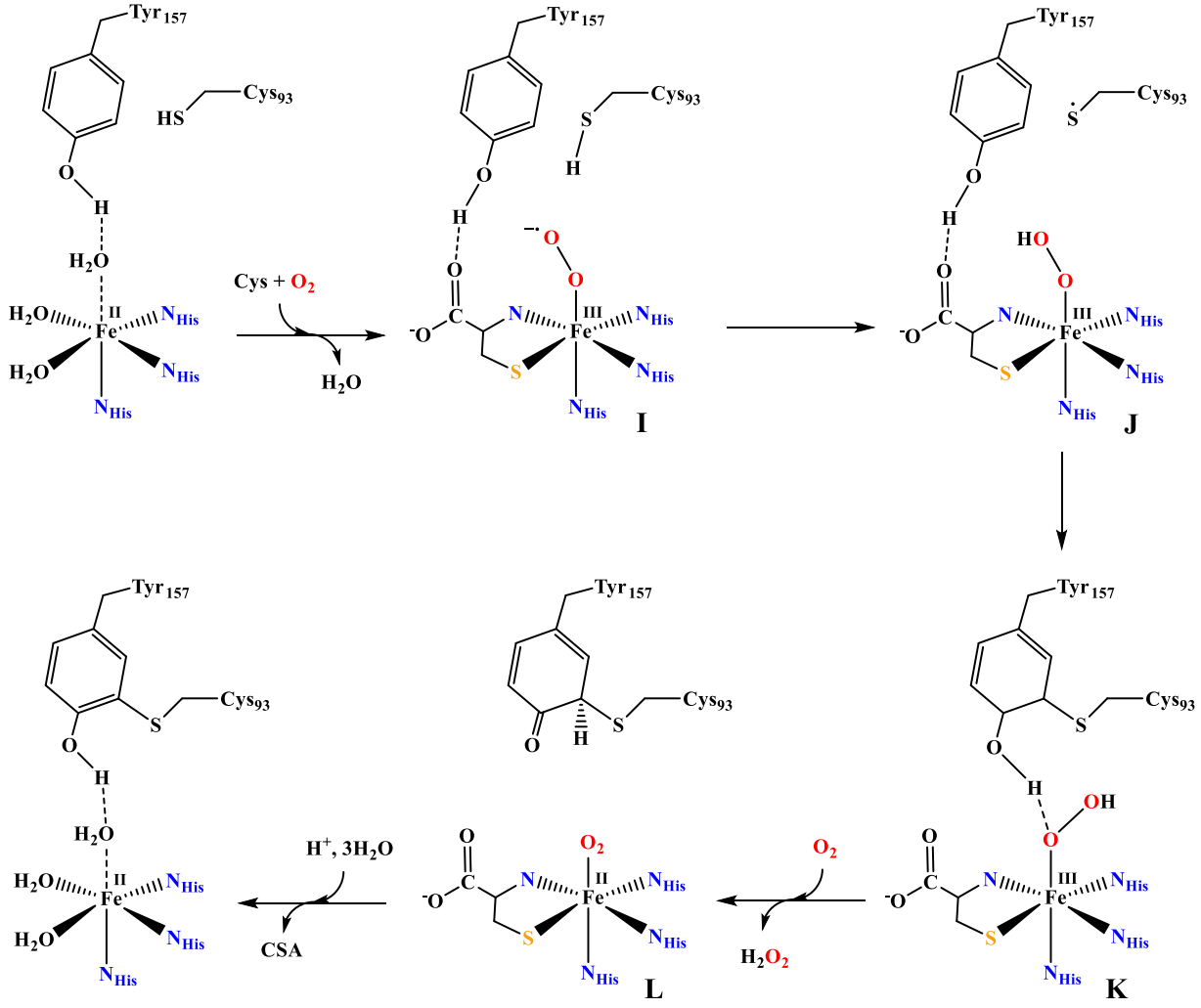

Figure 1.13. Proposed pathway for Tyr-Cys cross-link formation by Liu et al.[71]

In CDO's production of cystine sulfinic acid, the Tyr157-Cys93 cross-link plays a large role by interacting with the first intermediate that forms when O_2 is introduced. Like other proposed mechanisms the first intermediate is an Fe^{III}-superoxo (**M**) which through interacting with multiple active site residues (Figure 1.14). The distal oxygen is 2.9 Å from the phenolic oxygen of Tyr157, 3.1 Å from His155 and 3.2 Å from the sulfur of the Cys93. The Tyr-Cys cofactor and the His155 residues hold the distal oxygen in place allowing the proximal oxygen to

oxidize the sulfur (**O**). Then the attack of the peroxide on the radical thiol leads to the next intermediate and O-O bond cleavage. This completes the concerted mechanism for oxidation of cysteine to cysteine sulfinic acid. Their proposed mechanism reopens the possibility of a persulfate intermediate in the catalytic cycle as first suggest by the crystal structure.[61] Future work towards spectroscopic and structural studies of dioxygen intermediates are needed to provide a better understanding of CDO's mechanism.

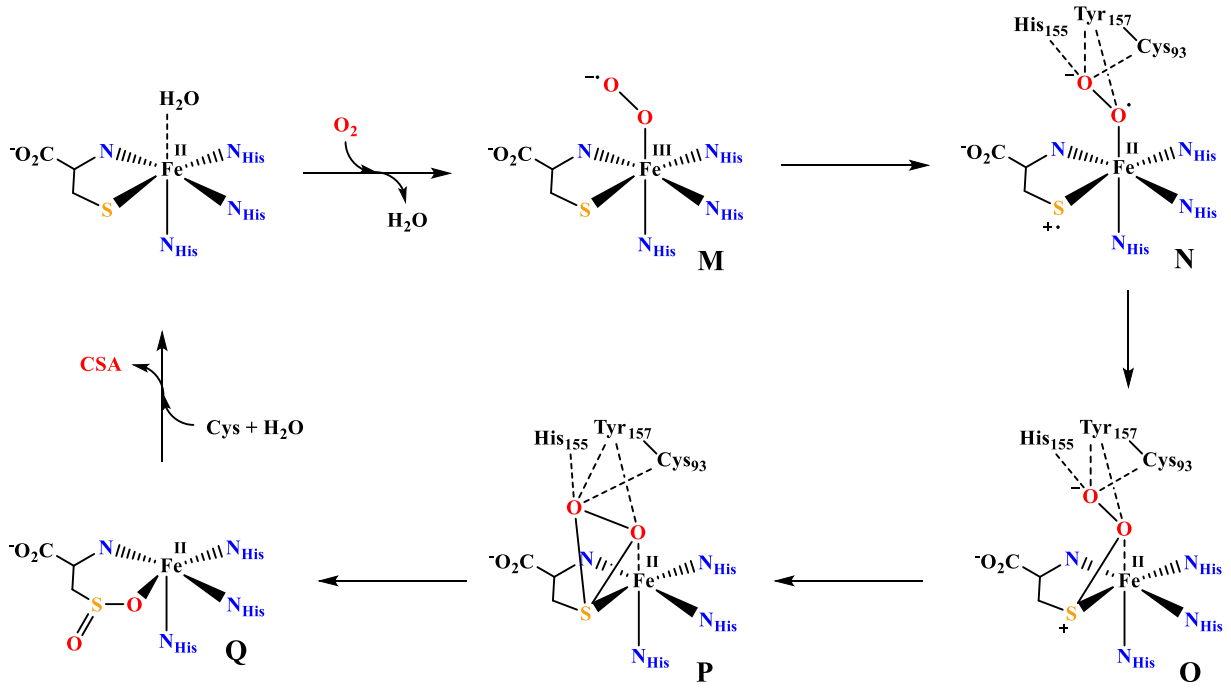

Figure 1.14. Proposed CDO pathway with assistance of the Tyr-Cys cross-link by Liu et al.[67,71]

Experimental evidence of CDO intermediates suggesting a specific mechanism is limited. Thus far only one intermediate has been observed transiently (for ~20 milliseconds) using stopped flow electronic absorption spectroscopy, which has absorption maxima at 500 nm and 640 nm.[72] This species was assigned as the Fe^{III}-bicyclic ring species using TD-DFT and *ab initio* (CASSCF/NEVPT2) methods resembling the intermediate D (Figure 1.10). They could not

conclusively rule out the Fe^{III}-superoxo as the identity of the transient intermediate from these calculations and recent small molecule intermediates suggest an Fe^{III}-superoxo assignment.[72,73] Further attempts to definitively characterize the observed enzyme intermediate were unsuccessful. Thiolate containing biomimetic models of these dioxygen intermediates may help elucidate the CDO mechanism and aid in the calibration of theoretically calculated intermediates.[32,59]

1.4.4 *Model Chemistry*

Prior to 2010 there were no reported examples of S-oxygenation of an Fe^{II}-thiolate complex using dioxygen analogous to CDO's reactivity. The majority of Fe^{II} plus O_2 reactions result in the oxygenation of the Fe ion producing a Fe^{III}_2-μ-oxo complexes or Fe-oxo clusters and disulfide products. For example, our group reported that $[Fe^{II}(S^{Me2}N_4(tren))]^+$ reacts with O_2 forming a Fe^{III}-O-Fe^{III} complex despite having a thiolate cis to the O_2 binding site.[74] The Goldberg lab was the first to report an Fe^{II} complex, $[Fe^{II}(LN_3S)(OTf)]$, reacting with dioxygen to produce a sulfonate (Figure 1.15).[75] Dioxygen was the sole source of oxygen atoms to produce the sulfonate.[75] Using isotope labeling, they found that the first two oxygen atoms were added from the same oxygen molecule, [75] the same as was found in the $^{18}O_2$ isotope studies reported for CDO.[76] The analogous Zn^{II} complex was synthesized and did not react with O_2. Emphasizing an inner-sphere mechanism is responsible for S-oxygenation since O_2 does not directly react with the thiolates. Later, a collaborative effort between Visser and the Goldberg groups carried out the first computational study on a biomimetic model $[Fe^{II}(N_3LS)(OTf)]$.[64] The calculated mechanism for this system produces a sulfinate through an analogous pathway to CDO that Visser reported the year before.[59,64] Importantly, dioxygen binding to the Fe ion is energetically favored over direct attack

of the thiolate.[64] Additional work towards a biomimetic CDO model that did not over oxidize to sulfonates was pursued by several groups.

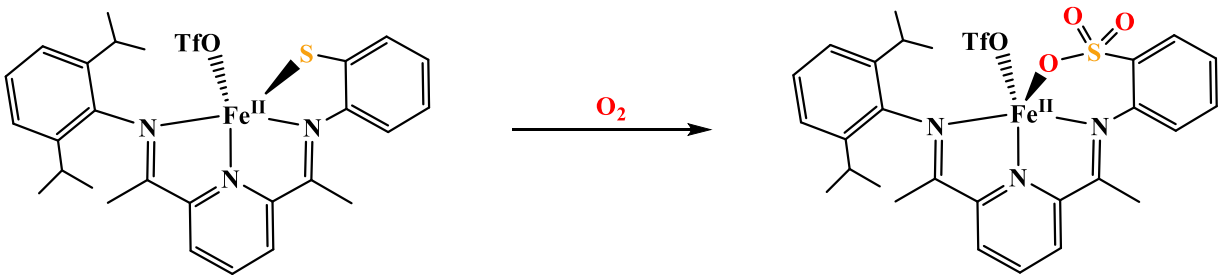

Figure 1.15. S-oxygenation mediated by [Fe^{II}(LN$_3$S)(OTf)] and O_2 producing a sulfonate complex.[75]

Successful imitation of the structure and function of CDO was reported by several groups but these models have yet to reveal characterizable intermediates. The first was a trispyrazolylborato Fe^{II} complex, [Fe(CysOEt)(^{Ph,Me}Tp)], with cysteine ethyl ether bound in a bidentate fashion through the sulfur and nitrogen atoms (Figure 1.16). This functional model reacts with O_2 produced sulfinic acid.[77] Shortly after that the first crystallographically characterized Fe-sulfinate, [Fe^{II}(N$_3$PySO$_2$)(NCS)], was reported (Figure 1.16).[78] The structure revealed the sulfinate is bound to the Fe ion through the thiolate and not the oxygen atoms. During the reaction of [Fe^{II}(N$_3$PyS)(CH$_3$CN)]$^+$ with O_2 a transient green intermediate is observed and the only insight into the identity of this intermediate can from chemical detection of a sulfenate. Dimedone which reacts selectively with sulfenic acids, was used to detect by mass spectroscopy the presence of a sulfenic acid in route to the end-sulfinate.[78] In agreement with the calculated mechanisms for CDO, [Fe^{II}(N$_3$PyS)(CH$_3$CN)]$^+$ adds O_2 through monooxygenase-like steps.[78]

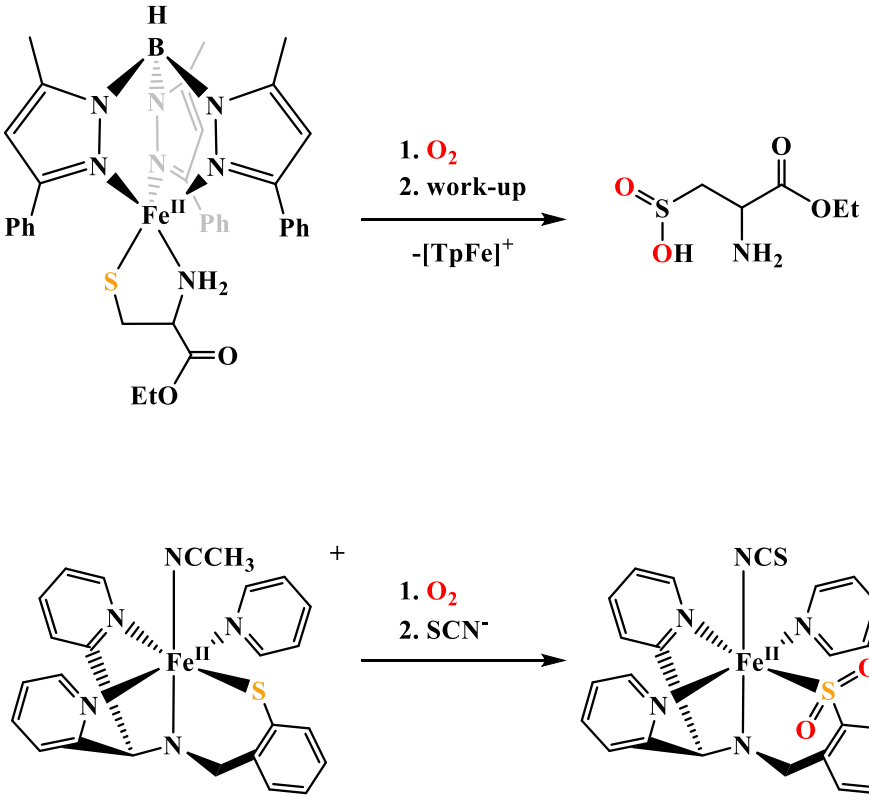

Figure 1.16. Top: $[Fe^{II}(CysOEt)(^{Ph,Me}Tp)]$ reacts with O_2 to produce a sulfenic acid. [77] Bottom: The reaction of $[Fe^{II}(N_3PyS)(CH_3CN)]^+$ with O_2 to make an isolatable sulfinate complex, $[Fe^{II}(N_3PySO_2)(NCS)]$.[78]

A more in depth look at how the covalency of the Fe-S and its influence on reactivity was carried out by Fiedler and Brunold.[79] The high spin Fe^{II} complexes features a ^{Ph2}TIP ligand that represented the three histidine triad and coordinates bidentate $_L$-cysteine ethyl ester (CysOEt) as found by X-ray crystallography, electronic absorption and MCD spectroscopies (Figure 1.17). They compare this system described above used by Limberg, $[Fe^{II}(CysOEt)(^{Ph,Me}Tp)]$, using a combination of kinetic studies of O_2 binding and density functional theory (DFT). The difference in ligands showed no effect on O_2 binding rates but the ^{Ph2}TIP-based model had more radical

character on the thiolate. This potentially aids in the formation of the peroxy-thiolate intermediate in the enzymatic system, but no intermediates prior to sulfinate formation were observed. Therefore, the unusual three histidine active site of CDO may be required for the modulation of the Fe-S bond covalency.

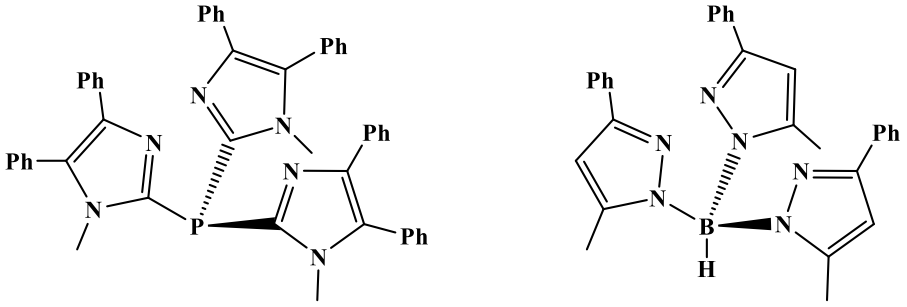

Figure 1.17. The tris(4,5-diphenyl-1-methylimidazol-2-yl)phosphine (^{Ph2}TIP) ligand right and the trispyrazolylborate (^{Ph,Me}Tp) ligand used by Fiedler and Brunold.[79]

The biomimetic models discussed above provided important information about the coordination environment and electronic factors needed for sulfinate formation, however no intermediates were observed en route. Recently, the first example of a thiolate ligated Fe^{III}-superoxo representing the proposed first intermediate in CDO's reaction pathway was reported (Figure 1.18).[73] The species was EPR silent and MCD spectroscopy showed it to be paramagnetic ($S \geq 1$). The electronic absorption spectrum features three absorption bands at 490 (εM = 1200), 655 (1800), 860 nm (2200) similar to the stopped-flow electronic absorption spectra of a CDO intermediate (λ_{max} = 350(sh), 500, 640 nm). Based on these results, Fiedler suggests that the CDO intermediate was incorrectly assigned as the peroxy-thiolate species and is potentially the superoxo species. To date no reactivity has been reported for [$Fe^{III}(O_2)(Tp^{Me2})$(2-ATP)] and decay of the species yields a disulfide product. A transition metal superoxo capable of forming a peroxy thiolate bond has not been reported. An end-on Cr^{III}-superoxo complex has been shown to carry out S-

oxygenation on *p*-methoxythioanisole in the presence of triflic acid (HOTf).[80] The electrophilic nature of the Cr^{III}-superoxo was demonstrated by using a range of para-substituted thioanisoles. Further examples of transition metal-superoxo complexes and their reactivity will be discussed below.

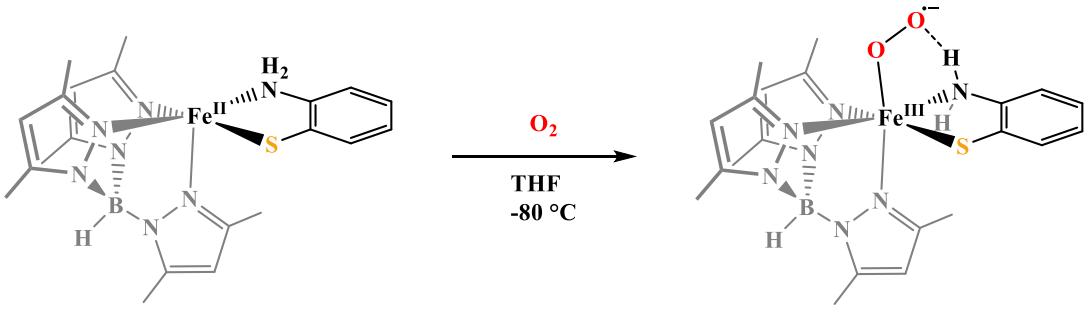

Figure 1.18. Reaction of [$Fe^{II}(Tp^{Me2})$(2-ATP)] with O_2 forming an Fe^{III}-Superoxo.[79]

1.5 Isopenicillin N Synthase

1.5.1 *Background*

Penicillin and other β-lactam antibiotics make up one of the most important classes of medicinal small molecules. The biosynthesis of the essential β-lactam and thiazoldine rings for antibiotic activity is carried out by isopenicillin N synthase (IPNS) (Figure 1.19).[81] IPNS is one of only a few enzymes that carries out a four-electron oxidation without any additional cofactors or co-substrates.[82] Instead it uses an Fe^{II} ion which activates O_2 forming the Fe^{III}-superoxo and Fe^{IV}-oxo intermediates that are both proposed to cleave the C-H bonds. The latter has been utilized as Nature's powerful oxidizer in many enzymatic reactions[83–90] however, the combination with the former intermediate to sequentially cleave C-H bonds using only O_2 is of synthetic interest.

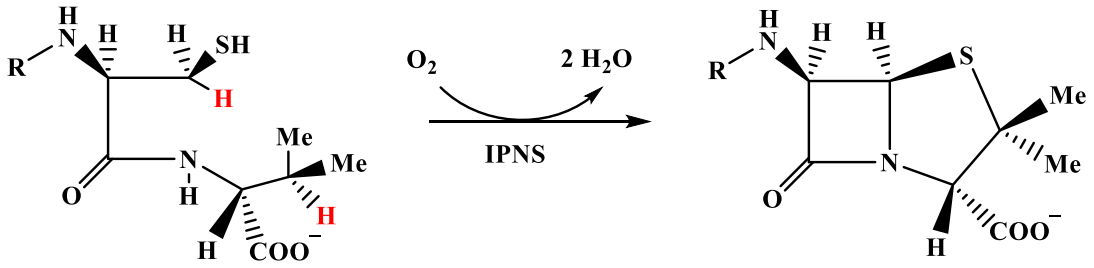

Figure 1.19. The oxidation of *δ*(L-α-aminoadipoyl)-L-cysteinyl-D-valine (ACV) to isopenicillin N (IPN) catalyzed by IPNS.

1.5.2 *Structure of Isopenicillin N Synthase*

Key insights into the mechanism of IPNS have been derived from crystallographic studies. Only the Mn^{II}-substituted IPNS in the resting state has been crystallized.[91] The active site sits in a hydrophobic cavity of a distorted double-stranded β-helix core. The metal ion is bound to a 2-His-1-carboxylate facial triad as well as the side chain of Gln330. Under anerobic conditions, the substrate bound IPNS-ACV-Fe^{II} was isolated (Figure 1.20). The binding of *δ*(L-α-aminoadipoyl)-L-cysteinyl-D-valine (ACV) to Fe^{II} through the cysteinyl thiolate displaces Gln330 causing the rearrangement of the *C*-terminal region.[92,93] The substrate is now held in place via hydrophobic and electrostatic interactions in the active site and is shielded from side reactions during catalysis.[94] From spectroscopic and DFT studies the binding of the cysteinyl thiolate to Fe^{II} is critical to making O_2 binding energetically favored.[7] A dioxygen analogue, NO, was bound to IPNS-ACV-Fe^{II} and crystallized showing the NO is positioned 3.3 Å from the cysteinyl-β-carbon of ACV (Figure 1.20).[93] This positioning may play a role in why IPNS abstracts a hydrogen atom instead of sulfur oxidation like CDO.

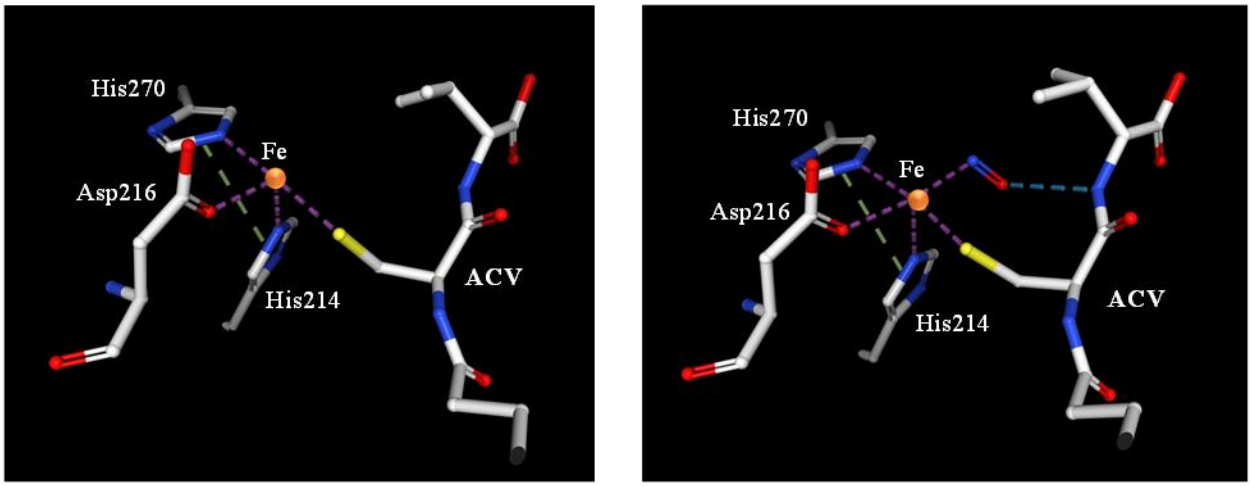

Figure 1.20. The structure of IPNS-ACV-Fe^{II} active site (PDB ID: 1BK0)[93] and IPNS-ACV-Fe^{II}-NO (PDB ID: 1BLZ).[93]

1.5.3 *Mechanism of Isopenicillin N Synthase*

Oxidative ring closures by IPNS has been examined using crystallographic, kinetic and spectroscopic studies leading to a consensus on a proposed mechanism that employs an Fe^{III}-superoxo and Fe^{IV}-oxo as the active oxidants.[93] The formation of the β-lactam ring occurs before the formation of the thiazolidine ring evidenced by kinetics studies on site-specific deuterium-labeled ACV substrates.[95] The reaction is initiated by ACV binding to the Fe^{II} via the cysteinyl thiolate making dioxygen binding more favorable. Dioxygen reacts with the Fe^{II} ion and forms an Fe^{III}-superoxo (A_{IPNS}) with the distal oxygen atom positioned to abstract of the hydrogen on the cysteinyl-β-carbon (β-C_{cys}-H). This reactive species (A_{IPNS}) has been spectroscopically observed using a combination of transient-state-kinetics, stopped-flow absorption and freeze-quench Mössbauer spectroscopies.[96] However, no vibrational data proving the bond order of the O-O bond

and its level of oxidation was reported. The A_{IPNS} intermediate accumulated in higher levels upon deuteration of the cysteinyl hydrogens implicating the observed intermediate as the oxidant responsible for cleaving the β-C_{cys}-H (93 kcal/mol).[97] The resulting Fe^{III}-hydroperoxo (B_{IPNS}) is then reduced by the thiolalkyl radical to an Fe^{II}-hydroperoxo species (C_{IPNS}). The heterolytic cleavage of the O-O bond produces a high-valent Fe^{IV}-oxo (D_{IPNS}) which abstracts a hydrogen atom from the valinyl-β-carbon (β-C_{val}-H). The attack of the valinyl radical (E_{IPNS}) on the thiolate closes the thiazolidine ring yielding the product isopenicillin N bound to the Fe^{II} ion (F_{IPNS}).

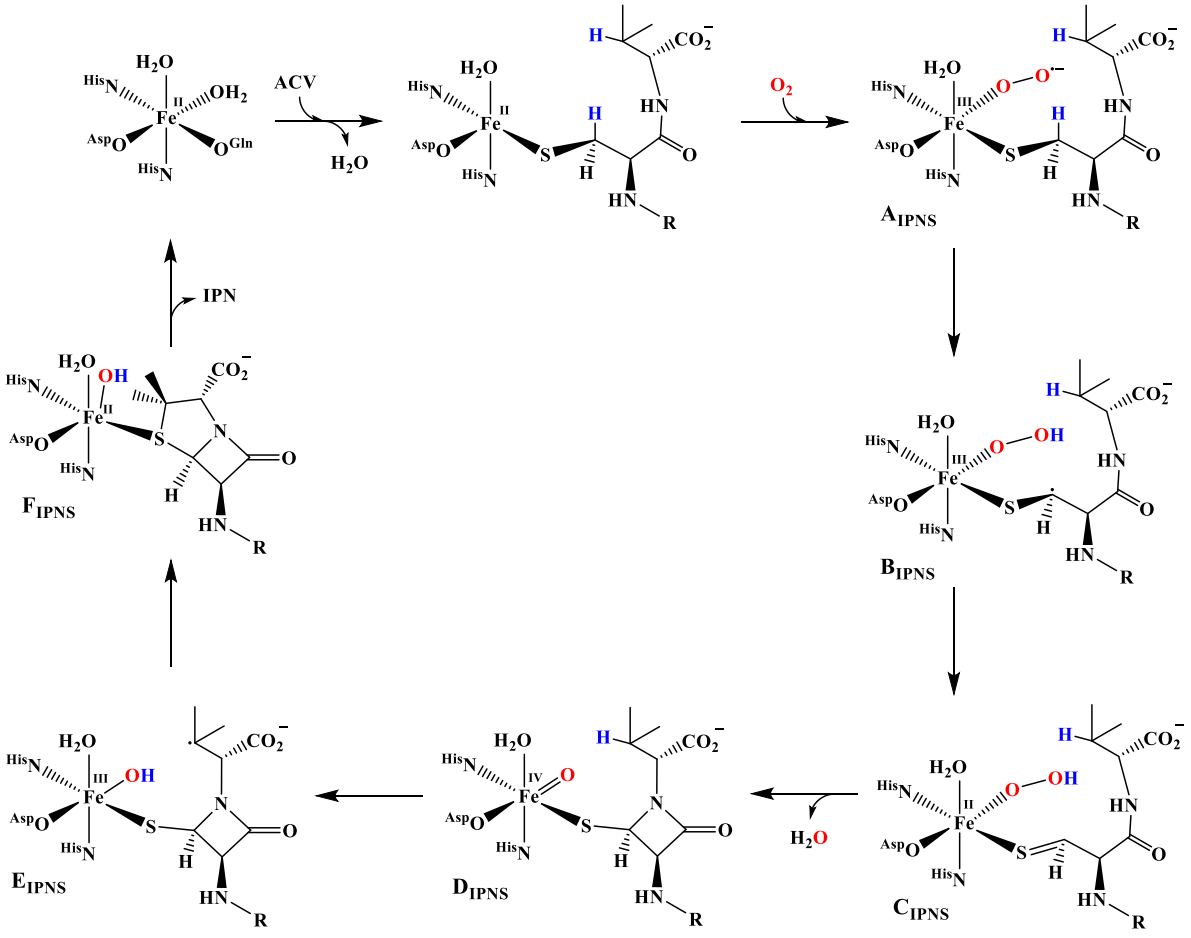

Figure 1.21. The proposed mechanism for IPNS by Baldwin et al.[93]

1.5.4 *Model Chemistry*

The oxidations IPNS carries out use an Fe^{III}-superoxo for the first C-H bond cleavage followed by and Fe^{IV}-oxo for the more difficult cleavage of the unactivated β bond of valine. The latter Fe^{IV}-oxo has been shown to be a powerful oxidant and numerous examples of small molecules models have been reported and reviewed elsewhere.[85,98–101] The former, Fe^{III}-superoxo, has been more elusive. In 2014, the first non-heme mono-nuclear Fe^{III}-superoxo was reported by Lee.[102] The Fe^{III}-superoxo was generated by the reaction of O_2 with a Fe^{II}(BDPP) in tetrahydrofuran (THF) at -80 °C. Complementary spectroscopic methods, resonance Raman and Mössbauer, confirmed the oxidation state of the Fe ion and the nature of the dioxygen adduct as an Fe^{III}-superoxo. This species is capable of abstracting a hydrogen atom from dihydroanthracene (DHA) (Figure 1.22). This supports the predication of an Fe^{III}-superoxo carrying out C-H bond cleavage, but these bonds (78 kcal/mol) were significantly weaker than the β-C_{Cys}-H bond (93 kcal/mol).

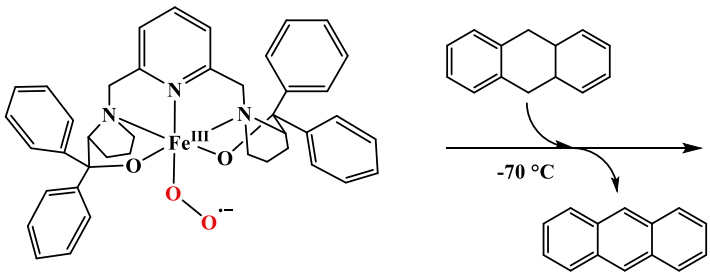

Figure 1.22. Hydrogen atom abstraction reaction of [Fe^{III}(BDPP)(O_2)] with dihydroanthracene (DHA) producing anthracene.[102]

Shortly after additional examples of non-heme mononuclear Fe^{III}-superoxos were reported by several groups. Hikichi characterized an Fe^{III}-superoxo, [Fe^{III}(L^{Ph})(Tp^{Me2})(O_2)], with a five-

azole ligand set in THF at -60 °C.[103] The electronic absorption features (λmax = 350 nm) and resonance Raman data (νO-O = 1168 cm^{-1}, $\Delta^{16O-18O}$ = (-)78 cm^{-1}) were similar to [Fe^{III}(BDPP)(O_2)]. This species has diamagnetic signals in ^{1}H NMR spectra revealing antiferromagnetic coupling between the low-spin (S=1/2) Fe^{III} ion and the superoxide radical. Reactivity studies revealed [Fe^{III}(L^{Ph})(Tp^{Me2})(O_2)] to be a poor oxidant not capable of cleaving weak C-H bonds (67.9 kcal/mol) but able to abstract hydrogen atoms from 2-hydroxy-2-azaadmantane (O-H 72.6 kcal/mol) (Figure 1.23). The reaction of [Fe^{III}(L^{Ph})(Tp^{Me2})(O_2)] with this substrate yielded another characterizable intermediate, Fe^{III}-hydroperoxo (Figure 1.23). The only crystallographically characterized Fe^{III}-superoxo was isolated from the reaction of Fe^{III}(TAML) and potassium superoxide (KO_2).[104] The superoxide was bound through a side-on interaction.[104] The [Fe^{III}(TAML)(O_2)]$^{2-}$ can do both electrophilic and nucleophilic oxidation reactions (Figure 1.23). No reactivity was seen when reacting [Fe^{III}(TAML)(O_2)]$^{2-}$ with weak C-H, such as cyclohexadiene and xanthene. Despite an Fe^{III}-superoxo being implicated as a key intermediate in the catalytic cycle of IPNS, the few biomimetic models have not demonstrating the oxidative power required to activate the β-C_{cys}-H of the precursor to penicillin N.

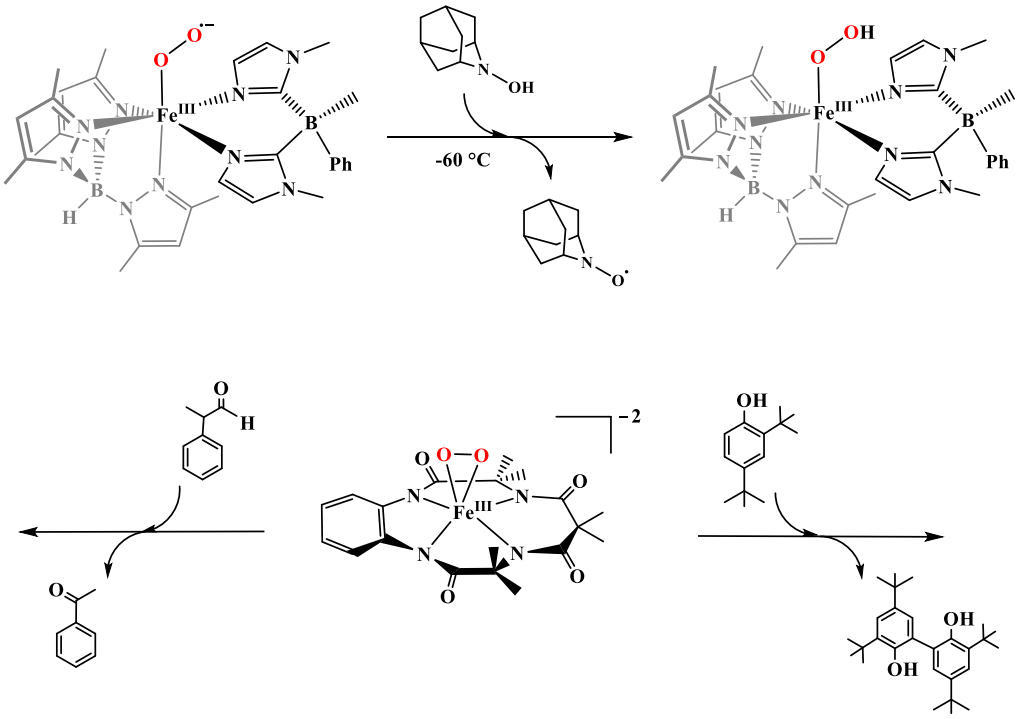

Figure 1.23. Top: Hydrogen atom abstraction from 2-hydroxy-2-azaadamantane (AZADOL) by $[Fe^{III}(L^{Ph})(Tp^{Me2})(O_2)]$.[103] Bottom: $[Fe^{III}(TAML)(\eta^2\text{-}O_2)]$ carrying out aldehyde deformylation of 2-phenylpropionaldehyde to acetophenone (right). $[Fe^{III}(TAML)(\eta^2\text{-}O_2)]$ activating the O-H bond of 2,4-di-tert-butylphenol resulting in the production of 2,2'-dihydroxy-3,3',5,5'-tetra butylbiphenyl (left).[104]

1.6 Concluding Remarks

This introduction provides a brief overview of non-heme iron-thiolate species and their reactivity with dioxygen or oxo atom donors to carry out important transformations. These examples demonstrate how small biomimetic models have aided in the understanding of reaction steps and could potentially add clarity to the active site formation of NHase and deviations in reactivity of the metalloenzymes, CDO and IPNS. Areas of considerable interest remain in the

elucidation of the intermediates involved in the formation of S-oxygenation species and emergence of Fe^{III}-superoxo intermediates as capable oxidants.

1.7 References

(1) Maret, W. The Metals in the Biological Periodic System of the Elements: Concepts and Conjectures. *Int. J. Mol. Sci.* **2016**, *17* (1), 1–8. DOI: 10.3390/ijms17010066.

(2) Williams, R. J. P. Bio-Inorganic Chemistry: Its Conceptual Evolution. *Coord. Chem. Rev.* **1990**, *100*, 573–610. DOI: 10.1016/0010-8545(90)85020-S.

(3) Holm, R. H.; Kennepohl, P.; Solomon, E. I. Structural and Functional Aspects of Metal Sites in Biology. *Chem. Rev.* **1996**, *96* (7), 2239–2314. DOI: 10.1021/cr9500390.

(4) Lippard, S. J.; Berg, J. M. *Principles of Bioinorganic Chemistry*; University Science Books: Mill Valley, CA, 1994.

(5) Guengerich, F. P. Cytochrome P450 and Chemical Toxicology. *Chem. Res. Toxicol.* **2008**, *21* (1), 70–83. DOI: 10.1021/tx700079z.

(6) Hegg, E. L.; Jr, L. Q. The 2-His-1-Carboxylate Facial Triad - An Emerging Structural Motif in Mononuclear Non-Heme Iron(II) Enzymes. *Eur. J. Biochem.* **1997**, *250* (3), 625–629. DOI: 10.1111/j.1432-1033.1997.t01-1-00625.x.

(7) Brown, C. D.; Neidig, M. L.; Neibergall, M. B.; Lipscomb, J. D.; Solomon, E. I. VTVH-MCD and DFT Studies of Thiolate Bonding to {FeNO}7/ {FeO2}8 Complexes of Isopenicillin N Synthase: Substrate Determination of Oxidase versus Oxygenase Activity in Nonheme Fe Enzymes. *J. Am. Chem. Soc.* **2007**, *129* (23), 7427–7438. DOI: 10.1021/ja071364v.

(8) Prasad, S.; Bhalla, T. C. Nitrile Hydratases (NHases): At the Interface of Academia and

Industry. *Biotechnol. Adv.* **2010**, *28* (6), 725–741. DOI: 10.1016/j.biotechadv.2010.05.020.

(9) Debabov, V. G.; Yanenko, A. S. Biocatalytic Hydrolysis of Nitriles. *Rev. J. Chem.* **2011**, *1* (4), 385–402. DOI: 10.1134/s2079978011030010.

(10) Li, T.; Liu, J.; Bai, R.; Ohandja, D. G.; Wong, F. S. Biodegradation of Organonitriles by Adapted Activated Sludge Consortium with Acetonitrile-Degrading Microorganisms. *Water Res.* **2007**, *41* (15), 3465–3473. DOI: 10.1016/j.watres.2007.04.033.

(11) Wyatt, J. M.; Knowles, C. J. Microbial Degradation of Acrylonitrile Waste Effluents: The Degradation of Effluents and Condensates from the Manufacture of Acrylonitrile. *Int. Biodeterior. Biodegrad.* **1995**, *35* (1–3), 227–248. DOI: 10.1016/0964-8305(95)00031-Y.

(12) Gagnaire, F.; Marignac, B.; P., B. Relative Neurotoxicological Properties of Five Unsaturated Aliphatic Nitriles in Rats. *J. Appl. Toxicol.* **1998**, *18* (1), 25–31. DOI: 10.1002/(SICI)1099-1263.

(13) Boadas-Vaello, P.; Riera, J.; Llorens, J. Behavioral and Pathological Effects in the Rat Define Two Groups of Neurotoxic Nitriles. *Toxicol. Sci.* **2005**, *88* (2), 456–466. DOI: 10.1093/toxsci/kfi314.

(14) Stavridis, J. C. Toxicity and Carcinogenicity of the Nitriles. In *Oxidation: The Cornerstone of Carcinogenesis*; Springer Netherlands: Dordrecht, 2008; pp 175–179DOI: 10.1007/978-1-4020-6704-4_12.

(15) Nelp, M. T.; Song, Y.; Wysocki, V. H.; Bandarian, V. A Protein-Derived Oxygen Is the Source of the Amide Oxygen of Nitrile Hydratases. *J. Biol. Chem.* **2016**, *291* (15), 7822–7829. DOI: 10.1074/jbc.M115.704791.

(16) Nagashima, S.; Nakasako, M.; Dohmae, N.; Tsujimura, M.; Takio, K.; Odaka, M.; Yohda,

M.; Kamiya, N.; Endo, I. Novel Non-Heme Iron Center of Nitrile Hydratase with a Claw Setting of Oxygen Atoms. *Nat. Struct. Biol.* **1998**, *5* (5), 347–351. DOI: 10.1038/nsb0698-432.

(17) Murakami, T.; Nojiri, M.; Nakayama, H.; Dohmae, N.; Takio, K.; Odaka, M.; Endo, I.; Nagamune, T.; Yohda, M. Post-Translational Modification Is Essential for Catalytic Activity of Nitrile Hydratase. *Protein Sci.* **2009**, *9* (5), 1024–1030. DOI: 10.1110/ps.9.5.1024.

(18) Tsujimura, M.; Odaka, M.; Nakayama, H.; Dohmae, N.; Koshino, H.; Asami, T.; Hoshino, M.; Takio, K.; Yoshida, S.; Maeda, M.; et al. A Novel Inhibitor for Fe-Type Nitrile Hydratase: 2-Cyano-2-Propyl Hydroperoxide. *J. Am. Chem. Soc.* **2003**, *125* (38), 11532–11538. DOI: 10.1021/ja035018z.

(19) Tyler, L. A.; Noveron, J. C.; Olmstead, M. M.; Mascharak, P. K. Modulation of the PKa of Metal-Bound Water via Oxidation of Thiolato Sulfur in Model Complexes of Co(III) Containing Nitrile Hydratase: Insight into Possible Effect of Cysteine Oxidation in Co-Nitrile Hydratase. *Inorg. Chem.* **2003**, *42* (18), 5751–5761. DOI: 10.1021/ic030088s.

(20) Lugo-Mas, P.; Dey, A.; Xu, L.; Davin, S. D.; Benedict, J.; Kaminsky, W.; Hodgson, K. O.; Hedman, B.; Solomon, E. I.; Kovacs, J. A. How Does Single Oxygen Atom Addition Affect the Properties of an Fe-Nitrile Hydratase Analogue? The Compensatory Role of the Unmodified Thiolate. *J. Am. Chem. Soc.* **2006**, *128* (34), 11211–11221. DOI: 10.1021/ja062706k.

(21) Dey, A.; Jeffrey, S. P.; Darensbourg, M.; Hodgson, K. O.; Hedman, B.; Solomon, E. I. Sulfur K-Edge XAS and DFT Studies on NiII Complexes with Oxidized Thiolate Ligands: Implications for the Roles of Oxidized Thiolates in the Active Sites of Fe and Co Nitrile

Hydratase. *Inorg. Chem.* **2007**, *46* (12), 4989–4996. DOI: 10.1021/ic070244l.

(22) Lee, C. M.; Chen, C. H.; Chen, H. W.; Hsu, J. L.; Lee, G. H.; Liaw, W. F. Nitrosylated Iron-Thiolate-Sulfinate Complexes with {Fe(NO)}6/7 Electronic Cores: Relevance to the Transformation between the Active and Inactive NO-Bound Forms of Iron-Containing Nitrile Hydratases. *Inorg. Chem.* **2005**, *44* (19), 6670–6679. DOI: 10.1021/ic050108l.

(23) Michael, J. R.; Nolan, M. B.; Allen, G. O.; Mascharak, P. K. Binding of Nitric Oxide to a Synthetic Model of Iron-Containing Nitrile Hydratase (Fe-NHase) and Its Photorelease: Relevance to Photoregulation of Fe-NHase by NO. *Inorg. Chem.* **2010**, *49* (4), 1854–1864. DOI: 10.1021/ic902220a.

(24) Hashimoto, K.; Suzuki, H.; Taniguchi, K.; Noguchi, T.; Yohda, M.; Odaka, M. Catalytic Mechanism of Nitrile Hydratase Proposed by Time-Resolved X-Ray Crystallography Using a Novel Substrate, Tert-Butylisonitrile. *J. Biol. Chem.* **2008**, *283* (52), 36617–36623. DOI: 10.1074/jbc.M806577200.

(25) Hopmann, K. H.; Guo, J. D.; Himo, F. Theoretical Investigation of the First-Shell Mechanism of Nitrile Hydratase. *Inorg. Chem.* **2007**, *46* (12), 4850–4856. DOI: 10.1021/ic061894c.

(26) Swartz, R. D.; Coggins, M. K.; Kaminsky, W.; Kovacs, J. A. Nitrile Hydration by Thiolate- and Alkoxide-Ligated Co-NHase Analogues. Isolation of Co(III)-Amidate and Co(III)-Iminol Intermediates. *J. Am. Chem. Soc.* **2011**, *133* (11), 3954–3963. DOI: 10.1021/ja108749f.

(27) Yamanaka, Y.; Kato, Y.; Hashimoto, K.; Iida, K.; Nagasawa, K.; Nakayama, H.; Dohmae, N.; Noguchi, K.; Noguchi, T.; Yohda, M.; et al. Time-Resolved Crystallography of the Reaction Intermediate of Nitrile Hydratase: Revealing a Role for the Cysteinesulfenic

Acid Ligand as a Catalytic Nucleophile. *Angew. Chemie - Int. Ed.* **2015**, *54* (37), 10763–10767. DOI: 10.1002/anie.201502731.

(28) Hopmann, K. H. Full Reaction Mechanism of Nitrile Hydratase: A Cyclic Intermediate and an Unexpected Disulfide Switch. *Inorg. Chem.* **2014**, *53* (6), 2760–2762. DOI: 10.1021/ic500091k.

(29) Kayanuma, M.; Shoji, M.; Yohda, M.; Odaka, M.; Shigeta, Y. Catalytic Mechanism of Nitrile Hydratase Subsequent to Cyclic Intermediate Formation: A QM/MM Study. *J. Phys. Chem. B* **2016**, *120* (13), 3259–3266. DOI: 10.1021/acs.jpcb.5b11363.

(30) Heinrich, L.; Mary-Verla, A.; Li, Y.; Vaissermann, J.; Chottard, J. C. Cobalt(III) Complexes with Carboxamido-N and Sulfenato-S or Sulfinato-S Ligands Suggest That a Coordinated Sulfenate-S Is Essential for the Catalytic Activity of Nitrile Hydratases. *Eur. J. Inorg. Chem.* **2001**, No. 9, 2203–2206. DOI: 10.1002/1099-0682(200109)2001:9<2203::AID-EJIC2203>3.0.CO;2-A.

(31) Kopf, M.-A.; Bonnet, D.; Artaud, I.; Pétré, D.; Mansuy, D. Key Role of Alkanoic Acids on the Spectral Properties, Activity, and Active-Site Stability of Iron-Containing Nitrile Hydratase from Brevibacterium R312. *Eur. J. Biochem.* **1996**, *240* (1), 239–244. DOI: 10.1111/j.1432-1033.1996.0239h.x.

(32) McQuilken, A. C.; Goldberg, D. P. Sulfur Oxygenation in Biomimetic Non-Heme Iron-Thiolate Complexes. *Dalton Trans.* **2012**, *41* (36), 10883–10899. DOI: 10.1039/c2dt30806a.

(33) Kumar, D.; Grapperhaus, C. A. Sulfur-Oxygenation and Functional Models of Nitrile Hydratase. In *Bioinspired Catalysis: Metal-Sulfur Complexes*; Weigand, W., Schollhammer, P., Eds.; Wiley-VCH Verlag GmbH & Co. KGaA: Weinheim, Germany,

2015; pp 327–348.

(34) Dilworth, J. R.; Zheng, Y.; Lu, S.; Wu, Q. Preparation and Characterization of a Novel Asymmetrically Oxidized Complex of 2-(Diphenylphosphino)-Benzenethiol with Ruthenium. The Crystal and Molecular Structure of [Ru(2-Ph2PC6H4S)·(2-Ph2PC6H4S−OH)(2-Ph2PC6H4SO2)]·1/2H2O. *Transit. Met. Chem.* **1992**, *17* (4), 364–368. DOI: 10.1007/BF02910910.

(35) Buonomo, R. M.; Font, I.; Maguire, M. J.; Reibenspies, J. H.; Tuntulani, T.; Darensbourg, M. Y. Study of Sulfinate and Sulfenate Complexes Derived from the Oxygenation of Thiolate Sulfur in [1,5-Bis(2-Mercapto-2-Methylpropyl)-1,5-Diazacyclooctanato(2—)]Nickel(II). *J. Am. Chem. Soc.* **1995**, *117* (3), 963–973. DOI: 10.1021/ja00108a013.

(36) Kung, I.; Schweitzer, D.; Shearer, J.; Taylor, W. D.; Jackson, H. L.; Lovell, S.; Kovacs, J. A. How Do Oxidized Thiolate Ligands Affect the Electronic and Reactivity Properties of a Nitrile Hydratase Model Compound? *J. Am. Chem. Soc.* **2000**, *122* (34), 8299–8300. DOI: 10.1021/ja0017561.

(37) Masitas, C. A.; Mashuta, M. S.; Grapperhaus, C. A. Asymmetric Oxygenation of a Ruthenium Dithiolate Mimics the Mixed Sulfenato/Sulfinato Donor Sets of Nitrile Hydratase and Thiocyanate Hydrolase. *Inorg. Chem.* **2010**, *49* (12), 5344–5346. DOI: 10.1021/ic100414c.

(38) Aucott, S. M.; Milto, H. L.; Robertson, S. D.; Slawin, A. M. Z.; Walker, G. D.; Woollins, J. D. Platinum Complexes of Naphthalene-1,8-Dichalcogen and Related Polyaromatic Hydrocarbon Ligands. *Chem. - A Eur. J.* **2004**, *10* (7), 1666–1676. DOI: 10.1002/chem.200305352.

(39) Rose, M. J.; Betterley, N. M.; Mascharak, P. K. Thiolate S-Oxygenation Controls Nitric

Oxide (NO) Photolability of a Synthetic Iron Nitrile Hydratase (Fe-NHase) Model Derived from Mixed Carboxamide/Thiolate Ligand. *J. Am. Chem. Soc.* **2009**, *131* (24), 8340–8341. DOI: 10.1021/ja9004656.

(40) Shoner, S. C.; Barnhart, D.; Kovacs, J. A. A Model for the Low-Spin, Non-Heme, Thiolate-Ligated Iron Site of Nitrile Hydratase. *Inorg. Chem.* **1995**, *34* (18), 4517–4518. DOI: 10.1021/ic00122a001.

(41) Ellison, J. J.; Nienstedt, A.; Shoner, S. C.; Barnhart, D.; Cowen, J. A.; Kovacs, J. A. Reactivity of Five-Coordinate Models for the Thiolate-Ligated Fe Site of Nitrile Hydratase. *J. Am. Chem. Soc.* **1998**, *120* (23), 5691–5700. DOI: 10.1021/ja973129q.

(42) Lugo-Mas, P.; Taylor, W.; Schweitzer, D.; Theisen, R. M.; Xu, L.; Shearer, J.; Swartz, R. D.; Gleaves, M. C.; DiPasquale, A.; Kaminsky, W.; et al. Properties of Square-Pyramidal Alkyl-Thiolate FeIII Complexes, Including an Analogue of the Unmodified Form of Nitrile Hydratase. *Inorg. Chem.* **2008**, *47* (23), 11228–11236. DOI: 10.1021/ic801704n.

(43) Kennepohl, P.; Neese, F.; Schweltzer, D.; Jackson, H. L.; Kovacs, J. A.; Solomon, E. I. Spectroscopy of Non-Heme Iron Thiolate Complexes: Insight into the Electronic Structure of the Low-Spin Active Site of Nitrile Hydratase. *Inorg. Chem.* **2005**, *44* (6), 1826–1836. DOI: 10.1021/ic0487068.

(44) Light, K. M.; Yamanaka, Y.; Odaka, M.; Solomon, E. I. Spectroscopic and Computational Studies of Nitrile Hydratase: Insights into Geometric and Electronic Structure and the Mechanism of Amide Synthesis. *Chem. Sci.* **2015**, *6* (11), 6280–6294. DOI: 10.1039/c5sc02012c.

(45) Heinrich, L.; Li, Y.; Vaissermann, J.; Chottard, Á.; Chottard, J.; Rene, Â. A Pentacoordinated Di- N -Carboxamido- Related to the Metal Site of Nitrile Hydratase.

Angew. Chemie - Int. Ed. **1999**, *38* (23), 3526–3528. .

(46) Dutta, A.; Flores, M.; Roy, S.; Schmitt, J. C.; Hamilton, G. A.; Hartnett, H. E.; Shearer, J. M.; Jones, A. K. Sequential Oxidations of Thiolates and the Cobalt Metallocenter in a Synthetic Metallopeptide: Implications for the Biosynthesis of Nitrile Hydratase. *Inorg. Chem.* **2013**, *52* (9), 5236–5245. DOI: 10.1021/ic400171z.

(47) Stipanuk, M. H. SULFUR AMINO ACID METABOLISM: Pathways for Production and Removal of Homocysteine and Cysteine. *Annu. Rev. Nutr.* **2004**, *24* (1), 539–577. DOI: 10.1146/annurev.nutr.24.012003.132418.

(48) Heafield, M. T.; Fearn, S.; Steventon, G. B.; Waring, R. H.; Williams, A. C.; Sturman, S. G. Plasma Cysteine and Sulphate Levels in Patients with Motor Neurone, Parkinson's and Alzheimer's Disease. *Neurosci. Lett.* **1990**, *110* (1–2), 216–220. DOI: 10.1016/0304-3940(90)90814-P.

(49) Jeschke, J.; O'Hagan, H. M.; Zhang, W.; Vatapalli, R.; Calmon, M. F.; Danilova, L.; Nelkenbrecher, C.; Van Neste, L.; Bijsmans, I. T. G. W.; Van Engeland, M.; et al. Frequent Inactivation of Cysteine Dioxygenase Type 1 Contributes to Survival of Breast Cancer Cells and Resistance to Anthracyclines. *Clin. Cancer Res.* **2013**, *19* (12), 3201–3211. DOI: 10.1158/1078-0432.CCR-12-3751.

(50) Joseph, C. A.; Maroney, M. J. Cysteine Dioxygenase: Structure and Mechanism. *Chem. Commun.* **2007**, No. 32, 3338–3349. DOI: 10.1039/b702158e.

(51) Simmons, C. R.; Liu, Q.; Huang, Q.; Hao, Q.; Begley, T. P.; Karplus, P. A.; Stipanuk, M. H. Crystal Structure of Mammalian Cysteine Dioxygenase. *J. Biol. Chem.* **2006**, *281* (27), 18723–18733. DOI: 10.1074/jbc.m601555200.

(52) Ye, S.; Wu, X.; Wei, L.; Tang, D.; Sun, P.; Bartlam, M.; Rao, Z. An Insight into the

Mechanism of Human Cysteine Dioxygenase. *J. Biol. Chem.* **2007**, *282* (5), 3391–3402. DOI: 10.1074/jbc.M609337200.

(53) Chai, S. C.; Bruyere, J. R.; Maroney, M. J. Probes of the Catalytic Site of Cysteine Dioxygenase. *J. Biol. Chem.* **2006**, *281* (23), 15774–15779. DOI: 10.1074/jbc.M601269200.

(54) Gardner, J. D.; Pierce, B. S.; Fox, B. G.; Brunold, T. C. Spectroscopic and Computational Characterization of Substrate-Bound Mouse Cysteine Dioxygenase: Nature of the Ferrous and Ferric Cysteine Adducts and Mechanistic Implications. *Biochemistry* **2010**, *49* (29), 6033–6041. DOI: 10.1021/bi100189h.

(55) Tchesnokov, E. P.; Wilbanks, S. M.; Jameson, G. N. L. A Strongly Bound High-Spin Iron(II) Coordinates Cysteine and Homocysteine in Cysteine Dioxygenase. *Biochemistry* **2012**, *51* (1), 257–264. DOI: 10.1021/bi201597w.

(56) Davies, C. G.; Fellner, M.; Tchesnokov, E. P.; Wilbanks, S. M.; Jameson, G. N. L. The Cys-Tyr Cross-Link of Cysteine Dioxygenase Changes the Optimal Ph of the Reaction without a Structural Change. *Biochemistry* **2014**, *53* (50), 7961–7968. DOI: 10.1021/bi501277a.

(57) Driggers, C. M.; Kean, K. M.; Hirschberger, L. L.; Cooley, R. B.; Stipanuk, M. H.; Karplus, P. A. Structure-Based Insights into the Role of the Cys–Tyr Crosslink and Inhibitor Recognition by Mammalian Cysteine Dioxygenase. *J. Mol. Biol.* **2016**, *428* (20), 3999–4012. DOI: 10.1016/j.jmb.2016.07.012.

(58) De Visser, S. P.; Straganz, G. D. Why Do Cysteine Dioxygenase Enzymes Contain a 3-His Ligand Motif Rather than a 2His/LAsp Motif like Most Nonheme Dioxygenases? *J. Phys. Chem. A* **2009**, *113* (9), 1835–1846. DOI: 10.1021/jp809700f.

(59) Kumar, D.; Thiel, W.; de Visser, S. P. Theoretical Study on the Mechanism of the Oxygen Activation Process in Cysteine Dioxygenase Enzymes. *J. Am. Chem. Soc.* **2011**, *133* (11), 3869–3882. DOI: 10.1021/ja107514f.

(60) Crawford, J. A.; Li, W.; Pierce, B. S. Single Turnover of Substrate-Bound Ferric Cysteine Dioxygenase with Superoxide Anion: Enzymatic Reactivation, Product Formation, and a Transient Intermediate. *Biochemistry* **2011**, *50* (47), 10241. DOI: 10.1021/bi2011724.

(61) Simmons, C. R.; Krishnamoorthy, K.; Granett, S. L.; Schuller, D. J.; Dominy, J. E.; Begley, T. P.; Stipanuk, M. H.; Karplus, P. A. A Putative Fe2+-Bound Persulfenate Intermediate in Cysteine Dioxygenase. *Biochemistry* **2008**, *47* (44), 11390–11392. DOI: 10.1021/bi801546n.

(62) Aluri, S.; De Visser, S. P. The Mechanism of Cysteine Oxygenation by Cysteine Dioxygenase Enzymes. *J. Am. Chem. Soc.* **2007**, *129* (48), 14846–14847. DOI: 10.1021/ja0758178.

(63) De Visser, S. P.; Nam, W. The Effect and Influence of Cis-Ligands on the Electronic and Oxidizing Properties of Nonheme Oxoiron Biomimetics. A Density Functional Study. *J. Phys. Chem. A* **2008**, *112* (50), 12887–12895. DOI: 10.1021/jp8018556.

(64) Kumar, D.; Sastry, G. N.; Goldberg, D. P.; De Visser, S. P. Mechanism of S-Oxygenation by a Cysteine Dioxygenase Model Complex. *J. Phys. Chem. A* **2012**, *116* (1), 582–591. DOI: 10.1021/jp208230g.

(65) Blaesi, E. J.; Gardner, J. D.; Fox, B. G.; Brunold, T. C. Spectroscopic and Computational Characterization of the NO Adduct of Substrate-Bound Fe(II) Cysteine Dioxygenase: Insights into the Mechanism of O2 Activation. *Biochemistry* **2013**, *52* (35), 6040–6051. DOI: 10.1021/bi400825c.

(66) Blaesi, E. J.; Fox, B. G.; Brunold, T. C. Spectroscopic and Computational Investigation of Iron(III) Cysteine Dioxygenase: Implications for the Nature of the Putative Superoxo-Fe(III) Intermediate. *Biochemistry* **2014**, *53* (36), 5759–5770. DOI: 10.1021/bi500767x.

(67) Li, J.; Griffith, W. P.; Davis, I.; Shin, I.; Wang, J.; Li, F.; Wang, Y.; Wherritt, D. J.; Liu, A. Cleavage of a Carbon–Fluorine Bond by an Engineered Cysteine Dioxygenase. *Nat. Chem. Biol.* **2018**, *14* (9), 853–860. DOI: 10.1038/s41589-018-0085-5.

(68) Siakkou, E.; Rutledge, M. T.; Wilbanks, S. M.; Jameson, G. N. L. Correlating Crosslink Formation with Enzymatic Activity in Cysteine Dioxygenase. *Biochim. Biophys. Acta - Proteins Proteomics* **2011**, *1814* (12), 2003–2009. DOI: 10.1016/j.bbapap.2011.07.019.

(69) Pierce, B. S.; Gardner, J. D.; Bailey, L. J.; Brunold, T. C.; Fox, B. G. Characterization of the Nitrosyl Adduct of Substrate-Bound Mouse Cysteine Dioxygenase by Electron Paramagnetic Resonance: Electronic Structure of the Active Site and Mechanistic Implications †. *Biochemistry* **2007**, *46* (29), 8569–8578. DOI: 10.1021/bi700662d.

(70) Close, D. M.; Wardman, P. Calculation of Standard Reduction Potentials of Amino Acid Radicals and the Effects of Water and Incorporation into Peptides. *J. Phys. Chem. A* **2018**, *122* (1), 439–445. DOI: 10.1021/acs.jpca.7b10766.

(71) Li, J.; Koto, T.; Davis, I.; Liu, A. Probing the Cys-Tyr Cofactor Biogenesis in Cysteine Dioxygenase by the Genetic Incorporation of Fluorotyrosine. *Biochemistry* **2019**, *58*, 2218–2227. DOI: 10.1021/acs.biochem.9b00006.

(72) Tchesnokov, E. P.; Faponle, A. S.; Davies, C. G.; Quesne, M. G.; Turner, R.; Fellner, M.; Souness, R. J.; Wilbanks, S. M.; de Visser, S. P.; Jameson, G. N. L. An Iron–Oxygen Intermediate Formed during the Catalytic Cycle of Cysteine Dioxygenase. *Chem. Commun.* **2016**, *52* (57), 8814–8817. DOI: 10.1039/c6cc03904a.

(73) Fischer, A. A.; Lindeman, S. V.; Fiedler, A. T. A Synthetic Model of the Nonheme Iron–Superoxo Intermediate of Cysteine Dioxygenase. *Chem. Commun.* **2018**, 11344–11347. DOI: 10.1039/C8CC06247A.

(74) Theisen, R. M.; Shearer, J.; Kaminsky, W.; Kovacs, J. A. Steric and Electronic Control over the Reactivity of a Thiolate-Ligated Fe(II) Complex with Dioxygen and Superoxide: Reversible μ-Oxo Dimer Formation. *Inorg. Chem.* **2004**, *43* (24), 7682–7690. DOI: 10.1021/ic0491884.

(75) Jiang, Y.; Widger, L. R.; Kasper, G. D.; Siegler, M. A.; Goldberg, D. P. Iron(II)-Thiolate S -Oxygenation by O2: Synthetic Models of Cysteine Dioxygenase. *J. Am. Chem. Soc.* **2010**, *132* (35), 12214–12215. DOI: 10.1021/ja105591q.

(76) Lombardini, J. B.; Singer, T. P.; Boyer, P. D. Cysteine Oxygenase II. Studies on the Mechanism of the Reaction with 18Oxygen. *J. Biol. Chem.* **1969**, *244* (5), 1172–1175. .

(77) Sallmann, M.; Siewert, I.; Fohlmeister, L.; Limberg, C.; Knispel, C. A Trispyrazolylborato Iron Cysteinato Complex as a Functional Model for the Cysteine Dioxygenase. *Angew. Chemie - Int. Ed.* **2012**, *51* (9), 2234–2237. DOI: 10.1002/anie.201107345.

(78) McQuilken, A. C.; Jiang, Y.; Siegler, M. A.; Goldberg, D. P. Addition of Dioxygen to an N 4 S(Thiolate) Iron(II) Cysteine Dioxygenase Model Gives a Structurally Characterized Sulfinato–Iron(II) Complex. *J. Am. Chem. Soc.* **2012**, *134* (21), 8758–8761. DOI: 10.1021/ja302112y.

(79) Fischer, A. A.; Stracey, N.; Lindeman, S. V.; Brunold, T. C.; Fiedler, A. T. Synthesis, X-Ray Structures, Electronic Properties, and O 2 /NO Reactivities of Thiol Dioxygenase Active-Site Models. *Inorg. Chem.* **2016**, *55* (22), 11839–11853. DOI:

10.1021/acs.inorgchem.6b01931.

(80) Cho, J.; Woo, J.; Nam, W. A Chromium(III)–Superoxo Complex in Oxygen Atom Transfer Reactions as a Chemical Model of Cysteine Dioxygenase. *J. Am. Chem. Soc.* **2012**, *134* (27), 11112–11115. DOI: 10.1021/ja304357z.

(81) Arnstein, H. R. V.; Clubb, M. E. The Biosynthesis of Penicillin 8. Investigation of Cyclic Cysteinylvaline Peptides as Precursors. *Biochem. J.* **1958**, *68*, 528–535. DOI: 10.1042/bj06900i5c.

(82) Peck, S. C.; van der Donk, W. A. Go It Alone: Four-Electron Oxidations by Mononuclear Non-Heme Iron Enzymes. *J. Biol. Inorg. Chem.* **2017**, *22* (2–3), 381–394. DOI: 10.1007/s00775-016-1399-y.

(83) Krebs, C.; Fujimori, D. G.; Walsh, C. T.; Bollinger, J. M. Non-Heme Fe (IV)– Oxo Intermediates. *Acc. Chem. Res.* **2007**, *40* (Iv), 484–492. .

(84) Costas, M.; Mehn, M. P.; Jensen, M. P.; Que, L. Dioxygen Activation at Mononuclear Nonheme Iron Active Sites: Enzymes, Models, and Intermediates. *Chem. Rev.* **2004**, *104* (2), 939–986. DOI: 10.1021/cr020628n.

(85) Nam, W. High-Valent Iron(IV)-Oxo Complexes of Heme and Non-Heme Ligands in Oxygenation Reactions. *Acc. Chem. Res.* **2007**, *40* (7), 522–531. DOI: 10.1021/ar700027f.

(86) Groves, J. T. High-Valent Iron in Chemical and Biological Oxidations. *J. Inorg. Biochem.* **2006**, *100* (4), 434–447. DOI: 10.1016/j.jinorgbio.2006.01.012.

(87) Hohenberger, J.; Ray, K.; Meyer, K. The Biology and Chemistry of High-Valent Iron-Oxo and Iron-Nitrido Complexes. *Nat. Commun.* **2012**, *3*DOI: 10.1038/ncomms1718.

(88) Denisov, I. G.; Makris, T. M.; Sligar, S. G.; Schlichting, I. Structure and Chemistry of Cytochrome P450. *Chem. Rev.* **2005**, *105* (6), 2253–2277. DOI: 10.1021/cr0307143.

(89) Henriksen, A.; Berglund, G. I.; Carlsson, G. H.; Hajdu, J.; Smith, A. T.; Szöke, H. The Catalytic Pathway of Horseradish Peroxidase at High Resolution. *Nature* **2002**, *417* (6887), 463–468. DOI: 10.1038/417463a.

(90) Baik, M. H.; Newcomb, M.; Friesner, R. A.; Lippard, S. J. Mechanistic Studies on the Hydroxylation of Methane by Methane Monooxygenase. *Chem. Rev.* **2003**, *103* (6), 2385–2419. DOI: 10.1021/cr950244f.

(91) Roach, P. L.; Cllftont, J.; Fiilipt, V.; Harlost, K.; Bartont, G. J.; Hajdut, J.; Anderssontt, I.; Schofield, C. J.; Baldwin, J. E. New Structural Family of Enzymes. *Nature* **1995**, *375* (June), 700–704. .

(92) Roach, P. L.; Hensgens, C. M. H.; Shibata, N.; Long, A. J.; Schofield, C. J.; Baldwin, J. E.; Clifton, I. J.; Hajdu, J.; Strange, R. W.; Hasnain, S. S. Anaerobic Crystallisation of an Isopenicillin N Synthase · Fe(II) · Substrate Complex Demonstrated by X-Ray Studies. *Eur. J. Biochem.* **1996**, *242* (3), 736–740. DOI: 10.1111/j.1432-1033.1996.0736r.x.

(93) Roach, P. L.; Clifton, I. J.; Hensgens, C. M.; Shibata, N.; Schofield, C. J.; Hajdu, J.; Baldwin, J. E. Structure of Isopenicillin N Synthase Complexed with Substrate and the Mechanism of Penicillin Formation. *Nature* **1997**, *387* (6635), 827–830. DOI: 10.1038/42990.

(94) McNeill, L. A.; Brown, T. J. N.; Sami, M.; Clifton, I. J.; Burzlaff, N. I.; Claridge, T. D. W.; Adlington, R. M.; Baldwin, J. E.; Rutledge, P. J.; Schofield, C. J. Terminally Truncated Isopenicillin N Synthase Generates a Dithioester Product: Evidence for a Thioaldehyde Intermediate during Catalysis and a New Mode of Reaction for Non-Heme Iron Oxidases. *Chem. - A Eur. J.* **2017**, *23* (52), 12815–12824. DOI: 10.1002/chem.201701592.

(95) Baldwin, J. E.; Abraham, E. The Biosynthesis of Penicillins and Cephalosporins. *Nat. Prod. Rep.* **1988**, *5* (2), 129. DOI: 10.1039/np9880500129.

(96) Tamanaha, E.; Zhang, B.; Guo, Y.; Chang, W.; Barr, E. W.; Xing, G.; St. Clair, J.; Ye, S.; Neese, F.; Bollinger, J. M.; et al. Spectroscopic Evidence for the Two C–H-Cleaving Intermediates of Aspergillus Nidulans Isopenicillin N Synthase. *J. Am. Chem. Soc.* **2016**, *138* (28), 8862–8874. DOI: 10.1021/jacs.6b04065.

(97) Rauk, A.; Yu, D.; Armstrong, D. A. Oxidative Damage to and by Cysteine in Proteins: An Ab Initio Study of the Radical Structures, C-H, S-H, and C-C Bond Dissociation Energies, and Transition Structures for H Abstraction by Thiyl Radicals. *J. Am. Chem. Soc.* **1998**, *120* (34), 8848–8855. DOI: 10.1021/ja9807789.

(98) Shan, X.; Que, L. High-Valent Nonheme Iron-Oxo Species in Biomimetic Oxidations. *J. Inorg. Biochem.* **2006**, *100* (4), 421–433. DOI: 10.1016/j.jinorgbio.2006.01.014.

(99) McDonald, A. R.; Que, L. High-Valent Nonheme Iron-Oxo Complexes: Synthesis, Structure, and Spectroscopy. *Coord. Chem. Rev.* **2013**, *257* (2), 414–428. DOI: 10.1016/j.ccr.2012.08.002.

(100) Ray, K.; Pfaff, F. F.; Wang, B.; Nam, W. Status of Reactive Non-Heme Metal-Oxygen Intermediates in Chemical and Enzymatic Reactions. *J. Am. Chem. Soc.* **2014**, *136* (40), 13942–13958. DOI: 10.1021/ja507807v.

(101) Sahu, S.; Goldberg, D. P. Activation of Dioxygen by Iron and Manganese Complexes: A Heme and Nonheme Perspective. *J. Am. Chem. Soc.* **2016**, *138* (36), 11410–11428. DOI: 10.1021/jacs.6b05251.

(102) Chiang, C. W.; Kleespies, S. T.; Stout, H. D.; Meier, K. K.; Li, P. Y.; Bominaar, E. L.; Que, L.; Münck, E.; Lee, W. Z. Characterization of a Paramagnetic Mononuclear

Nonheme Iron-Superoxo Complex. *J. Am. Chem. Soc.* **2014**, *136* (31), 10846–10849. DOI: 10.1021/ja504410s.

(103) Oddon, F.; Chiba, Y.; Nakazawa, J.; Ohta, T.; Ogura, T.; Hikichi, S. Characterization of Mononuclear Non-Heme Iron(III)-Superoxo Complex with a Five-Azole Ligand Set. *Angew. Chemie Int. Ed.* **2015**, *54* (25), 7336–7339. DOI: 10.1002/anie.201502367.

(104) Hong, S.; Sutherlin, K. D.; Park, J.; Kwon, E.; Siegler, M. a; Solomon, E. I.; Nam, W. Crystallographic and Spectroscopic Characterization and Reactivities of a Mononuclear Non-Haem Iron(III)-Superoxo Complex. *Nat. Commun.* **2014**, *5*, 5440. DOI: 10.1038/ncomms6440.

Chapter 2. Formation of a Reactive, Alkyl Thiolate-Ligated Fe^{III}-Superoxo Intermediate Derived from Dioxygen

Components of this chapter were republished with permission of the Journal of the American Chemical Society, from Formation of a Reactive, Alkyl Thiolate-Ligated Fe^{III}-Superoxo Intermediate Derived from Dioxygen, Blakely, Maike N.; Dedushko, Maksym. A.; Poon, Penny Chaau Yan; Villar-Acevedo, Gloria; Kovacs, Julie A. *J. Am. Chem. Soc.* **2019**, 141, 1867−1870.;

2.1 Introduction

Cysteine dioxygenase (CDO) and isopenicillin N synthase (IPNS) are non-heme Fe enzymes that potentially utilize an Fe^{III}-superoxo intermediate for oxidation reactions, such as S-oxygenation or hydrogen atom abstraction, respectively. [1–6] The CDO-Fe^{III}-superoxo intermediate has potentially been transiently observed using electronic absorbance spectroscopy and has two distinct features (λ_{max} = 500 nm and 640 nm).[7] Initially, these features were attributed to a later peroxy-thiolate intermediate from computational studies. Using TD-DFT and ab initio (CASSCF/NEVTP2) methods, electronic absorption spectra of the possible intermediates in the catalytic cycle were generated and the peroxy-thiolate intermediate spectra most closely matched the observed features.[7] However, from those studies they could not definitely rule out an Fe^{III}-superoxo as the observed intermediate.[7] This CDO-Fe^{III}-superoxo selectively oxidzies the *cis*-thiolate instead of abstracting a hydrogen atom from a nearby cysteine-cross-linked tyrosine

residue.[8] The IPNS-Fe^{III}-superoxo, was spectroscopically observed with transient electronic absorption spectroscopy (λ_{max} = ~ 500 nm and ~ 630 nm), however no vibrational data has been reported to support these assignment.[9] Transient-state-kinetic and spectroscopic methods with the specific labeling of the *δ*(L-α-aminoadipoyl)-L-cysteinyl-D-valine (ACV) substrate assigned the observed spectroscopic features as the β-C_{cys}-H cleaving intermediate.[9] This bond is activated by the heteroatom (S_{cys}) and has a bond dissociative energy of 93 kcal/mol.[10] This is believed to be the potential thermodynamic limit for superoxo intermediates and the strongest bond proposed to by cleaved by a metalloenzyme superoxo.[11]

Despite the important roles of Fe^{III}-superoxo in oxidation reactions, few biomimetic models have been reported compared to other dioxygen derived intermediates.[12–14] Non-heme Fe^{III}-superoxo model complexes possess short lifetimes even at low temperatures, and their potential to be silent not only in ⊥-mode EPR spectroscopy but also ∥-mode hinders characterization. Therefore, only a few well-characterized examples of non-heme Fe^{III}-superoxo compounds have been reported.[15–18] Lee demonstrated that a mononuclear Fe^{III}-superoxo, $[Fe^{III}(BDPP)(O_2)]$, can cleave C-H bonds of dihydroanthracene (~78 kcal/mol),[16] while other Fe^{III}-superoxo complexes, $[Fe^{III}(TAML)(\eta^2\text{-}O_2)]$ and $[Fe^{III}(L^{Ph})(Tp^{Me2})(O_2)]$, are not capable of cleaving C-H bonds.[18,19] The latter's weak oxidative reactivity was hypothesized to be due to its low spin state.[18] These examples lack a thiolate in the coordination sphere, which have been shown to have a profound effect on reactivity.[20] Recently, the first thiolate-ligated Fe^{III}-superoxo, $[Fe^{III}(O_2)(Tp^{Me2})(2\text{-ATP})]$, was reported, however the ligand was an aryl thiolate where the sulfur's lone pair is tied up in π-bonding to the aryl carbon in one of its resonance forms, which makes it less donating than an alkyl thiolate.[15] The $[Fe^{III}(O_2)(Tp^{Me2})(2\text{-ATP})]$ species eventually decays to disulfide products and its reactivity towards substrates has yet to be studied.[15] This

thiolate ligated Fe^{III}-superoxo was the first to display similar features (λ_{max} = 490 and 655) to the electronic absorption spectra of CDO and IPNS. Fiedler suggests the presence of two charge transfer bands above 500 nm may be a characteristic feature of thiolate-coordinated non-heme Fe^{III}–superoxo species in small molecule compounds and enzymatic environments.[15] Providing spectroscopic handles from well characterized models can aid in the assignment of transient metalloenzyme intermediates and additional thiolate ligated models that use O_2 to form Fe^{III}-superoxo intermediates would further the understanding of the mechanisms of CDO and IPNS.

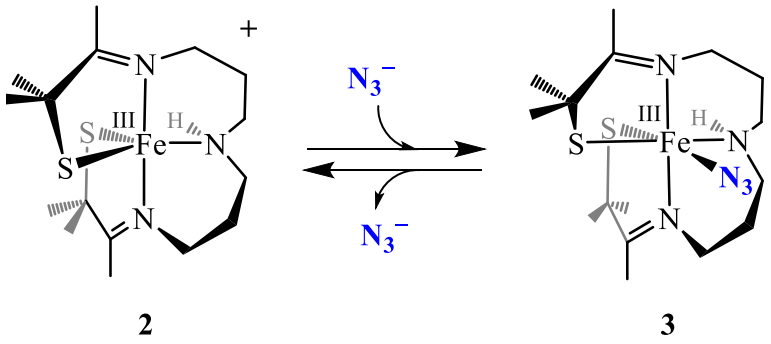

2 **3**

Figure 2.1. Reversible binding of azide (N_3^-) to **2** generating **3**.

Herein, the synthesis of an alkyl thiolate-ligated $[Fe^{II}(S_2{}^{Me2}N_3(Pr,Pr)]$ (**1**) and the spectroscopic characterization of intermediates derived from **1** and dioxygen is reported. Previously, our group reported the oxidized derivative, $[Fe^{III}(S_2{}^{Me2}N_3(Pr,Pr)]^+$ (**2**), was capable of binding azide (N_3^-) between S(1) and N(2), forming $[Fe^{III}(S_2{}^{Me2}N_3(Pr,Pr)(N_3)]$ (**3**), (Figure 2.1). Azide is commonly used to probe enzymatic superoxide binding sites since azide has similar frontier orbitals and the same charge as superoxide ($O_2^{\bullet-}$).[3,21,22] Thus, the ability to bind azide

suggested that the formation of a thiolate-ligated Fe^{III}-superoxo intermediate could be feasible from the reaction between reduced **1** and O_2 and/or oxidized **2** and KO_2.

2.2 Experimental

General Methods. All reactions were performed under an atmosphere of dinitrogen in a glove box or using a custom–built two-neck solution sample holder equipped with a threaded glass connector (sized to fit an ATR probe). Reagents purchased from commercial vendors were of the highest purity available and used without further purification. $[Fe^{III}(S_2{}^{Me2}N_3(Pr,Pr)]PF_6$ and 3-methyl-3-mercapto-2-butanone were synthesized as previously described.[23] Methylene chloride (DCM), tetrahydrofuran (THF), diethyl ether (Et_2O), and acetonitrile (MeCN) were rigorously degassed, and purified using solvent purification columns housed in a custom stainless-steel cabinet, dispensed via a stainless steel schlenk-line (GlassContour). 2-Methyltetrahydrofuran (Me-THF) was distilled under an inert atmosphere from Na/benzophenone and degassed with argon prior to use. Methanol (MeOH) was distilled from calcium hydride and degassed prior to use. ^1H NMR spectra were recorded on a Bruker AV 300 FT-NMR, Bruker AV 500 FT-NMR, or Bruker AV 700 FT-NMR spectrometer and are referenced to an external standard of TMS (paramagnetic compounds). Chemical shifts are reported in ppm and coupling constants (*J*) in Hz. EPR spectra were recorded on a Bruker EPX CW-EPR spectrometer operating at X-band frequency at 120 K. The EPR spectra were simulated using EasySpin (version 5.2.23), a computational package developed by Stoll and Schweiger [24] and based on Matlab (The MathWorks, Massachusetts, USA). Electrospray-ionization mass spectra (ESI-MS) were obtained on a Bruker Esquire Liquid Chromatograph-Ion Trap mass spectrometer. Cyclic voltammograms were recorded in MeCN (100 mM $NBu_4(PF_6)$ solutions) on a PAR 273 potentiostat utilizing a glassy carbon working

electrode, platinum auxiliary electrode, and an SCE reference electrode. Magnetic moments (solution state) were obtained using the Evans' method as modified for superconducting solenoids.[25,26] Electronic absorption spectra were recorded using a Varian Cary 50 spectrophotometers equipped with a fiber optic cable connected to a C-technologies ATR probe.

Synthesis of [$Fe^{II}(S_2^{Me2}N_3$(Pr,Pr)] (1) 3-methyl-3-mercapto-2-butanone (0.38 g, 3.2 mmol) was dissolved in 10 ml of MeOH. To this NaOMe (0.172 g, 3.2 mmol) was added and the mixture was stirring for 10 min then 3,3'-iminobis(propylamine) (0.21 ml, 1.5 mmol) was added. After stirred for 20 mins at room temperature, this solution of organics was cooled to -40 ℃ for over 1 hour. This solution was added dropwise to a solution of anhydrous ferrous chloride (0.19 g, 1.5 mmol) in 10 ml of MeOH also cooled to -40 ℃ for over 1 hour. The combined solutions were allowed to stir for 3 hours at room temperature before being stored in the freezer overnight. The solution was filtered through a bed of Celite, the solvent was removed by vacuum. The resulting crude black powder was dissolved in a minimal amount of cooled MeCN and the undissolved salts were then removed by filtering through a bed of Celite. The solvent was removed by vacuum then <4 ml of THF was added and layered with 15 ml of pentane and cooled at -40 ℃ for ~12 h to afford 0.438 g (1.13 mmol, 76 %) of green-brown micro-crystalline solid. Electronic absorption (THF): λ_{max} (ε, M^{-1} cm^{-1}) = 420 nm (1509). IR υ(cm^{-1}): 1636 (imine). Cyclic Voltammertry: $E_{1/2}$ (MeCN) = -425 mV vs SCE. Solution magnetic moment (298 K; MeCN): μ_{eff} = 2.63 μ_B. ^{1}H NMR (THF-d_8): δ 242, 210, 84, 74, 59, 57, 44, 38, 3.0, -4.0, -19.

Synthesis of Anhydrous $^{57}FeCl_2$ from ^{57}Fe powder. Under N_2 atmosphere, 38-250 mg of Fe was weighted out in a Schlenk flask. Concentrated HCl (1.5-10.1 ml) was added and carefully warmed

up to 90 ºC (at RT it takes a very long time to dissolve the Fe). The iron pellets/powder dissolved after some minutes and gas release is observed, stir the solution for 30 min at 90-100 ºC. Cooled to room temperature, N_2 gas was bubbled through the solution for at least 30 minutes. In a round bottom flask, H_2O was removed under vacuum and reduced pressure until a light green paste (ferrous chloride tetrahydrate) was obtained. On a Schlenk line, the paste was dried under vacuum while heated to 120℃ for over 48 hrs. (The tetrahydrate loses 2 H_2O molecules at 105-115 ℃. The dihydrate loses 2 H_2O molecules at 120 ℃).[27] The resulting powder is a tan color and will readily oxidize. Yield 0.115 grams (88%). Mössbauer Spectroscopy: Anhydrous $FeCl_2$: δ = 1.21 mm/s, ΔE_q = 1.03 mm/s, $FeCl_2 \bullet 2H_2O$: δ = 1.26 mm/s, ΔE_q = 2.60 mm/s, $FeCl_2 \bullet 4H_2O$: δ = 1.40 mm/s, ΔE_q = 3.29 mm/s.

Mossbauer Spectroscopy. Mössbauer spectra were recorded with a spectrometer using Janis Research (Wilmington, MA) SuperVaritemp dewars that allow studies in applied magnetic fields up to 8 T in the temperature range from 1.5 to 200 K. Isomer shifts are quoted relative to iron metal at 298 K. Mössbauer spectral simulations were performed using the WMOSS software package (SEE Co, Edina, MN) and SpinCount software, and all the spectral figures were prepared by using SpinCount software.[28]

Formation of [$Fe^{III}(S_2{}^{Me2}N_3$(Pr,Pr)-O_2] (6) via the addition of O_2 to 1. A 0.238-0.476 mM solution of **1** was prepared in MeOH, THF or DCM under an inert atmosphere in a drybox. The resulting solution was transferred via gastight syringe to a custom-made two-neck vial equipped with a septum cap and threaded dip-probe feed-through adaptor that had been previously been purged with argon for at least 30 minutes. This solution was cooled in an acetone and dry ice bath

to -73 ˚C. Argon stream was removed from the vial and a stream of O_2 gas or 5 ml of pure O_2 gas was bubbled through the solution over the course of 30 seconds, resulting in the formation of metastable **6**. The same process in an NMR tube was used to produce a 6 mM solution of **6** for ^{1}H NMR spectroscopy at -73 ℃.

Formation of [$Fe^{III}(S_2^{Me2}N_3$(Pr,Pr)-O_2] (6) via the addition of KO_2 to 2. A 0.238-0.476 mM solution of **2** was prepared in THF under an inert atmosphere in a drybox. The resulting solution was transferred via gastight syringe to a custom-made two-neck vial equipped with a septum cap and threaded dip-probe feed-through adaptor that had been previously been purged with argon for at least 30 minutes. This solution was cooled in an acetone and dry ice bath to -73 ˚C. A slurry of 1.1-50 equivalents of KO_2 in the presence of 18-crown-6 in 100 μL of THF was added via a gas tight syringe resulting in the formation of metastable **6**.

Formation of [$Fe^{III}(S_2^{Me2}N_3$(Pr,Pr)OOH] (7) via the addition of O_2 to 1. A 0.238-0.476 mM solution of **1** was prepared in MeOH or THF under an inert atmosphere in a drybox. The resulting solution was transferred via gastight syringe to a custom-made two-neck vial equipped with a septum cap and threaded dip-probe feed-through adaptor that had been previously been purged with argon for at least 30 minutes. This solution was cooled in an acetone and dry ice bath to -73 ˚C. Argon stream was removed from the vial and a stream of O_2 gas or 5 ml of pure O_2 gas was bubbled through the solution over the course of 30 seconds, after 40 mins, **6** is fully converted to **7**. Alternatively, **7** can be instantaneously generated by addition of 10 equivalents of TEMPOH to **6** at -73 ˚C.

Hydrogen Atom Transfer (HAT) Reactions. Aliquots of **1** in THF or THF-d_8 (1 ml of a 0.476 mM solution) were used to generate **6** from O_2 as stated above. Kinetic measurements were started immediately after generation of **6**. Reactions between **6** and H-atom donors were monitored by electronic absorption spectroscopy and involved pseudo first-order conditions (with respect to Fe) at -73 ˚C, with the H-atom donors held in excess (CHD: 47.6 mM; THF: 12.3 M). Pseudo first-order plots monitored the decrease in absorbance at λ= 523 nm.

Resonance Raman Spectroscopy. Resonance Raman (rR) spectra were obtained from frozen solution samples at liquid nitrogen temperature (77 K) in a backscattering sample geometry. The visible excitation wavelength at 527 nm is provided by the CW (continuous wave) output of the second harmonic of neodymium-doped yttrium lithium fluoride (Nd:YLF) laser (Photonics Industries International, GM-30–527). Laser power at the sample varies from 1.4 to 6.0 mW. The scattered light from the sample was collected and focused onto a triple spectrograph (Spex 1877) equipped with a CCD detector (Roper Scientific, Model 7375-0001) operating at -110 ℃. Spectra were calibrated with dimethylformamide and acetone. The laser line of 527 nm was chosen to be in the proximity of the absorption spectrum of the transient intermediates probed. Sample concentrations of 5-10 mM **1** in THF, d^8-THF or CD_2Cl_2 were added to the quartz EPR sample tubes. The samples of **1** were capped with rubber septa, cooled to -73 ℃ and then **1** was generated by the addition of 2 ml of either $^{16}O_2$ or $^{18}O_2$ gas to solutions. After 5 minutes, the samples were cooled in LN_2 to 77 K. Samples were run at 77 K in a quartz liquid nitrogen finger dewar and hand spun to minimize sample decomposition during scan collection. Resonance Raman spectra were processed with Spectragryph software.[29]

H_2O_2 Detection Assay. Hydrogen peroxide produced from the reaction of **7** with H_2SO_4 was determined spectroscopically with titanium(IV) oxysulfate.[30–32] The reaction of **1** and O_2 in THF was monitored to ensure all **6** formed was converted to **7** (λ_{max} = 696 nm). After a single drop of concentrated H_2SO_4 was added to the solution, distilled water (10 ml) and CH_2Cl_2 (20 ml) were added. To the separated aqueous layer, 0.1 ml of commercially available $Ti^{IV}O(SO_4)$ solution (15 % in sulfuric acid) was added. The concentration of the hydrogen peroxide was spectroscopically measured from the absorption at 408 nm. The calibration curve was derived from the absorbance measurements of 0.12 mM to 2.42 mM solutions of urea H_2O_2 in distilled water after addition of 0.1 ml of $Ti^{IV}O(SO_4)$ solution.

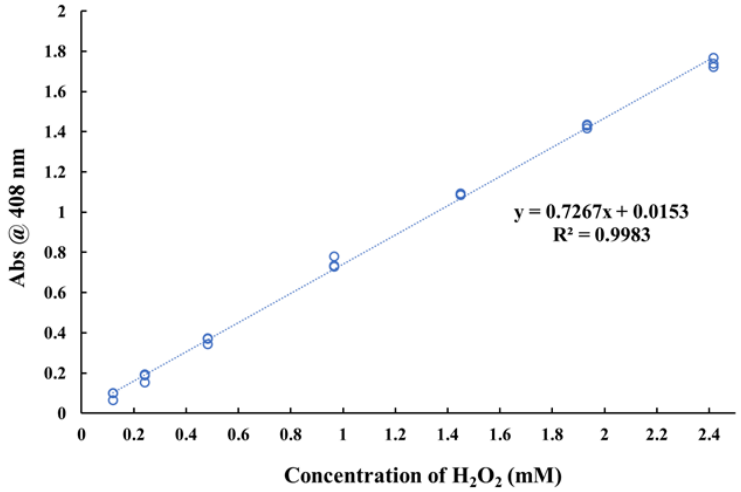

Figure 2.2. Calibration curve for the determination of the concentration of hydrogen peroxide in aqueous solution with $Ti^{IV}O(SO_4)$.

Spin Quantitation of EPR Spectra. Spectra were collected at 120 K using the following parameters: 9.28 GHz frequency, 2.0 mW power, 6×10^4 gain, 100 kHz modulation frequency,

0.2 mT modulation amplitude, and 40.96 ms conversion time. Samples of **6** and **5** for quantification of spin concentration were prepared as follows. A 1.0 mM solution of **1** was prepared in 98:2 THF:Me-THF under an inert atmosphere in a drybox. 0.5 ml of the resulting solution was then transferred into EPR tubes, and 2 ml of pure O_2 was bubbled through the solution at 293 K over the course of 30 seconds, and left to react for 10 mins, resulting in the formation of **5**. Samples of **7** for quantification of spin concentration were prepared as follows. A 1.0 mM solution of **1** was prepared in 98:2 THF:Me-THF under an inert atmosphere in a drybox. 0.5 ml of the resulting solution was transferred into EPR tubes. This solution was cooled to -73 ˚C in an acetone/dry ice bath, and 2 ml of pure O_2 was then bubbled through the solution over the course of 30 seconds, and left to react for 40 mins, resulting in the formation of metastable **7**. Quantification of the unpaired spin concentration within a sample was achieved by comparison of the double integral of the EPR intensity to that of a standard curve made from solutions of 0.25 mM-1.4mM azide-bound $[Fe^{III}(S_2{}^{Me2}N_3(Pr,Pr)\text{-}N_3]$ in 98:2 THF:Me-THF. Purity of these standard solutions were determined by electronic absorption spectroscopy prior to use.

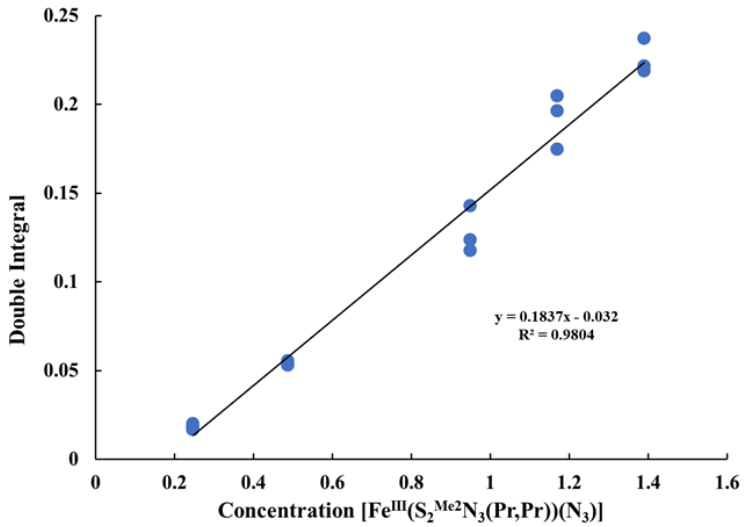

Figure 2.3. Calibration curve for the double-integral of the S = ½ EPR signal of azide-bound **3** versus the concentration.

X-ray Crystallographic Structure Determination. A black green prism, [(Fe^{II}($S_2^{Me2}N_3$(Pr,Pr))-μ-(Fe^{II})]$^{2+}$ (**4**), measuring 0.35 x 0.15 x 0.10 mm^3 was mounted on a loop with oil. Data was collected at -173 ℃ on a Bruker APEX II single crystal X-ray diffractometer, Mo-radiation. Crystal-to-detector distance was 40 mm and exposure time was 240 seconds per frame for all sets. The scan width was 1°. Data collection was 77.6 % complete to 25° in θ. A total of 31,546 reflections were collected covering the indices, -16<=h<=17, -15<=k<=15, -18<=l<=17. 7405 reflections were symmetry independent and the R_{int} = 0.0458 indicated that the data was of better than average quality (0.07). Indexing and unit cell refinement indicated a triclinic lattice. The space group was found to be P $\bar{1}$ (No. 2).

A yellow green prism, **1**, measuring 0.32 x 0.03 x 0.03 mm^3 was mounted on a loop with oil. Data was collected at -173 ℃ on a Bruker APEX II single crystal X-ray diffractometer, Mo-radiation. Crystal-to-detector distance was 40 mm and exposure time was 180 seconds per frame for all sets. The scan width was 1º. Data collection was 100 % complete to 25° in θ. A total of 32,245 reflections were collected covering the indices, -23<=h<=23, -11<=k<=11, -25<=l<=25. 3547 reflections were symmetry independent and the elevated R_{int} = 0.04355 indicated that the data was of better than average quality (0.07). Indexing and unit cell refinement indicated a primitive orthorhombic lattice. The space group was found to be Pbca (No. 61).

Data was integrated and scaled using SAINT, SADABS within the APEX2 software package by Bruker.[33] Solution by direct methods (SHELXS, SIR97) produced a complete heavy atom phasing model consistent with the proposed structure.[34,35] The structure was completed by difference Fourier synthesis with SHELXL.[36,37] Scattering factors are from Waasmair and Kirfel.[38] Hydrogen atoms were placed in geometrically idealized positions and constrained to ride on their

parent atoms with C---H distances in the range 0.95-1.00 Angstrom. Isotropic thermal parameters U_{eq} were fixed such that they were 1.2 U_{eq} of their parent atom U_{eq} for CH's and 1.5 U_{eq} of their parent atom U_{eq} in case of methyl groups. All non-hydrogen atoms were refined anisotropically by full-matrix least-squares. Final solutions were plotted using ORTEP and POV-Ray programs.[39,40]

Table 2.1. Crystal Data, Intensity Collections [a] and Structure Refinement Parameters for $[(Fe^{II}(S_2{}^{Me2}N_3(Pr,Pr))\text{-}\mu\text{-}(Fe^{II})]^{2+}$ (**4**), and $[Fe^{II}(S_2{}^{Me2}N_3(Pr,Pr)]$ (**1**).

	4	**1**
Formula	$C_{40}\,H_{78}\,F_{12}\,Fe_3\,N_6\,O_2\,P_2\,S_4$	$C_{16}\,H_{31}\,Fe\,N_3\,S_2$
Molecular Weight	1260.81	385.41
Temperature (K)	100(2)	100(2)
Crystal System	Triclinic	Orthorhombic
Space Group	$P\ \bar{1}$	Pbca
a, (Å)	13.2731(8)	19.5588(9)
b, (Å)	13.6099(8)	9.3044(5)
c, (Å)	16.3002(10)	21.1744(10)
α (deg)	95.064(2)	90
β (deg)	105.476(2)	90
γ (deg)	106.629(2)	90
V ($Å^3$)	2675.6(3)	385.4(3)
Z	2	8
R_1	0.0646[b]	0.0251[b]
R_w	0.1614[c]	0.055 [c]
GOF	1.024	1.021

[a] Mo Ko(α,-) (λ = 0.71070 Å) radiation; graphite monochromator; -90 ºC. [b] $R = \Sigma\,||F_o| - |F_c||\,/\,\Sigma\,|F_o|$. [c] $R_w = [\Sigma w(|F_o| - |F_c|)^2/\Sigma w F_o{}^2]^{1/2}$, where $w^{-1} = [\sigma^2_{count} + (0.05\,F^2)^2]/4F^2$.

Computational Details. Calculations were performed using the ORCA v. 4.0.0 quantum chemistry package[41] and employed a polarized triple-zeta def2-TZVP basis set, the def2/J auxiliary basis set for Coulomb fitting, and the atom-pairwise dispersion correction of Grimme (D3BJ).[42]

Tight convergence criteria were required for self-consistent field (SCF) solutions. The Grid4 (GridX4) integration grid size, and the conductor-like polarizable continuum model with the dielectric constant ε = 7.25 for tetrahydrofuran solvent (CPCM(THF)), were used for geometry optimizations.[43] Geometry optimizations and analytical frequency calculations were performed using the PBE0 functional, with the resolution of identity (RI) chain-of-spheres (RIJCOSX) approximation,[44,45] and initiated from the crystallographic coordinates when available. Analytical frequency calculations were performed on all optimized structures to determine whether the obtained stationary points corresponded to local minima.

Previously reported[23] crystallographically determined structure of azide-bound [$Fe^{III}(S_2{}^{Me2}N_3(Pr,Pr)(N_3)$] was used as a starting point for the calculated superoxo-bound structure, [$Fe^{III}(S_2{}^{Me2}N_3(Pr,Pr)(O_2)$]. Specifically, the distal azide nitrogen N(6) atom was deleted, and the proximal N(4) and middle N(5) atoms were replaced with oxygen atoms. The Fe^{III} metal center was assumed to be in the S = ½ state. A low spin-state was shown previously to be stabilized with thiolate-ligated Fe^{III} complexes due to the thiolate's nephelauxetic effect.[23,46–48] Based on optimized bond lengths reported for aryl-thiolate-ligated [$Fe^{III}(LN_3S(O_2))$],[49] $r_{Fe\text{-}O}$ and $r_{O\text{-}O}$ were set to 2.089 Å, and 1.290 Å, respectively, as a starting point.

Calculations for the Fe^{III}-superoxo complex, [$Fe^{III}(S_2{}^{Me2}N_3(Pr,Pr)(O_2)$] (**6**) employed the broken-symmetry formalism to model coupled paramagnetic sites. An SCF calculation was first performed for the high spin (HS) state of the iron-superoxo complex, Fe^{III}(S = ½, ↑)-$O_2^{\bullet-}$ (S = ½, ↑). Next, a broken symmetry state was set up with the spin-flip chosen at the iron center (final total ms = 0) and another SCF calculation was ran to calculate energy of the "broken symmetry" (BS), Fe^{III}(S = ½, ↓)-$O_2^{\bullet-}$ (S = ½, ↑), state. Finally, the energies of both HS and BS states were used to estimate the coupling constant, J, (associated with the phenomenological Hamiltonian $\hat{H}$ = –

$2J_{12}\hat{S}_1\hat{S}_2$) using the equation $J = -(E_{HS} - E_{BS})/(\langle S^2\rangle_{HS} - \langle S^2\rangle_{BS})$, which is valid over the entire coupling strength regime. E_{HS} and E_{BS} are the energies of the high-spin (HS), and the broken-symmetry (BS) states, respectively, and $\langle S^2\rangle$ are the expectation values of the squared spin operator for the HS and BS states.[50]

Hybrid time-dependent DFT (TD-DFT) calculations employed the RIJCOSX and the Tamm-Dancoff approximations (TDA).[51,52] The Fermi level, i.e. the halfway between the calculated HOMO and LUMO energies, was set to 0 eV in molecular orbital (MO) analysis. Excited states from TD-DFT calculations were analyzed using Natural Transition orbitals (NTOs) and by visualizing their difference densities between the ground and excited states. Canonical molecular orbital isosurfaces and natural transition orbitals in the TD-DFT calculations were visualized at an isovalue of 0.05 a_0^3 using UCSF Chimera.[53]

Gaussian 16[54] was used to calculate resonance Raman frequencies, and isotope displacements for $[Fe^{III}(S_2^{Me2}N_3(Pr,Pr)(O_2)]$. A UPBE1PBE functional, and a polarized triple- S9 zeta def2-TZVP basis set were employed to calculate analytical vibrational frequencies (freq = (raman, anharmonic)). Analytical frequencies of the isotopically substituted $[Fe^{III}(S_2^{Me2}N_3(Pr,Pr)(^{18}O_2)]$ complex were performed by specifying the mass (iso = 17.999) of the oxygen atoms in the geometry input file.

2.3 Results and Discussion

2.3.1 *Isolation and Characterization of [$Fe^{II}(S^{Me2}N_3(Pr,Pr))$](1)*

Our research group has previously synthesized a series of inorganic model compounds with bis-thiolate ligands that wrap around the metal ion.[55] However, the Fe^{II} derivative containing gem-dimethyl adjacent to the thiolates, [$Fe^{II}(S^{Me2}N_3(Pr,Pr))$](**1**), had yet to be successfully isolated and characterized. The synthesis of this complex is challenging due to the extra lone pairs of the thiolate ligand which can form multiple bonds to a single Fe-ion or form bridges to additional Fe-ions.[56,57] In addition to this susceptibility to form dimeric or polymeric structures, the desired mononuclear complex is extremely oxygen sensitive and predicted have a neutral charge further complicating its isolation. In initial attempts to synthesis **1**, a trimetallic complex [$(Fe^{II}(S_2{}^{Me2}N_3(Pr,Pr))$-μ-$(Fe^{II})]^{2+}$ (**4**), was crystallized (Figure 2.4). After modifications to the synthetic procedure used for **2** such as lowering the molarity of the reaction mixture, changing the order of addition of the reagents, and stopping prior to oxidation allowed for the isolation of reduced [$Fe^{II}(S_2Me_2N_3(Pr,Pr))$] (**1**). Crystallization from a solvent diffusion (THF/pentane) yields single crystals suitable for X-ray diffraction. The structure showed the Fe^{II} ion in a distorted trigonal bipyramidal coordination environment ($\tau = 0.78$) (Figure 2.4, **Error! Reference source not found.**). The $[S_2{}^{Me2}N_3(Pr,Pr)]^{2-}$ ligand helically wraps around the Fe^{II} ion. Both enantiomers are present and related by a crystallographic inversion center. UV-Vis spectroscopy has a characteristic electronic absorption band at λ_{max} = 420 (1260) nm in THF and λ_{max} = 385 (1500) nm in MeOH at 293 K (Figure 2.5).

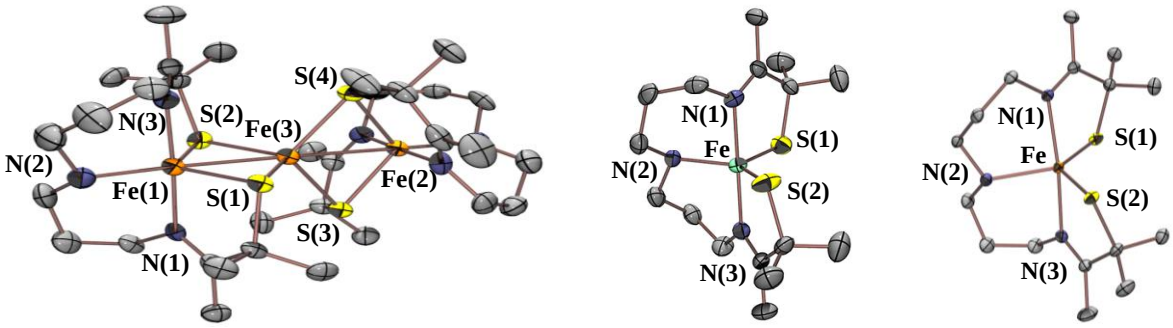

4 **2** **1**

Figure 2.4. Displacement ellipsoid plots of $[(Fe^{II}(S_2{}^{Me2}N_3(Pr,Pr))\text{-}\mu\text{-}(Fe^{II})]^{2+}$ (**4**), $[Fe^{III}(S_2{}^{Me2}N_3(Pr,Pr)]^{+}$ (**2**), and $[Fe^{II}(S^{Me2}N_3(Pr,Pr))]$ (**1**) with thermal ellipsoids at the 50% probability level. Counter-ions, solvent molecules and hydrogen atoms have been removed for clarity.

Table 2.2. Comparison of selected metrical parameters for the five-coordinate oxidized $[Fe^{III}(S_2{}^{Me2}N_3(Pr,Pr)]^{+}$ (**2**), and five-coordinate reduced $[Fe^{II}(S^{Me2}N_3(Pr,Pr))]$(**1**).[23]

	2	**1**
Fe-S(1)	2.161(2) Å	2.3306(5) Å
Fe-S(2)	2.133(2) Å	2.3263(5) Å
Fe-N(1)	1.967(4) Å	2.1556(16) Å
Fe-N(2)	2.049(4) Å	2.1656(16) Å
Fe-N(3)	1.954 (4) Å	2.1815(15) Å
S(1)-Fe-N(2)	132.3(1) °	125.70(4) °
S(2)-Fe-N(2)	106.5(1) °	107.79(4) °
S(1)-Fe-S(2)	121.01(1) °	126.17(2) °
τ^a	0.76	0.78

[a] 5-coordinate geometry index, $\tau = (\beta - \alpha)/60$. β is the largest bond angle observed, and α is the second largest bond angle.[58]

The structure and geometry of **1**, specifically the orientation of the thiolate ligands, provides insights into the unusual spin-state of **1**. In solution, **1** has a magnetic moment of μ = 2.63 μB at 298 K in MeCN consistent with a S = 1 spin-state. The zero-field Mössbauer spectra at 4.2 K on a frozen solution of 0.476 mM **1** in THF produces a quadruple doublet with an isomer shift δ = 0.86 mm/s and ΔE_q = 3.36 mm/s (Figure 2.5. Quantitative electronic absorption spectra of 0.238 mM of [$Fe^{II}(S^{Me2}N_3(Pr,Pr))$] (**1**) in MeOH (red) and THF (blue) at 293 K. Inset: The zero-field ^{57}Fe Mössbauer spectra at 4.2 K of a frozen solution of 0.476 mM **1** in THF.). There are few S = 1 systems and none with similar coordination environments to compare to and isomer shift valves depend on the coordination environment. The isomer shift of **1** is between the reported values for thiolate ligated Fe^{II} complexes with S = 0 (δ = 0.36-0.44 mm/s)[59–61] and S = 2 complexes (δ = 0.93-1.08 mm/s)[60,62]. This value differs significantly from the oxidized derivative **2** (S = 1/2), δ = 0.21 mm/s and ΔEq = 3.01 mm/s.[63] Analysis of the spin-state S = 1, implies there is a large energy separation between the d_{z^2} and the dxy and $d_{x^2-y^2}$ orbitals. In addition, it suggests the energies of d_{xy} and $d_{x^2-y^2}$ are similar if not degenerate. The $Fe^{II/III}$ redox potential of **1** was measured as -425 mV vs SCE, this converts[64] to -805 mV vs Fc/Fc^+ which is below the redox potential of than the of -100 mV vs Fc/Fc^+ required for O_2 reactivity.[65] The study of dioxygen activation for S-oxygenation was **1** promising since it fulfilled the requirement of an open site for O_2 binding *cis* to the thiolate and a low redox potential.

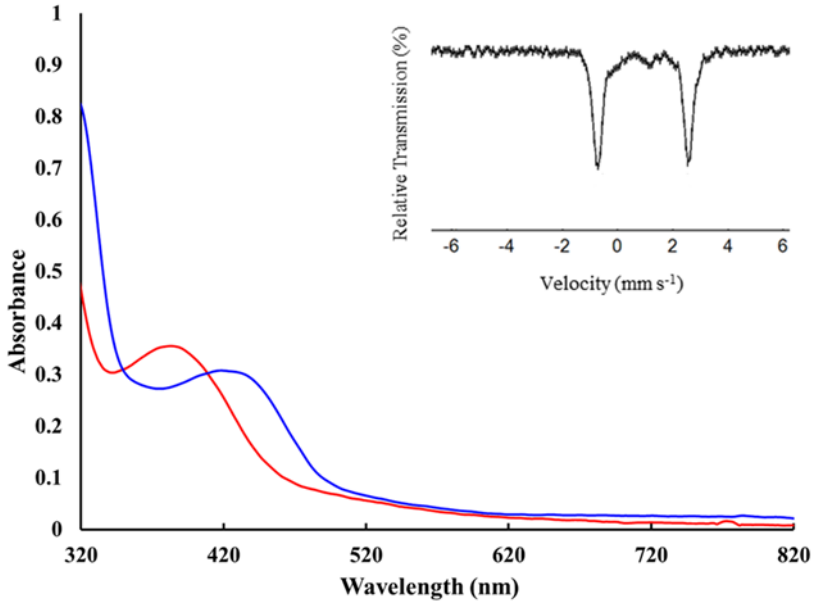

Figure 2.5. Quantitative electronic absorption spectra of 0.238 mM of [$Fe^{II}(S^{Me2}N_3(Pr,Pr))$] (**1**) in MeOH (red) and THF (blue) at 293 K. Inset: The zero-field ^{57}Fe Mössbauer spectra at 4.2 K of a frozen solution of 0.476 mM **1** in THF.

2.3.2 *Reactivity of [$Fe^{II}(S^{Me2}N_3(Pr,Pr))$](1) with Dioxygen at Room Temperature*

Bubbling dry O_2 gas through a solution of **1** in THF at 25 °C causes an immediate color change from pale greenish-yellow to watermelon pink, with an associated shift in λ_{max} to 510 nm (Figure 2.6). This reaction is not solvent dependent and the same feature (λ_{max} = 510 nm) is observed in MeOH. This feature in MeOH indicated the product of the reaction of **1** with O_2 was the previously characterized [$Fe^{III}(\eta^2$-$S^{Me2}O)(S^{Me2}N_3(Pr,Pr))]^+$ (**5**) (Figure 2.7).[46] The stable complex **5** was first synthesized from **3** using oxo atom donors and structurally characterized with X-ray crystallography.[46] Using the reported molar absorptivity, the reaction of **1** and O_2 produced **5** in a 94 % yield. Electron paramagnetic resonance (EPR) spectra of the product showed the

growth of an intense rhombic signal (g = 2.17, 2.11, 1.98) also consistent with the formation of **5** in 93% yield. Electrospray mass spectroscopy (ESI-MS) of isotopically labeled samples shows that the oxo of **5** is derived from $^{18}O_2$ (Figure 2.8). This is the first example of an isolated and characterized sulfenate derived from O_2. Formation of the sulfenate could occur via a direct attack on the thiolate by O_2 or metal-centered dioxygen activation motivating the search for low-temperature intermediates to determine the pathway.

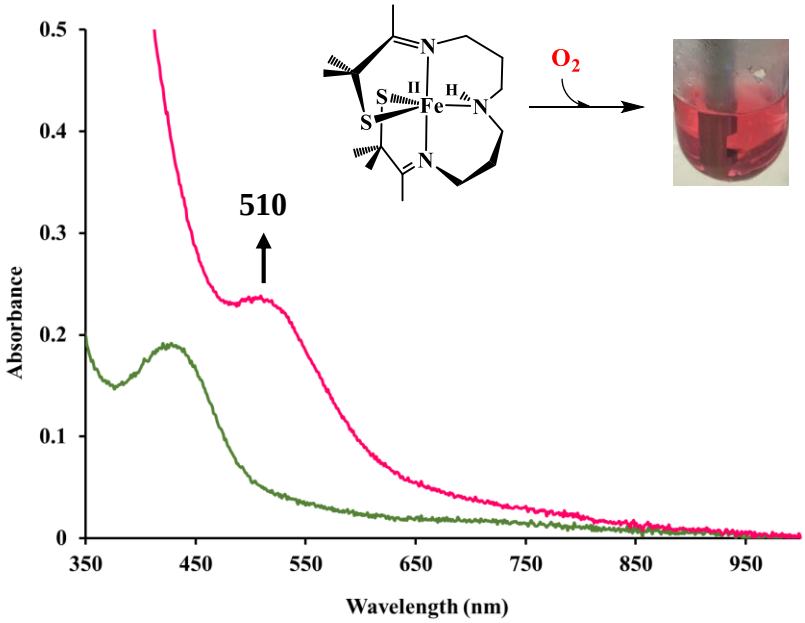

Figure 2.6. Quantitative electronic absorption spectrum of 0.238 mM of [$Fe^{II}(S^{Me2}N_3(Pr,Pr))$] (**1**) (green line) reacting with O_2 to form [$Fe^{III}(\eta^2$-$S^{Me2}O)(S^{Me2})N_3(Pr,Pr))]^+$ (**5**) in THF at 295 K.

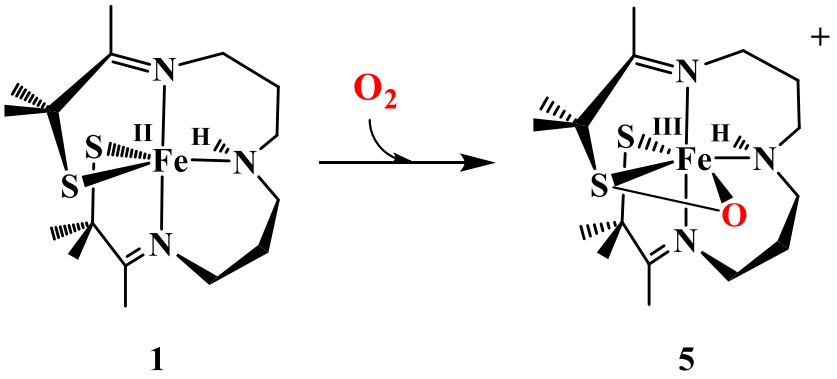

Figure 2.7. The reaction of **1** with O_2 to form the sulfenate **5.**

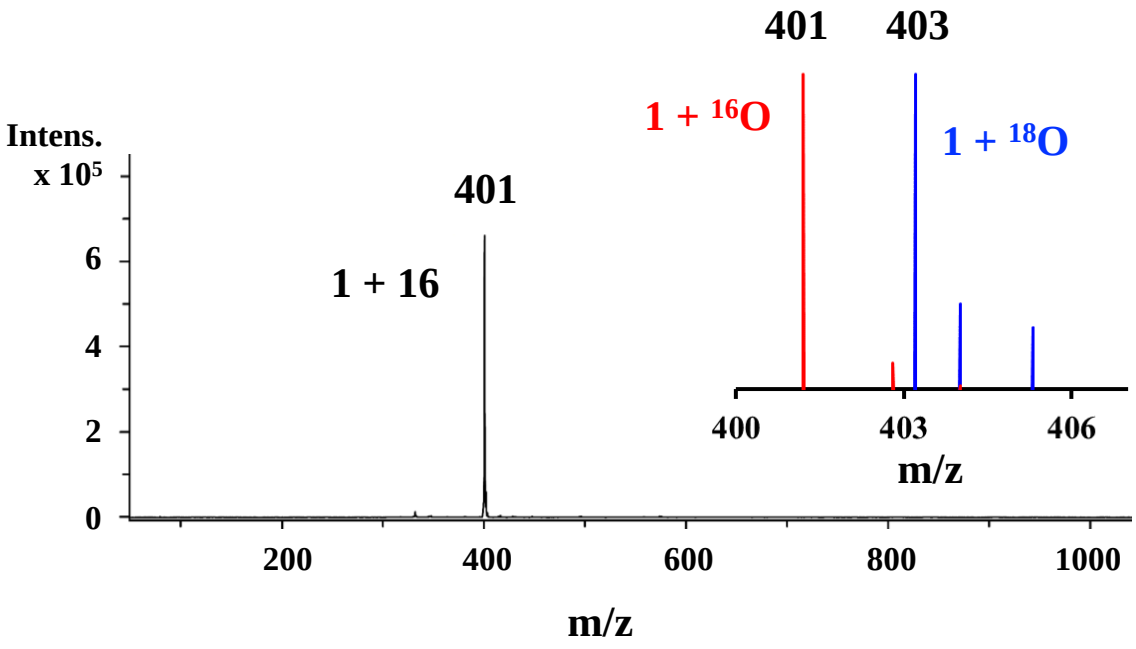

Figure 2.8. Positive mode ESI-MS spectra of the reaction of **1** with O_2. Inset: ESI-MS spectra of $[Fe^{III}(\eta^2\text{-}S^{Me16}O)(S^{Me2})N_3(Pr,Pr))]^+$ (**5**) (red line) generated from **1** and $^{16}O_2$. The ^{18}O-derivative, $[Fe^{III}(\eta^2\text{-}S^{Me18}O)(S^{Me2})N_3(Pr,Pr))]^+$(blue line) indicating the sulfenate is formed from dioxygen

2.3.3 *Reactivity of [$Fe^{II}(S^{Me2}N_3(Pr,Pr))$](1) with Dioxygen at Low Temperature*

A new metastable cranberry red O_2-derived intermediate is observed *en* route to singly oxygenated **5**. This intermediate is generated by bubbling dry O_2 through the solution **1** in THF and has a $t_{1/2}$ = ~20 mins at -73 ℃ (Figure 2.9). This intermediate display several electronic absorption features at 409, 523, and 707 nm (Figure 2.9). The latter low-energy feature is characteristic of six-coordinate, bis-thiolate-ligated Fe^{III} complexes. From an in-depth computational and spectroscopic study on the electronic structure of the five coordinate **2** versus the six-coordinate **3**, the appearance of the low-energy feature is attributed to the pure π interactions between this acceptor orbital and both thiolate donor ligands in the equatorial plane in the octahedral geometry.[66] This metastable intermediate is not solvent dependent and may also be formed in 2-methyltetrahydrofuran (2-MeTHF), dichloromethane (DCM), or methanol. An identical low temperature intermediate (**6**) can be generated from $[Fe^{III}(S^{Me2}N_3(Pr,Pr))]^+$ and an excess of potassium superoxide (KO_2) (Figure 2.10).

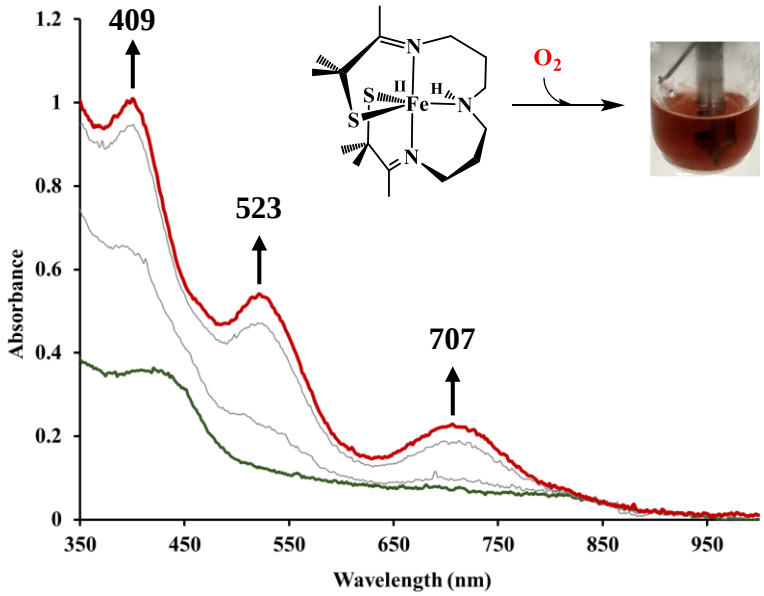

Figure 2.9. Monitoring the low temperature (-73 °C) reaction between **1** (0.238 mM) and excess O_2 in THF by electronic absorption spectroscopy.

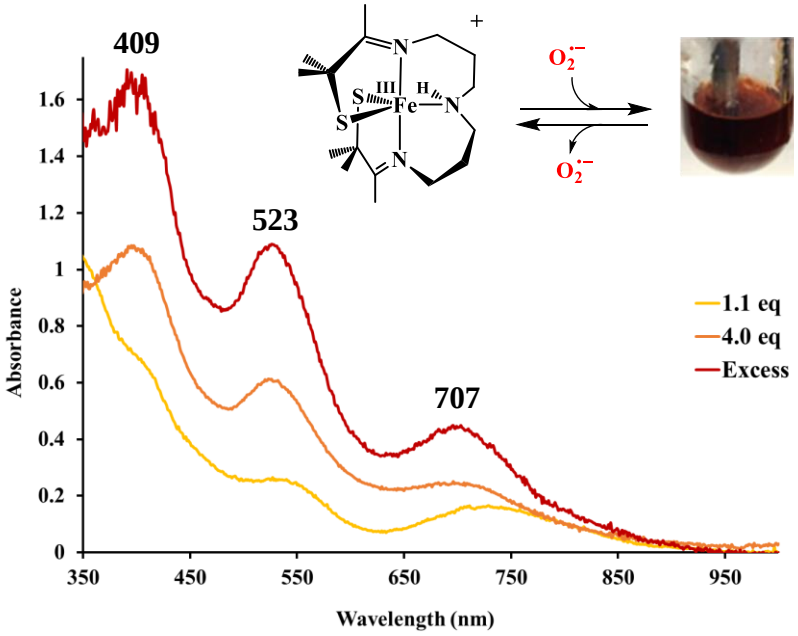

Figure 2.10. Electronic absorption spectra of an identical intermediate forms upon the addition of excess (50 equiv) KO_2 (solubilized in THF with 18-crown-6) to 0.476 mM of oxidized $[Fe^{III}(S_2{}^{Me2}N_3(Pr,Pr)]^+$ (**2**) at -73 °C in THF.

In the presence of azide at low temperatures the cranberry red intermediate and subsequent sulfenate **5** cannot be formed the open coordination site of **1** was occupied by an azide anion. The mechanism of S-oxygenation by CDO occurs via a metal centered reaction and showed by inhibition by azide.[67] This type of inhibition study is commonly used in bioinorganic chemistry.[68–71] Upon introduction of an excess of azide followed by bubbling O_2 gas through the solution, results in outer sphere oxidation of the metal to form previously reported azide-bound [$Fe^{III}(S_2{}^{Me2}N_3(Pr,Pr)(N_3)$] (**3**) (Figure 2.11).[23] Azide inhibition of this reaction indicates that O_2 must bind to the metal ion in order for oxo-atom transfer to occur.

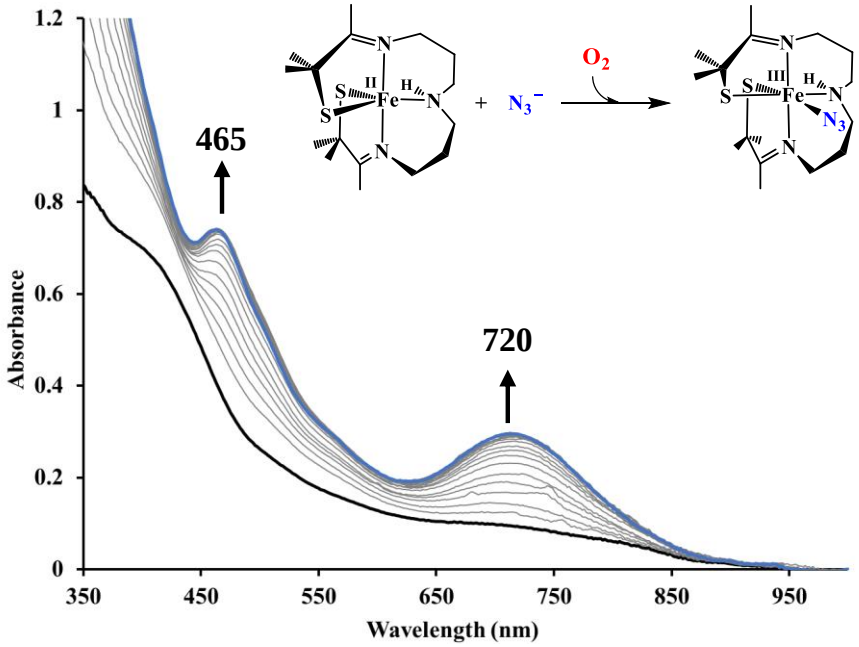

Figure 2.11. Monitoring the low temperature (-73 °C) reaction between **1** (0.476 mM) and excess N_3 followed by the addition of excess O_2 in THF by electronic absorption spectroscopy.

2.3.4 *Characterization of Low-Temperature Dioxygen Derived Intermediate*

The assignment of the dioxygen derived intermediate as an Fe^{III}-superoxo was supported by computational studies and a variety of spectroscopies. The time-dependent DFT (TD-DFT) calculated electronic absorption spectra replicated the three features in the experimental spectra well. The superoxo $\pi^*(O{-}O) \rightarrow d_{xy}(Fe^{III})$ charge transfer transitions contribute to the two higher energy bands, and a $RS^- \rightarrow$ orbital $Fe{-}O_2^{\bullet-}$ charge transfer transitions contribute to all three major features and are responsible for nearly all of the lower energy band (Figure 2.12). The density functional theory (DFT) calculated structure of $[Fe^{III}(S_2{}^{Me2}N_3(Pr,Pr))(O_2)]$ (**6**) contains an O_2 moiety cis to one of the thiolate sulfurs (Figure 2.12), with bond lengths (O−O = 1.289 Å), and a calculated ν_{O-O} stretch (1154 cm^{-1}), consistent with a Fe^{III}-superoxo, analogous to the proposed IPNS and CDO intermediates.

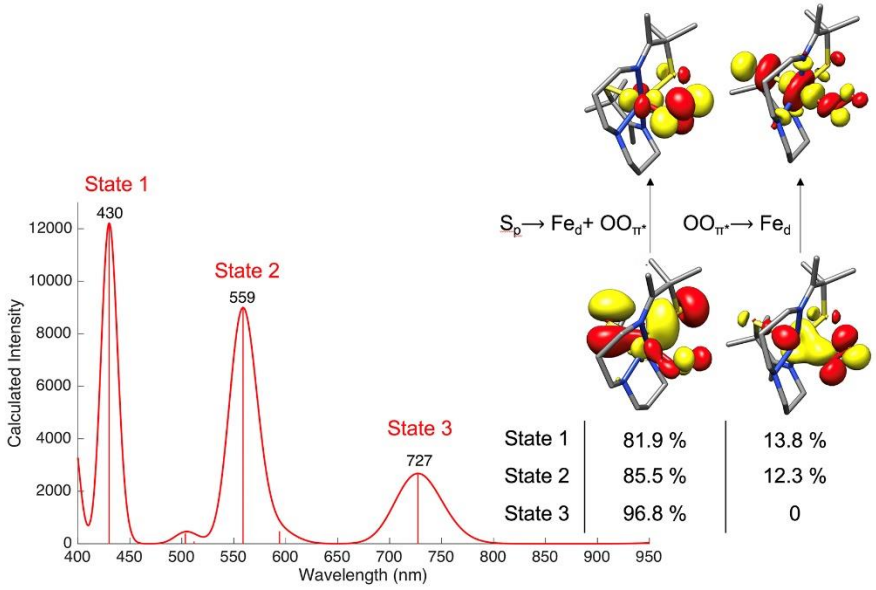

Figure 2.12. TD-DFT calculated electronic absorption spectrum of superoxo complex $[Fe^{III}(S_2{}^{Me2}N_3(Pr,Pr))(O_2)]$ (**6**) including natural transition orbitals (NTO) describing the charge transfer (CT) transitions.

Experimental evidence confirming the presence of a O_2 moiety bound to **1** was obtained using ESI-MS spectroscopy and resonance Raman spectroscopy showed the degree of oxygen activation consistent with a superoxo species. The ESI-MS spectrum of **1** contains a transient (6 s) M + 32 peak at m/z = 417.3, consistent with the addition of two oxygen atoms to the parent ion, **1** (m/z = 385.4). The resonance Raman (rR) spectrum of **6** reproducibly shows a transient feature (a Fermi doublet) at 1093 and 1122 cm^{-1} (Figure 2.13) in THF that disappears over the course of 30 minutes. Isotope labeling with $^{18}O_2$ in THF resulted in the absence of the Fermi doublet, but the predicted downshifted signals were undetectable under the dominating solvent features. The corresponding experiment carried out in a different solvent, CD_2Cl_2, shows a feature at 1093 cm^{-1} that shifts to 1022 cm^{-1} when generated from $^{18}O_2$ (Figure 2.14). These values are consistent with other reported transition metal-superoxo *ν*(O-O) frequencies (Table 2.3).

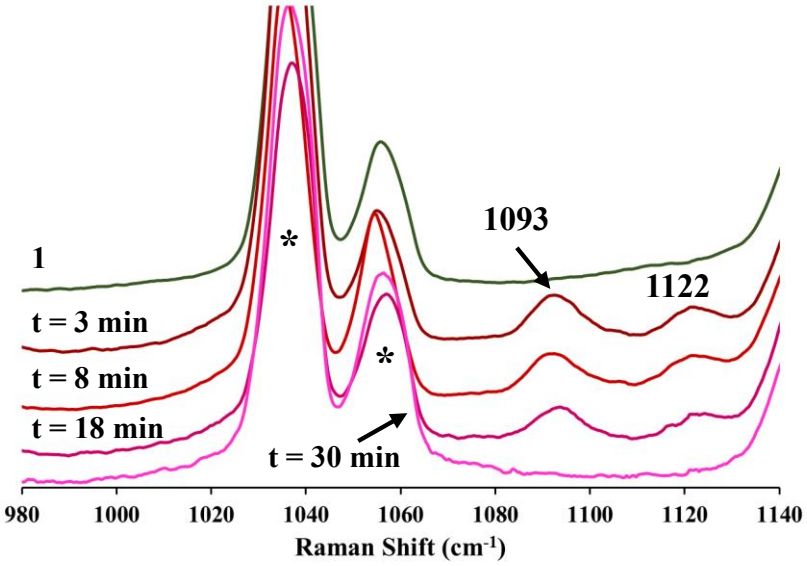

Figure 2.13. Monitoring the reaction between **1** (5 mM) and O_2 in THF at −73 °C by resonance Raman spectroscopy. Samples were frozen in liquid N_2 (77 K) at the time-intervals indicated (λ_{ex} = 527 nm; 4.0 mW power; * = solvent peak).

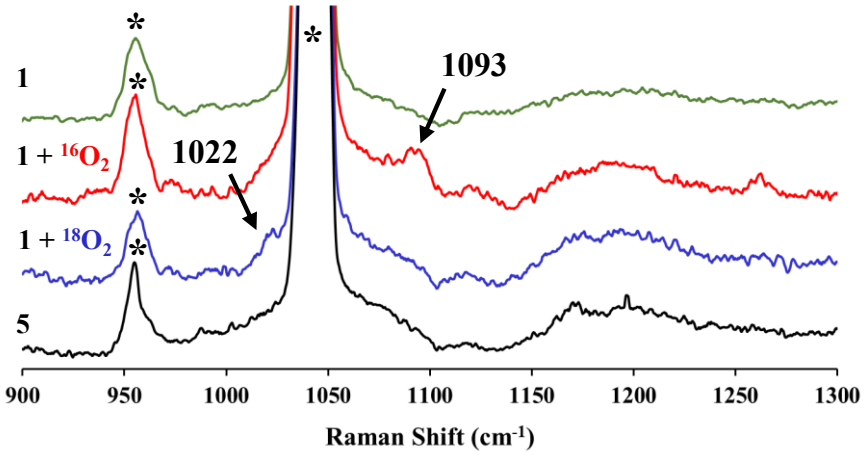

Figure 2.14. Comparison of the resonance Raman spectra of 10 mM (**1**), **6** formed with $^{16}O_2$, **6** formed with $^{18}O_2$, and the end-product, **5** in CD_2Cl_2 at 77 K (λ_{ex} = 527 nm; 6 mW power; *= solvent peak.). Vertical dotted lines mark the ν ^{16}O-^{16}O stretch at 1093 cm^{-1}, and the $\nu^{18}O$-^{18}O stretch at 1022 cm^{-1}.

Table 2.3. Selected Resonance Raman Stretching Frequencies of First-Row Transition Metal-Superoxo Complexes.

Complex	$\nu(^{16}O\text{-}^{16}O)$, cm^{-1}	$\nu(^{18}O\text{-}^{18}O)$, cm^{-1}	**Δ16/18**	**ref**
$[(H_2O)_5Cr^{III}(O_2^{\bullet-})]^{2+}$	1166	1098	68	[72]
$[(Cl)(TMC)Cr^{III}(O_2^{\bullet-})]^{+}$	1170	1104	66	[73]
$[(13\text{-}TMC)Ni^{III}(O_2^{\bullet-})]^{+}$	1130	1070	60	[74]
$[(14\text{-}TMC)Ni^{III}(O_2^{\bullet-})]^{+}$	1131	1067	64	[75]
$[Cu^{II}(O_2^{\bullet-})(TMPA)]^{+}$	1119	1058*	61	[76]
$[Cu^{II}(O_2^{\bullet-})(BA)]^{+}$	1123*	1059*	64	[76]
$[Cu^{II}(O_2^{\bullet-})(F_5BA)]^{+}$	1126*	1062*	64	[76]
$[Cu^{II}(O_2^{\bullet-})(MPPA)]^{+}$	1130	1067*	63	[76]
$[Mn^{III}(O_2^{\bullet-})(L)(H_2O)]^{2+}$	1124	1035	89	[77]
$Co^{II}(O_2)(Me_3TACN)(S_2SiMe_2)$	1133/1123	1070/1059	64	[78]
$[Co^{III}(L^{Ph})(Tp^{Me2})(O_2)]$	1150	1088	62	[18]
$[Fe^{III}(L^{Ph})(Tp^{Me2})(O_2)]$	1168	1090	78	[18]
$[Fe^{III}(BDPP)(O_2)]$	1125	1062	63	[16]
$[Fe^{III}(TAML)(\eta^2\text{-}O_2)]$	1260	1183	77	[17]
$[Fe(O_2)(Tp^{Me2})(2\text{-}ATP)]$	1135/1105	1055	65	[15]
$[Fe^{III}(Pr,Pr)(O_2^{\bullet-})]$(**6**)	1121/1093	1022	71	[79]

* Indicates the center of a Fermi Doublet.

The electronic properties of first-row transition metal-superoxos remains unclear since the degree of charge transfer from the metal to the dioxygen adduct is variable.[78,80–83] Formal oxidation states of an Fe-superoxo may be described as $Fe^{II}\text{-}O_2$ or $Fe^{III}\text{–}O_2^{\bullet-}$. The latter, Fe^{III} complexes are typically studied using ⊥-mode EPR spectroscopy. The EPR spectra of **6** had no detectable signal indicating it may be diamagnetic. A superoxo species with $S = 0$ is expected for this system since **2** was shown to antiferromagnetically coupled with a bound nitric oxide radical producing diamagnetic signals in the ^1H NMR spectra.[84] When the reaction of **1** and O_2 is monitored by ^1H NMR spectroscopy at -40 and -70 °C, the paramagnetic signals of **1** collapse to diamagnetic ($S = 0$) signals upon the addition of O_2 (Figure 2.15). The calculated overlap parameter of $T = 0.17$ and

coupling constant $J^{calc} = -450\ cm^{-1}$ indicate that the two unpaired spins are strongly coupled antiferromagnetically, consistent with the absence of paramagnetically shifted peaks in the ^1H NMR and ⊥-mode EPR silence of **1** at 117 K. In addition, the vibrational data for **6** supports the electronic description as an Fe^{III} ion coupled to a superoxide radical. The available $\nu_{O\text{-}O}$ vibrational data for Fe-O_2 species that forms of *trans* cysteinate-ligated cytochrome P450 (range $\nu_{O\text{-}O}$: 1136 - 1151 cm^{-1}), and synthetic *trans* thiolate-ligated Fe porphyrins (range $\nu_{O\text{-}O}$: 1140 - 1147 cm^{-1}), albeit with fluorinated aromatic thiolates for the latter.[85] The lower $\nu_{O\text{-}O}$ stretching frequency (1093 cm^{-1}) for **6** likely reflects the *cis* orientation of the thiolate and delocalization of electron density between the electron donating thiolate and the Fe-O_2 moiety, which shifts electron density into the superoxo π*(O-O) orbital. Altogether, the above data support an electronic description for **6** involving a low-spin Fe ion antiferromagnetically coupled to a superoxide radical, indicating that an electron is transferred to O_2 upon binding.

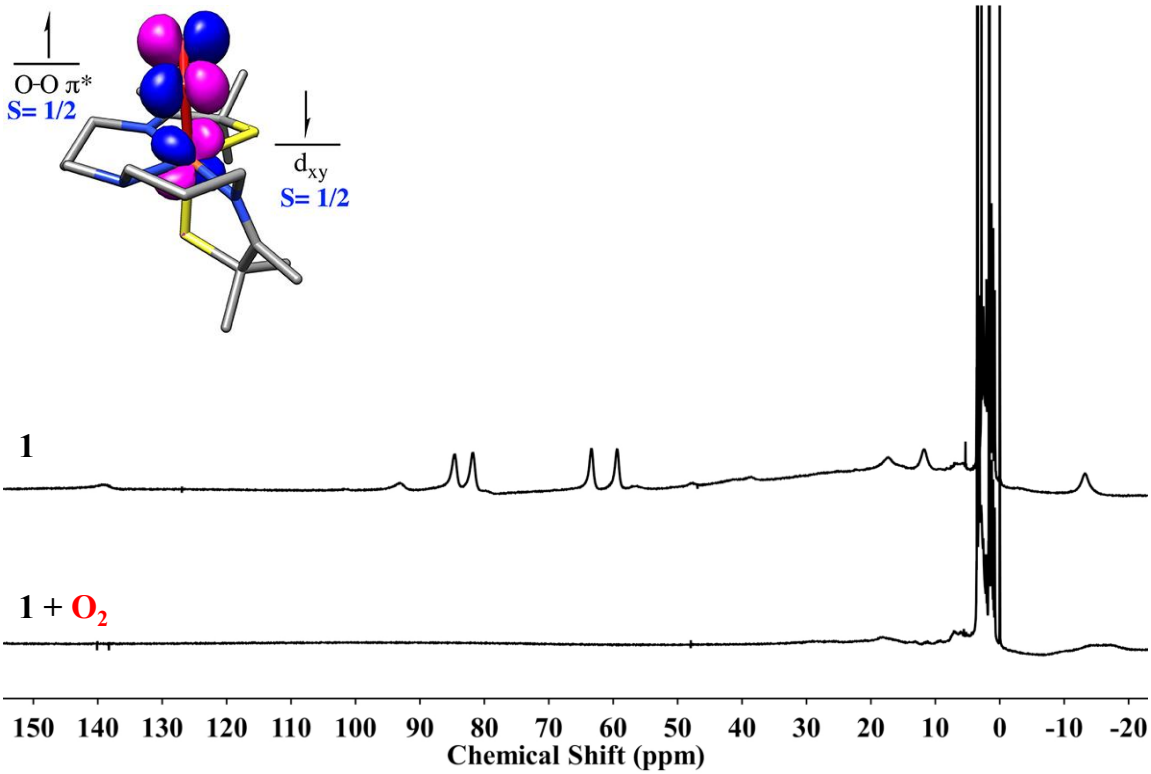

Figure 2.15. The paramagnetically shifted signals in the ^{1}H NMR spectra (500 MHz) of **1** (top) collapse to diamagnetic signals upon the addition of O_2 and formation of intermediate **6** (bottom) in d^8-THF at -40 ˚C. Inset: Singly occupied molecular orbitals (SOMO) of **6** contain strongly coupled electrons of opposite spin, one on the superoxo ($O_2^{\bullet-}$) and the other on the metal ion.

2.3.5 *Hydrogen Atom Abstraction by an Fe^{III}-Superoxo*

In enzymatic systems, Fe^{III}-superoxo intermediates are proposed to be capable oxidants thus an investigation into the reactivity of **6** was carried out. Ferric superoxo, **6**, converts to a second metastable intermediate, a putative Fe^{III}-hydroperoxo, [Fe^{III}($S_2{}^{Me2}N_3$(Pr,Pr))(OOH)] (**7**) (λ_{max} = 696 nm), at −73 °C in THF, at a rate that is dependent on the C−H bond strength of the solvent or hydrogen atom donor (Figure 2.16 & Figure 2.17). The solvent, THF, has C-H bonds

that are slightly activated by the lone pair of electrons on the THF oxygen atom to the adjacent C-H bond.[86] This makes the C-H bonds good analogues of the β-C_{cys}-H bonds of ACV since they are similarly activated by the adjacent thiolate ($BDE_{β\text{-}Ccys\text{-}H}$ = 93 kcal/mol and BDE_{THF} = 92 kcal/mol).[10,87,88] Reaction rates decrease in deuterated THF (Figure 2.17) and the observed deuterium isotope effect of kH/kD = 4.8 is comparable to that of IPNS (kH/kD = 5.6). This indicates that superoxo **6** is capable of abstracting hydrogen atoms from strong C−H bonds (BDE(THF) = 92 kcal/ mol).[86] The reaction rate increases upon the addition of a sacrificial hydrogen atom donor (100 equiv. of 1,4-cyclohexadiene (CHD), $BDE_{C\text{-}H}$ = 76 kcal/mol). [86]

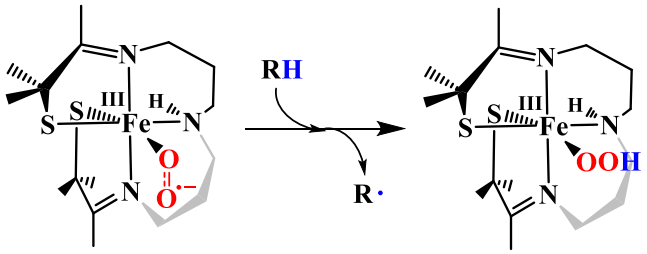

6 **7**

Figure 2.16. Depiction of hydrogen atom abstraction by **6** to produce **7.**

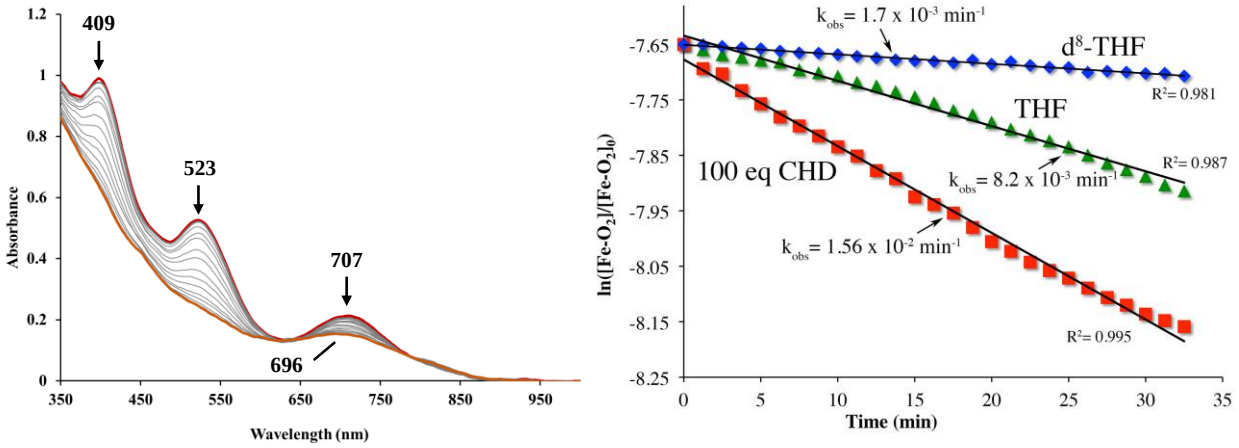

Figure 2.17. Left: Electronic absorption spectra of the conversion of **6** to a second metastable intermediate, **7**, at -73 °C in THF. Right: Pseudo-first-order kinetic plots associated with the reaction between **1** (0.48 mM) and THF (12 M), or CHD (48 mM) in THF at −73 °C. Reprinted with permission from Blakely, M. N.; Dedushko, M. A.; Poon, P. C. Y.; Villar-Acevedo, G.; Kovacs, J. A. *J. Am. Chem. Soc.* **2019**, 141, 1867−1870. Copyright 2019 American Chemical Society.[79]

Since the product of the reaction of **6** and hydrogen atom donors is believed to be a **7**. Consistent with this, a new rhombic signal grows in after 40 minutes when the reaction between **1** and O_2 is monitored by EPR (Figure 2.18). Spin quantitation indicates that the EPR signal of **7** represents 87% of the sample. The remaining 13% can be attributed to **1** and/or **6**, both of which are EPR-silent in ⊥-mode. In addition, the reaction of **6** and the hydrogen atom donor, TEMPOH (BDE_{O-H} = 66.5 kcal/mol)[89], instantaneously generates an identical rhombic signal and the TEMPO• in the EPR spectrum showing the cleavage of the O-H bond (Figure 2.19). When H_2SO_4 was added to the putative peroxo species the production of 73 ± 4 % H_2O_2 was detected by using a titanium(IV) oxysulfate. Further characterization is needed to definitively identify the

intermediate **7** but the EPR spectra and hydrogen peroxide detection are consistent with a Fe^{III}-hydroperoxo species. This species once warmed to -40 ℃ converts to the singly oxygenated species **5** implying the cleavage of the O-O bond (Figure 2.20 & Figure 2.21). Further discussion of potential intermediates following the O-O bond will be discussed in later chapters.

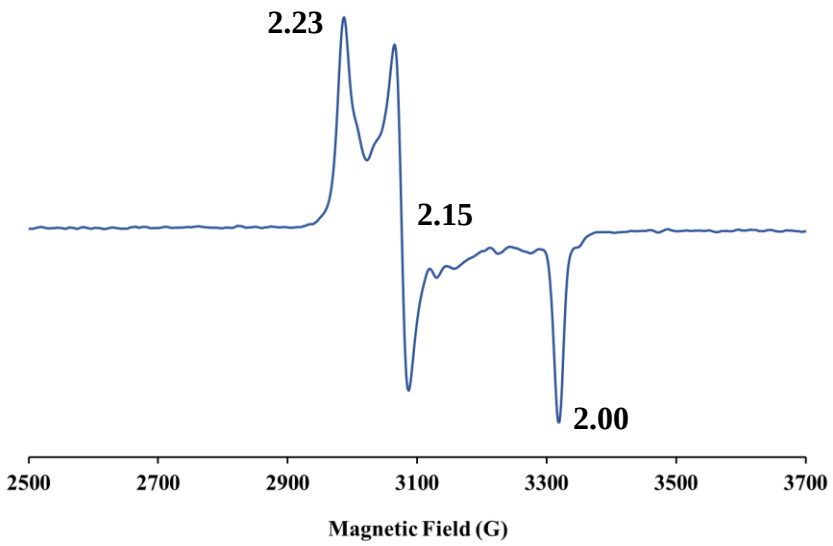

Figure 2.18. CW X-band EPR spectrum (⊥-mode) of putative hydroperoxo Fe^{III}–OOH (**7**), formed from superoxo Fe^{III}–$O_2^{\bullet-}$ (**6**) via H atom abstraction (RH = THF, CHD). in 98:2 THF:2-MeTHF glass at 117 K.

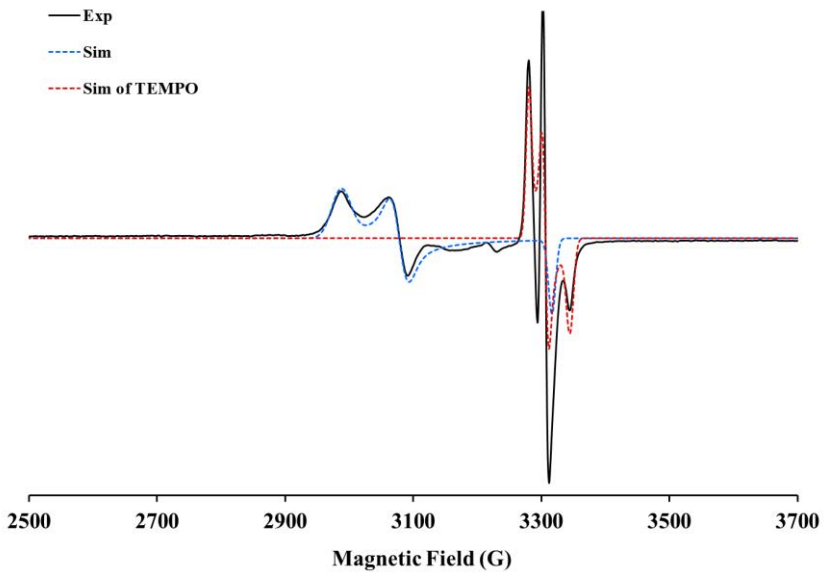

Figure 2.19. CW X-band EPR spectrum (⊥-mode) of putative hydroperoxo Fe^{III}–OOH (**7**) and TEMPO•, formed from superoxo Fe^{III}–$O_2^{\bullet-}$ (**6**) via H atom abstraction from TEMPOH in 98:2 THF:2-MeTHF glass at 117 K. (Experimental spectra (black) and simulations of FeOOH (blue) and TEMPO•(red)).

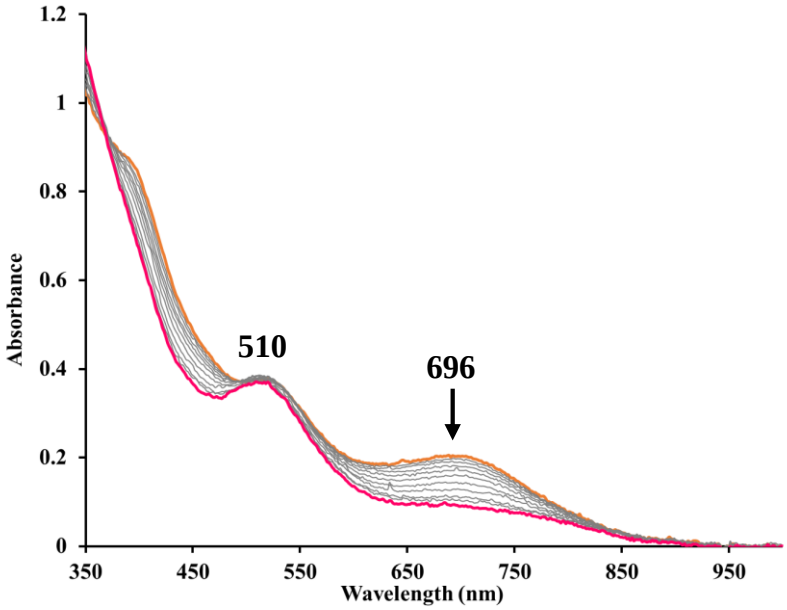

Figure 2.20. Electronic absorption spectra of the conversion of [$Fe^{III}(S_2{}^{Me2}N_3(Pr,Pr))(OOH)$] (**7**) to the singly oxygenated, **5**, over the course of 110 mins at -40 °C in THF.

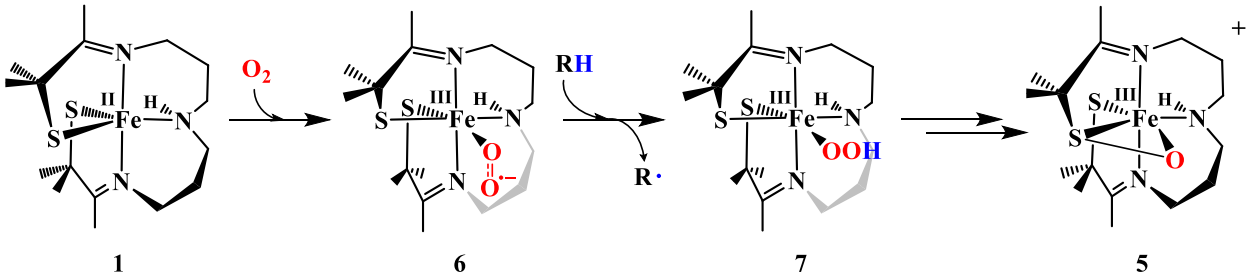

Figure 2.21. Reactivity of **2** with dioxygen to produce **5**.

2.4 Conclusion

Herein an alkylthiolate-ligated Fe^{II} complex was reported that is capable of reacting with dioxygen to form two metastable intermediates. The first intermediate, identified as an Fe^{III}-superoxo, is the first example of an alkylthiolate Fe^{III}-superoxo. Spectroscopic characterization of

6, along with calibrated DFT calculations, provides additional evidence to support the assignment of the IPNS and CDO intermediates detected via transient absorption spectroscopy, as *cis* RS-Fe^{III}-superoxo species. Electronic absorption spectral features of **6** are similar to the reported CDO and IPNS intermediates. The electronic structure of **6** is described as a S = ½ antiferromagnetically coupled to the superoxide racial producing an integer spin (S = 0) species that is EPR silent and shows diamagnetic signals in the ^{1}H NMR spectra. This EPR silent species converts to an EPR active putative **7** species, requiring the abstraction of a hydrogen atom.

In contrast to the few reported Fe^{III}-superoxo complexes, alkylthiolate-ligated **6** is capable of abstracting H atoms from strong C−H bonds, on par with that of the β-C_{cys}-H bonds of cysteine (93 kcal/mol).[10] It is plausible that π-back-donation by the electron-rich alkyl thiolate facilitates this reactivity by increasing the basicity of the distal oxygen. This is the first example of hydrogen atom abstraction by a thiolate ligated transition metal superoxo demonstrating the oxidative capabilities of an Fe-^{III} superoxo.

2.5 Reference

(1) Aluri, S.; De Visser, S. P. The Mechanism of Cysteine Oxygenation by Cysteine Dioxygenase Enzymes. *J. Am. Chem. Soc.* **2007**, *129* (48), 14846–14847. DOI: 10.1021/ja0758178.

(2) Blaesi, E. J.; Gardner, J. D.; Fox, B. G.; Brunold, T. C. Spectroscopic and Computational Characterization of the NO Adduct of Substrate-Bound Fe(II) Cysteine Dioxygenase: Insights into the Mechanism of O2 Activation. *Biochemistry* **2013**, *52* (35), 6040–6051. DOI: 10.1021/bi400825c.

(3) Blaesi, E. J.; Fox, B. G.; Brunold, T. C. Spectroscopic and Computational Investigation of Iron(III) Cysteine Dioxygenase: Implications for the Nature of the Putative Superoxo-Fe(III) Intermediate. *Biochemistry* **2014**, *53* (36), 5759–5770. DOI: 10.1021/bi500767x.

(4) Li, J.; Koto, T.; Davis, I.; Liu, A. Probing the Cys-Tyr Cofactor Biogenesis in Cysteine Dioxygenase by the Genetic Incorporation of Fluorotyrosine. *Biochemistry* **2019**, *58*, 2218–2227. DOI: 10.1021/acs.biochem.9b00006.

(5) Li, J.; Griffith, W. P.; Davis, I.; Shin, I.; Wang, J.; Li, F.; Wang, Y.; Wherritt, D. J.; Liu, A. Cleavage of a Carbon–Fluorine Bond by an Engineered Cysteine Dioxygenase. *Nat. Chem. Biol.* **2018**, *14* (9), 853–860. DOI: 10.1038/s41589-018-0085-5.

(6) Roach, P. L.; Clifton, I. J.; Hensgens, C. M.; Shibata, N.; Schofield, C. J.; Hajdu, J.; Baldwin, J. E. Structure of Isopenicillin N Synthase Complexed with Substrate and the Mechanism of Penicillin Formation. *Nature* **1997**, *387* (6635), 827–830. DOI: 10.1038/42990.

(7) Tchesnokov, E. P.; Faponle, A. S.; Davies, C. G.; Quesne, M. G.; Turner, R.; Fellner, M.; Souness, R. J.; Wilbanks, S. M.; de Visser, S. P.; Jameson, G. N. L. An Iron–Oxygen Intermediate Formed during the Catalytic Cycle of Cysteine Dioxygenase. *Chem. Commun.* **2016**, *52* (57), 8814–8817. DOI: 10.1039/c6cc03904a.

(8) Ye, S.; Wu, X.; Wei, L.; Tang, D.; Sun, P.; Bartlam, M.; Rao, Z. An Insight into the Mechanism of Human Cysteine Dioxygenase: Key Roles of the Thioether-Bonded Tyrosine-Cysteine Cofactor. *J. Biol. Chem.* **2007**, *282* (5), 3391–3402. DOI: 10.1074/jbc.M609337200.

(9) Tamanaha, E.; Zhang, B.; Guo, Y.; Chang, W.; Barr, E. W.; Xing, G.; St. Clair, J.; Ye, S.; Neese, F.; Bollinger, J. M.; et al. Spectroscopic Evidence for the Two C–H-Cleaving

Intermediates of Aspergillus Nidulans Isopenicillin N Synthase. *J. Am. Chem. Soc.* **2016**, *138* (28), 8862–8874. DOI: 10.1021/jacs.6b04065.

(10) Rauk, A.; Yu, D.; Armstrong, D. A. Oxidative Damage to and by Cysteine in Proteins: An Ab Initio Study of the Radical Structures, C-H, S-H, and C-C Bond Dissociation Energies, and Transition Structures for H Abstraction by Thiyl Radicals. *J. Am. Chem. Soc.* **1998**, *120* (34), 8848–8855. DOI: 10.1021/ja9807789.

(11) Bollinger, J. M.; Krebs, C. Enzymatic C-H Activation by Metal-Superoxo Intermediates. *Curr. Opin. Chem. Biol.* **2007**, *11* (2), 151–158. DOI: 10.1016/j.cbpa.2007.02.037.

(12) Costas, M.; Mehn, M. P.; Jensen, M. P.; Que, L. Dioxygen Activation at Mononuclear Nonheme Iron Active Sites: Enzymes, Models, and Intermediates. *Chem. Rev.* **2004**, *104* (2), 939–986. DOI: 10.1021/cr020628n.

(13) Ray, K.; Pfaff, F. F.; Wang, B.; Nam, W. Status of Reactive Non-Heme Metal-Oxygen Intermediates in Chemical and Enzymatic Reactions. *J. Am. Chem. Soc.* **2014**, *136* (40), 13942–13958. DOI: 10.1021/ja507807v.

(14) Sahu, S.; Goldberg, D. P. Activation of Dioxygen by Iron and Manganese Complexes: A Heme and Nonheme Perspective. *J. Am. Chem. Soc.* **2016**, *138* (36), 11410–11428. DOI: 10.1021/jacs.6b05251.

(15) Chiang, C. W.; Kleespies, S. T.; Stout, H. D.; Meier, K. K.; Li, P. Y.; Bominaar, E. L.; Que, L.; Münck, E.; Lee, W. Z. Characterization of a Paramagnetic Mononuclear Nonheme Iron-Superoxo Complex. *J. Am. Chem. Soc.* **2014**, *136* (31), 10846–10849. DOI: 10.1021/ja504410s.

(16) Hong, S.; Sutherlin, K. D.; Park, J.; Kwon, E.; Siegler, M. a; Solomon, E. I.; Nam, W. Crystallographic and Spectroscopic Characterization and Reactivities of a Mononuclear

Non-Haem Iron(III)-Superoxo Complex. *Nat. Commun.* **2014**, *5*, 5440. DOI: 10.1038/ncomms6440.

(17) Oddon, F.; Chiba, Y.; Nakazawa, J.; Ohta, T.; Ogura, T.; Hikichi, S. Characterization of Mononuclear Non-Heme Iron(III)-Superoxo Complex with a Five-Azole Ligand Set. *Angew. Chemie - Int. Ed.* **2015**, *54* (25), 7336–7339. DOI: 10.1002/anie.201502367.

(18) Fischer, A. A.; Lindeman, S. V.; Fiedler, A. T. A Synthetic Model of the Nonheme Iron–Superoxo Intermediate of Cysteine Dioxygenase. *Chem. Commun.* **2018**, 11344–11347. DOI: 10.1039/C8CC06247A.

(19) Hong, S.; Pfaff, F. F.; Kwon, E.; Wang, Y.; Seo, M. S.; Bill, E.; Ray, K.; Nam, W. Spectroscopic Capture and Reactivity of a Low-Spin Cobalt(IV)-Oxo Complex Stabilized by Binding Redox-Inactive Metal Ions. *Angew. Chemie - Int. Ed.* **2014**, *53* (39), 10403–10407. DOI: 10.1002/anie.201405874.

(20) Green, M. T. CH Bond Activation in Heme Proteins: The Role of Thiolate Ligation in Cytochrome P450. *Curr. Opin. Chem. Biol.* **2009**, *13* (1), 84–88. DOI: 10.1016/j.cbpa.2009.02.028.

(21) Lah, M. S.; Dixon, M. M.; Pattridge, K. A.; Stallings, W. C.; Fee, J. A.; Ludwig, M. L. Structure-Function in Escherichia Coli Iron Superoxide Dismutase: Comparisons with the Manganese Enzyme from Thermus Thermophilus. *Biochemistry* **1995**, *34* (5), 1646–1660. DOI: 10.1021/bi00005a021.

(22) Whittaker, M. M.; Whittaker, J. W. Low-Temperature Thermochromism Marks a Change in Coordination for the Metal Ion in Manganese Superoxide Dismutase. *Biochemistry* **1996**, *35* (21), 6762–6770. DOI: 10.1021/bi960088m.

(23) Ellison, J. J.; Nienstedt, A.; Shoner, S. C.; Barnhart, D.; Cowen, J. A.; Kovacs, J. A.

Reactivity of Five-Coordinate Models for the Thiolate-Ligated Fe Site of Nitrile Hydratase. *J. Am. Chem. Soc.* **1998**, *120* (23), 5691–5700. DOI: 10.1021/ja973129q.

(24) Stoll, S.; Schweiger, A. EasySpin, a Comprehensive Software Package for Spectral Simulation and Analysis in EPR. *J. Magn. Reson.* **2006**, *178* (1), 42–55. DOI: 10.1016/j.jmr.2005.08.013.

(25) Live, D. H.; Chan, S. I. Bulk Susceptibility Corrections in Nuclear Magnetic Resonance Experiments Using Superconducting Solenoids. *Anal. Chem.* **1970**, *42* (7), 791–792. DOI: 10.1021/ac60289a028.

(26) Evans, D. F. The Determination of the Paramagnetic Susceptibility of Substances in Solution by Nuclear Magnetic Resonance. *J. Chem. Soc.* **1959**, 2003–2005. DOI: 10.1039/jr9590002003.

(27) Armarego, W. L. F.; Chai, C. L. L. *Purification of Laboratory Chemicals*, 7th ed.; Butterworth-Heinemann: London, 2013.

(28) Petasis, D. T.; Hendrich, M. P. *Quantitative Interpretation of Multifrequency Multimode EPR Spectra of Metal Containing Proteins, Enzymes, and Biomimetic Complexes*, 1st ed.; Elsevier Inc., 2015; Vol. 563DOI: 10.1016/bs.mie.2015.06.025.

(29) Menges, F. Spectragryph - Optical Spectroscopy Software. 2017.

(30) Chaudhuri, P.; Hess, M.; Müller, J.; Hildenbrand, K.; Bill, E.; Weyhermüller, T.; Wieghardt, K. Aerobic Oxidation of Primary Alcohols (Including Methanol) by Copper(II)- and Zinc(N)-Phenoxyl Radical Catalysts. *J. Am. Chem. Soc.* **1999**, *121* (41), 9599–9610. DOI: 10.1021/ja991481t.

(31) Eisenberg, G. M. Colorimetric Determination of Hydrogen Peroxide. *Ind. Eng. Chem. - Anal. Ed.* **1943**, *15* (5), 327–328. DOI: 10.1021/i560117a011.

(32) Lee, Y.; Park, G. Y.; Lucas, H. R.; Vajda, P. L.; Kamaraj, K.; Vance, M. A.; Milligan, A. E.; Woertink, J. S.; Siegler, M. A.; Sarjeant, A. A. N.; et al. Copper (I)/O2 Chemistry with Imidazole Containing Tripodal Tetradentate Ligands Leading to μ -1 , 2-Peroxo - Dicopper (II) Species. *Inorg. Chem.* **2009**, *48*, 11297–11309. DOI: 10.1021/ic9017695.

(33) Bruker. APEX2 (Version 2.1-4), SAINT (Version 7.34A), SADABS (Version 2007/4). BrukerAXS Inc: Madison 2007.

(34) Altomare, A.; Cascarano, G.; Giacovazzo, C.; Guagliardi, A.; Burla, M. C.; Polidori, G.; Camalli, M. SIR 92 – a Program for Automatic Solution of Crystal Structures by Direct Methods. *J. Appl. Crystallogr.* **1994**, *27* (3), 435–435. DOI: 10.1107/S002188989400021X.

(35) Altomare, A.; Burla, M. C.; Camalli, M.; Cascarano, G. L.; Giacovazzo, C.; Guagliardi, A.; Moliterni, A. G. G.; Polidori, G.; Spagna, R. SIR97: A New Tool for Crystal Structure Determination and Refinement. *J. Appl. Crystallogr.* **1999**, *32* (1), 115–119. DOI: 10.1107/S0021889898007717.

(36) Sheldrick, G. M. SHELXL-97, Program for the Refinement of Crystal Structures. University of Göttingen, Germany. 1997.

(37) Sheldrick, G. M. Crystal Structure Refinement with SHELXL. *Acta Crystallogr. Sect. C Struct. Chem.* **2015**, *71* (Md), 3–8. DOI: 10.1107/S2053229614024218.

(38) Waasmaier, D.; Kirfel, A. New Analytical Scattering-factor Functions for Free Atoms and Ions. *Acta Crystallogr. Sect. A* **1995**, *51* (3), 416–431. DOI: 10.1107/S0108767394013292.

(39) Burnett, M. N.; Johnson, C. K. ORTEP-III: Oak Ridge Thermal Ellipsoid Plot Program for Crystal Structure Illustrations. Oak Ridge National Laboratory Report ORNL-6895

1996.

(40) Persistence of Vision Raytracer. Persistence of Vision Pty. Ltd.: Williamstown, Victoria, Australia 2004.

(41) Neese, F. The ORCA Program System. *WIREs Comput. Mol. Sci.* **2012**, *2*, 73–78. DOI: 10.1002/wcms.81.

(42) Grimme, S.; Ehrlich, S.; Goerigk, L. Effect of the Damping Function in Dispersion Corrected Density Functional Theory. *J. Comput. Chem.* **2011**, *32* (7), 1456–1465. DOI: 10.1002/jcc.21759.

(43) Barone, V.; Cossi, M. Quantum Calculation of Molecular Energies and Energy Gradients in Solution by a Conductor Solvent Model. *J. Phys. Chem. A* **1998**, *102* (11), 1995–2001. DOI: 10.1021/jp9716997.

(44) Adamo, C.; Barone, V. Toward Reliable Density Functional Methods without Adjustable Parameters: The PBE0 Model. *J. Chem. Phys.* **1999**, *110* (13), 6158–6170. DOI: 10.1063/1.478522.

(45) Neese, F.; Wennmohs, F.; Hansen, A.; Becker, U. Efficient, Approximate and Parallel Hartree–Fock and Hybrid DFT Calculations. A 'Chain-of-Spheres' Algorithm for the Hartree–Fock Exchange. *Chem. Phys.* **2009**, *356* (1–3), 98–109. DOI: 10.1016/j.chemphys.2008.10.036.

(46) Villar-Acevedo, G.; Lugo-Mas, P.; Blakely, M. N.; Rees, J. A.; Ganas, A. S.; Hanada, E. M.; Kaminsky, W.; Kovacs, J. A. Metal-Assisted Oxo Atom Addition to an Fe(III) Thiolate. *J. Am. Chem. Soc.* **2017**, *139* (1), 119–129. DOI: 10.1021/jacs.6b03512.

(47) Shearer, J.; Scarrow, R. C.; Kovacs, J. A. Synthetic Models for the Cysteinate-Ligated Non-Heme Iron Enzyme Superoxide Reductase: Observation and Structural

Characterization by XAS of an Fe III −OOH Intermediate. *J. Am. Chem. Soc.* **2002**, *124* (39), 11709–11717. DOI: 10.1021/ja012722b.

(48) Villar-Acevedo, G.; Nam, E.; Fitch, S.; Benedict, J.; Freudenthal, J.; Kaminsky, W.; Kovacs, J. A. Influence of Thiolate Ligands on Reductive N-O Bond Activation. Probing the O2- Binding Site of a Biomimetic Superoxide Reductase Analogue and Examining the Proton-Dependent Reduction of Nitrite. *J. Am. Chem. Soc.* **2011**, *133* (5), 1419–1427. DOI: 10.1021/ja107551u.

(49) Kumar, D.; Sastry, G. N.; Goldberg, D. P.; De Visser, S. P. Mechanism of S-Oxygenation by a Cysteine Dioxygenase Model Complex. *J. Phys. Chem. A* **2012**, *116* (1), 582–591. DOI: 10.1021/jp208230g.

(50) Soda, T.; Kitagawa, Y.; Onishi, T.; Takano, Y.; Shigeta, Y.; Nagao, H.; Yoshioka, Y.; Yamaguchi, K. Ab Initio Computations of Effective Exchange Integrals for H–H, H–He–H and Mn2O2 Complex: Comparison of Broken-Symmetry Approaches. *Chem. Phys. Lett.* **2000**, *319* (3–4), 223–230. DOI: 10.1016/S0009-2614(00)00166-4.

(51) Hirata, S.; Head-Gordon, M. Time-Dependent Density Functional Theory within the Tamm–Dancoff Approximation. *Chem. Phys. Lett.* **1999**, *314* (3–4), 291–299. DOI: 10.1016/S0009-2614(99)01149-5.

(52) Neese, F.; Olbrich, G. Efficient Use of the Resolution of the Identity Approximation in Time-Dependent Density Functional Calculations with Hybrid Density Functionals. *Chem. Phys. Lett.* **2002**, *362* (1–2), 170–178. DOI: 10.1016/S0009-2614(02)01053-9.

(53) Pettersen, E. F.; Goddard, T. D.; Huang, C. C.; Couch, G. S.; Greenblatt, D. M.; Meng, E. C.; Ferrin, T. E. UCSF Chimera--a Visualization System for Exploratory Research and Analysis. *J. Comput. Chem.* **2004**, *25* (13), 1605–1612. DOI: 10.1002/jcc.20084.

(54) Frisch, M. J.; Trucks, G. W.; Schlegel, H. B.; Scuseria, G. E.; Robb, M. A.; Cheeseman, J. R.; Scalmani, G.; Barone, V.; Petersson, G. A.; Nakatsuji, H.; et al. Gaussian 16. *Gaussian, Inc. Wallingford CT* **2016**.

(55) Shoner, S. C.; Nienstedt, A. M.; Ellison, J. J.; Kung, I. Y.; Barnhart, D.; Kovacs, J. A. Structural Comparison of Five-Coordinate Thiolate-Ligated M II = Fe II , Co II , Ni II , and Zn II Ions Wrapped in a Chiral Helical Ligand. *Inorg. Chem.* **1998**, *37* (22), 5721–5726. DOI: 10.1021/ic980882r.

(56) Hagen, K. S.; Holm, R. H. Systematic Iron(II)-Thiolate Chemistry: Synthetic Entry to Trinuclear Complexes. *J. Am. Chem. Soc.* **1982**, *104* (20), 5496–5497. DOI: 10.1021/ja00384a045.

(57) Corwin, D. T.; Gruff, E. S.; Koch, S. A. Zinc, Cobalt, and Cadmium Thiolate Complexes: Models for the Zinc (S-Cys)2(His)2 Centre in Transcription Factor IIIA (Cys = Cysteine; His = Histidine). *J. Chem. Soc. Chem. Commun.* **1987**, *272* (13), 966. DOI: 10.1039/c39870000966.

(58) Addison, A. W.; Rao, T. N.; Reedijk, J.; van Rijn, J.; Verschoor, G. C. Synthesis, Structure, and Spectroscopic Properties of Copper(II) Compounds Containing Nitrogen–Sulphur Donor Ligands; the Crystal and Molecular Structure of Aqua[1,7-Bis(N-Methylbenzimidazol-2′-Yl)-2,6-Dithiaheptane]Copper(II) Perchlorate. *J. Chem. Soc., Dalt. Trans.* **1984**, No. 7, 1349–1356. DOI: 10.1039/DT9840001349.

(59) McQuilken, A. C.; Jiang, Y.; Siegler, M. A.; Goldberg, D. P. Addition of Dioxygen to an N 4 S(Thiolate) Iron(II) Cysteine Dioxygenase Model Gives a Structurally Characterized Sulfinato–Iron(II) Complex. *J. Am. Chem. Soc.* **2012**, *134* (21), 8758–8761. DOI: 10.1021/ja302112y.

(60) Confer, A. M.; Vilbert, A. C.; Dey, A.; Lancaster, K. M.; Goldberg, D. P. A Mononuclear, Nonheme Fe II -Piloty's Acid (PhSO 2 NHOH) Adduct: An Intermediate in the Production of {FeNO} 7/8 Complexes from Piloty's Acid. *J. Am. Chem. Soc.* **2019**, *141* (17), 7046–7055. DOI: 10.1021/jacs.9b01700.

(61) Leipzig, B. K.; Rees, J. A.; Kowalska, J. K.; Theisen, R. M.; Kavčič, M.; Poon, P. C. Y.; Kaminsky, W.; DeBeer, S.; Bill, E.; Kovacs, J. A. How Do Ring Size and π-Donating Thiolate Ligands Affect Redox-Active, α-Imino- N -Heterocycle Ligand Activation? *Inorg. Chem.* **2018**, *57* (4), 1935–1949. DOI: 10.1021/acs.inorgchem.7b02748.

(62) Gordon, J. B.; McGale, J. P.; Prendergast, J. R.; Shirani-Sarmazeh, Z.; Siegler, M. A.; Jameson, G. N. L.; Goldberg, D. P. Structures, Spectroscopic Properties, and Dioxygen Reactivity of 5- and 6-Coordinate Nonheme Iron(II) Complexes: A Combined Enzyme/Model Study of Thiol Dioxygenases. *J. Am. Chem. Soc.* **2018**, *140* (44), 14807–14822. DOI: 10.1021/jacs.8b08349.

(63) Schweitzer, D. Unpublished Result. *Lab Noteb. 2*, 100. .

(64) Pavlishchuk, V. V; Addison, A. W. Conversion Constants for Redox Potentials Measured versus Different Reference Electrodes in Acetonitrile Solutions at 25°C. *Inorganica Chim. Acta* **2000**, *298* (1), 97–102. DOI: 10.1016/S0020-1693(99)00407-7.

(65) Hong, S.; Lee, Y.-M.; Ray, K.; Nam, W. Dioxygen Activation Chemistry by Synthetic Mononuclear Nonheme Iron, Copper and Chromium Complexes. *Coord. Chem. Rev.* **2017**, *334*, 25–42. DOI: 10.1016/j.ccr.2016.07.006.

(66) Kennepohl, P.; Neese, F.; Schweltzer, D.; Jackson, H. L.; Kovacs, J. A.; Solomon, E. I. Spectroscopy of Non-Heme Iron Thiolate Complexes: Insight into the Electronic Structure of the Low-Spin Active Site of Nitrile Hydratase. *Inorg. Chem.* **2005**, *44* (6), 1826–1836.

DOI: 10.1021/ic0487068.

(67) Chai, S. C.; Bruyere, J. R.; Maroney, M. J. Probes of the Catalytic Site of Cysteine Dioxygenase. *J. Biol. Chem.* **2006**, *281* (23), 15774–15779. DOI: 10.1074/jbc.M601269200.

(68) *Perspectives on Bioinorganic Chemistry*, 1st Editio.; Hay, R. W., Dilworth, J. ., Nolan, K. B., Eds.; JAI Press: Stamford, CT, 1999.

(69) Shearer, J.; Fitch, S. B.; Kaminsky, W.; Benedict, J.; Scarrow, R. C.; Kovacs, J. A. How Does Cyanide Inhibit Superoxide Reductase? Insight from Synthetic FeIIIN4S Model Complexes. *Proc. Natl. Acad. Sci.* **2003**, *100* (7), 3671–3676. DOI: 10.1073/pnas.0637029100.

(70) Juda, G. A.; Shepard, E. M.; Elmore, B. O.; Dooley, D. M. A Comparative Study of the Binding and Inhibition of Four Copper-Containing Amine Oxidases by Azide: Implications for the Role of Copper during the Oxidative Half-Reaction. *Biochemistry* **2006**, *45* (29), 8788–8800. DOI: 10.1021/bi060481k.

(71) Collman, J. P.; Dey, A.; Barile, C. J.; Ghosh, S.; Decréau, R. A. Inhibition of Electrocatalytic O2 Reduction of Functional CcO Models by Competitive, Non-Competitive, and Mixed Inhibitors. *Inorg. Chem.* **2009**, *48* (22), 10528–10534. DOI: 10.1021/ic900825y.

(72) Bakac, A.; Espenson, J. H.; Scott, S. L.; Rodgers, K. R. Interaction of Chromium (II) Complexes with Molecular Oxygen. Spectroscopic and Kinetic Evidence for H1-Superoxo Complex Formation. *J. Am. Chem. Soc.* **1995**, *117* (24), 6483–6488. DOI: 10.1021/ja00129a010.

(73) Cho, J.; Woo, J.; Nam, W. An “End-On” Chromium(III)-Superoxo Complex:

Crystallographic and Spectroscopic Characterization and Reactivity in C−H Bond Activation of Hydrocarbons. *J. Am. Chem. Soc.* **2010**, *132* (17), 5958–5959. DOI: 10.1021/ja1015926.

(74) Cho, J.; Kang, H. Y.; Liu, L. V.; Sarangi, R.; Solomon, E. I.; Nam, W. Mononuclear Nickel(Ii)-Superoxo and Nickel(Iii)-Peroxo Complexes Bearing a Common Macrocyclic TMC Ligand. *Chem. Sci.* **2013**, *4* (4), 1502. DOI: 10.1039/c3sc22173c.

(75) Kieber-Emmons, M. T.; Annaraj, J.; Seo, M. S.; Van Heuvelen, K. M.; Tosha, T.; Kitagawa, T.; Brunold, T. C.; Nam, W.; Riordan, C. G. Identification of an "End-on" Nickel−Superoxo Adduct, [Ni(Tmc)(O 2)] +. *J. Am. Chem. Soc.* **2006**, *128* (44), 14230–14231. DOI: 10.1021/ja0644879.

(76) Bhadra, M.; Lee, J. Y. C.; Cowley, R. E.; Kim, S.; Siegler, M. A.; Solomon, E. I.; Karlin, K. D. Intramolecular Hydrogen Bonding Enhances Stability and Reactivity of Mononuclear Cupric Superoxide Complexes. *J. Am. Chem. Soc.* **2018**, *140* (29), 9042–9045. DOI: 10.1021/jacs.8b04671.

(77) Liu, L.-L. L.; Li, H.-X. X.; Wan, L.-M. M.; Ren, Z.-G. G.; Wang, H.-F. F.; Lang, J.-P. P. A Mn(Iii)–Superoxo Complex of a Zwitterionic Calix[4]Arene with an Unprecedented Linear End-on Mn(Iii)–O2 Arrangement and Good Catalytic Performance for Alkene Epoxidation. *Chem. Commun.* **2011**, *47* (39), 11146–11148. DOI: 10.1039/c1cc14262c.

(78) Gordon, J. B.; Vilbert, A. C.; Siegler, M. A.; Lancaster, K. M.; Goldberg, D. P.; Moe, P.; Moënne-Loccoz, P.; Goldberg, D. P. A Nonheme Thiolate-Ligated Cobalt Superoxo Complex: Synthesis and Spectroscopic Characterization, Computational Studies, and Hydrogen Atom Abstraction Reactivity. *J. Am. Chem. Soc.* **2019**, *141* (8), 3641–3653. DOI: 10.1021/jacs.8b13134.

(79) Blakely, M. N.; Dedushko, M. A.; Yan Poon, P. C.; Villar-Acevedo, G.; Kovacs, J. A. Formation of a Reactive, Alkyl Thiolate-Ligated Fe III -Superoxo Intermediate Derived from Dioxygen. *J. Am. Chem. Soc.* **2019**, *141* (5), 1867–1870. DOI: 10.1021/jacs.8b12670.

(80) Cramer, C. J. Bioinorganic Chemistry Special Feature: Variable Character of OO and MO Bonding in Side-on (Eta 2) 1:1 Metal Complexes of O2. *Proc. Natl. Acad. Sci.* **2003**, *100* (7), 3635–3640. DOI: 10.1073/pnas.0535926100.

(81) Smirnov, V. V.; Roth, J. P. Evidence for Cu-O2 Intermediates in Superoxide Oxidations by Biomimetic Copper(II) Complexes. *J. Am. Chem. Soc.* **2006**, *128* (11), 3683–3695. DOI: 10.1021/ja056741n.

(82) Holland, P. L. Metal–Dioxygen and Metal–Dinitrogen Complexes: Where Are the Electrons? *Dalt. Trans.* **2010**, *39* (23), 5415. DOI: 10.1039/c001397h.

(83) Rybak-Akimova, E. V. Mechanisms of Oxygen Binding and Activation at Transition Metal Centers. In *Physical Inorganic Chemistry*; John Wiley & Sons, Inc.: Hoboken, NJ, USA, 2010; Vol. Vol. 2., pp 109–188DOI: 10.1002/9780470602577.ch4.

(84) Schweitzer, D.; Ellison, J. J.; Shoner, S. C.; Lovell, S.; Kovacs, J. a; Herein, R. A Synthetic Model for the NO-Inactivated Form of Nitrile Hydratase Nitric Oxide (NO) 1 Has Been Shown to Perform a Number of Important Functions in Medicine and Biology , Including Blood Pressure Control , Neurotransmission , and Inhibition of Tumor The. **1998**, No. 24, 10996–10997. .

(85) Singha, A.; Das, P. K.; Dey, A. Resonance Raman Spectroscopy and Density Functional Theory Calculations on Ferrous Porphyrin Dioxygen Adducts with Different Axial Ligands: Correlation of Ground State Wave Function and Geometric Parameters with

Experimental Vibrational Frequencies. *Inorg. Chem.* **2019**, *58* (16), 10704–10715. DOI: 10.1021/acs.inorgchem.9b00656.

(86) Xue, X. S.; Ji, P.; Zhou, B.; Cheng, J. P. The Essential Role of Bond Energetics in C-H Activation/Functionalization. *Chem. Rev.* **2017**, *117* (13), 8622–8648. DOI: 10.1021/acs.chemrev.6b00664.

(87) Luo, Y.-R. *Comprehensive Handbook of Chemical Bond Energies*; CRC Press, 2007DOI: 10.1201/9781420007282.

(88) Laarhoven, L. J. J.; Mulder, P. α-C-H Bond Strengths in Tetralin and THF: Application of Competition Experiments in Photoacoustic Calorimetry. *J. Phys. Chem. B* **1997**, *101* (1), 73–77. DOI: 10.1021/jp960982n.

(89) Warren, J. J.; Tronic, T. a.; Mayer, J. M.; Bond, S. V. G. Thermochemistry of Proton-Coupled Electron Transfer Reagents and Its Implications - Chemical Reviews (ACS Publications). *Chem. Rev.* **2010**, *110* (12), 6961–7001. DOI: 10.1021/cr100085k.

Chapter 3. Cryogenic Stopped-Flow Kinetic Studies Involving the Formation of a Thiolate-Ligated Fe^{III}-Superoxo

Reproduced in part with the permission of Inorganic Chemistry, from Cryogenic Stopped-Flow Kinetic Studies Involving the Formation of a Thiolate-Ligated Fe^{III}-Superoxo, Blakely, Maike N.; Piquette, Marc C.; Greiner, Maria B.; Kovacs, Julie A. *Inorg. Chem.* Submitted for Publication.

3.1 Introduction

Dioxygen is a versatile, abundant, and clean oxidant for catalytic oxidation reactions that is harnessed in Nature by first-row transition metal-containing enzymes.[1–5] Reactions involving dioxygen are kinetically slow in the absence of a transition-metal catalyst, because they are spin-forbidden.[6] Non-heme Fe enzymes, such as isopenicillin N-synthase (IPNS) and cysteine dioxygenase (CDO), utilize dioxygen in order to carry out processes that are relevant to human health. The former catalyzes the oxidative bicyclization of a cysteine-containing tripeptide precursor to penicillin.[7] The latter, CDO, catalyzes the oxidation of cysteine to cysteine sulfinic acid.[8] High levels of cysteine have been linked to neurological disorders, such as Alzheimer's and Parkinson's,[9] and the metastasis of cancerous tumors.[10] Both IPNS and CDO are non-heme iron enzymes proposed to bind O_2 *cis* to a cysteinate sulfur to afford a reactive Fe^{III}-superoxo intermediate.[7,11–13] The high covalency of the IPNS Fe^{III}-SR bond was shown by magnetic circular dichroism (MCD) and density functional theory (DFT) calculations to lower the activation barrier to dioxygen binding, and stabilize the Fe^{III}-superoxo intermediate.[14–16] The IPNS Fe^{III}-superoxo intermediate has been shown to abstract a β H-atom adjacent to the thiolate sulfur (BDE(C-H)= 93

kcal/mol) to afford an Fe^{III}-hydroperoxo intermediate,[17] and with CDO is proposed to attack the adjacent cysteine sulfur to form a peroxythiolate intermediate (Figure 3.1). Both of these oxidation steps involve an intramolecular reaction, thus making observation of the Fe^{III}-superoxo intermediate extremely challenging.

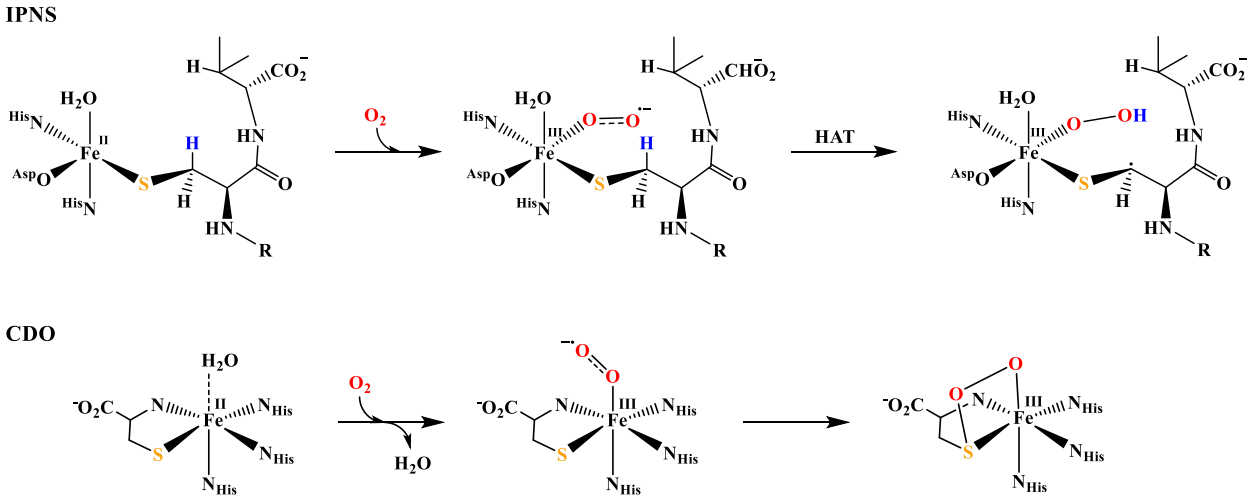

Figure 3.1. Schematic illustration of the active site of ACV-bound IPNS where the five-coordinate iron binds O_2 generating an Fe^{III}-superoxo intermediate that abstracts a hydrogen atom (blue) (top).[7] Depiction of the active site of cysteine bound CDO where O_2 binds *cis* to the $^{cys}S^-$, to generate an Fe^{III}-superoxo intermediate (bottom).[12]

Generally, non-heme Fe–superoxo intermediates are short-lived even at low temperatures, and are thus difficult to spectroscopically characterize.[17,18] The putative IPNS Fe^{III}-superoxo intermediate is only spectroscopically observed upon deuteration of the cysteinate β-hydrogens, and even then in only small amounts (14%), using either transient absorption spectroscopy (λ_{max}= ~500 and ~630 nm; t = 2-10 ms), or by rapid freeze quench Mössbauer spectroscopy (δ = 0.53

mm/s).[17] Vibrational data has yet to be reported. An Fe intermediate, tentatively assigned as an Fe^{III}-peroxythiolate based on computational studies, is also transiently observed (~20 ms) during the catalytic cycle of CDO via stopped-flow absorption spectroscopy (λ_{max}= 500 nm, 640 nm). However, an Fe^{III}-superoxo assignment was not entirely ruled out.[18] Prior to the observation of the dioxygen-derived CDO intermediate, a putative Fe^{III}-superoxo species was generated via the chemical-rescue of a catalytically inactive substrate-bound form of Fe^{III}-CDO using superoxide ($O_2^{\bullet-}$).[19] A transient absorption feature associated with this species (at λ_{max} = 565 nm) was attributed to a putative Fe^{III}-superoxo. This species was also observed via parallel-mode X-band EPR spectroscopy, and shown to contain a *g-value of* ~11, consistent with an *S* =3 ground state, and a high-spin S= 5/2 ferric ion ferromagnetically coupled to a S= ½ $O_2^{\bullet-}$ radical.[19] Although the observation of these intermediates is remarkable, examining the mechanism of formation of these intermediates would be difficult due to their extremely fast timescales and limitations regarding accessible temperatures due to the high freezing point of water.

Small molecule analogues of metalloenzyme active sites can be used to study the mechanism of dioxygen activation and provide insights into the metal-centered intermediate's oxidation state and electronic structure.[20–22] The first intermediate in dioxygen activation pathways is a metal-superoxo. The degree of electron transfer is variable and the formal oxidation of first-row transition-metal superoxo complexes has been debated.[23,24] Only five well-characterized examples of small molecule, non-heme Fe^{III}-superoxo complexes have been reported.[25–29] For those generated from O_2, the reversibility of the reaction was qualitatively evaluated by purging a solution with an inert gas and monitoring the intensity of the Fe^{III}-superoxo electronic absorption bands. A decrease in intensity, followed by an increase to its original value upon the re-introduction of O_2 over several cycles provides qualitative evidence for reversible O_2 binding.

Using this method, synthetic small-molecule complexes, [Fe^{II}(BDPP)] and [$Fe^{II}(L^{Ph})(Tp^{Me2})$], have been shown to reversibly bind O_2 in tetrahydrofuran (THF) at -80 ˚C and -60 ˚C, respectively.[25,27] In contrast, the arylthiolate-ligated complex, [$Fe^{II}(Tp^{Me2})$(2-ATP)] was qualitatively shown to irreversibly bind O_2 in THF at -80 ˚C.[29] An S = 2 ground state indicates that the electronic structure of [$Fe^{III}(O_2)(Tp^{Me2})$(2-ATP)] is best described as a high-spin S= 5/2 Fe^{III} center antiferromagnetically coupled to a superoxide radical.[29] Another example of irreversible O_2 binding to a thiolate-ligated first row transition-metal complex, involved [$Co^{II}(Me_3TACN)(S_2SiMe_2)$].[30] Interestingly, EPR and XAS data, as well as DFT computational studies indicate that the cobalt ion maintains electron density consistent with an oxidation state of Co^{II} throughout the reaction suggesting that the bis-thiolate ligand is redox active.[30] These examples illustrate differing metal- and ligand-dependent reactivities with respect to O_2 binding and the transfer of electron density onto the O_2 moiety, however, limited information can be obtained from qualitative studies.

We recently reported a crystallographically characterized, five-coordinate, reduced alkyl thiolate-ligated complex, [$Fe^{II}(S_2^{Me2}N_3$(Pr,Pr)] (**1**) that reacts with O_2 to form a well-characterized ferric superoxo intermediate, [$Fe^{III}(S_2^{Me2}N_3$(Pr,Pr)(O_2)] (**6**).[28] Computational studies, vibrational data, EPR and ^{1}H NMR spectroscopic data established that the electronic structure of **2** consists of a low-spin Fe^{III} (S = ½) ion strongly antiferromagnetically coupled (J^{calc}= – 450 cm^{-1}) to an S= ½ superoxo radical.[28] This indicates that the reduced Fe^{II} ion transfers an electron to O_2 upon dioxygen binding to the metal ion, to afford a superoxo (Fe^{II} (**1**) + O_2→Fe^{III}-$O_2^{\bullet}$ (**6**)).[28] The study reported herein explores the mechanism of formation of metastable [$Fe^{III}(S_2^{Me2}N_3$(Pr,Pr)(O_2)] (**6**),[28] via two distinct pathways (Figure 3.2): one involving inner-sphere electron transfer, and the other involving outer sphere electron transfer. Kinetic studies are described in which we

quantitatively assess the reversibility of, and barrier to, O_2 binding to five-coordinate $[Fe^{II}(S_2{}^{Me2}N_3(Pr,Pr)]$ (**1**), as well as KO_2 addition to crystallographically characterized $[Fe^{III}(S_2{}^{Me2}N_3(Pr,Pr)]^+$ (**2**). .

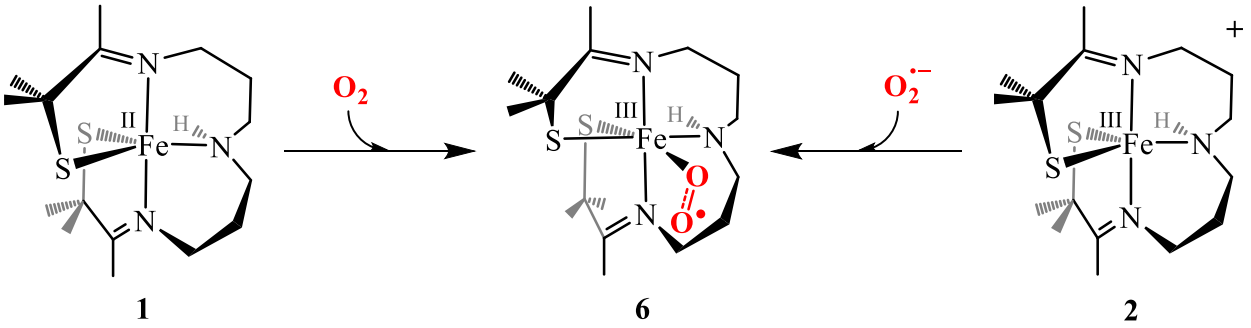

Figure 3.2. Two pathways for the formation of metastable Fe^{III}-Superoxo (**6**).

3.2 Experimental

General Methods. Reagents purchased from commercial vendors were of the highest purity available and used without further purification. $[Fe^{II}(S_2{}^{Me2}N_3(Pr,Pr)]$ (**1**) and $[Fe^{III}(S_2{}^{Me2}N_3(Pr,Pr)]PF_6$ (**2**) were synthesized as previously described (*vide supra*).[28,31] Methanol (MeOH) was distilled over calcium hydride and degassed prior to use. Un-stabilized tetrahydrofuran (THF) was rigorously degassed and purified using solvent purification columns housed in a custom stainless-steel cabinet, dispensed via a stainless steel Schlenk line (GlassContour). All manipulations were performed using Schlenk line techniques or under an N_2 atmosphere in a glovebox.

Kinetic Measurements. Preparation of solutions was carried out in a N_2-filled anaerobic glove-box ([O_2] <1 ppm) and placed in Hamilton gastight® syringes equipped with three-way valves. Time-resolved spectra (350−820 nm) were acquired at low temperatures using a TgK Scientific (U.K.) CSF-61DX2 Multi-Mixing CryoStopped-Flow Instrument equipped with a tungsten visible light source. The stopped-flow instrument is equipped with PEEK tubing fitted inside stainless-steel plumbing, a 1.00 cm^3 quartz mixing cell, and an anaerobic kit purged with an inert gas. The temperature in the mixing cell was maintained to ± 0.1 °C, and the mixing time was 2-3 ms. All flow lines of the instrument were extensively washed with degassed, anhydrous THF before charging the driving syringes with solutions containing the reactants. The reactions were studied by rapid scanning spectrophotometry under pseudo-first order conditions with excess oxygen or superoxide. Saturated solutions of O_2 were prepared by bubbling dry O_2 gas for 15 min into gastight syringes containing dry THF at 25 °C. The solubility of O_2 was taken as 7.9 mM in THF at 25 °C and as 8.5 mM in MeOH at 25 °C.[32,33] The O_2 concentration was assumed not to change upon cooling, given that the system is closed, and the solutions were not in contact with the gas phase (small variations in the solvent density were not taken into account). Dilutions of the O_2-saturated solvent were performed anaerobically to obtain the desired [O_2]. Potassium superoxide solutions were prepared as described below. All concentrations reported in stopped-flow experiments refer to the "after mixing" conditions. Experiments were performed in single-mixing mode, with a 1:1 (v/v) mixing ratio. A series of three or four measurements gave an acceptable standard deviation (within 10%). Rates reported for the oxygen dependence are the average of at least three different trials. Data analysis was performed with Kinetic Studio software from TgK Scientific.[34] Data was fit at a single wavelength (523.5 nm) using the following equation:

$$A_t = A_\infty - (A_\infty - A_0)e^{-k_{obs}t}$$

Preparation of Potassium Superoxide Solutions. A very fine powder of KO_2 was weighed out on an analytical balance, and then 1 eq. Kyrptofix®222 was added to solubilize the KO_2 in THF. An appropriate amount of Bu_4NPF_6 ([Bu_4NPF_6] = 1.5-11.5 mM (pre-mix concentration)) was added to maintain an ionic strength of 10 mM (post-mix concentration). These solutions were vigorously stirred at RT in glovebox for at least 20 mins and used within 6 hrs of preparation.

3.3 Results and Discussion

3.3.1 *Kinetic Measurements for O_2 Binding*

Electronic absorption spectroscopy was used to monitor the reaction between [$Fe^{II}(S_2{}^{Me2}N_3(Pr,Pr)$] (**1**) and O_2, using a cryogenic stopped-flow instrument. The growth of spectral features associated with [$Fe^{III}(S_2{}^{Me2}N_3(Pr,Pr)(O_2)$] (**6**) (Figure 3.3) were monitored under pseudo first order conditions with excess O_2. Saturated solutions of O_2 were prepared by bubbling dry O_2 gas into a gastight syringe containing dry THF for 15 min at 25 °C. The solubility of O_2 was taken as 7.9 mM in THF at 25 °C and as 8.5 mM in MeOH at 25 °C.[32,33] Dilutions of the O_2-saturated solvent were performed anaerobically to obtain the desired O_2 concentration. As illustrated in the time-resolved absorption spectrum, Figure 3.3, superoxo **6** forms in less than 20 sec. The kinetic trace for the change in absorbance at λ_{max} = 523 nm, can be

$$A_t = A_\infty - (A_\infty - A_0)e^{-k_{obs}t} \qquad (1)$$

fit to the single exponential of eqn (1) with very small residuals. The general kinetic scheme is shown in eqns (2) – (4).[35] The observed rate constant (k_{obs}) was found to be independent of the concentration of **1** (Figure 3.4), confirming that the reaction is first-order overall with respect to **1**, consistent with the formation of a 1:1 dioxygen adduct.

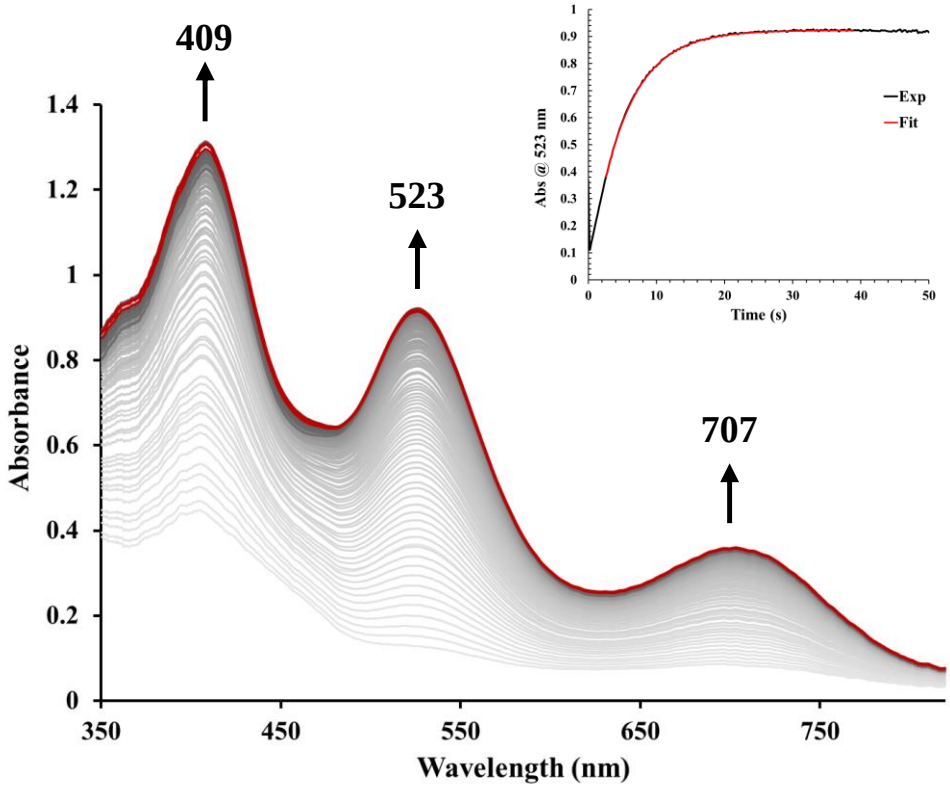

Figure 3.3. Time-resolved spectral changes obtained upon mixing THF solutions of [$Fe^{II}(S_2{}^{Me2}N_3(Pr,Pr)$](**1**) and O_2 (4.0 mM) at -40 ˚C. Inset: Kinetic trace (λ = 523 nm) showing the formation of the Fe-O_2 intermediate **6**. All reported concentrations are after mixing in the stopped-flow cell.

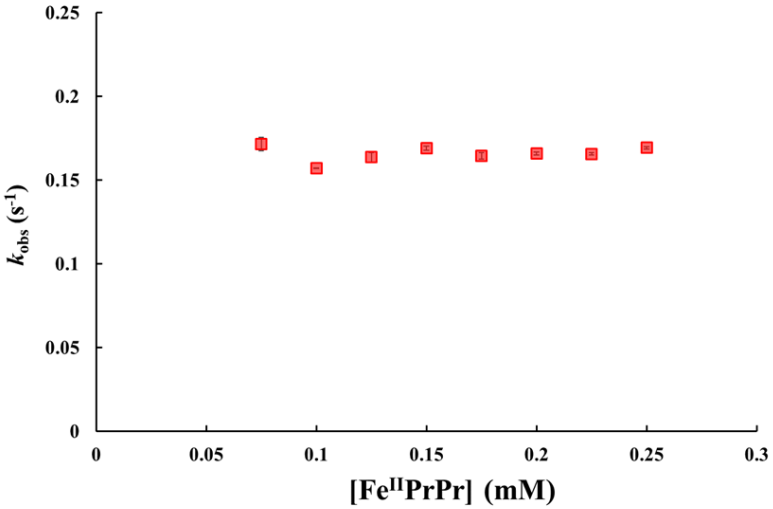

Figure 3.4. Plot of observed rate constants (*k*obs) for the formation of Fe^{III}-superoxo (**6**) versus [$Fe^{II}(S_2{}^{Me2}N_3$(Pr,Pr)](**1**) concentration at -40 °C in THF. [O_2] after mixing = 4.0 mM.

The reaction order with respect to dioxygen was determined by varying the concentration of dioxygen over the range [O_2] = 2.4 mM to 4.0 mM in THF and [O_2] = 2.55 mM to 4.25 mM in MeOH. The observed rate constant, k_{obs}, was shown to increase linearly with increasing dioxygen concentration (Figure 3.5 and Table 3.4) consistent with first order dependence on dioxygen. For

$$Fe^{II} + O_2 \underset{k_{off}}{\overset{k_{on}}{\rightleftharpoons}} Fe^{III}O_2 \qquad (2)$$

$$\frac{d[Fe^{III}O_2]}{dt} = k_{obs}[Fe^{II}] \qquad (3)$$

$$k_{obs} = k_{on}[O_2] + k_{off} \qquad (4)$$

a reversible process (eqn (1)), k_{obs} would be dependent on both the rate constant for O_2 binding (k_{on}), as well as the dissociation rate constant (k_{off}). Thus, under pseudo-first order conditions with excess O_2 eq. (3) holds.[35] Data was collected over a range of [O_2] concentrations, and temperatures (-40 to -10 ˚C). From k_{obs} vs. [O_2] plots, the second order rate constant for dioxygen binding (k_{on}) to **1**, and dioxygen release (k_{off}) from **6** in THF and MeOH were obtained from the slope and intercept of the straight line, respectively (Figure 3.5). The intercept of these plots for the THF reaction was found to be close to zero over the temperature-range examined indicating that the rate constants for dioxygen release (k_{off}) from **1** are essentially zero, and that O_2 binds irreversibly to **6**. In MeOH, the rate constant for dissociation, $k_{off,}$ increases with increasing temperatures (Figure 3.5) as one would expect for a dissociative process, thus there is reversible O_2 binding in MeOH.

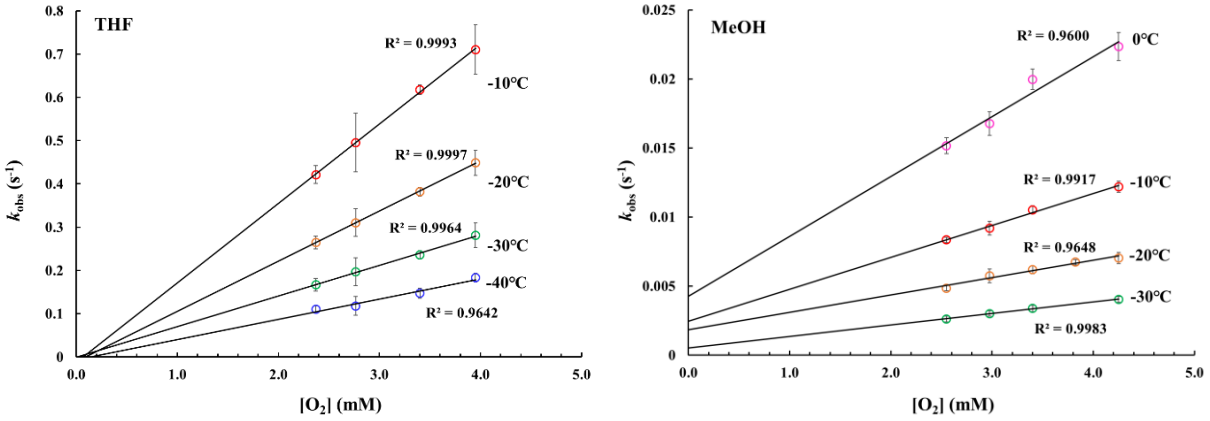

Figure 3.5. Plot of the observed rate constants for the formation of Fe^{III}-superoxo intermediate versus O_2 concentration at different temperatures in THF (left) and MeOH (right). Initial concentration of [$Fe^{II}(S_2{}^{Me2}N_3(Pr,Pr)$] (**1**) = 2.5 x 10^{-4} M.

Table 3.4. Experimentally-Measured Temperature-Dependent Rate Constants for the Formation of Fe^{III}-Superoxo (**6**) in the Reaction Between [$Fe^{II}(S_2^{Me2}N_3(Pr,Pr)]$(**1**) and O_2.

Temperature, ˚C	***k*$_{on}$, ($M^{-1}s^{-1}$) in THF**	***k*$_{on}$, ($M^{-1}s^{-1}$) in MeOH**	***k*$_{off}$, (s^{-1}) in MeOH**
0		6.00(43)	$4.24(21) \times 10^{-3}$
-10	$1.89(14) \times 10^{2}$	3.15(18)	$2.46(51) \times 10^{-3}$
-20	$1.184(7) \times 10^{2}$	1.89(13)	$1.83(47) \times 10^{-3}$
-30	$7.43(8) \times 10^{1}$	1.04(1)	$5.24(79) \times 10^{-4}$
-40	$4.71(19) \times 10^{1}$		

Rate constants for O_2 binding to **1** and the formation of Fe^{III}-superoxo **6**, k_{on}, were obtained at four different temperatures in two different solvents (Table 3.4), and activation parameters ($\Delta H^{\ddagger}_{THF}$ = 21.57± 0.67 kJ mol^{-1}, $\Delta S^{\ddagger}_{THF} = -118.5 \pm 2.7$ J mol^{-1} K^{-1} and $\Delta H^{\ddagger}_{MeOH}$ = 29.62 ± 1.44 kJ•mol^{-1}, $\Delta S^{\ddagger}_{MeOH} = -121.1 \pm 5.6$ J mol^{-1} K^{-1}) were obtained from Eyring plots (Figure 3.6). The negative entropy of activation, $\Delta S^{\ddagger}$, is consistent with an associative process involving O_2 binding, as opposed to a process involving solvent dissociation.

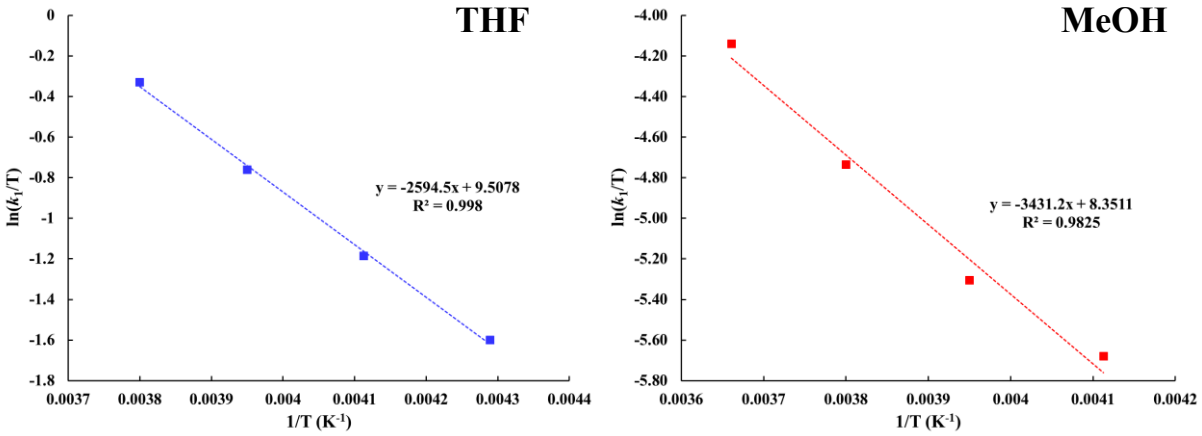

Figure 3.6. Eyring plot for O_2 binding to **1** to form the Fe^{III}-superoxo intermediate (**6**) in THF (left) and MeOH (right), from which activation parameters were derived.

3.3.2 *Kinetic Measurements for KO_2 Binding*

The reaction between oxidized $[Fe^{III}(S^{Me2}N_3(Pr,Pr))]^+$ (**2**) and potassium superoxide (KO_2) was monitored using a cryogenic stopped-flow UV-Vis spectrometer. Specifically, the growth of spectral features associated with $[Fe^{III}(S_2{}^{Me2}N_3(Pr,Pr)(O_2)]$ (**6**) were monitored, under pseudo 1st order conditions with excess KO_2 (Figure 3.7). Kryptofix ® 222 was used to solubilize KO_2 (5 mM to 10 mM) in THF, and a constant ionic strength was maintained for all reactions using 0.1 mM (post-mix concentration) of Bu_4NPF_6. Rates were too fast to measure at temperatures above -20 ˚C when a large excess of KO_2 was used. Therefore, these experiments were carried out over the temperature range -50 ˚C to -20 ˚C. The observed rate constants (k_{obs}) for superoxide binding were found to increase linearly with increasing superoxide concentration (Figure 3.8) and were independent of the concentration of **2**, confirming that the reaction is first-order with respect to **2**, consistent with the formation of a 1:1 superoxide adduct.

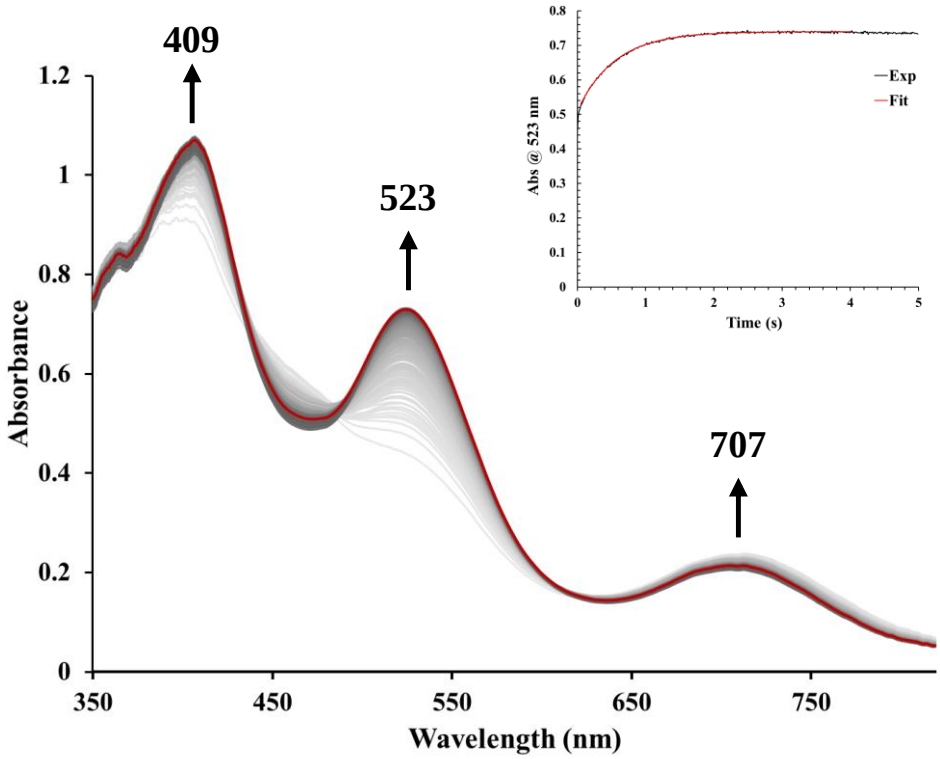

Figure 3.7. Time-resolved spectral changes obtained upon mixing THF solutions of $[Fe^{III}(S_2{}^{Me2}N_3(Pr,Pr)]^+$(**2**) and KO_2 (2.0 mM) at -30 ˚C. Inset: Kinetic trace (λ = 523 nm) showing the formation of the Fe-O_2 intermediate **6**. All reported concentrations are after mixing in the stopped-flow cell.

Second order rate constants, k_{on}, for KO_2 binding to **2** were obtained from the slopes of k_{obs} vs [KO_2] plots at four different temperatures (Figure 3.8 and Table 3.5). At warmer temperatures (-30 to -20 ℃) the dissociation constants determined, indicating the $O_2^{\bullet-}$ binding reversibly at higher temperatures although the reaction favors $O_2^{\bullet-}$ binding (Keq > 47.5 M^{-1}). For the formation of **6** from KO_2 binding to **2**, activation parameters ($\Delta H^{\ddagger}$ = 39.95 ± 5.26 kJ mol^{-1} and $\Delta S^{\ddagger}$ = -41.47 ± 19.3 J mol^{-1} K^{-1}) were obtained from an Eyring plot (Figure 3.8). The negative entropy of

activation, $\Delta S^{\ddagger}$, is consistent with an associative process involving KO_2 binding to **2**. The smaller magnitude of $\Delta S^{\ddagger}$ is likely due to either solvent rearrangement around the superoxide anion, or, dissociation of a loosely coordinated THF solvent, required for binding.

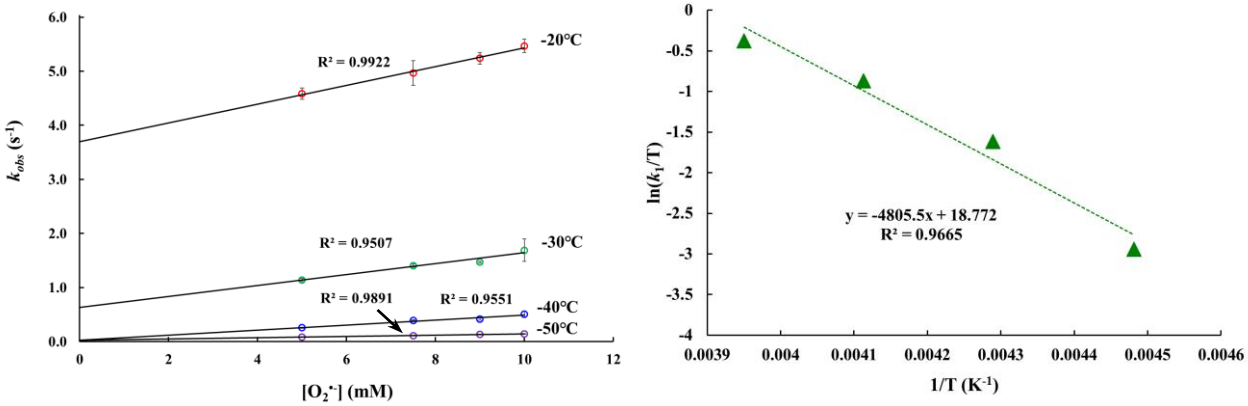

Figure 3.8. Left: Plot of the observed rate constants for the formation of Fe^{III}-superoxo **6** versus KO_2 concentration at four different temperatures. Initial concentration of $[Fe^{III}(S_2{}^{Me2}N_3(Pr,Pr)]^+$ (**2**) = 1.0 x 10^{-4} M in THF after mixing. Right: Eyring plot for KO_2 binding to **2** to form the Fe^{III}-superoxo intermediate (**6**) in THF, from which activation parameters were derived.

Table 3.5. Experimentally-Measured Temperature-Dependent Rate Constants for the Formation of Fe^{III}-Superoxo (**6**) in the Reaction Between $[Fe^{III}(S_2{}^{Me2}N_3(Pr,Pr)]^+$ (**2**) and KO_2 , solubilized with Kryptofix ® 222 in THF.

Temperature, °C	k_{on}, (M^{-1} s^{-1})	k_{off}, (s^{-1})
-20	1.738(109) x 10^2	3.66(9)
-30	1.017(163) x 10^2	5.89(13) x 10^{-1}
-40	4.646(713) x 10^1	
-50	1.175(87) x 10^1	

3.3.3 *Discussion*

The kinetics of dioxygen binding to five-coordinate bis-thiolate ligated Fe^{II} (**1**), and superoxide binding to Fe^{III} (**2**), were investigated in order to determine the mechanism of formation of Fe^{III}-superoxo (**6**). These complexes, in the reduced and oxidized states, maintain a vacant coordination site, thereby avoiding the need to tease out the influence of solvent dissociation versus O_2 binding on kinetic parameters. This has hampered other dioxygen binding studies where solvent or ligand dissociation is rate-determining, making it difficult to determine the barrier to O_2 binding.[36,37] Fits to the temperature-dependent kinetics data indicate that the reaction between **1** and O_2 displays first-order dependence on iron and first-order dependence on O_2 over the temperature range examined. An analysis of the Eyring plots of Figure 3.6 shows that the entropy of activation, $\Delta S^{\ddagger}$, for O_2 binding to **1** in MeOH ($\Delta S^{\ddagger}_{\mathrm{MeOH}} = -128.1 \pm 10.4$ J mol^{-1} K^{-1}) and THF $\Delta S^{\ddagger}_{\mathrm{THF}} = -118.5 \pm 2.7$ J mol^{-1} K^{-1}) is comparable and negative, consistent with an associative process involving O_2 binding, as opposed to solvent dissociation. Thus the study herein provides new insight regarding solvent-dependent kinetic barriers associated with O_2 binding to a five-coordinate non-heme Fe complex relevant to tumor suppressor enzymes,[38] and enzymes used for the synthesis of β-lactam antibiotics.[39]

The solvent environment has been shown to influence the rate of dioxygen binding to previously reported iron complexes,[40,41] it was essential that we take this into consideration for comparative purposes.[40,41] As shown in Table 3.4, the rate constants for O_2 binding to **1**, k_{on}, are consistently and significantly greater in the aprotic solvent, THF, versus the protic solvent MeOH over the temperature range examined. The enthalpy of activation for O_2 binding to **1** is 7 kJ•mol^{-1} higher in MeOH ($\Delta H^{\ddagger}_{\mathrm{MeOH}} = 28.52 \pm 2.69$ kJ•mol^{-1}) versus THF ($\Delta H^{\ddagger}_{\mathrm{THF}} = 21.57 \pm 0.67$ kJ•mol^{-1}). The blue shift in the electronic absorption spectra for the Fe^{II} precursor, **1**, and Fe^{III}-superoxo, **6**,

in MeOH versus THF suggests that hydrogen bonding to the thiolates plays a role in the slower rates and the higher enthalpy of activation. The nature of this band has previously been shown to involve a $RS^{-}\rightarrow Fe$ charge transfer transition,[16] and H-bonding was previously shown to blue-shift this band by stabilizing the π-symmetry sulfur orbitals involved in this transition.[42] Evaluating the kinetics of dioxygen binding in both a protic and aprotic environment expands the comparisons that can be made to previously reported model complexes and biological systems (Table 3.6).

Table 3.6. Comparison of Kinetic Parameters for Dioxygen Binding to mononuclear Fe(II), Mn(II), Co(II), and Cu(I) model complexes and biological systems.

	τ	Solvent (Temp)	k_{on}, M^{-1} s^{-1}	$\Delta H^{\ddagger}$, kJ/mol	$\Delta S^{\ddagger}$, J/mol	ref
Pentadentate Model Complexes						
$[Fe^{II}(S_2{}^{Me2}N_3(Pr,Pr)]$ (**1**)	0.78	THF (-40 ˚C)	4.3(4) x 10^1	22(1)	-119(3)	this work
		THF (25 ˚C)	6.67 x 10^3 [a]			this work
		MeOH (-30 ˚C)	7.43(8) x 10^1	30(1)	-121(6)	this work
		MeOH (25 ˚C)	1.89 x 10^1 [a]			this work
$[Fe(Tp^{Ph2})BF]$	0.65	Benzene (30 ˚C)	1.1 x 10^{-1}	25(2) [a]	-179(6) [b]	43
$[Mn^{II}(S^{Me2}(6\text{-MeDPEN})]^+$	0.59	MeCN (-40 ˚C)	7.17(45) x 10^2	26(2)	-76(7)	44,45
$[Cu^{I}(TPA)]^+$		THF (25 ˚C)	1.3 x 10^9	7.62	-45.1	46
Co^{II}(acacMeDPT)		Acetone (-50 ˚C)	1.0(1) x 10^6	5.0	-108	47
Co^{II}(SalMeDPT)	0.86	Acetone (-50 ˚C)	2.10(4) x 10^5	12.7	-80	47,48
Co^{II}(pXyacacMeDPT)		Acetone (-50 ˚C)	1.74(5) x 10^6	28	-13	47
Porphyrin Model Complexes						
$[Fe(Piv_3 5CIm)]$		Toluene (25 ˚C)	4.3 x 10^8	0.75(33)	-117(3)	49
Biological Systems						
Cyt P450-cholestrol bound		H_2O (25 ˚C)	5.3 x 10^{-2}			50
FeMb (horse)		H_2O (25 ˚C)	1.4 x 10^7	23	-30	51

[a] Extrapolation from a different temperature range [b] These are composite values, containing several elementary reactions and care must be exercised in their interpretation. No intermediates were optically observed. [c] These values were obtained using flash photolysis methods.

The rate constants for O_2 binding to **1** are significantly slower than biological oxygen carriers, even when extrapolated to 25 ˚C, using the activation parameters obtained (Table 3.6). The experimentally obtained $\Delta H^{\ddagger}$ values for dioxygen binding to **1** fall within the reported range: 0.5 kJ $mol^{-1} \leq \Delta H^{\ddagger} \leq 25$ kJ mol^{-1} for O_2 binding to other first row transition metal complexes that contain open-coordination sites (Table 3.6). The lower range of $\Delta H^{\ddagger}$ values are associated with

transition-metal porphyrin complexes, as well as other five-coordinate transition-metal complexes, containing a readily accessible open coordinate site (e.g., [Fe($Piv_3$5CIm)], Co^{II}(acacMeDPT), and $[Cu^{I}(TPA)]^{+}$ (Table 3.6). The higher $\Delta H^{\ddagger}$ value for the formation of **6** is likely due to a reorganizational barrier associated with the requisite unwinding of the helical ligand of **6** in order to accommodate a sixth ligand. The single chain ligand, $[S_2{}^{Me2}N_3(Pr,Pr)]^{2-}$, wraps around the Fe ion in a helical manner placing the metal ion of **2** in a near trigonal bipyramidal coordination environment (τ = 0.78).[28] A comparison of the structure of **1** to the DFT geometry optimized structure of superoxo **6** shows the distortion that is required in order to increase in coordination number (Figure 3.9).[28] The angles most affected by this structural rearrangement are in the equatorial plane consisting of the thiolates, imine nitrogen, N(2), and the Fe ion. The S(1)-Fe-N(2) angle opens from 125.70(4)° in **1** to 172.5° in **6**. In response to this, the S(1)-Fe-S(2) and S(2)-Fe-N(2) close from 126.17(2)° to 95.3°, and from 107.79(4)° to 90.5°, respectively. These dramatic angle changes indicate that the large distortion required in order to accommodate a sixth ligand are likely the cause for the relatively high $\Delta H^{\ddagger}$ for O_2 binding to **1**. The influence of steric effects on activation enthalpy, $\Delta H^{\ddagger}$, has been observed previously with a series of five-coordinate Co^{II} complexes containing pentadentate ligands, in which the bulkiest ligand was shown to have a considerably larger $\Delta H^{\ddagger}$ value for 28 kJ/mol binding.[47]

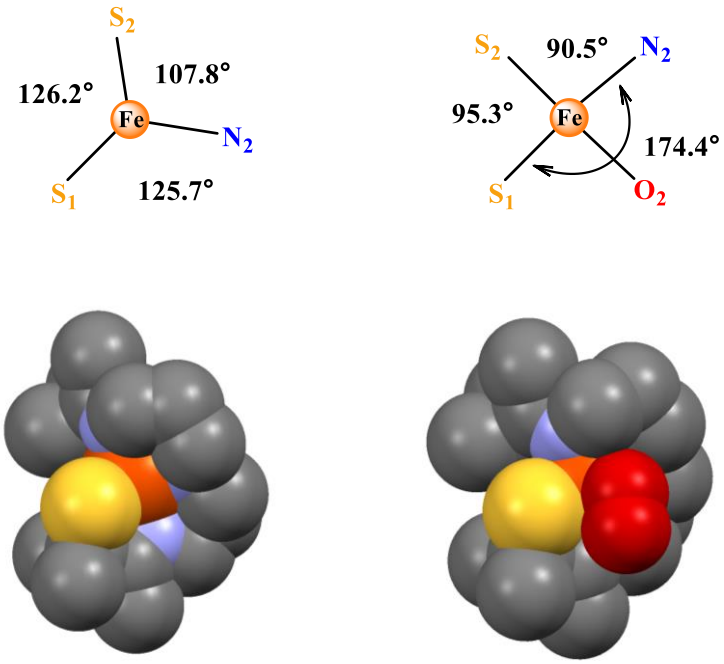

Figure 3.9. Top: Diagram of the bond angles around the Fe ion in the xy-plane for **6** (right) and **1** (left). Bottom: Space-filling models generated from the X-ray crystallographic determined structure of **1** (left) and the DFT-optimized geometry of **6** (right) displaying the large amount of distortion required to bind O_2.[28]

The dissociation of O_2 from **6** to convert back to the precursor **1** was found to be solvent dependent. As mentioned above the solvent environment effects oxygen binding. While it is difficult to conclusively determine why O_2 binding is reversible in MeOH, one contributing factor may be the increased solubility of O_2 in MeOH. At 25 °C, dioxygen saturated THF has an O_2 concentration of 7.9 mM and MeOH has an O_2 concentration of 8.5 mM.[32,33] In enzymatic systems, the O_2 pathways to the active site, as well as the active site itself, are often hydrophobic.[52] The IPNS active site, buried deep in "jelly-roll" motif, and the active site of CDO, have hydrophobic residues lining the active sites.[53,54] Therefore, the solvent, THF, best represents the O_2 binding environment.

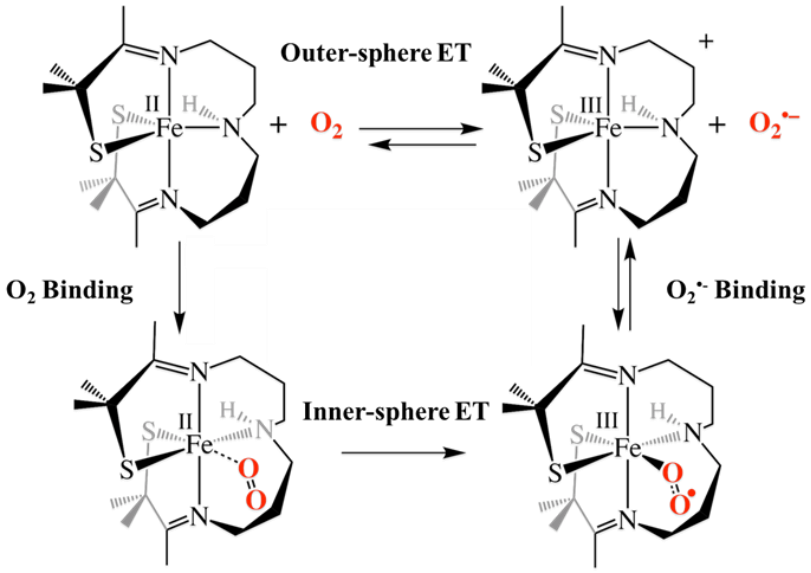

Figure 3.10. Schematic of the possible pathways for the formation of Fe^{III}-superoxo (**6**): outer-sphere electron transfer from **1** to O_2, followed by binding of the resulting $O_2^{\bullet-}$ to the Fe^{III} center to produce **6** and binding of O_2 to **1**, followed by inner-sphere electron transfer from Fe^{II} complexes to O_2.

The $[Fe(S_2{}^{Me2}N_3(Pr,Pr)]^{0/+}$ system afforded the opportunity to study the mechanism of Fe^{III}-superoxo formation from Fe^{II} and O_2 as well as Fe^{III} and $O_2^{\bullet-}$. The first of two possible pathways for Fe^{III}-superoxo formation could be the outer-sphere electron transfer from the $[Fe^{II}(S_2{}^{Me2}N_3(Pr,Pr)]$ to O_2 resulting in a superoxide anion which then binds to the now Fe^{III} center forming **6** (Figure 3.10). The second pathway begins with the binding of O_2 to Fe^{II} followed by the inner-sphere electron transfer resulting in **6** (Figure 3.10). The rate constants for $O_2^{\bullet-}$ binding to Fe^{III} were similar to those found for O_2 binding to Fe^{II}. From Arrhenius plots, the activation energies (E_a) for O_2 binding to **1** and $O_2^{\bullet-}$ binding to **2** were determined to be 24(1) and 42(3) respectively (Figure 3.11). The activation energy for $O_2^{\bullet-}$ binding is greater than O_2 binding

combined with an unfavorable K_{eq} for outer sphere electron transfer ($1.6x10^{-8}$), calculated using the Nernst equation ($E_{1/2}(Fe^{+2/+3}) – E_{1/2}(O_2/O_2^{\bullet-})$ = -0.46 V vs SCE), thus the above results imply that the dioxygen reaction involves inner-sphere, as opposed to outer-sphere electron transfer.

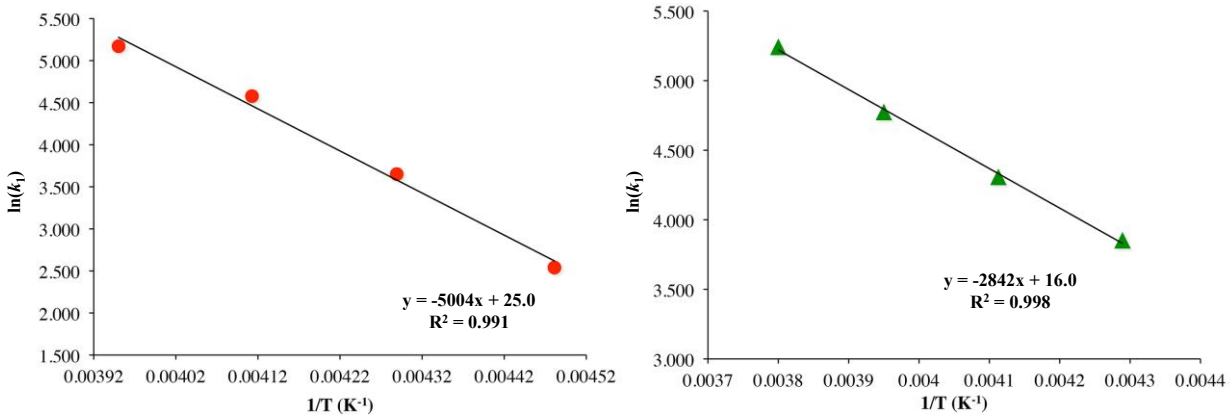

Figure 3.11. Arrhenius plots for the formation of Fe^{III}-superoxo (**6**) via the addition of O_2 to **1** (left) and KO_2 to **2** (right) in THF, from which the activation energies, E_a = 24(1) kJ mol^{-1} and E_a = 42(3) kJ mol^{-1} respectively, were obtained.

3.4 Summary and Conclusions

A kinetic study of dioxygen binding to a trigonal bipyramidal Fe^{II} complex (**1**) revealed slower rates of dioxygen binding than natural O_2 carriers. This may be due to the ligand rearrangement required to accommodate a sixth ligand. In THF, binding of dioxygen was found to be irreversible like the other reported thiolate ligated Fe^{III}-superoxo.[29] Electronic structure has been shown to have a significant effect on O_2 dissociation.[32,55] Our finding of irreversible binding in THF and reversible binding that is strongly favored in MeOH supports computational studies predict covalent bond been RS-Fe-$O_2^{\bullet-}$ stabilized the Fe^{III} oxidation state, however further

investigations are required to fully understand the role of the thiolate on favored dioxygen binding. Additionally, the oxidized complex **2** binds superoxide and the activation energy of this reaction was found to be greater than that for O_2 binding to **1**. Thus, the formation of the Fe^{III}-superoxo (**6**) was found to occur via O_2 binding followed by an inner-sphere electron transfer.

3.5 Reference

(1) Maxwell, P. H.; Wlesener, M. S.; Chang, G. W.; Clifford, S. C.; Vaux, E. C.; Cockman, M. E.; Wykoff, C. C.; Pugh, C. W.; Maher, E. R.; Ratcliffe, P. J. The Tumour Suppressor Protein VHL Targets Hypoxia-Inducible Factors for Oxygen-Dependent Proteolysis. *Nature* **1999**, *399* (6733), 271–275. DOI: 10.1038/20459.

(2) Ivan, M.; Kondo, K.; Yang, H.; Kim, W.; Valiando, J.; Ohh, M.; Salic, A.; Asara, J. M.; Lane, W. S.; Kaelin, J. HIFα Targeted for VHL-Mediated Destruction by Proline Hydroxylation: Implications for O2 Sensing. *Science.* **2001**, *292* (5516), 464–468. DOI: 10.1126/science.1059817.

(3) Kovaleva, E. G.; Lipscomb, J. D. Versatility of Biological Non-Heme Fe(II) Centers in Oxygen Activation Reactions. *Nat. Chem. Biol.* **2008**, *4* (3), 186–193. DOI: 10.1038/nchembio.71.

(4) Holm, R. H.; Kennepohl, P.; Solomon, E. I. Structural and Functional Aspects of Metal Sites in Biology. *Chem. Rev.* **1996**, *96* (7), 2239–2314. DOI: 10.1021/cr9500390.

(5) Bollinger, J. M.; Krebs, C. Enzymatic C-H Activation by Metal-Superoxo Intermediates. *Curr. Opin. Chem. Biol.* **2007**, *11* (2), 151–158. DOI: 10.1016/j.cbpa.2007.02.037.

(6) Kovacs, J. A. How Iron Activates O2. *Science.* **2003**, *299* (5609), 1024–1025. DOI:

10.1126/science.1081792.

(7) Roach, P. L.; Clifton, I. J.; Hensgens, C. M.; Shibata, N.; Schofield, C. J.; Hajdu, J.; Baldwin, J. E. Structure of Isopenicillin N Synthase Complexed with Substrate and the Mechanism of Penicillin Formation. *Nature* **1997**, *387* (6635), 827–830. DOI: 10.1038/42990.

(8) Sörbo, B.; Ewetz, L. The Enzymatic Oxidation of Cysteine to Cysteinesulfinate in Rat Liver. *Biochem. Biophys. Res. Commun.* **1965**, *18* (3), 359–363. DOI: 10.1016/0006-291X(65)90714-X.

(9) Heafield, M. T.; Fearn, S.; Steventon, G. B.; Waring, R. H.; Williams, A. C.; Sturman, S. G. Plasma Cysteine and Sulphate Levels in Patients with Motor Neurone, Parkinson's and Alzheimer's Disease. *Neurosci. Lett.* **1990**, *110* (1–2), 216–220. DOI: 10.1016/0304-3940(90)90814-P.

(10) Jeschke, J.; O'Hagan, H. M.; Zhang, W.; Vatapalli, R.; Calmon, M. F.; Danilova, L.; Nelkenbrecher, C.; Van Neste, L.; Bijsmans, I. T. G. W.; Van Engeland, M.; et al. Frequent Inactivation of Cysteine Dioxygenase Type 1 Contributes to Survival of Breast Cancer Cells and Resistance to Anthracyclines. *Clin. Cancer Res.* **2013**, *19* (12), 3201–3211. DOI: 10.1158/1078-0432.CCR-12-3751.

(11) Ye, S.; Wu, X.; Wei, L.; Tang, D.; Sun, P.; Bartlam, M.; Rao, Z. An Insight into the Mechanism of Human Cysteine Dioxygenase: Key Roles of the Thioether-Bonded Tyrosine-Cysteine Cofactor. *J. Biol. Chem.* **2007**, *282* (5), 3391–3402. DOI: 10.1074/jbc.M609337200.

(12) Kumar, D.; Thiel, W.; de Visser, S. P. Theoretical Study on the Mechanism of the Oxygen

Activation Process in Cysteine Dioxygenase Enzymes. *J. Am. Chem. Soc.* **2011**, *133* (11), 3869–3882. DOI: 10.1021/ja107514f.

(13) Li, J.; Griffith, W. P.; Davis, I.; Shin, I.; Wang, J.; Li, F.; Wang, Y.; Wherritt, D. J.; Liu, A. Cleavage of a Carbon–Fluorine Bond by an Engineered Cysteine Dioxygenase. *Nat. Chem. Biol.* **2018**, *14* (9), 853–860. DOI: 10.1038/s41589-018-0085-5.

(14) Kovacs, J. A.; Brines, L. M. Understanding How the Thiolate Sulfur Contributes to the Function of the Non-Heme Iron Enzyme Superoxide Reductase. *Acc. Chem. Res.* **2007**, *40* (7), 501–509. DOI: 10.1021/ar600059h.

(15) Brown, C. D.; Neidig, M. L.; Neibergall, M. B.; Lipscomb, J. D.; Solomon, E. I. VTVH-MCD and DFT Studies of Thiolate Bonding to {FeNO}7/ {FeO2}8 Complexes of Isopenicillin N Synthase: Substrate Determination of Oxidase versus Oxygenase Activity in Nonheme Fe Enzymes. *J. Am. Chem. Soc.* **2007**, *129* (23), 7427–7438. DOI: 10.1021/ja071364v.

(16) Kennepohl, P.; Neese, F.; Schweltzer, D.; Jackson, H. L.; Kovacs, J. A.; Solomon, E. I. Spectroscopy of Non-Heme Iron Thiolate Complexes: Insight into the Electronic Structure of the Low-Spin Active Site of Nitrile Hydratase. *Inorg. Chem.* **2005**, *44* (6), 1826–1836. DOI: 10.1021/ic0487068.

(17) Tamanaha, E.; Zhang, B.; Guo, Y.; Chang, W.; Barr, E. W.; Xing, G.; St. Clair, J.; Ye, S.; Neese, F.; Bollinger, J. M.; et al. Spectroscopic Evidence for the Two C–H-Cleaving Intermediates of Aspergillus Nidulans Isopenicillin N Synthase. *J. Am. Chem. Soc.* **2016**, *138* (28), 8862–8874. DOI: 10.1021/jacs.6b04065.

(18) Tchesnokov, E. P.; Faponle, A. S.; Davies, C. G.; Quesne, M. G.; Turner, R.; Fellner, M.;

Souness, R. J.; Wilbanks, S. M.; de Visser, S. P.; Jameson, G. N. L. An Iron–Oxygen Intermediate Formed during the Catalytic Cycle of Cysteine Dioxygenase. *Chem. Commun.* **2016**, *52* (57), 8814–8817. DOI: 10.1039/c6cc03904a.

(19) Crawford, J. A.; Li, W.; Pierce, B. S. Single Turnover of Substrate-Bound Ferric Cysteine Dioxygenase with Superoxide Anion: Enzymatic Reactivation, Product Formation, and a Transient Intermediate. *Biochemistry* **2011**, *50* (47), 10241. DOI: 10.1021/bi2011724.

(20) Costas, M.; Mehn, M. P.; Jensen, M. P.; Que, L. Dioxygen Activation at Mononuclear Nonheme Iron Active Sites: Enzymes, Models, and Intermediates. *Chem. Rev.* **2004**, *104* (2), 939–986. DOI: 10.1021/cr020628n.

(21) Nam, W. Synthetic Mononuclear Nonheme Iron–Oxygen Intermediates. *Acc. Chem. Res.* **2015**, *48* (8), 2415–2423. DOI: 10.1021/acs.accounts.5b00218.

(22) Kovacs, J. A. Tuning the Relative Stability and Reactivity of Manganese Dioxygen and Peroxo Intermediates via Systematic Ligand Modification. *Acc. Chem. Res.* **2015**, *48* (10), 2744–2753. DOI: 10.1021/acs.accounts.5b00260.

(23) Cramer, C. J. Bioinorganic Chemistry Special Feature: Variable Character of OO and MO Bonding in Side-on (Eta 2) 1:1 Metal Complexes of O2. *Proc. Natl. Acad. Sci.* **2003**, *100* (7), 3635–3640. DOI: 10.1073/pnas.0535926100.

(24) Gherman, B. F.; Cramer, C. J. Modeling the Peroxide/Superoxide Continuum in 1:1 Side-on Adducts of O 2 with Cu. *Inorg. Chem.* **2004**, *43* (23), 7281–7283. DOI: 10.1021/ic049958b.

(25) Chiang, C. W.; Kleespies, S. T.; Stout, H. D.; Meier, K. K.; Li, P. Y.; Bominaar, E. L.;

Que, L.; Münck, E.; Lee, W. Z. Characterization of a Paramagnetic Mononuclear Nonheme Iron-Superoxo Complex. *J. Am. Chem. Soc.* **2014**, *136* (31), 10846–10849. DOI: 10.1021/ja504410s.

(26) Hong, S.; Sutherlin, K. D.; Park, J.; Kwon, E.; Siegler, M. a; Solomon, E. I.; Nam, W. Crystallographic and Spectroscopic Characterization and Reactivities of a Mononuclear Non-Haem Iron(III)-Superoxo Complex. *Nat. Commun.* **2014**, *5*, 5440. DOI: 10.1038/ncomms6440.

(27) Oddon, F.; Chiba, Y.; Nakazawa, J.; Ohta, T.; Ogura, T.; Hikichi, S. Characterization of Mononuclear Non-Heme Iron(III)-Superoxo Complex with a Five-Azole Ligand Set. *Angew. Chemie Int. Ed.* **2015**, *54* (25), 7336–7339. DOI: 10.1002/anie.201502367.

(28) Blakely, M. N.; Dedushko, M. A.; Yan Poon, P. C.; Villar-Acevedo, G.; Kovacs, J. A. Formation of a Reactive, Alkyl Thiolate-Ligated Fe III -Superoxo Intermediate Derived from Dioxygen. *J. Am. Chem. Soc.* **2019**, *141* (5), 1867–1870. DOI: 10.1021/jacs.8b12670.

(29) Fischer, A. A.; Lindeman, S. V.; Fiedler, A. T. A Synthetic Model of the Nonheme Iron–Superoxo Intermediate of Cysteine Dioxygenase. *Chem. Commun.* **2018**, 11344–11347. DOI: 10.1039/C8CC06247A.

(30) Gordon, J. B.; Vilbert, A. C.; Siegler, M. A.; Lancaster, K. M.; Goldberg, D. P.; Moe, P.; Moënne-Loccoz, P.; Goldberg, D. P. A Nonheme Thiolate-Ligated Cobalt Superoxo Complex: Synthesis and Spectroscopic Characterization, Computational Studies, and Hydrogen Atom Abstraction Reactivity. *J. Am. Chem. Soc.* **2019**, *141* (8), 3641–3653. DOI: 10.1021/jacs.8b13134.

(31) Ellison, J. J.; Nienstedt, A.; Shoner, S. C.; Barnhart, D.; Cowen, J. A.; Kovacs, J. A. Reactivity of Five-Coordinate Models for the Thiolate-Ligated Fe Site of Nitrile Hydratase. *J. Am. Chem. Soc.* **1998**, *120* (23), 5691–5700. DOI: 10.1021/ja973129q.

(32) Kryatov, S. V.; Rybak-Akimova, E. V.; Schindler, S. Kinetics and Mechanisms of Formation and Reactivity of Non-Heme Iron Oxygen Intermediates. *Chem. Rev.* **2005**, *105* (6), 2175–2226. DOI: 10.1021/cr030709z.

(33) Battino, R. Oxygen and Ozone. In *Solubility Data Series*; Permgamon Press: New York, 1981; Vol. 7.

(34) Burnett, M. N.; Johnson, C. K. ORTEP-III: Oak Ridge Thermal Ellipsoid Plot Program for Crystal Structure Illustrations. Oak Ridge National Laboratory Report ORNL-6895 1996.

(35) Espenson, J. H. *Chemical Kinetics and Reaction Mechanisms*; McGraw-Hill Book Company: New York, 1981.

(36) Riley, D. P.; Henke, S. L.; Lennon, P. J.; Weiss, R. H.; Neumann, W. L.; Rivers; Aston, K. W.; Sample, K. R.; Rahman, H.; Ling, C.-S.; et al. Synthesis, Characterization, and Stability of Manganese(II) C-Substituted 1,4,7,10,13-Pentaazacyclopentadecane Complexes Exhibiting Superoxide Dismutase Activity. *Inorg. Chem.* **1996**, *35* (18), 5213–5231. DOI: 10.1021/ic960262v.

(37) Zhang, M.; van Eldik, R.; Espenson, J. H.; Bakac, A. Volume Profiles for the Reversible Binding of Dioxygen to Cobalt(II) Complexes. Evidence for a Substitution-Controlled Process. *Inorg. Chem.* **1994**, *33* (1), 130–133. DOI: 10.1021/ic00079a024.

(38) Brait, M.; Ling, S.; Nagpal, J. K.; Chang, X.; Park, H. L.; Lee, J.; Okamura, J.; Yamashita, K.; Sidransky, D.; Kim, M. S. Cysteine Dioxygenase 1 Is a Tumor Suppressor Gene Silenced by Promoter Methylation in Multiple Human Cancers. *PLoS One* **2012**, *7* (9)DOI: 10.1371/journal.pone.0044951.

(39) Arnstein, H. R. V.; Clubb, M. E. The Biosynthesis of Penicillin 8. Investigation of Cyclic Cysteinylvaline Peptides as Precursors. *Biochem. J.* **1958**, *68*, 528–535. DOI: 10.1042/bj06900i5c.

(40) Busch, D. H.; Alcock, N. W. Iron and Cobalt "Lacunar" Complexes as Dioxygen Carriers. *Chem. Rev.* **1994**, *94* (3), 585–623. DOI: 10.1021/cr00027a003.

(41) Niederhoffer, E. C.; Timmons, J. H.; Martell, A. E. Thermodynamics of Oxygen Binding in Natural and Synthetic Dioxygen Complexes. *Chem. Rev.* **1984**, *84* (2), 137–203. DOI: 10.1021/cr00060a003.

(42) Jackson, H. L.; Shoner, S. C.; Rittenberg, D.; Cowen, J. A.; Lovell, S.; Barnhart, D.; Kovacs, J. A. Probing the Influence of Local Coordination Environment on the Properties of Fe-Type Nitrile Hydratase Model Complexes. *Inorg. Chem.* **2001**, *40* (7), 1646–1653. DOI: 10.1021/ic001271d.

(43) Mehn, M. P.; Fujisawa, K.; Hegg, E. L.; Que, L. Oxygen Activation by Nonheme Iron(II) Complexes: α-Keto Carboxylate versus Carboxylate. *J. Am. Chem. Soc.* **2003**, *125* (26), 7828–7842. DOI: 10.1021/ja028867f.

(44) Coggins, M. K.; Toledo, S.; Shaffer, E.; Kaminsky, W.; Shearer, J.; Kovacs, J. A. Characterization and Dioxygen Reactivity of a New Series of Coordinatively Unsaturated Thiolate-Ligated Manganese(II) Complexes. *Inorg. Chem.* **2012**, *51* (12), 6633–6644.

DOI: 10.1021/ic300192q.

(45) Coggins, M. K.; Sun, X.; Kwak, Y.; Solomon, E. I.; Rybak-Akimova, E.; Kovacs, J. A. Characterization of Metastable Intermediates Formed in the Reaction between a Mn(II) Complex and Dioxygen, Including a Crystallographic Structure of a Binuclear Mn(III)-Peroxo Species. *J. Am. Chem. Soc.* **2013**, *135* (15), 5631–5640. DOI: 10.1021/ja311166u.

(46) Fry, H. C.; Scaltrito, D. V; Karlin, K. D.; Meyer, G. J. The Rate of O 2 and CO Binding to a Copper Complex , Determined by a " Flash-and-Trap " Technique , Exceeds That for Hemes. **2003**, No. 12, 11866–11871. DOI: 10.1021/ja034911v.

(47) Rybak-akimova, E. V; Otto, W.; Deardorf, P.; Roesner, R.; Busch, D. H. Kinetics and Equilibria of Dioxygen Binding to a Vacant Site in Cobalt (II) Complexes with Pentadentate Ligands. **1997**, *2* (Ii), 2746–2753. DOI: 10.1021/ic961371c.

(48) Cini, R.; Orioli, P. Crystal and Molecular Structure of Two Oxygen-Inactive Forms of [N,N′-(3,3′-Dipropylmethylamine)Bis(Salicylideneiminato) Cobalt(II)]. *Inorganica Chim. Acta* **1982**, *63* (C), 243–248. DOI: 10.1016/S0020-1693(00)81919-2.

(49) Collman, J. P.; Brauman, J. I.; Iverson, B. L.; Sessler, J. L.; Morris, R. M.; Gibson, Q. H. O2 and CO Binding to Iron(II) Porphyrins: A Comparison of the "Picket Fence" and "Pocket" Porphyrins. *J. Am. Chem. Soc.* **1983**, *105* (10), 3052–3064. DOI: 10.1021/ja00348a019.

(50) Tuckey, R. C.; Kamin, H. Kinetics of O2 and CO Binding to Adrenal Cytochrome P-450scc. Effects of Cholesterol, Intermediates, and Phosphatidylcholine Vesicles. *J. Biol. Chem.* **1983**, *258* (7), 4232–4237. .

(51) Antonini, E.; Brunori, M. *Hemoglobin and Myoglobin in Their Reactions with Ligands*; North-Holland: Amsterdam, 1971.

(52) Rybak-Akimova, E. V. Mechanisms of Oxygen Binding and Activation at Transition Metal Centers. In *Physical Inorganic Chemistry*; John Wiley & Sons, Inc.: Hoboken, NJ, USA, 2010; Vol. Vol. 2., pp 109–188DOI: 10.1002/9780470602577.ch4.

(53) Roach, P. L.; Cllftont, J.; Fiilipt, V.; Harlost, K.; Bartont, G. J.; Hajdut, J.; Anderssontt, I.; Schofield, C. J.; Baldwin, J. E. New Structural Family of Enzymes. *Nature* **1995**, *375* (June), 700–704. .

(54) McCoy, J. G.; Bailey, L. J.; Bitto, E.; Bingman, C. A.; Aceti, D. J.; Fox, B. G.; Phillips, G. N. Structure and Mechanism of Mouse Cysteine Dioxygenase. *Proc. Natl. Acad. Sci. U. S. A.* **2006**, *103* (9), 3084–3089. DOI: 10.1073/pnas.0509262103.

(55) Yan Poon, P. C.; Dedushko, M. A.; Sun, X.; Yang, G.; Toledo, S.; Hayes, E. C.; Johansen, A.; Piquette, M. C.; Rees, J. A.; Stoll, S.; et al. How Metal Ion Lewis Acidity and Steric Properties Influence the Barrier to Dioxygen Binding, Peroxo O–O Bond Cleavage, and Reactivity. *J. Am. Chem. Soc.* **2019**, *141* (38), 15046–15057. DOI: 10.1021/jacs.9b04729.

Chapter 4. Metal-Assisted Oxo Atom Addition to an Fe^{III} Thiolate

Components of this chapter were republished with permission of the Journal of the American Chemical Society, from Metal-Assisted Oxo Atom Addition to an Fe(III) Thiolate, Villar-Acevedo, G.; Lugo-Mas, P.; Blakely, M. N.; Rees, J. A.; Ganas, A. S.; Hanada, E. M.; Kaminsky, W.; Kovacs, J. A. *J. Am. Chem. Soc.* 2017, *139* (1), 119.; permission conveyed through Copyright Clearance Center, Inc.

Components of this chapter were taken from: Blakely, Maike N.; Kovacs, Julie A. "Using Kinetics to Investigate the Mechanism of Oxo Atom Addition to an Fe(III) Thiolate Complex." *In preparation.*

4.1 Introduction

Sulfur oxygenation is an integral part of the post-translationally modified active form of nitrile hydratase (NHase)[1–3] and the catalytic conversion of cysteine to cysteine sulfenic acid by cysteine dioxygenase (CDO).[4] However, there is little known about these transformations. This is especially true for NHase, where the S-oxygenation occurs either in a metallochaperone prior to insertion into NHase via "subunit swapping"[5,6] or in the α-subunit of NHase itself.[7] The active form of NHase contains three cysteine sulfurs, two are post-translationally modified, one to the doubly oxygenated sulfinate and the other to the singly oxygenated ($RS\text{-}O^-$) sulfenate (Figure 4.1).[8] The latter is proposed to be directly involved in nitrile hydrolysis while the other modification is essential for electronic modulation of the Fe center. [9–13] The enzyme CDO's function is to carry out S-oxygenation and only one CDO intermediate has been transiently

observed.[14] Current proposed mechanisms are based almost solely on theoretical calculations.[15–22] Several of these computational studies propose a CDO-persulfate intermediate based off of the structural characterization of a CDO-Fe persulfenate adduct (Figure 4.2).[23] However, persulfate given as a substrate to CDO did not turn over implying the Fe-persulfenate is an off pathway species.[24] A computational study carried out by Sam de Visser proposed a 4-membered ring structure of an Fe^{III}-peroxo intermediate that cleaves the O-O bond heterolytically producing a sulfenate and an Fe^{IV}=O (Figure 4.2).[15–18] This stepwise oxygen atom addition to the thiolate is yet to be supported by spectroscopic evidence in the enzymatic system, but there is evidence for a sulfenate forming prior to sulfinic acid in a biomimetic model system.[25]

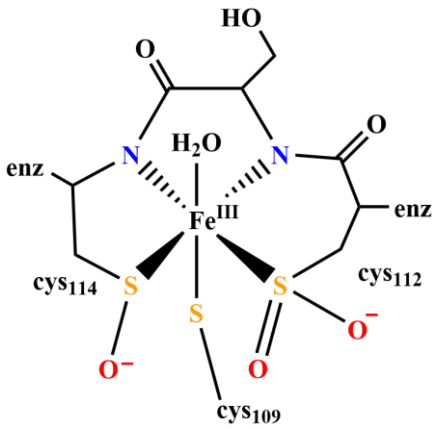

Figure 4.1. Depiction of the post-translationally modified active site of NHase containing a singly oxygenated sulfenate (RS-O^-) on cys114, a doubly oxygenated sulfinate on cys112 and the unmodified cys109.

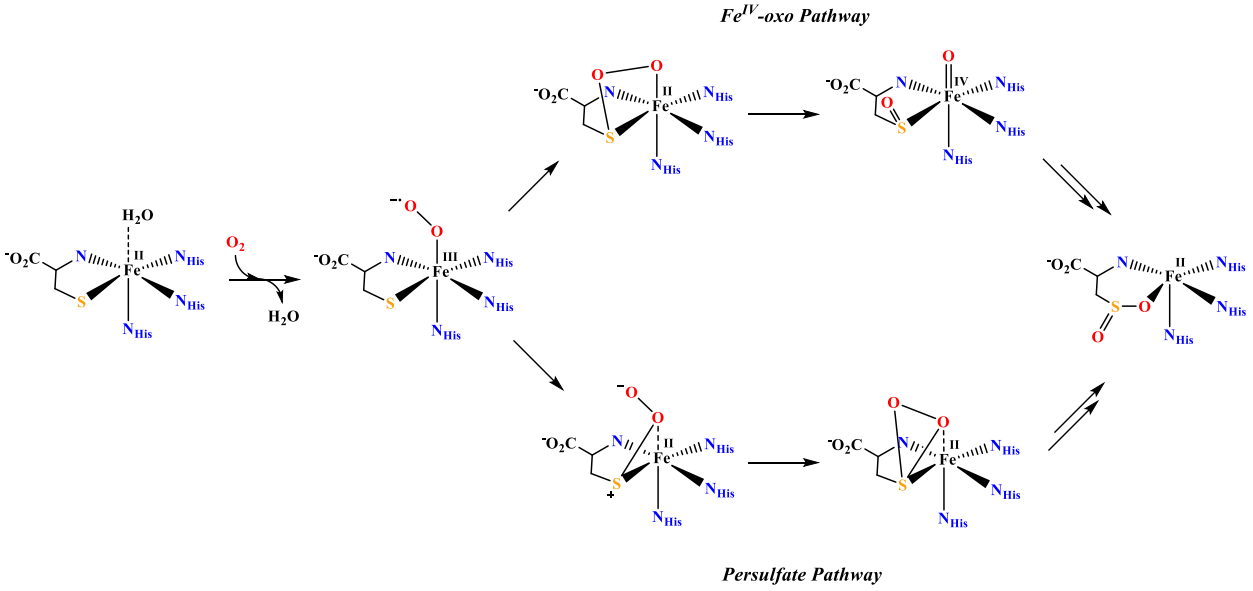

Figure 4.2. Simplified proposed mechanistic pathways for CDO-catalyzed oxidation of cysteine to cysteine sulfenic acid.

Small molecules can provide insights to the possible routes to sulfenate or sulfinate formation. A small molecule model, $[Fe^{II}(N_3PyS)(CH_3CN)]^+$, reacts with O_2 to produce a doubly oxygenated sulfinate bound to Fe through the sulfur atom as determined by X-ray crystallography.[25] This complex not only forms the biologically relevant sulfinato product but provides a glimpse into a possible mechanism. When $[Fe^{II}(N_3PyS)(CH_3CN)]^+$ is reacted with O_2 at 25 °C a transient green intermediate is observed by electronic absorption spectroscopy with a λ_{max} at 674 nm.[25] This green intermediate was found to react with the sulfenate-selective trapping agent dimedone, indicating the presence of a sulfenate.[25] This observation demonstrated a sulfenate is likely to form en route to the sulfinic acid, consistent with the calculated mechanism for another aryl-thiolate containing model[18] and CDO[15–17,19,20] that goes through an Fe^{IV}-oxo and sulfenate intermediate. There is a sparse amount of experimental data available for the formation

of S-oxygenation species from dioxygen, thus the pathways that thiolate containing models and metalloenzymes follow have yet to be fully revealed.

Sulfenates have been proven to be difficult to trap in comparison to sulfinates ($RS(=O)(O^-)$) or the over oxygenated sulfonate metal-bound species of which there are many examples.[11,26–31] A strategy to form and study an Fe-bound sulfenate species is to use oxo-atom donors instead of dioxygen. This approach has been used by our group and yielded the first structurally characterized Fe^{III}-sulfenate.[12] The six-coordinate sulfenate compound, $[Fe^{III}(ADIT)(ADIT\text{-}O)]^+$, can be produced by reacting a potent oxidant, *tert*-butyl N-sulfonyloxaziridine, with $[Fe^{III}(ADIT)(ADIT)]^+$ (Figure 4.3). The addition of the oxygen atom causes the Fe-S bond length of the unmodified thiolate to shorten. A combination of S K-edge X-ray absorption spectroscopy and density functional theory calculations showed the unmodified thiolate increases its covalent bond strength thus compensating for the loss of π bonding from the modified $RS\text{-}O^-$ fragment.[12] These experiments using an oxo atom donor provided an improved understanding how a mix of oxygenated cysteinates influence the electronic structure of NHase active sites.[12]

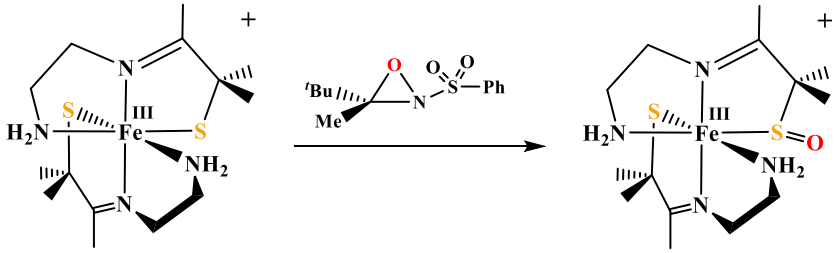

Figure 4.3. Addition of *tert*-butyl N-sulfonyloxaziridine, with $[Fe^{III}(ADIT)(ADIT)]^+$ to produce a sulfenate.[12]

Additional work in our lab showed that the bis-thiolate ligated complex $[Fe^{III}(S_2{}^{Me2}N_3(Pr,Pr)]^+$ (**2)** reacts with the oxo atom donors iodosylbenzene (PhIO) and hydrogen peroxide at room temperature to form a rare singly oxygenated sulfenate complex, $[Fe^{III}(\eta^2\text{-}S^{Me2}O)(S^{Me2})N_3(Pr,Pr)]^+$ (**5**).[32] Unlike $[Fe^{III}(ADIT)(ADIT)]^+$, **2** is five coordinate and contains a flexible ligand that opens up to accommodate a sixth ligand.[33] The addition of excess oxidants did not result in further oxygenation, which is unusual for small molecule metal thiolate complexes. This implies that sulfur oxygenation requires an accessible open coordination site and/or the low-spin state and possibly cationic molecular charge. The observed reactivity of **2** with oxo-atom donors suggests a metal-centered intermediate, such as a Fe^{III}-oxo atom donor adduct (Fe^{III}-OX) and/or an Fe^{V}-oxo, forms en route to the singly oxygenated sulfenate. This unusually stable sulfenate **5** can also be formed from **1** and O_2 (vide supra).[34] The **1** and O_2 pathway has two observable intermediates en route to **5**. Both intermediates are prior to O-O bond cleavage. If the O-O bond cleaves heterolytically then it would afford an Fe^{V}-oxo (Scheme 4.2), and OH^-. The Fe^{V}-oxo would likely be quickly internally trapped forming the sulfenate. Herein, alternate routes to an Fe^{V}-oxo, via the addition of oxo atom donors (OX) to the five-coordinate Fe^{III} complex **2** are explored to examine the mechanism of oxo atom transfer to the *cis*-thiolate sulfur.

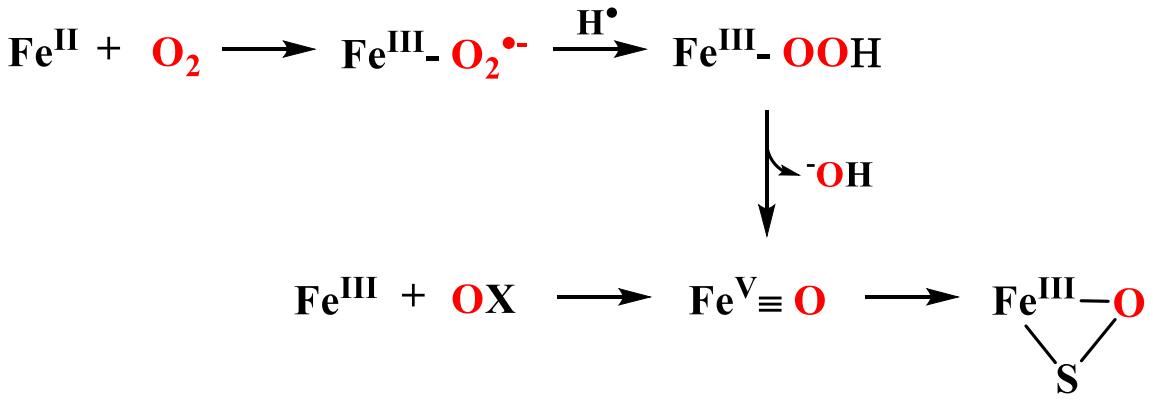

Figure 4.4. Possible pathways to the singly oxygenated sulfenate, **5**. (Oxo atom donors, PhIO and H_2O_2, are represented by OX.)

4.2 Experimental

General Methods. All reactions were performed under an atmosphere of dinitrogen in a glove box or using a custom–built two-neck solution sample holder equipped with a threaded glass connector (sized to fit an ATR probe). Reagents purchased from commercial vendors were of the highest purity available and used without further purification unless otherwise noted. 3-methyl-3-mercapto-2-butanone, $[Fe^{III}(S_2{}^{Me2}N^{Me}N_2{}^{amide}(Pr,Pr)]^{1-}$ and isopropyl 2-iodoxybenzoate (IBX-ester) were synthesized as previously described.[33,35,36] Methylene chloride (DCM), tetrahydrofuran (THF), diethyl ether (Et_2O), and acetonitrile (MeCN) were rigorously degassed, and purified using solvent purification columns housed in a custom stainless-steel cabinet, dispensed via a stainless steel schlenk-line (GlassContour). 2-Methyltetrahydrofuran (Me-THF) was distilled under an inert atmosphere from Na/benzophenone and degassed with argon prior to use. Methanol (MeOH) was distilled from calcium hydride and degassed prior to use. ^{1}H NMR spectra were recorded on a

Bruker AV 300 FT-NMR or Bruker AV 500 FT-NMR spectrometer and are referenced to residual solvent protons (diamagnetic compounds) or an external standard of TMS (paramagnetic compounds). ^{19}F chemical shifts were set to the known internal standard fluorobenzene (-113.15 ppm). Chemical shifts are reported in ppm. Electrospray-ionization mass spectra were obtained on a Bruker Esquire Liquid Chromatograph-Ion Trap mass spectrometer. Cyclic voltammograms were recorded in MeCN (100 mM $NBu_4(PF_6)$ solutions) on a PAR 273 potentiostat utilizing a glassy carbon working electrode, platinum auxiliary electrode, and an SCE reference electrode. Magnetic moments (solution state) were obtained using the Evans' method as modified for superconducting solenoids.[37,38] Electronic absorption spectra were recorded using a Varian Cary 50 spectrophotometer equipped with a fiber optic cable connected to a C-technologies ATR probe.

Synthesis of Iodosylbenzene (PhIO) and *p*-Substituted Derivatives. Synthesis adapted from reference [39] and [40]. *Caution: Older reported methods for the synthesis of the diacetoxyiodobenzene precursors are explosive!* [41] The precursors diacetoxyiodobenzene ($ArI(OAc)_2$) and *p*-substituted derivatives (R = $-CF_3$, -Me) were synthesized as described in reference [39]. Further purification of R-$ArI(OAc)_2$ was required and achieved by stirring the crude residue in 5 mL of ethyl acetate with sodium acetate (0.328 g, 4 mmol) for 30 mins at room temperature. The solution was filtered through a fine frit and then concentrated under reduced pressure to produce a white solid. Finely ground R-$ArI(OAc)_2$ (1-43 mmol) was added to 20 mL vial with a stir bar. Over the course of 5 minutes, 20-100 mL of 3 M aqueous sodium hydroxide added. The solution was stirred vigorously for 1 hour. The crude product was collected in a fine frit and washed with minimal amounts of DI water. The solid was allowed to dry on the frit while suction was pulled. Trituration with chloroform yielded the dried solid in a vial. The solid was dried in a vacuum desiccator overnight

to produce a light yellow solid. Iodosylbenzene: (9.48 g, 43.0 mmol, 98 %) ^{1}H NMR (300 MHz, DMSO-d_6) δ 8.10-8.07 (m, 2 H), 7.63-7.56 (m, 3 H). IR (nujol) ν(cm^{-1}): 685, 668, 492. 4-Trifluoromethyliodosylbenzene: (0.91 g, 3.2 mmol, 68%) ^{1}H NMR (300 MHz, MeOD-d_4) δ 8.24 (d, 2 H), 7.90 (m, 2 H). 4-Methyliodosylbenzene: (0.013 g, 0.05 mmol, 5 %) ^{1}H NMR (300 MHz, MeOD-d_4) δ 7.92 (d, 2 H), 7.40 (d, 2 H), 2.47 (s, 3 H).

Synthesis of Iodoxybenzene ($PhIO_2$). Synthesis adapted from reference 42 and 43. *Caution: Peracetic acid is an especially dangerous reagent and all reactions involving peracetic acid should be run behind a blast shield. Please review safety procedures before carrying out this reaction.* To a 50 mL three neck flask equipped with a reflux condenser and stir bar iodobenzene (2.04 g, 10 mmol) was added. Over the course of 30 minutes 32 % weight peracetic acid in acetic acid (6.5 mL, 30.9 mmol) was added and the solution was then diluted with 8 mL of DI water. The solution was heated from 35 ℃ to 100 ℃ for 45 minutes, foaming was observed. The solution was cooled, and the white solid was collected on a fine frit and washed with cold DCM and Et_2O. Drying in a vacuum desiccator overnight afforded a white powder (1.84 g, 7.8 mmol, 78 %). ^{1}H NMR (300 MHz, DMSO-d_6) δ 8.08-8.03 (m, 2 H), 7.72-7.61 (m, 3 H). IR (nujol) ν(cm^{-1}): 771 758.

Synthesis of Pentafluoroiodosylbenzene (PFIB). Synthesis adapted from references 42 and 44. *Caution: Older reported methods for the synthesis of the diacetoxyiodobenzene precursors are explosive!*[41] The precursor (bis(trifluoroacetoxy)iodo)pentafluorobenzene ($C_6F_5I(OAcF_3)_2$) was either purchased from Sigma Aldrich or if unavailable synthesized as described in reference [39]. The precursor ($C_6F_5I(OAcF_3)_2$) (1.00g, 1.92 mmol) was stirred in a saturated solution of sodium bicarbonate (100 ml) open to the air for 24 hours. The resulting solution was filtered to produce a

white solid. This solid was washed several times with small aliquots (~ 2ml) water. This solid was then dried under vacuum at room temperature in a vacuum desiccator overnight, to give PFIB as a very pale-yellow powder, 0.565 g (1.8 mmol, 93 %). *Caution: Heating PFIB under vacuum has been reported to result in an explosion.*[45] Literature reports that PFIB can be stored for up to two weeks at -20 ℃ before decomposition to C_6F_5I was noted. Purity of PFIB was evaluated daily by ^{19}F NMR spectroscopy. PFIB: ^{19}F NMR (500 MHz, CD_2Cl_2): δ -123.5 (2F), -146.6 (1 F), -157.1 (2F), (500 MHz, MeOD-d_4): -123.2 (2F), -147.9 (1F), -157.7 (2F). C_6F_5I: (500 MHz, CD_2Cl_2): δ -119.8 (2F), -152.9 (1 F), -160.0 (2F), (500 MHz, MeOD-d_4): -119.3 (2F), -152.8 (1F), -159.9 (2F).

Synthesis of $[Fe^{III}(S_2^{Me2}N_3(Pr,Pr)]^+$ (2) Synthesis adapted from reference [33]. 3-methyl-3-mercapto-2-butanone (0.19 g, 1.6 mmol) was dissolved in 10 ml of MeOH. To this sodium methoxide (NaOMe) (0.086 g, 1.6 mmol) was added and the mixture was stirred for 10 min, after which 3,3'-iminobis(propylamine) (0.105 ml, 0.75 mmol) was added. After stirring for 20 mins at room temperature, this solution of organics was cooled to -40 ℃ for over 1 hour. A chilled (-40 ℃) solution of anhydrous ferrous chloride (0.19 g, 1.5 mmol) in 5 ml of MeOH was slowly added dropwise over a period of 5 minutes to the chilled solution of organics. The combined solutions were allowed to stir for 3 hours at room temperature before being stored in the freezer overnight. Next, 1.8 equivalents of Cp_2FeBF_4 (0.367 g, 1.35 mmol) or Cp_2FePF_6 (0.447 g, 1.35 mmol) in 5 ml of MeCN was added dropwise to the greenish yellow brown solution producing a deep red brown solution. This solution was immediately placed in the freezer overnight. The following day, the solution was reduced to ~ 4 ml and filtered through a bed of Celite. The remaining solvent was removed by vacuum. The resulting solids were placed in a fine frit and washed with 5 ml aliquots of Et_2O until the Et_2O ran clear indicating all the ferrocene had been removed from the powder.

The solid was dissolved in less than 4 ml of chilled THF and layered with 15 ml of pentane and cooled at -40 ºC for ~12 h to afford $[Fe^{III}(S_2{}^{Me2}N_3(Pr,Pr)](BF_4)$ 0.198 g (0.42 mmol, 56 %) or $[Fe^{III}(S_2{}^{Me2}N_3(Pr,Pr)](PF_6)$ 0.260 g (0.49 mmol, 65 %) of deep red micro-crystalline solid. Electronic absorption (MeOH): λ_{max} (ε, M^{-1} cm^{-1}) = 316 (6800), 416 (4200), 475 (sh), 774 (440); (THF): λ_{max} (ε, M^{-1} cm^{-1}) = 415 (4200), 486 (sh), 770 (319).

Synthesis of $[Fe^{III}(S_2{}^{Me2}N_3Me(Pr,Pr)](PF_6)$ (9). Sodium methoxide (NaOMe) (0.13 g, 2.4 mmol) and 3-methyl-3-mercapto-2-butanone (0.28 g, 2.4 mmol) were dissolved in MeOH (8 mL) and stirred for 10 minutes. 3,3′-diamino-N-methyldipropylamine (0.19 mL, 1.2 mmol) was added to the solution of organics and stirred for 20 minutes. Separately, anhydrous ferrous chloride (0.15 g, 1.2 mmol) was dissolved in MeOH (8 mL). The solutions were cooled at -40 °C. The metal solution was added dropwise over a period of 5 minutes to the solution of organics and stirred for 3 hours at room temperature. The solution was then cooled at -40 °C overnight. Ferrocenium hexafluorophosphate (0.40 g, 1.2 mmol) in MeCN (4 mL) was added dropwise and stirred for 30 minutes before returning to the -40 °C freezer overnight. The solvent was reduced to ~ 4 mL under vacuum and filtered over Celite. All remaining solvent in the filtrate was removed by vacuum. The solids were recrystallized from THF/pentane layering and the product was obtained as a dark red solid (0.1823 g, 0.447 mmol, 38% yield). Electronic absorption (MeCN): λ_{max} (ε, M^{-1} cm^{-1}) = 318 (4280), 364 (2570), 423 (4710), 559 (437), 768 (353) nm; (THF): λ_{max} (ε, M^{-1} cm^{-1}) = 317 (3900), 366 (2600), 424 (4600), 562 (400), 778 (360) nm. ESI-MS calculated for $[FeC_{17}N_3S_2H_{33}]^+$: 399.4, found: 399.3 m/z. μ_{eff} = 3.48 B.M. Reduction potential (MeCN): $E_{1/2}$ = − 0.470 V vs SCE.

Synthesis of [Fe^{III}(η^2-$S^{Me2}O$)($S^{Me2}N_3$(Pr,Pr)](PF$_6$) (5) via the Addition of PhIO to 2. To a stirred solution of [Fe^{III}($S_2{}^{Me2}N_3$(Pr,Pr))](PF$_6$) (**2**) (275 mg, 0.52 mmol) in MeOH (20 mL) at – 35 °C was added dropwise a 2 mL MeOH solution containing 1.2 equivalents of PhIO (0.137 g, 0.62 mmol). The solution was stirred for 1 hour at –35 °C, and then stored in the freezer overnight. After filtration, the volume was reduced to 3 mL, layered with 25 mL of Et_2O, and cooled to – 35 °C overnight to afford **5** (153 mg, 0.28 mmol, 54%) as a pink crystalline solid. Electronic absorption (MeCN): λ_{max} (ε) = 333(4410), 510(1540) nm; (MeOH): λmax (ε) = 325(4870), 510(1700), 760(248) nm, (THF) λ_{max} (ε) = 510(1500) nm. IR (KBr pellet) ν(cm^{-1}): 1625 (C=N); 1024 (S-O). Reduction Potential (MeCN): Ep,c = – 0.960 V (irrev.) vs SCE. Solution magnetic moment (310.2 K; MeOH) μeff = 1.99 BM. EPR (DCM/toluene glass (1:1), 120 K): g_1 = 2.17, g_2 = 2.11, g_3 = 1.98, (MeTHF, 120 K): g_1 = 2.17, g_2 = 2.11, g_3 = 1.98, (MeOH/EtOH (9:1): g_1 = 2.18, g_2 = 2.12, g_3 = 2.00. ESI-MS calculated for $[FeC_{16}N_3S_2H_{31}O]^+$: 401.3; found: 401.2. Anal. calculated for $FeC_{16}H_{31}N_3OS_2PF_6$: C, 35.2; H, 5.7; N, 7.7. Found: C, 35.39; H, 5.57; N, 7.77.

Formation of a 3, via the Addition of Azide to 2. A 0.238 mM solution of **2** was prepared in 5 mL of THF under an inert atmosphere in a drybox. The resulting solution was transferred *via* gas-tight syringe to a custom-made two-neck vial equipped with a septum cap and threaded dip-probe feed-through adaptor that had previously been purged with argon and contained a stir bar. This solution was cooled in an acetone/dry ice bath to -73 °C and 1.5 eq. tetrabutylammonium azide (100 μL of 14.2 mM in THF) was added. Once **3** was fully formed and no further changes in absorbance were observed, 2 eq. of IBX-ester (100 μL of 23.8 mM in THF) was added and monitored for 2 hours.

Formation of a Green Intermediate, via the Addition of IBX-ester to 2. A 0.238 mM solution of **2** was prepared in 5 mL of MeOH or THF under an inert atmosphere in a drybox. The resulting solution was transferred *via* gas-tight syringe to a custom-made two-neck vial equipped with a septum cap and threaded dip-probe feed-through adaptor that had previously been purged with argon and contained a stir bar. This solution was cooled in an acetone/dry ice bath to -73 °C. To this, 2-10 eq. of IBX-ester (100 μL of 23.8-119 mM) was added, resulting in the formation of a metastable green intermediate (λ_{max}= 675 nm).

Formation of a Green Intermediate, via the Addition of $PhIO_2$ to 2. A 0.238 mM solution of **2** was prepared in 5 mL of MeOH or THF under an inert atmosphere in a drybox. The resulting solution was transferred *via* gas-tight syringe to a custom-made two-neck vial equipped with a septum cap and threaded dip-probe feed-through adaptor that had previously been purged with argon and contained a stir bar. This solution was cooled in an acetone/dry ice bath to -73 °C. To this, 1-4 eq. of $PhIO_2$ (50-200 μL of 23.8 mM solution in MeOH) was added, resulting in the formation of a metastable intermediate (λ_{max}= 675 nm).

Formation of a Yellow-Orange Intermediate, via the Addition of *m*CPBA to 2. The oxidant *m*CPBA was purified prior to use as described by reference [46]. A 0.238 mM solution of **2** was prepared in 4 mL of THF or MeTHF under an inert atmosphere in a drybox. The resulting solution was transferred *via* gas-tight syringe to a custom-made two-neck vial equipped with a septum cap and threaded dip-probe feed-through adaptor that had previously been purged with argon and contained a stir bar. This solution was cooled in an acetone/dry ice bath to -73 °C or in an LN2/n-pentane bath to -120 °C. To this, a solution of 10 eq. of mCPBA (95.2 mM) and 10 eq. of

triethylamine (95.2 mM) in THF were added in an aliquot of 100 μL, resulting in the formation of a metastable intermediate (λ_{max}= 455 nm and λ_{max}= 760 nm).

Formation of a Green Species, via the Addition of Pyridine N-Oxide (PNO) to 2. A 0.238 mM solution of **2** was prepared in 4 mL of THF or MeTHF under an inert atmosphere in a drybox. The resulting solution was transferred *via* gas-tight syringe to a custom-made two-neck vial equipped with a septum cap and threaded dip-probe feed-through adaptor that had previously been purged with argon and contained a stir bar. This solution was cooled in an acetone/dry ice bath to -73 °C or in an LN_2/n-pentane bath to -120 °C. To this, a solution of 10 eq. of PNO (95.2 mM) in THF were added in an aliquot of 100 μL, resulting in the formation of a metastable intermediate (λ_{max}= 702 nm).

Pyridine N-Oxide (PNO) Binding Studies. Pyridine N-oxide binding studies were performed using freshly prepared solutions of $[Fe^{III}(S_2{}^{Me2}N_3(Pr,Pr)]^+$ (**2**) and PNO in THF. Equilibrium constants were determined by monitoring electronic spectral changes at four different temperatures (-70 °C, -60 °C, -50 °C, and -40 °C). Low-temperature electronic absorption spectra were obtained on a Cary bio-50 UV−vis spectrophotometer equipped with an Unisoku USP-203-B cryostat using a 1 cm modified Schlenk cuvette. To minimize error in the measurements, electronic spectral data was collected at the wavelength (650 nm) which displays the least overlap in absorbance for the two complexes of interest, $[Fe^{III}(S_2{}^{Me2}N_3(Pr,Pr)]^+$ (**2**) vs $[Fe^{III}(S_2{}^{Me2}N_3(Pr,Pr)(PNO)]^+$ (**10**). The initial concentration of $[Fe^{III}(S_2{}^{Me2}N_3(Pr,Pr)]^+$ (**2**) ($[\mathbf{2}]_0$) was 0.20 mM. Solutions were prepared by varying the equivalents of PNO (5-100 eq.) so that 20% to 80% of the iron complex was PNO-bound. This range gave the least amount of error. The 650 nm extinction coefficient of **2** (ε_2(650

nm)) was measured at all four temperatures, and shown to vary from 243 M^{-1} cm^{-1} at -40 °C to 250 M^{-1} cm^{-1} at -70 °C. Extinction coefficients for the PNO-bound species ($\varepsilon_{\mathbf{10}}$), $[Fe^{III}(S_2{}^{Me2}N_3(Pr,Pr)(PNO)]^+$ (**10**), were obtained using a 1000-fold excess of PNO. Complete binding under these conditions was confirmed by showing that further addition of PNO had no influence on the spectrum. The 650 nm extinction coefficient of **10** ($\varepsilon_{\mathbf{10}}$(650 nm)) was determined at all four temperatures and shown to vary from 1098 M^{-1} cm^{-1} at -40 °C to 1165 M^{-1} cm^{-1} at -70 °C. Equilibrium constants were calculated using equations 1 and 2,[47,48] and determined to be K_{eq} (-70 °C) = 1917 ± 258 M^{-1}, Keq (-60 °C) = 1082 ± 147 M^{-1}, K_{eq} (-50 °C) = 329.1 ± 9.6 M^{-1}, and K_{eq} (-40 °C) = 137.1 ± 17.3 M^{-1}. Thermodynamic parameters, ΔH = -35.92 ± 0.38 kcal/mol and ΔS = -112.5 ± 17.5, were determined from a van't Hoff plot.

$$[\boldsymbol{Fe-PNO}] = \frac{\boldsymbol{A-\varepsilon_{Fe}[Fe]_0}}{\boldsymbol{\varepsilon_{Fe-PNO}-\varepsilon_{Fe}}} \quad (1)$$

$$\boldsymbol{K_{eq}} = \frac{[\boldsymbol{Fe-PNO}]}{([\boldsymbol{Fe}]_\mathbf{0}-[\boldsymbol{Fe-PNO}])([\boldsymbol{PNO}]_\mathbf{0}-[\boldsymbol{Fe-PNO}])} \quad (2)$$

Electron Paramagnetic Resonance Spectroscopy. EPR spectra were recorded on a Bruker EMX CW-EPR spectrometer operating at X-band frequency at 120 K using the following parameters: 9.28 GHz frequency, 2.0 mW power, 6 × 10^4 gain, 100 kHz modulation frequency, 0.2 mT modulation amplitude, and 40.96 ms conversion time. All EPR samples were frozen solutions of 0.476 mM of the respective Fe species (**2**, **5**, or **3**) in a glassing solvent (MeTHF) or a glassing solvent mixture of THF/MeTHF (98:2) in place of THF or MeOH/EtOH (9:1) in place of MeOH. Solutions of the metastable green intermediate were prepared as described for the electron

absorption spectroscopy with the change to a glassing solvent (MeTHF) or a glassing solvent mixture of THF/MeTHF (98:2) in place of THF or MeOH/EtOH (9:1) in place of MeOH. The solutions were then pipetted in a LN_2 chilled pipet from the dip-probe cell into a LN_2 chilled EPR tube and hand-quenched in a LN_2 filled dewar. The EPR spectra were simulated using EasySpin (version 5.2.23), a computational package developed by Stoll and Schweiger [49] and based on Matlab (The MathWorks, Massachusetts, USA).

DFT Calculations. All geometry optimizations were performed utilizing the ORCA v.3.0 quantum chemistry package[50] and originated from X-ray crystallographic coordinates. A BP86 functional,[51,52] with the resolution of identity approximation (RI),[53] dispersion correction (D3BJ),[54] and zeroth-order regular approximation for relativistic effects (ZORA),[55] was employed, using a dense integration grid (Grid4), def2-TZVP basis set,[56] and def2-TZVP/J auxiliary basis set.[53] In addition, the conductor-like screening model (COSMO) using acetonitrile (ε =37.5) as the solvent,[57] was employed.

X-ray Crystallographic Structure Determination. A red prism of, $[Fe^{III}(S_2{}^{Me2}N^{Me}N_2(Pr,Pr))]^+$ **(9)**, measuring 0.15 x 0.08 x 0.08 mm^3 was mounted on a loop with oil. Data was collected at -173 °C on a Bruker APEX II single crystal X-ray diffractometer, Mo-radiation. Crystal-to-detector distance was 40 mm and exposure time was 240 seconds per frame for all sets. The scan width was 1º. Data collection was 99.3% complete to 25º in ϑ. A total of 32,245 reflections were collected covering the indices, -15<=h<=15, -12<=k<=12, -16<=l<=16. 2,987 reflections were symmetry independent and the elevated R_{int} = 0.1613 indicated that the data was less than average quality (0.07). Indexing and unit cell refinement indicated a primitive monoclinic lattice. The space group was found to be P 2/c (No. 13).

A dark green prism of, $[Fe^{III}(S_2{}^{Me2}N_3(Pr,Pr)(PNO)]^+$ **(10)**, measuring 0.15 x 0.15 x 0.15 mm^3 was mounted on a loop with oil. Data was collected at -173 °C on a Bruker APEX II single crystal X-ray diffractometer, Mo-radiation. Crystal-to-detector distance was 40 mm and exposure time was 180 seconds per frame for all sets. The scan width was 0.5°. Data collection was 100% complete to 25° in ϑ. A total of 34,896 reflections were collected covering the indices, -11<=h<=11, -14<=k<=14, -29<=l<=29. 5490 reflections were symmetry independent and the elevated R_{int} = 0.0839 indicated that the data was near average quality (0.07). Indexing and unit cell refinement indicated a primitive orthorhombic lattice. The space group was found to be P $2_12_12_1$ (No. 19).

Data was integrated and scaled using SAINT, SADABS within the APEX2 software package by Bruker.[58] Solution by direct methods (SHELXS, SIR97) produced a complete heavy atom phasing model consistent with the proposed structure.[59,60] The structure was completed by difference Fourier synthesis with SHELXL.[61,62] Scattering factors are from Waasmair and Kirfel.[11] Hydrogen atoms were placed in geometrically idealized positions and constrained to ride on their parent atoms with C---H distances in the range 0.95-1.00 Angstrom. Isotropic thermal parameters Ueq were fixed such that they were 1.2 Ueq of their parent atom Ueq for CH's and 1.5Ueq of their parent atom Ueq in case of methyl groups. All non-hydrogen atoms were refined anisotropically by full-matrix least-squares. Final solution plotted using ORTEP and POV-Ray programs.[63,64]

Table 4.7. Crystal Data, Intensity Collections[a] and Structure Refinement Parameters for $[Fe^{III}(S_2{}^{Me2}N^{Me}N_2(Pr,Pr))]^+$ (**9**), and $[Fe^{III}(S_2{}^{Me2}N_3(Pr,Pr)(PNO)]^+$ (**10**).

	9	**10**
Formula	$C_{17}\ H_{33}\ Fe\ N_3\ P_1\ F_6\ S_2$	$C_{21}\ H_{36}\ Fe\ N_4\ O_1\ P_1\ F_6\ S_2$
Molecular Weight	544.40	625.48
Temperature (K)	100(2)	100(2)
Crystal System	Monoclinic	Orthorhombic
Space Group	P 2/c	P $2_12_12_1$
a, (Å)	11.4498(11)	9.5140(16)
b, (Å)	9.0351(8)	11.9423(18)
c, (Å)	12.4215(12)	23.590(3)
α (deg)	90	90
β (deg)	111.426(6)	90
γ (deg)	90	90
V ($Å^3$)	385.4(3)	2680.3(7)
Z	2	4
R_1	0.0644[b]	0.0400[b]
R_w	0.1263[c]	0.0702[c]
GOF	1.028	1.016

[a] Mo Ko(α,-) (λ = 0.71070 Å) radiation; graphite monochromator; -90 ºC. [b] $R = \Sigma\ ||F_o| - |F_c|| / \Sigma\ |F_o|$. [c] $R_w = [\Sigma w(|F_o| - |F_c|)^2/\Sigma wF_o^2]^{1/2}$, where $w^{-1} = [\sigma^2_{count} + (0.05\ F^2)^2]/4F^2$.

4.3 Results and Discussion

4.3.1 *Comparison of the Reactivity of Carboxamide-Ligated **8** vs. Imine-Ligated Fe Complexes*

The first indication that the S-oxygenation of **2** is metal-based came from the comparison of susceptibility to direct attack and reactivity of derivatives of **2**. Initially a more electron rich complex, $[Fe^{III}(S_2{}^{Me2}N^{Me}N_2{}^{amide}(Pr,Pr)]^{1-}$ (**8**), was synthesized as a derivative of **2** to better resemble the structure of NHase and potentially support high-valent Fe species (Figure 4.5). However, **8** is unreactive with H_2O_2 or PhIO, even when a ~1,000-fold excess of oxidant was used. Computational studies suggested that the thiolates on **8** have more electron density and would thus

be more likely to be directly oxidized, this indicates that oxo-atom donor reactivity correlates with the ligand binding properties of the complexes.[32] Even when added in excess, CN^- and N_3^- do not bind to the open coordination site of **8**. The 5-coordinate geometry index (τ) of **8** was found to be 0.56, indicating that the molecular geometry can best be described as halfway between trigonal bipyramidal and square pyramidal (Table 4.8). This differs from **2**, which is closer to a distorted trigonal pyramidal geometry ($\tau = 0.76$) (Table 4.8). Usually a complex with a geometry closer to square pyramidal would have a more accessible 6th binding site, however the largest angle is between the sulfur atoms (Table 4.8). If a sixth ligand binds there it would force the thiolates to be *trans* to each other, this is unlikely to occur. Another possibly is the methyl group on the backbone of **8** inhibits a sixth ligand from binding, since it may sterically clash with the thiolate *trans* to the oxo atom. The dissimilarity of **2** and **8** in regards to charge, geometry, sterics, and spin state (S =1/2 vs. S =3/2, respectively), a new derivative, $[Fe^{III}(S_2{}^{Me2}N^{Me}N_2(Pr,Pr))]^+$ (**9**), was synthesized. The complex **9** is structurally similar to **2**, differing in the addition of a methyl group on the amine. Structural characterization of **9** showed a distorted trigonal bipyramidal geometry ($\tau = 0.73$). This complex is capable of binding N_3^- and when reacted with oxo atom donors it does form a stable sulfenate complex analogous to **5**.[65] This implies that sulfur oxygenation requires an accessible open coordination site and/or the cationic nature of **2**, and further suggests a metal-bound intermediate, such as Fe^{III}-OX and Fe^{V}-Oxo.

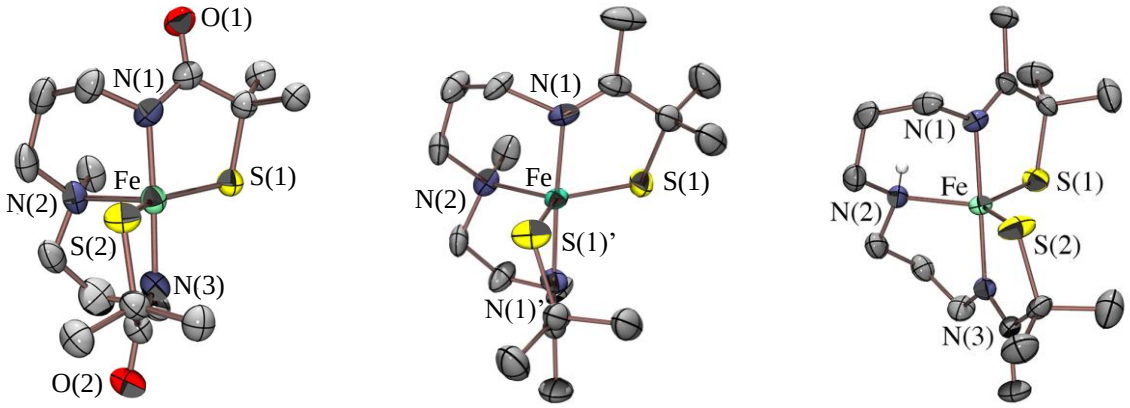

8 **9** **2**

Figure 4.5. Displacement ellipsoid plots of $[Fe^{III}(S_2{}^{Me2}N^{Me}N_2{}^{amide}(Pr,Pr)]^{1-}$ (**8**), $[Fe^{III}(S_2{}^{Me2}N^{Me}N_2(Pr,Pr))]^{+}$ (**9**) and $[Fe^{III}(S_2{}^{Me2}N_3(Pr,Pr)]^{+}$ (**2**) thermal ellipsoids at the 50% probability level. Counter-ions, solvent molecules and hydrogen atoms have been removed for clarity.

Table 4.8. Comparison of selected metrical parameters for $[Fe^{III}(S_2{}^{Me2}N^{Me}N_2{}^{amide}(Pr,Pr)]^{1-}$ (**8**),[35] $[Fe^{III}(S_2{}^{Me2}N^{Me}N_2(Pr,Pr))]^{+}$ (**9**), and $[Fe^{III}(S_2{}^{Me2}N_3(Pr,Pr)]^{+}$ (**2**).[33]

	8	**9**	**2**
Fe-S(1)	2.231(1) Å	2.2003(12) Å	2.161(2) Å
Fe-S(2)	2.210(1) Å	NA	2.133(2) Å
Fe-N(1)	1.934(3) Å	1.951(4) Å	1.967(4) Å
Fe-N(2)	2.212(3) Å	2.132(5) Å	2.049(4) Å
Fe-N(3)	1.924(3) Å	NA	1.954 (4) Å
S(1)-Fe-N(2)	107.14(9) °	116.8(4) °	132.3(1) °
S(2)-Fe-N(2)	108.43(9) °	111.0(4) °	106.5(1) °
S(1)-Fe-S(2)	144.40(5) °	132.11(8) °	121.01(1) °
τ^a	0.56	0.73	0.76

[a] 5-coordinate geometry index, $\tau = (\beta - \alpha)/60$. β is the largest bond angle observed, and α is the second largest bond angle.[66]

4.3.2 *Azide Inhibition of Sulfur Oxidation*

The mechanism of sulfur oxidation producing **5** likely involves initial coordination of the oxo atom donor to the metal ion. Consistent with this hypothesis, azide (N_3^-) was found to competitively inhibit sulfur oxidation of **2.** When 1.5 equivalents of N_3^- is added to **2** in THF at -73 ˚C, the intense band at 415 nm, characteristic of **2**, converts into bands at 465 nm and 720 nm, which are characteristic of the coordinatively saturated azide-bound [Fe^{III}-($S^{Me2}N_3$(Pr,Pr))N_3] (**3**) (Figure 4.3).[33] If following the formation of azide-bound **3** in THF, 2 equivalents of isopropyl 2-iodoxybenzoate (IBX-ester) are added, no reaction is observed, even after prolonged reaction times (2 hours) (Figure 4.3). If under the same conditions (-73 ˚C in THF), 2 equivalents IBX-ester are added to **2** in the absence of N_3^-, then within minutes a metastable intermediate is observed, which then converts to the singly oxygenated **5** (λ_{max}= 510 nm (1500 $M^{-1}cm^{-1}$) (*vida infra*). Azide inhibits sulfur oxidation of **2** by preventing the oxo atom donor from binding to the metal ion. In the absence of N_3^-, a new metastable intermediate is observed in the oxo atom donor reaction.

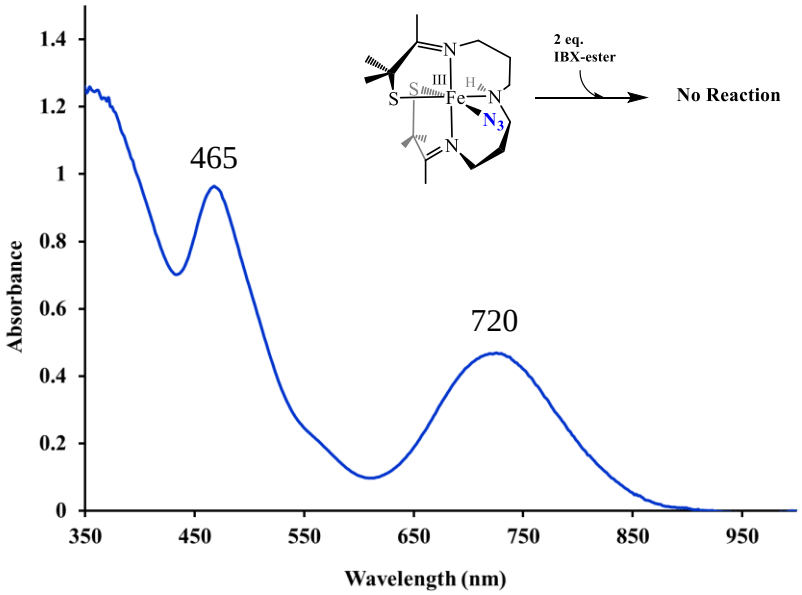

Figure 4.6. Monitoring the addition of 2 eq. isopropyl 2-iodoxybenzoate (IBX-ester) to [Fe^{III}-($S^{Me2}N_3$(Pr,Pr))N_3] (**3**) in THF at -73 ℃ vis electronic absorption spectroscopy, showing no reaction occurs.

4.3.3 *Observation of a Metastable Intermediate in the Reaction between **2** and IBX-ester*

A new green metastable intermediate is observed in the reaction **2** and hypervalent iodine oxo atom donors. When the reaction between 2 equivalents of IBX-ester and five-coordinate **2** is monitored by electronic absorption at -73 ˚C in MeOH or THF, a green metastable intermediate with λ_{max}= 677 nm immediately observed (Figure 4.7). When warmed to -10 ℃ the green intermediate converts to sulfenate ligated **5** ($t_{1/2}$ = 24 min). The observation of an intermediate provides evidence that sulfur oxidation is assisted by the metal ion and involves the initial binding of the oxo atom donor to the Fe ion. The new metastable intermediate could possibly be an oxo

atom donor adduct, Fe^{III}-OX, or an Fe^{V}-oxo. Given how rare Fe^{III}-OX[67,68] and Fe^{V}-oxo[69–71] species are, both possibilities are of great interest. The λ_{max} of this green intermediate falls within the range of reported for Fe^{III}-O=I-Ph (λ_{max}= 660 nm)[68] and Fe^{V}-oxo (λ_{max}= 630 nm (5400 cm^{-1})) compounds.[69,72] Both Fe^{III}-O=I-Ph and Fe^{V}-oxo species have been shown to be competent oxidants in oxo atom transfer reactions and may be responsible for the formation of the sulfenate **5**.[73]

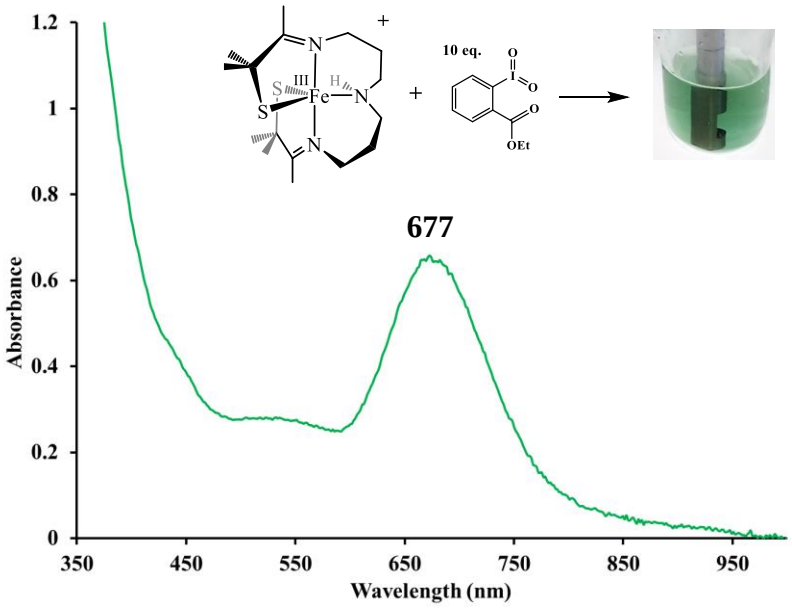

Figure 4.7. Electronic absorption spectrum of the reaction between 0.238 mM **2** and 10 eq. IBX-ester in THF at -73 °C.

To gain further insight into the identity of the green intermediate, continuous wave (CW) X-band electron paramagnetic resonance (EPR) spectroscopy was used. Previous work identified the magnetic properties of both **2** and **5** in a MeOH/EtOH (9:1) and DCM/Toluene (1:1)

respectively.[32,33] Complex **2** is low spin $S = 1/2$ and has g values at 2.20, 2.15 and 2.00 in a MeTHF glass, while singly oxygenated **5** is also low spin, and has distinct g values at 2.16, 2.10, and 1.97.[32] The green intermediate would be expected to have a rhombic signal if the substrate binds *cis* to one thiolate, but *trans* to the other. An Fe^{V}-oxo would likely be $S = 1/2$ as well due to the two strong π donors in the xy plane elevating the energy of the d_{xy} orbital. Collins and co-workers observed g values at 1.99, 1.97 and 1.74 for their spectroscopically characterized $S = 1/2$ Fe^{V}-oxo, which are markedly lower than that of low-spin Fe^{III} complexes.[69] However, another Fe^{V}-oxo with its oxidation state confirmed by Mössbauer spectroscopy exhibited g values of 2.053, 2.010, and 1.971.[74] There are only two reported EPR spectra for non-heme Fe^{III}-O=I-Ph adducts, both of which are high spin $S = 5/2$, and only a handful of well characterized Fe^{V}-oxo complexes exist, making it difficult to draw conclusions about the identity of the green species from EPR data. The observed $S = 1/2$ signal for the intermediate observed in the reaction of **2** with IBX-ester (Figure 4.5) is consistent with the proposed intermediate being either an Fe^{III}-OX or an Fe^{V}-oxo. Three species are observed by EPR in solution, two rhombic signals associated with the green intermediate, and a third signal from the sulfenate end product **5** (Figure 4.5). The two different EPR signals may be due to the possibility of different conformations of the IBX-ester when bound to the Fe^{III} complex.

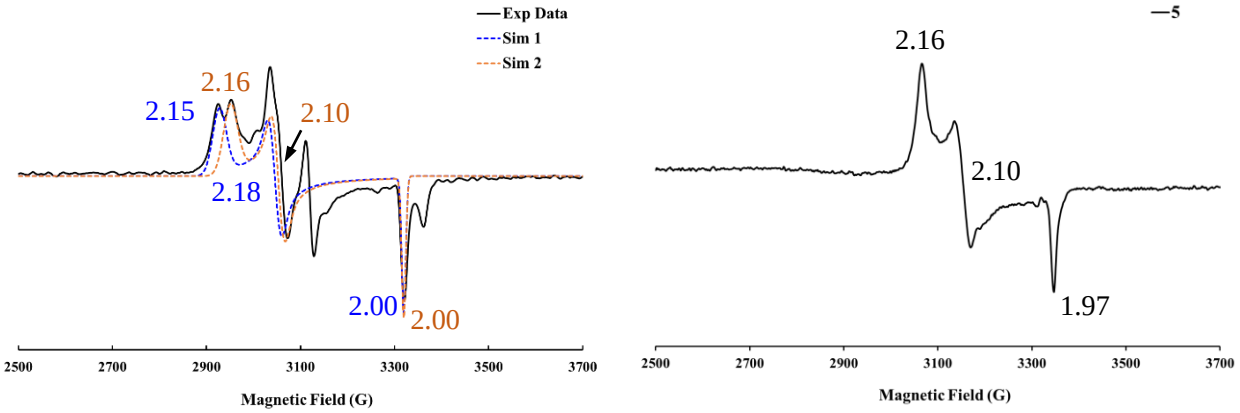

Figure 4.8. CW X-band EPR spectra of the intermediate generated from **2** and IBX-ester (left) and **5** (right) in MeTHF glass at 120 K.

4.3.4 *Observation of Metastable Intermediates in the Reaction between **2** and Oxo Atom Donors*

In order to determine if the observable intermediates are oxo atom donor adducts and not an Fe^{V}-oxo, alternate oxidants should not produce the same electronic absorption feature at 677 nm and EPR spectra as reaction of **2** and IBX-ester. If an identical green intermediate can be produced using different oxo atom donors, then this would suggest that the intermediate is an Fe^{V}-oxo. Two other commonly used oxidants, 3-chloroperoxybenzoic acid (*m*CPBA), and pyridine-*N*-oxide (PNO), were reacted with **2** and were monitored by electronic absorption spectroscopy. The organic peroxide type oxidant, *m*CPBA, when deprotonated binds to **2** and the O-O bond would need to heterolytically cleave to form an Fe^{V}-oxo. The peroxide bond strength is approximately 45 kcal/mol, which is near that of hyper-valent oxo atom donors (BDE_{I-O} = 44 kcal/mol).[75,76] Deprotonated *m*CPBA reacts with **2** readily at low temperatures to produce a new metastable intermediate (λ_{max} = 460 and 760 nm) (Figure 4.9). The perpendicular mode EPR spectra of the

reaction of *m*CPBA and **2** displays an intense rhombic signal with *g*-values of 2.23, 2.17, and 2.00 (Figure 4.9), near the *g*-values of the putative Fe^{III}-hydroperoxo species generated from O_2 (2.23, 2.15 and 2.00).[34] The reaction between **2** and 20 eq. PNO at low temperatures produces an electronic absorption spectra with a low-energy peak with similar intensity to that of **2**-*m*CPBA (Figure 4.10). The EPR spectra was also similar and displayed a rhombic signal with *g*-values of 2.23, 2.17, and 2.00 (Figure 4.10). The observed shift in λ_{max} depending on the identity of the oxo atom donors and EPR spectra consistent with other known species in with this ligand provides evidence that the green intermediate is indeed an Fe^{III}-OX adduct (Table 4.9).

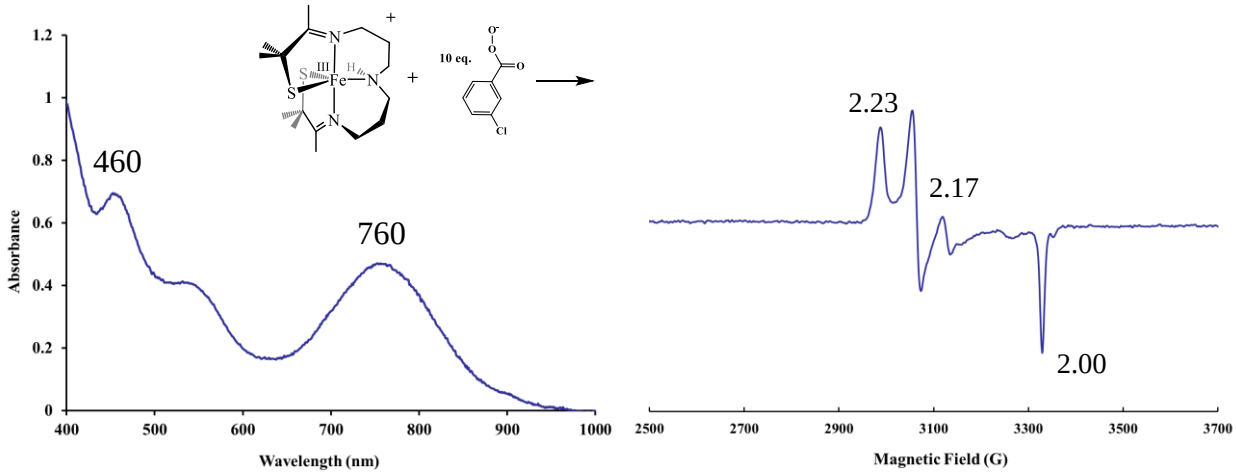

Figure 4.9. Electronic absorption spectrum of the reaction between 0.238 mM **2** and 10 eq. *m*CPBA with base in MeTHF at -120 ℃ (left). X-band EPR spectra of the reaction between 0.476 mM **2** and 10 eq. *m*CPBA with base in MeTHF glass at 120 K (right).

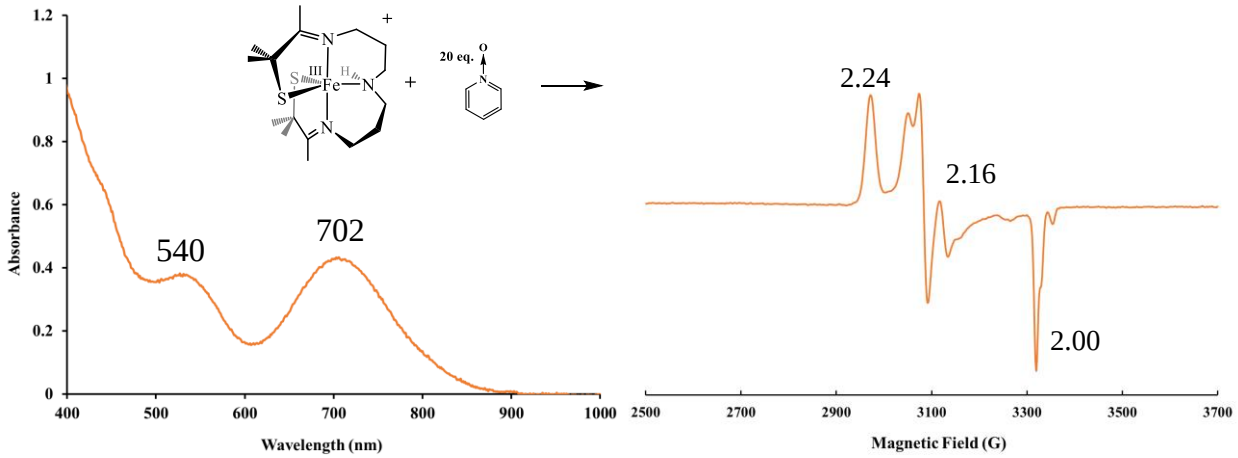

Figure 4.10. Electronic absorption spectrum of the reaction between 0.238 mM **2** and 20 eq. PNO in MeTHF at -120 ℃ (left). X-band EPR spectra of the reaction between 0.476 mM **2** and 20 eq. PNO in MeTHF glass at 120 K (right).

Table 4.9. Comparison of the properties of **2**, **5** and oxo atom donor adducts (electronic absorption: Me-THF -120 ℃, EPR: Me-THF glass at 117 K).

	λmax (nm)	***g*-values**	***g*-spread**
2	416, 764	2.20, 2.15, 2.00	0.20
5	510	2.16, 2.10, 1.97	0.19
2 + IBX-ester	677	2.25, 2.18, 2.00	0.25
		2.24, 2.16, 2.00	0.24
2 + *m*CPBA	460, 760	2.23, 2.17, 2.00	0.23
2 + PNO	540, 702	2.24, 2.16, 2.00	0.24

4.3.5 *X-ray Crystal Structure of [$Fe^{III}(S_2^{Me2}N_3$(Pr,Pr)(PNO)]$^+$ (**10**)*

The intermediate in the reaction between **2** and PNO results in a temperature sensitive intermediate that does not go on to produce the sulfenate, **5**. This allowed for the crystallization of **10** from a solvent diffusion crystallization at -80 ℃. The helical ligand opened to accommodate the binding of PNO through the oxygen atom to the Fe ion. The PNO binds *trans* to one of the thiolate sulfurs (S(2)) and *trans* to the proton on N(2) (Figure 4.11). The N-O bond length is not significantly changed relative to free PNO (1.31 Å),[77] and the long Fe-O distance is indicative of a weak interaction that does not result in oxo atom transfer (Table 4.10). PNO contains a stronger N-O bond (72 kcal/mol)[78] than hypervalent iodine oxo atom donors and *m*CBPA which have weaker I-O and O-O bonds estimated to be approximately 44 kcal/mol and 45 kcal/mol respectively.[75,76] Whether **2** is only capable of cleaving weak bonds to form an Fe^V-oxo, which is then trapped intramolecularly, or whether it proceeds through a concerted mechanism has yet to be determined.

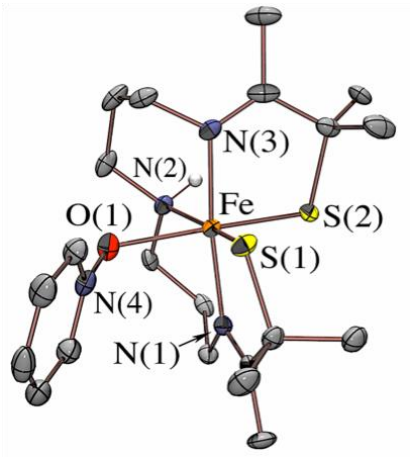

Figure 4.11. Displacement ellipsoid plots of [Fe^{III}($S^{Me2}N_3$(Pr,Pr))PNO]$^+$(**10**) with thermal ellipsoids at the 50% probability level. Hydrogen removed for clarity except on N(2).

Table 4.10. Comparison of selected metrical parameters for $[Fe^{III}(S_2{}^{Me2}N_3(Pr,Pr)(N_3)]$ (**3**),[33] and $[Fe^{III}(S_2{}^{Me2}N_3(Pr,Pr)(PNO)]^+$ (**10**).

	3	**10**
Fe-S(1)	2.196(1) Å	2.1780(12) Å
Fe-S(2)	2.209(1) Å	2.1731(13) Å
Fe-N(1)	1.978(3) Å	1.986(3) Å
Fe-N(2)	2.157(3) Å	2.110(3) Å
Fe-N(3)	1.970(3) Å	1.957(4) Å
S(1)-Fe-N(2)	172.5(1)°	166.68(11)°
S(2)-Fe-N(2)	90.6(1)°	95.12(11)°
S(1)-Fe-S(2)	95.3(1)°	96.58(5)°

4.3.6 *Variable-Temperature Equilibrium Study of Oxo Atom Donors Binding to **2***

Obtaining thermodynamic parameters for the formation of oxo atom donor adducts with first row transition metals are useful due their use as shunt pathways to study the active oxidants in enzymatic systems.[79,80] The initial binding of any of the oxo atom donors occurs too rapidly to observe even when using stopped flow techniques therefore no kinetic parameters could be obtained. However, even at room temperature with a 20-fold excess of PNO, there was no detectable amount of **10**. When a solution containing **2** and 20 eq. of PNO is cooled to -73 ℃, there is a noticeable color change from orange to a clover green. This change is reversible upon warming to ambient temperature, and upon cooling it forms the same clover green solution by electronic absorption spectroscopy. This is expected for an associative binding process, as the entropy disfavors PNO binding at warmer temperatures. The reversible binding of PNO to **2** allowed for the determination of thermodynamic parameters. Equilibrium constants were determined by electronic absorption spectroscopy over a range of temperatures (Figure 4.12). The

enthalpy and entropy (ΔH = -35.9 ± 0. 4 kJ/mol and ΔS = -112 ± 18 J/mol) for PNO binding was determined from a Van't Hoff plot (Figure 4.13). The negative entropy of binding is as expected for an associative process. The fast reactivity of IBX-ester made collecting equilibrium constants only possible with use of stopped flow electronic spectroscopy. Interestingly, near quantitative IBX-ester binding to **1** is observed, making reliable equilibrium constants difficult to obtain. However, it is clear from the near quantitative IBX-ester binding that **2** binds IBX-ester binds more readily than PNO.

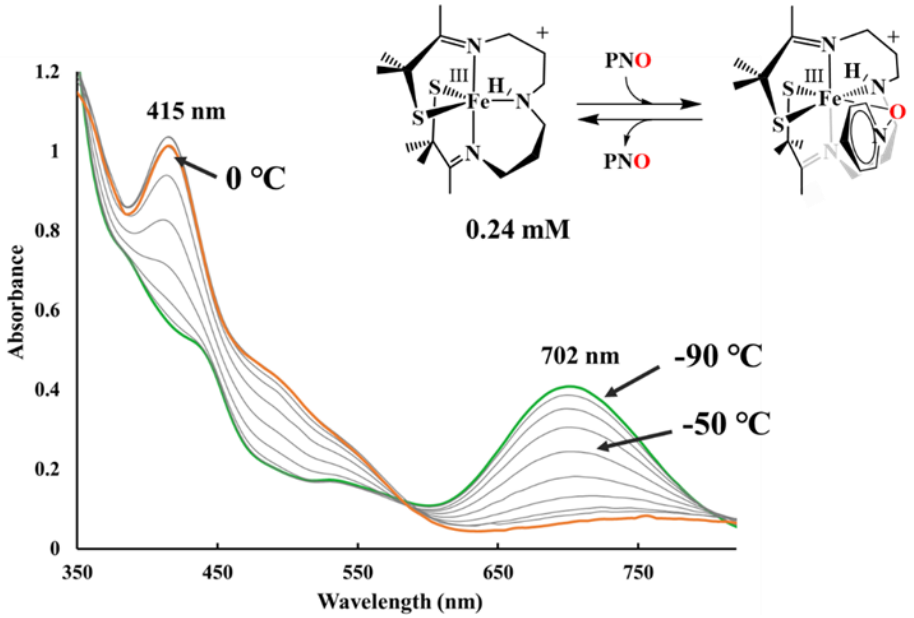

Figure 4.12. Variable-temperature electronic absorption spectrum of 0.24 mM of **2** with 20 equivalents of PNO in THF. Displaying temperature from -90 °C to 0 °C, each line is a 10 °C step.

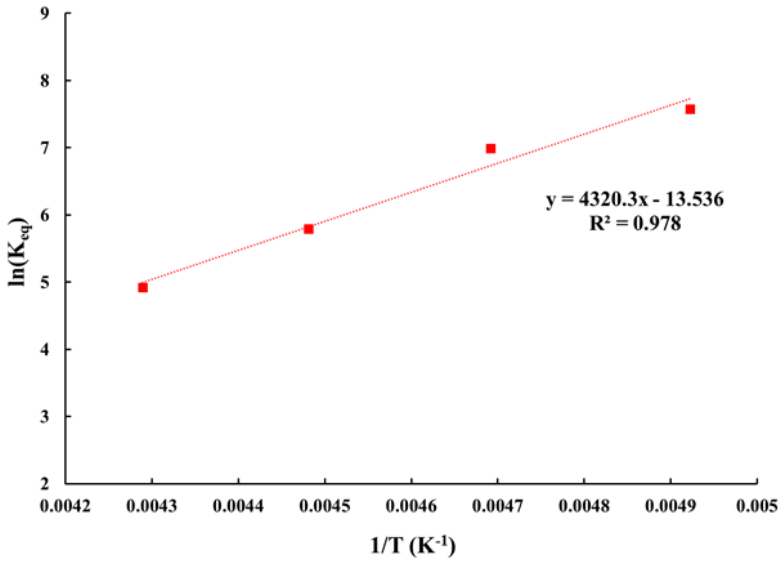

Figure 4.13. Van't Hoff plot for the binding of PNO to **2** determined from the equilibrium constants from – 70 ℃ to – 40 ℃.

4.3.7 *Distinguishing the Pathway from Oxo Atom Donor Adduct, Fe^{III}-OX, to Sulfenate **5***

Possible mechanisms for sulfur oxygenation (Scheme 4.3) would involve initial formation of an oxo atom donor adduct that can undergo direct attack by the adjacent nucleophilic sulfur (pathway a, Figure 4.14), or converts to an Fe^{V}-oxo, which is then rapidly trapped by the adjacent sulfur (pathway b, Figure 4.14). The observation of one intermediate, as opposed to two, suggests either (a) *cis*-migration of a thiolate sulfur to the oxo of a coordinated Fe^{III}-OX is rate-determining, or (b) cleavage of the X-O bond to afford an unobserved Fe^{V}-oxo is rate-determining. For both of these pathways, the green intermediate is likely an oxo atom donor adduct (Figure 4.14). The anticipated fast rate of intramolecular trapping of an Fe^{V}-oxo, relative to its rate of formation, would mean that the Fe^{V}-oxo would be unobservable. While oxo atom exchange with $H_2{}^{18}O$ is commonly used to provide evidence for high valent metal-oxo intermediates in reaction

pathways,[81] hyper-valent iodine oxo atom donors are also capable of fast exchange with $H_2{}^{18}O$. Therefore the incorporation of ^{18}O would not necessarily be indicative of the formation of a high valent metal-oxo.[82] However, inhibition studies involving iodoarene (IAr) could possibly distinguish between mechanisms.

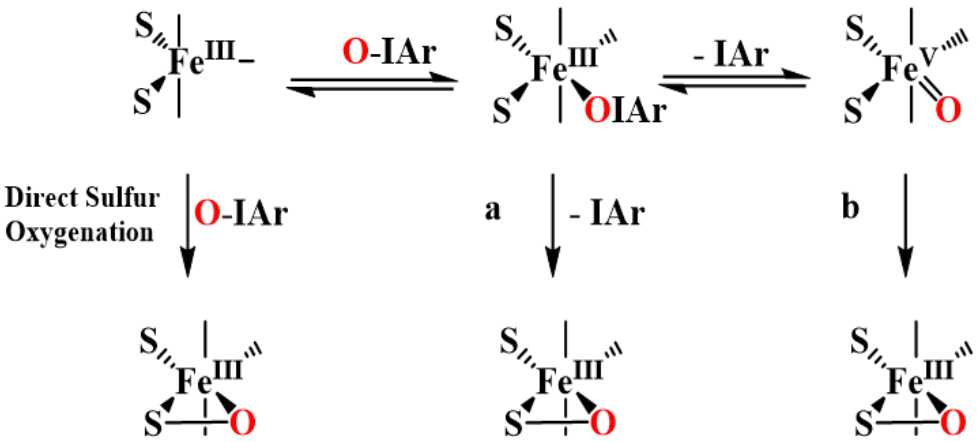

Figure 4.14. Potential reaction pathways for S-oxygenation

Previous work with Fe-porphyrin systems revealed that the O-I bond cleavage is reversible.[83] Thus the presence of excess iodoarene (IAr) should decrease the rate of formation of **5** if an Fe^{V}-oxo intermediate is involved by through a competing pathway that redirects the Fe^{V}-oxo back to the oxo atom adduct Fe^{III}-OIAr. This approach to probe the identity of the active oxidant has been used for several systems.[43,68,83–85] Hypervalent iodine oxo-atom donors that are doubly oxygenated (such as IBX-ester) will have more complicated kinetics for the heterolysis of the I-O bond as the singly oxygenated iodine is a capable oxidant as well. As such, a singly oxygenated hypervalent iodine oxo-atom donor such as iodosylbenzene (PhIO) should be mechanistically cleaner than the peroxyacid, *m*CPBA, and IBX-ester. Iodosylbenzene (PhIO)

should be mechanistically cleaner than the peroxyacid, *m*CPBA, and IBX-ester.[85] The use of an oxo atom donor with a single oxygen atom to transfer to the Fe^{III} thiolate should allow for kinetic studies to determine the pathway of S-oxygenation.

A systematic kinetic study using *p*-substituted derivatives of PhIO will allow for deeper insights into the reaction mechanism of metal-assisted sulfur oxygenation. A Hammett plot using OIAr-^{p}X (X= Me, OMe, H, CF_3) will be generated to determine whether the mechanism remains the same throughout and whether positive or negative charge builds up. If the I-O bond cleaves heterolytically then electron withdrawing groups (EWG) would speed up the reaction and electron donating groups (EDG) would slow down the reaction. While at room temperature in MeOH, 1.4 equivalents of PhIO has been shown to produce the sulfenate **5** instantly, at low temperatures (-73 °C) using 10 eq. of PhIO and **2** in MeOH, a green intermediate (λ_{max} = 675 nm) forms (Figure 4.10), analogous to the intermediate formed in the reaction of **2** with IBX-ester. However, this intermediate could not be reproduced after newly synthesized PhIO was used. The reason for this inability to reproduce the intermediate at λ_{max} = 675 nm was the identity of the oxo atom donor adduct was actually iodoxybenzene ($PhIO_2$), formed as a result of the disproportionation of PhIO into PhI and $PhIO_2$, which has been previously reported.[43,86] The reaction of **2** with independently prepared $PhIO_2$ lead to the reproduction of the green intermediate seen with the older vial of PhIO (Figure 4.15). At low temperatures none of the single oxygen atom donors, OIAr-^{p}X (X= Me, OMe, H, CF_3) bind to **2** but upon warming to room temperature all derivatives do go onto transfer an oxygen atom to form the sulfenate. Another completely fluorinated C_6F_5IO derivative was synthesized to produce a singly oxygenated oxo atom donor that would bind at low temperatures to allow for an inhibition study.

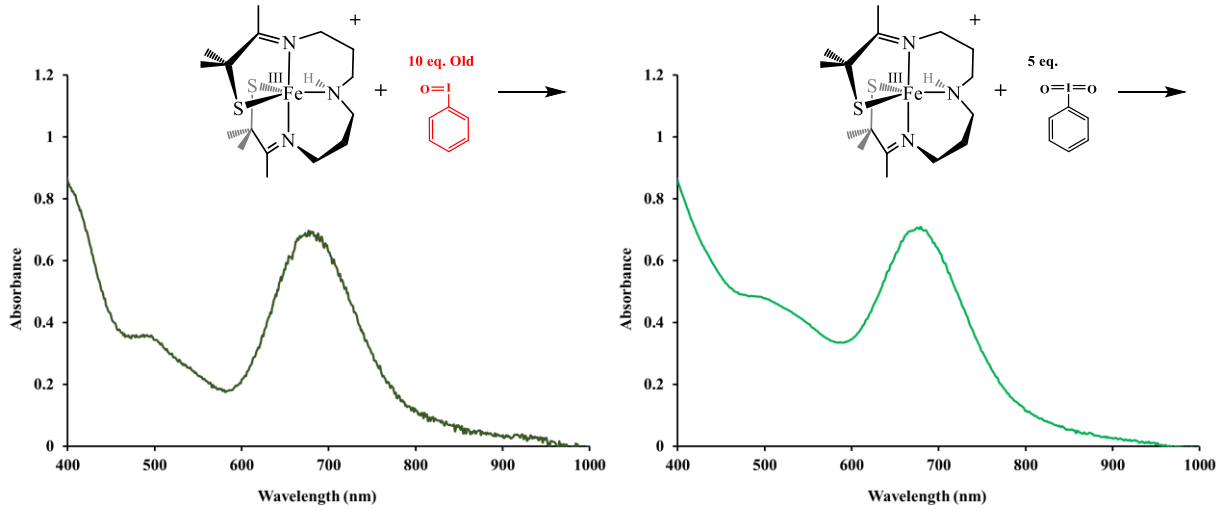

Figure 4.15. Electronic absorption spectra of the reaction between 0.238 mM **2** and 10 eq. Old PhIO suspected to have disproportionated to 5 eq. $PhIO_2$ and 5 eq IAr in MeOH at -73 ℃ (left) and the reaction between 0.238 mM **2** and 5 eq. $PhIO_2$ in MeOH at -73 ℃ (right).

4.3.8 *Reactivity of Pentafluoroiodosylbenzene (PFIB) and $[Fe^{III}(S_2{}^{Me2}N_3(Pr,Pr))]^+$ (**2**)*

Pentafluoro-iodosylbenzene (PFIB) was selected for this experiment due to its ability to bind to **2** and its increased solubility in organic solvents. The formation of the sulfenate species **5** does not appear to be reversible since no reaction was observed when the reaction between **5** and pentafluoroiodobenzene ($IArF_5$) was monitored by electronic absorption spectroscopy at -73 ˚C in THF for three hours. The starting material **2** also does not react with $IArF_5$. The reaction of **2** with 5 equivalents PFIB -73 ˚C in THF instantly produces a metastable intermediate with a λ_{max} at 691 nm that converts to the 510 nm species, **5**, in 5 minutes. Reaction of **2** with 5 eq. PFIB in the presence of 200 eq. $IArF_5$ requires 30 min in order to convert to **5**, which is significantly slower than in the absence of the $IArF_5$ (Figure 4.16). This observation using dip-probe electronic

absorbance spectroscopy suggests that an Fe^{V}-oxo forms *en route* to **5**, which then undergoes oxo *cis*-migration onto the thiolate to generate the sulfenate end product, **5**. This oxo *cis*-migration is similar to a step in the proposed mechanism of CDO. The derived rate expressions for pathway a (eq 1 & 2) and pathway b (eq 3 & 4) assuming a rapid pre-equilibrium step involving OIAr binding to **2**, and the simplified equations using pseudo-first-order conditions are shown below (Figure 4.17).

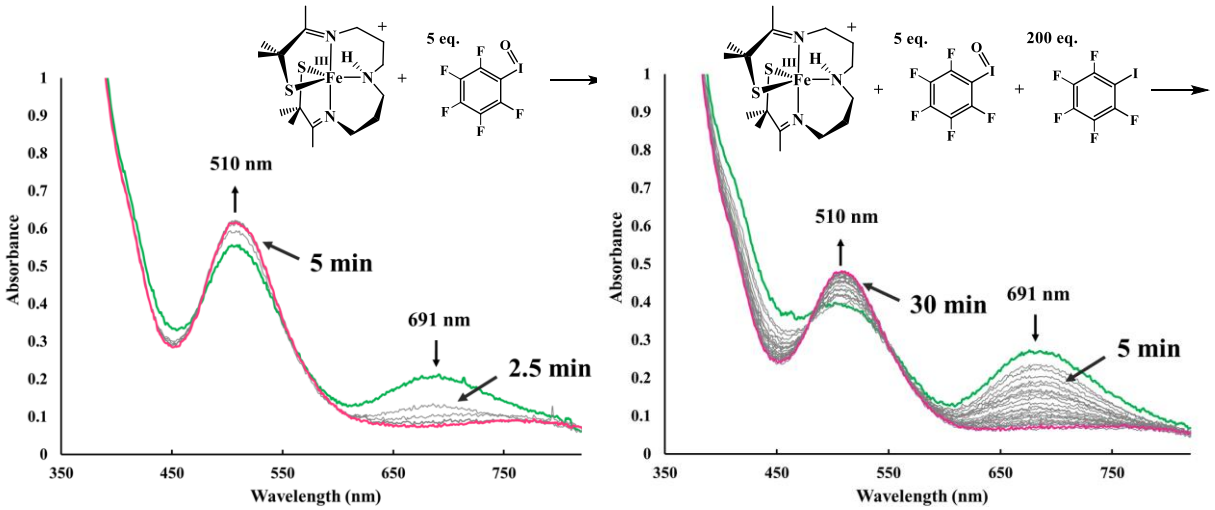

Figure 4.16. Monitoring the electronic absorption spectra of the conversion of the green intermediate formed from 0.476 mM **2** and 5 eq. PFIB to **5** in THF at -73 ℃ over the course of 5 minutes (left) and the same reaction in the presence of 200 eq. $IArF_5$ in THF at -73 ℃ over the course of 30 mins (right).

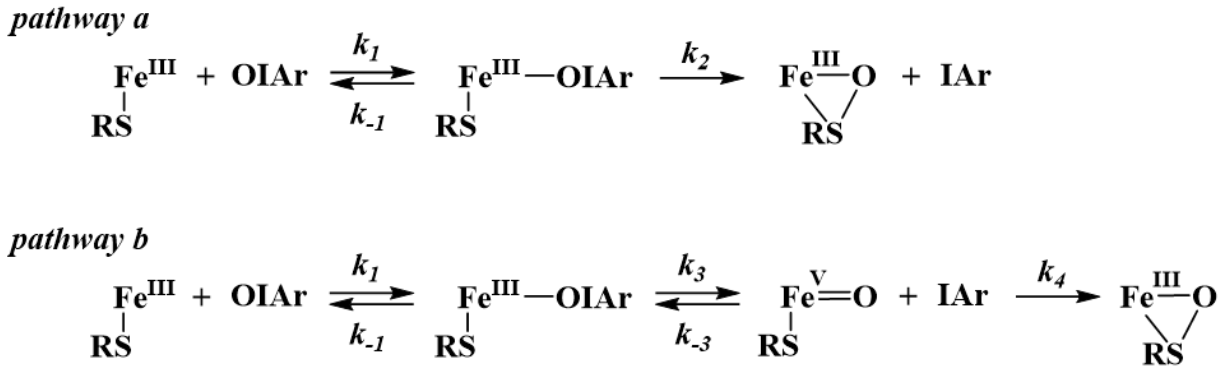

Figure 4.17. Possible metal-assisted pathways for sulfenate formation.

$$Rate_a = k_2 \frac{k_1}{k_{-1}} [Fe^{III}][OIAr] \quad (1)$$

$$Rate_a = k_{obs}[Fe^{III}] \quad (2)$$

$$Rate_b = k_4 k_3 \frac{k_1}{k_{-1}} \frac{[Fe^{III}][OIAr]}{(k_{-3}[IAr]+k_4)} \quad (3)$$

$$Rate_b = k_{obs} \frac{[Fe^{III}]}{[IAr]} \quad (4)$$

If the mechanism follows pathway b, then competitive inhibition by IAr should be observed in the regime where k_{-3}[IAr] >>> k_4. Under these conditions, eq. 3 would simplify to eq. 4 and slower reaction rates would be observed. This is consistent with the drastic slowing of the conversion to **5** when $IArF_5$ is present providing indirect evidence for an Fe^V-oxo prior to the formation of the sulfenate. This promising result warrants a more in-depth kinetic study aimed at obtaining more data points and generating a k_{obs} vs 1/[IAr] plot for PFIB, in order to show that inhibition is consistently observed over a range of inhibitor concentrations.

4.4 Summary and Conclusions

The isolation and structural characterization of a rare singly oxygenated sulfenate **5** led to the investigation of its mechanism of formation. While **5** can be generated from dioxygen, its formation from a proposed Fe^{V}-oxo follows the rate determining O-O cleavage step, thus oxo atom donors were employed as an alternate route. Collectively, N_3^- inhibition of the formation of **5** from oxo atom donors, and the observation of a new green intermediate, eliminate the possibility of direct nucleophilic attack by the sulfur on the electrophilic oxygen atom. The use of many types of oxo atom donors aided in the identification of the observed green intermediate as an Fe^{III} oxo atom donor adduct. Since these adducts species are capable oxidants themselves,[68,87] or could undergo heterolysis to form a transient Fe^{V}-oxo active species, an inhibition study was pursued in which we looked for a slowing of rate. This would provide indirect evidence for a high valent oxo that transfers it's oxo to a *cis*-thiolate via an intramolecular mechanism. Complex **2** has several previously characterized derivatives, such as $[Fe^{III}(S_2{}^{Me2}N_3(Et,Pr))]^+$, which should have a higher barrier to Fe^{V}-oxo trapping the due to the shorter ethyl linker constraining ligand movement.[88] The mechanism of transfer of an oxo to a thiolate to form a sulfenate has yet to be thoroughly understood even though sulfenates are biologically important species for cysteine catabolism and for biocatalysis of amides.[9–13] Oxo atom donors provide shunt pathways to observe highly reactive intermediates in model systems and enzymatic catalytic cycles.[79,89,90] The study of the formation of oxo atom donor adducts and heterolysis of the O-X bonds to form high-valent oxo species from **2** and its derivatives remains an exciting area for further research.

4.5 Reference

(1) Murakami, T.; Nojiri, M.; Nakayama, H.; Dohmae, N.; Takio, K.; Odaka, M.; Endo, I.; Nagamune, T.; Yohda, M. Post-Translational Modification Is Essential for Catalytic Activity of Nitrile Hydratase. *Protein Sci.* **2000**, *9*, 1024–1030. DOI: 10.1110/ps.9.5.1024.

(2) Murakami, T.; Nojiri, M.; Nakayama, H.; Dohmae, N.; Takio, K.; Odaka, M.; Endo, I.; Nagamune, T.; Yohda, M. Post-Translational Modification Is Essential for Catalytic Activity of Nitrile Hydratase. *Protein Sci.* **2009**, *9* (5), 1024–1030. DOI: 10.1110/ps.9.5.1024.

(3) Tsujimura, M.; Odaka, M.; Nakayama, H.; Dohmae, N.; Koshino, H.; Asami, T.; Hoshino, M.; Takio, K.; Yoshida, S.; Maeda, M.; et al. A Novel Inhibitor for Fe-Type Nitrile Hydratase: 2-Cyano-2-Propyl Hydroperoxide. *J. Am. Chem. Soc.* **2003**, *125* (38), 11532–11538. DOI: 10.1021/ja035018z.

(4) Stipanuk, M. H. SULFUR AMINO ACID METABOLISM: Pathways for Production and Removal of Homocysteine and Cysteine. *Annu. Rev. Nutr.* **2004**, *24* (1), 539–577. DOI: 10.1146/annurev.nutr.24.012003.132418.

(5) Zhou, Z.; Hashimoto, Y.; Kobayashi, M. Self-Subunit Swapping Chaperone Needed for the Maturation of Multimeric Metalloenzyme Nitrile Hydratase by a Subunit Exchange Mechanism Also Carries out the Oxidation of the Metal Ligand Cysteine Residues and Insertion of Cobalt. *J. Biol. Chem.* **2009**, *284* (22), 14930–14938. DOI: 10.1074/jbc.M808464200.

(6) Zhou, Z.; Hashimoto, Y.; Cui, T.; Washizawa, Y.; Mino, H.; Kobayashi, M. Unique

Biogenesis of High-Molecular Mass Multimeric Metalloenzyme Nitrile Hydratase: Intermediates and a Proposed Mechanism for Self-Subunit Swapping Maturation. *Biochemistry* **2010**, *49* (44), 9638–9648. DOI: 10.1021/bi100651v.

(7) Nelp, M. T.; Astashkin, A. V.; Breci, L. A.; McCarty, R. M.; Bandarian, V. The Alpha Subunit of Nitrile Hydratase Is Sufficient for Catalytic Activity and Post-Translational Modification. *Biochemistry* **2014**, *53* (24), 3990–3994. DOI: 10.1021/bi500260j.

(8) Nagashima, S.; Nakasako, M.; Dohmae, N.; Tsujimura, M.; Takio, K.; Odaka, M.; Yohda, M.; Kamiya, N.; Endo, I. Novel Non-Heme Iron Center of Nitrile Hydratase with a Claw Setting of Oxygen Atoms. *Nat. Struct. Biol.* **1998**, *5* (5), 347–351. DOI: 10.1038/nsb0698-432.

(9) Hopmann, K. H. Full Reaction Mechanism of Nitrile Hydratase: A Cyclic Intermediate and an Unexpected Disulfide Switch. *Inorg. Chem.* **2014**, *53* (6), 2760–2762. DOI: 10.1021/ic500091k.

(10) Kayanuma, M.; Shoji, M.; Yohda, M.; Odaka, M.; Shigeta, Y. Catalytic Mechanism of Nitrile Hydratase Subsequent to Cyclic Intermediate Formation: A QM/MM Study. *J. Phys. Chem. B* **2016**, *120* (13), 3259–3266. DOI: 10.1021/acs.jpcb.5b11363.

(11) Tyler, L. A.; Noveron, J. C.; Olmstead, M. M.; Mascharak, P. K. Modulation of the PKa of Metal-Bound Water via Oxidation of Thiolato Sulfur in Model Complexes of Co(III) Containing Nitrile Hydratase: Insight into Possible Effect of Cysteine Oxidation in Co-Nitrile Hydratase. *Inorg. Chem.* **2003**, *42* (18), 5751–5761. DOI: 10.1021/ic030088s.

(12) Lugo-Mas, P.; Dey, A.; Xu, L.; Davin, S. D.; Benedict, J.; Kaminsky, W.; Hodgson, K. O.; Hedman, B.; Solomon, E. I.; Kovacs, J. A. How Does Single Oxygen Atom Addition Affect

the Properties of an Fe-Nitrile Hydratase Analogue? The Compensatory Role of the Unmodified Thiolate. *J. Am. Chem. Soc.* **2006**, *128* (34), 11211–11221. DOI: 10.1021/ja062706k.

(13) Dey, A.; Jeffrey, S. P.; Darensbourg, M.; Hodgson, K. O.; Hedman, B.; Solomon, E. I. Sulfur K-Edge XAS and DFT Studies on NiII Complexes with Oxidized Thiolate Ligands: Implications for the Roles of Oxidized Thiolates in the Active Sites of Fe and Co Nitrile Hydratase. *Inorg. Chem.* **2007**, *46* (12), 4989–4996. DOI: 10.1021/ic070244l.

(14) Tchesnokov, E. P.; Faponle, A. S.; Davies, C. G.; Quesne, M. G.; Turner, R.; Fellner, M.; Souness, R. J.; Wilbanks, S. M.; de Visser, S. P.; Jameson, G. N. L. An Iron–Oxygen Intermediate Formed during the Catalytic Cycle of Cysteine Dioxygenase. *Chem. Commun.* **2016**, *52* (57), 8814–8817. DOI: 10.1039/c6cc03904a.

(15) Aluri, S.; De Visser, S. P. The Mechanism of Cysteine Oxygenation by Cysteine Dioxygenase Enzymes. *J. Am. Chem. Soc.* **2007**, *129* (48), 14846–14847. DOI: 10.1021/ja0758178.

(16) De Visser, S. P.; Nam, W. The Effect and Influence of Cis-Ligands on the Electronic and Oxidizing Properties of Nonheme Oxoiron Biomimetics. A Density Functional Study. *J. Phys. Chem. A* **2008**, *112* (50), 12887–12895. DOI: 10.1021/jp8018556.

(17) Kumar, D.; Thiel, W.; de Visser, S. P. Theoretical Study on the Mechanism of the Oxygen Activation Process in Cysteine Dioxygenase Enzymes. *J. Am. Chem. Soc.* **2011**, *133* (11), 3869–3882. DOI: 10.1021/ja107514f.

(18) Kumar, D.; Sastry, G. N.; Goldberg, D. P.; De Visser, S. P. Mechanism of S-Oxygenation by a Cysteine Dioxygenase Model Complex. *J. Phys. Chem. A* **2012**, *116* (1), 582–591.

DOI: 10.1021/jp208230g.

(19) Blaesi, E. J.; Gardner, J. D.; Fox, B. G.; Brunold, T. C. Spectroscopic and Computational Characterization of the NO Adduct of Substrate-Bound Fe(II) Cysteine Dioxygenase: Insights into the Mechanism of O2 Activation. *Biochemistry* **2013**, *52* (35), 6040–6051. DOI: 10.1021/bi400825c.

(20) Blaesi, E. J.; Fox, B. G.; Brunold, T. C. Spectroscopic and Computational Investigation of Iron(III) Cysteine Dioxygenase: Implications for the Nature of the Putative Superoxo-Fe(III) Intermediate. *Biochemistry* **2014**, *53* (36), 5759–5770. DOI: 10.1021/bi500767x.

(21) Li, J.; Griffith, W. P.; Davis, I.; Shin, I.; Wang, J.; Li, F.; Wang, Y.; Wherritt, D. J.; Liu, A. Cleavage of a Carbon–Fluorine Bond by an Engineered Cysteine Dioxygenase. *Nat. Chem. Biol.* **2018**, *14* (9), 853–860. DOI: 10.1038/s41589-018-0085-5.

(22) Li, J.; Koto, T.; Davis, I.; Liu, A. Probing the Cys-Tyr Cofactor Biogenesis in Cysteine Dioxygenase by the Genetic Incorporation of Fluorotyrosine. *Biochemistry* **2019**, *58*, 2218–2227. DOI: 10.1021/acs.biochem.9b00006.

(23) Simmons, C. R.; Krishnamoorthy, K.; Granett, S. L.; Schuller, D. J.; Dominy, J. E.; Begley, T. P.; Stipanuk, M. H.; Karplus, P. A. A Putative Fe2+-Bound Persulfenate Intermediate in Cysteine Dioxygenase. *Biochemistry* **2008**, *47* (44), 11390–11392. DOI: 10.1021/bi801546n.

(24) Souness, R. J.; Kleffmann, T.; Tchesnokov, E. P.; Wilbanks, S. M.; Jameson, G. B.; Jameson, G. N. L. Mechanistic Implications of Persulfenate and Persulfide Binding in the Active Site of Cysteine Dioxygenase. *Biochemistry* **2013**, *52* (43), 7606–7617. DOI: 10.1021/bi400661a.

(25) McQuilken, A. C.; Jiang, Y.; Siegler, M. A.; Goldberg, D. P. Addition of Dioxygen to an N 4 S(Thiolate) Iron(II) Cysteine Dioxygenase Model Gives a Structurally Characterized Sulfinato–Iron(II) Complex. *J. Am. Chem. Soc.* **2012**, *134* (21), 8758–8761. DOI: 10.1021/ja302112y.

(26) Sahu, S.; Goldberg, D. P. Activation of Dioxygen by Iron and Manganese Complexes: A Heme and Nonheme Perspective. *J. Am. Chem. Soc.* **2016**, *138* (36), 11410–11428. DOI: 10.1021/jacs.6b05251.

(27) Harrop, T. C.; Mascharak, P. K. Fe(III) and Co(III) Centers with Carboxamido Nitrogen and Modified Sulfur Coordination: Lessons Learned from Nitrile Hydratase. *Acc. Chem. Res.* **2004**, *37* (4), 253–260. DOI: 10.1021/ar0301532.

(28) Lugo-Mas, P.; Taylor, W.; Schweitzer, D.; Theisen, R. M.; Xu, L.; Shearer, J.; Swartz, R. D.; Gleaves, M. C.; DiPasquale, A.; Kaminsky, W.; et al. Properties of Square-Pyramidal Alkyl-Thiolate FeIII Complexes, Including an Analogue of the Unmodified Form of Nitrile Hydratase. *Inorg. Chem.* **2008**, *47* (23), 11228–11236. DOI: 10.1021/ic801704n.

(29) Noveron, J. C.; Olmstead, M. M.; Mascharak, P. K. A Synthetic Analogue of the Active Site of Fe-Containing Nitrile Hydratase with Carboxamido N and Thiolato S as Donors: Synthesis, Structure, and Reactivities. *J. Am. Chem. Soc.* **2001**, *123* (14), 3247–3259. DOI: 10.1021/ja001253v.

(30) Heinrich, L.; Li, Y.; Vaissermann, J.; Chottard, Á.; Chottard, J.; Rene, Â. A Pentacoordinated Di- N -Carboxamido- Related to the Metal Site of Nitrile Hydratase. *Angew. Chemie - Int. Ed.* **1999**, *38* (23), 3526–3528. .

(31) McQuilken, A. C.; Goldberg, D. P. Sulfur Oxygenation in Biomimetic Non-Heme Iron-

Thiolate Complexes. *Dalton Trans.* **2012**, *41* (36), 10883–10899. DOI: 10.1039/c2dt30806a.

(32) Villar-Acevedo, G.; Lugo-Mas, P.; Blakely, M. N.; Rees, J. A.; Ganas, A. S.; Hanada, E. M.; Kaminsky, W.; Kovacs, J. A. Metal-Assisted Oxo Atom Addition to an Fe(III) Thiolate. *J. Am. Chem. Soc.* **2017**, *139* (1), 119–129. DOI: 10.1021/jacs.6b03512.

(33) Ellison, J. J.; Nienstedt, A.; Shoner, S. C.; Barnhart, D.; Cowen, J. A.; Kovacs, J. A. Reactivity of Five-Coordinate Models for the Thiolate-Ligated Fe Site of Nitrile Hydratase. *J. Am. Chem. Soc.* **1998**, *120* (23), 5691–5700. DOI: 10.1021/ja973129q.

(34) Blakely, M. N.; Dedushko, M. A.; Yan Poon, P. C.; Villar-Acevedo, G.; Kovacs, J. A. Formation of a Reactive, Alkyl Thiolate-Ligated Fe III -Superoxo Intermediate Derived from Dioxygen. *J. Am. Chem. Soc.* **2019**, *141* (5), 1867–1870. DOI: 10.1021/jacs.8b12670.

(35) Lugo-Mas, P. Synthetic Analogues of Cysteinate-Ligated Non-Heme Iron: Enzymes: Understanding the Structure-Function Relationship of Nitrile Hydratase (NHase) and Superoxide Reductase (SOR), University of Washington, 2007.

(36) Zhdankin, V. V.; Koposov, A. Y.; Litvinov, D. N.; Ferguson, M. J.; McDonald, R.; Luu, T.; Tykwinski, R. R. Esters of 2-Iodoxybenzoic Acid: Hypervalent Iodine Oxidizing Reagents with a Pseudobenziodoxole Structure. *J. Org. Chem.* **2005**, *70* (16), 6484–6491. DOI: 10.1021/jo051010r.

(37) Live, D. H.; Chan, S. I. Bulk Susceptibility Corrections in Nuclear Magnetic Resonance Experiments Using Superconducting Solenoids. *Anal. Chem.* **1970**, *42* (7), 791–792. DOI: 10.1021/ac60289a028.

(38) Evans, D. F. The Determination of the Paramagnetic Susceptibility of Substances in Solution by Nuclear Magnetic Resonance. *J. Chem. Soc.* **1959**, 2003–2005. DOI: 10.1039/jr9590002003.

(39) Watanabe, A.; Miyamoto, K.; Okada, T.; Asawa, T.; Uchiyama, M. Safer Synthesis of (Diacetoxyiodo)Arenes Using Sodium Hypochlorite Pentahydrate. *J. Org. Chem.* **2018**, *83*, 14262–14268. DOI: 10.1021/acs.joc.8b02541.

(40) Saltzman, H.; Sharefkin, J. G. IODOSOBENZENE. *Org. Synth.* **1963**, *43* (2), 60. DOI: 10.15227/orgsyn.043.0060.

(41) Sharefkin, J. G.; Saltzman, H. IODOSOBENZENE DIACETATE. *Org. Synth.* **1963**, *43*, 62. DOI: 10.15227/orgsyn.043.0062.

(42) Sharefkin, J. G.; Saltzman, H. IODOXYBENZENE. *Org. Synth.* **1963**, *43*, 65. DOI: 10.15227/orgsyn.043.0065.

(43) Hill, E. A.; Kelty, M. L.; Filatov, A. S.; Anderson, J. S. Isolable Iodosylarene and Iodoxyarene Adducts of Co and Their O-Atom Transfer and C-H Activation Reactivity. *Chem. Sci.* **2018**, *9* (19), 4493–4499. DOI: 10.1039/c8sc01167b.

(44) McGown, A. J.; Kerber, W. D.; Fujii, H.; Goldberg, D. P. Catalytic Reactivity of a Meso-N-Substituted Corrole and Evidence for a High-Valent Iron-Oxo Species. *J. Am. Chem. Soc.* **2009**, *131* (23), 8040–8048. DOI: 10.1021/ja809183z.

(45) Collman, J. P. Caution for Researchers Using PFIB. *Chem. Eng. News* **1985**, *63* (11), 2. DOI: 10.1021/cen-v063n011.p002.

(46) Armarego, W. L. F.; Chai, C. L. L. *Purification of Laboratory Chemicals*, 7th ed.;

Butterworth-Heinemann: London, 2013.

(47) Guidry, R. M.; Drago, R. S. Evaluation of the Thermodynamic Data Reported for the Reversible Oxygenation of the Amine Complexes of Cobalt(II) Protoporphyrin IX Dimethyl Ester. *J. Am. Chem. Soc.* **1973**, *95* (20), 6645–6648. DOI: 10.1021/ja00801a020.

(48) Drago, R. S.; Epley, T. D. Enthalpies of Hydrogen Bonding and Changes in Δv Oh for a Series of Adducts with Substituted Phenols. *J. Am. Chem. Soc.* **1969**, *91* (11), 2883–2890. DOI: 10.1021/ja01039a010.

(49) Stoll, S.; Schweiger, A. EasySpin, a Comprehensive Software Package for Spectral Simulation and Analysis in EPR. *J. Magn. Reson.* **2006**, *178* (1), 42–55. DOI: 10.1016/j.jmr.2005.08.013.

(50) Neese, F. The ORCA Program System. *WIREs Comput. Mol. Sci.* **2012**, *2*, 73–78. DOI: 10.1002/wcms.81.

(51) Becke, A. D. Density-Functional Exchange-Energy Approximation with Correct Asymptotic Behavior. *Phys. Rev. A* **1988**, *38* (6), 3098–3100. DOI: 10.1103/PhysRevA.38.3098.

(52) Perdew, J. P. Density-Functional Approximation for the Correlation Energy of the Inhomogeneous Electron Gas. *Phys. Rev. B* **1986**, *33* (12), 8822–8824. DOI: 10.1103/PhysRevB.33.8822.

(53) Weigend, F. Accurate Coulomb-Fitting Basis Sets for H to Rn. *Phys. Chem. Chem. Phys.* **2006**, *8* (9), 1057–1065. DOI: 10.1039/b515623h.

(54) Grimme, S.; Ehrlich, S.; Goerigk, L. Effect of the Damping Function in Dispersion

Corrected Density Functional Theory. *J. Comput. Chem.* **2011**, *32* (7), 1456–1465. DOI: 10.1002/jcc.21759.

(55) Van Lenthe, E.; Van Der Avoird, A.; Wormer, P. E. S. Density Functional Calculations of Molecular Hyperfine Interactions in the Zero Order Regular Approximation for Relativistic Effects. *J. Chem. Phys.* **1998**, *108* (12), 4783–4796. DOI: 10.1063/1.475889.

(56) Weigend, F.; Ahlrichs, R. Balanced Basis Sets of Split Valence, Triple Zeta Valence and Quadruple Zeta Valence Quality for H to Rn: Design and Assessment of Accuracy. *Phys. Chem. Chem. Phys.* **2005**, *7* (18), 3297–3305. DOI: 10.1039/b508541a.

(57) Klamt, A.; Schüürmann, G. COSMO: A New Approach to Dielectric Screening in Solvents with Explicit Expressions for the Screening Energy and Its Gradient. *J. Chem. Soc. Perkin Trans. 2* **1993**, No. 5, 799–805. DOI: 10.1039/P29930000799.

(58) Bruker. APEX2 (Version 2.1-4), SAINT (Version 7.34A), SADABS (Version 2007/4). BrukerAXS Inc: Madison 2007.

(59) Altomare, A.; Cascarano, G.; Giacovazzo, C.; Guagliardi, A.; Burla, M. C.; Polidori, G.; Camalli, M. SIR 92 – a Program for Automatic Solution of Crystal Structures by Direct Methods. *J. Appl. Crystallogr.* **1994**, *27* (3), 435–435. DOI: 10.1107/S002188989400021X.

(60) Altomare, A.; Burla, M. C.; Camalli, M.; Cascarano, G. L.; Giacovazzo, C.; Guagliardi, A.; Moliterni, A. G. G.; Polidori, G.; Spagna, R. SIR97: A New Tool for Crystal Structure Determination and Refinement. *J. Appl. Crystallogr.* **1999**, *32* (1), 115–119. DOI: 10.1107/S0021889898007717.

(61) Sheldrick, G. M. SHELXL-97, Program for the Refinement of Crystal Structures.

University of Göttingen, Germany. 1997.

(62) Sheldrick, G. M. Crystal Structure Refinement with SHELXL. *Acta Crystallogr. Sect. C Struct. Chem.* **2015**, *71* (Md), 3–8. DOI: 10.1107/S2053229614024218.

(63) Burnett, M. N.; Johnson, C. K. ORTEP-III: Oak Ridge Thermal Ellipsoid Plot Program for Crystal Structure Illustrations. Oak Ridge National Laboratory Report ORNL-6895 1996.

(64) Persistence of Vision Raytracer. Persistence of Vision Pty. Ltd.: Williamstown, Victoria, Australia 2004.

(65) Downing, A. Unpublished Work.

(66) Addison, A. W.; Rao, T. N.; Reedijk, J.; van Rijn, J.; Verschoor, G. C. Synthesis, Structure, and Spectroscopic Properties of Copper(II) Compounds Containing Nitrogen–Sulphur Donor Ligands; the Crystal and Molecular Structure of Aqua[1,7-Bis(N-Methylbenzimidazol-2′-Yl)-2,6-Dithiaheptane]Copper(II) Perchlorate. *J. Chem. Soc., Dalt. Trans.* **1984**, No. 7, 1349–1356. DOI: 10.1039/DT9840001349.

(67) Lennartson, A.; McKenzie, C. J. An Iron(III) Iodosylbenzene Complex: A Masked Non-Heme Fe(V)O. *Angew. Chemie - Int. Ed.* **2012**, *51* (27), 6767–6770. DOI: 10.1002/anie.201202487.

(68) Hong, S.; Wang, B.; Seo, M. S.; Lee, Y. M.; Kim, M. J.; Kim, H. R.; Ogura, T.; Garcia-Serres, R.; Clémancey, M.; Latour, J. M.; et al. Highly Reactive Nonheme Iron(III) Iodosylarene Complexes in Alkane Hydroxylation and Sulfoxidation Reactions. *Angew. Chemie - Int. Ed.* **2014**, *53* (25), 6388–6392. DOI: 10.1002/anie.201402537.

(69) de Oliveira, F. T.; Chanda, A.; Banerjee, D.; Shan, X.; Mondal, S.; Que, L.; Bominaar, E.

L.; Munck, E.; Collins, T. J. Chemical and Spectroscopic Evidence for an FeV-Oxo Complex. *Science.* **2007**, *315* (5813), 835–838. DOI: 10.1126/science.1133417.

(70) Prat, I.; Mathieson, J. S.; Güell, M.; Ribas, X.; Luis, J. M.; Cronin, L.; Costas, M. Observation of Fe(V)=O Using Variable-Temperature Mass Spectrometry and Its Enzyme-like C–H and C=C Oxidation Reactions. *Nat. Chem.* **2011**, *3* (10), 788–793. DOI: 10.1038/nchem.1132.

(71) McDonald, A. R.; Que, L. Iron–Oxo Complexes: Elusive Iron(V) Species Identified. *Nat. Chem.* **2011**, *3* (10), 761–762. DOI: 10.1038/nchem.1153.

(72) Kundu, S.; Thompson, J. V. K.; Ryabov, A. D.; Collins, T. J. On the Reactivity of Mononuclear Iron (V) Oxo Complexes. *J. Am. Chem. Soc.* **2011**, *133* (46), 18546–18549. DOI: 10.1021/ja208007w.

(73) Kang, Y.; Li, X.; Cho, K.; Sun, W.; Xia, C.; Nam, W.; Wang, Y. Mutable Properties of Nonheme Iron(III)–Iodosylarene Complexes Result in the Elusive Multiple-Oxidant Mechanism. *J. Am. Chem. Soc.* **2017**, *139* (22), 7444–7447. DOI: 10.1021/jacs.7b03310.

(74) Van Heuvelen, K. M.; Fiedler, a. T.; Shan, X.; De Hont, R. F.; Meier, K. K.; Bominaar, E. L.; Munck, E.; Que, L. One-Electron Oxidation of an Oxoiron(IV) Complex to Form an [OboxHFeVboxHNR]+ Center. *Proc. Natl. Acad. Sci.* **2012**, *109* (30), 11933–11938. DOI: 10.1073/pnas.1206457109.

(75) Coleman, E. H.; Gaydon, A. G.; Vaidya, W. M. Spectrum of Iodine Oxide(IO) in Flames. *Nature* **1948**, *162*, 108–109. DOI: 10.1038/162108b0.

(76) Bach, R. D.; Ayala, P. Y.; Schlegel, H. B. A Reassessment of the Bond Dissociation

Energies of Peroxides. An Ab Initio Study. *J. Am. Chem. Soc.* **1996**, *118* (50), 12758–12765. DOI: 10.1021/ja961838i.

(77) Hong, S.; Gupta, A. K.; Tolman, W. B. Intermediates in Reactions of Copper(I) Complexes with N-Oxides: From the Formation of Stable Adducts to Oxo Transfer. *Inorg. Chem.* **2009**, *48* (14), 6323–6325. DOI: 10.1021/ic900435p.

(78) Shaofeng, L.; Pilcher, G. Enthalpy of Formation of Pyridine- the Dissociation Enthalpy of the (N-O) Bond. *J. Chem. Thermodyn.* **1988**, No. 20, 436–465. .

(79) Cho, K. Bin; Moreau, Y.; Kumar, D.; Rock, D. A.; Jones, J. P.; Shaik, S. Formation of the Active Species of Cytochrome P450 by Using Iodosylbenzene: A Case for Spin-Selective Reactivity. *Chem. - A Eur. J.* **2007**, *13* (14), 4103–4115. DOI: 10.1002/chem.200601704.

(80) Gustafsson, J.-Å.; Bergman, J. Iodine- and Chlorine-Containing Oxidation Agents as Hydroxylating Catalysts in Cytochrome P -450-Dependent Fatty Acid Hydroxylation Reactions in Rat Liver Microsomes. *FEBS Lett.* **1976**, *70* (1–2), 276–280. DOI: 10.1016/0014-5793(76)80774-0.

(81) Puri, M.; Company, A.; Sabenya, G.; Costas, M.; Que, L. Oxygen Atom Exchange between H2O and Non-Heme Oxoiron(IV) Complexes: Ligand Dependence and Mechanism. *Inorg. Chem.* **2016**, *55* (12)DOI: 10.1021/acs.inorgchem.6b00023.

(82) Nam, W.; Valentine, J. S. Reevaluation of the Significance of 18O Incorporation in Metal Complex-Catalyzed Oxygenation Reactions Carried out in the Presence of H218O. *J. Am. Chem. Soc.* **1993**, *115* (5), 1772–1778. DOI: 10.1021/ja00058a023.

(83) Song, W. J.; Sun, Y. J.; Choi, S. K.; Nam, W. Mechanistic Insights into the Reversible

Formation of Iodosylarene-Iron Porphyrin Complexes in the Reactions of Oxoiron(IV) Porphyrin π-Cation Radicals and Iodoarenes: Equilibrium, Epoxidizing Intermediate, and Oxygen Exchange. *Chem. - A Eur. J.* **2006**, *12* (1), 130–137. DOI: 10.1002/chem.200500128.

(84) Nam, W.; Choi, S. K.; Lim, M. H.; Rohde, J.; Kim, I.; Kim, J.; Kim, C.; Que, L. Reversible Formation of Iodosylbenzene±Iron Porphyrin Intermediates in the Reaction of Oxoiron(IV) Porphyrin p-Cation Radicals and Iodobenzene. *Angew. Chemie - Int. Ed.* **2003**, *42*, 109–111. DOI: 10.1002/anie.200390036.

(85) Guo, M.; Dong, H.; Li, J.; Cheng, B.; Huang, Y.; Feng, Y.; Lei, A. Spectroscopic Observation of Iodosylarene Metalloporphyrin Adducts and Manganese(V)-Oxo Porphyrin Species in a Cytochrome P450 Analogue. *Nat. Commun.* **2012**, *3* (V), 1190. DOI: 10.1038/ncomms2196.

(86) Macikenas, D.; Skrzypczak-Jankun, E.; Protasiewicz, J. D. Redirecting Secondary Bonds To Control Molecular and Crystal Properties of an Iodosyl- and an Iodylbenzene. *Angew. Chemie Int. Ed.* **2000**, *39* (11), 2007–2010. DOI: 10.1002/1521-3773(20000602)39:11<2007::AID-ANIE2007>3.0.CO;2-Z.

(87) Wang, B.; Lee, Y. M.; Seo, M. S.; Nam, W. Mononuclear Nonheme Iron(III)-Iodosylarene and High-Valent Iron-Oxo Complexes in Olefin Epoxidation Reactions. *Angew. Chemie - Int. Ed.* **2015**, *54* (40), 11740–11744. DOI: 10.1002/anie.201505796.

(88) Shearer, J.; Nehring, J.; Lovell, S.; Kaminsky, W.; Kovacs, J. A. Modeling the Reactivity of Superoxide Reducing Metalloenzymes with a Nitrogen and Sulfur Coordinated Iron Complex. *Inorg. Chem.* **2001**, *40* (22), 5483–5484. DOI: 10.1021/ic010221l.

(89) Ortiz De Montellano, P. R. Hydrocarbon Hydroxylation by Cytochrome P450 Enzymes. *Chem. Rev.* **2010**, *110* (2), 932–948. DOI: 10.1021/cr9002193.

(90) McDonald, A. R.; Que, L. High-Valent Nonheme Iron-Oxo Complexes: Synthesis, Structure, and Spectroscopy. *Coord. Chem. Rev.* **2013**, *257* (2), 414–428. DOI: 10.1016/j.ccr.2012.08.002.

Chapter 5. Modification and Synthesis of Anionic Ligand Systems

5.1 Introduction

The understanding of dioxygen derived intermediates and the role they play in catalytic cycles of metalloenzymes has been aided by the characterization of small molecule intermediate analogues. Cysteinate ligated non-heme Fe enzymes like NHase, CDO and IPNS, all are proposed to use dioxygen derived oxidants such as Fe-superoxo, Fe-peroxo, or Fe-oxos. However, there are very few well-characterized biological[1,2] or synthetic models of such thiolate ligated species.[3–8] Since thiolates have been predicted to lower the activation barrier to O_2 binding and enhance reactivity,[9–12] an emphasis on synthesizing model complexes is a promising approach to further understand the properties thiolates impart on enzymatic intermediates.

Structural modifications on synthetic models can impact reactivity, stability and ability to isolate additional dioxygen intermediates.[13] The previously reported, $[Fe^{III}(S_2{}^{Me2}N^{Me}N_2{}^{amide}(Pr,Pr)]^{1-}$ (**8**) (Figure 5.1), is a five coordinate, anionic complex that is inert, even in an excess (>100 eq.) of anionic, neutral or/and σ-donor ligands binding is not observed.[14] The spin-state of **8** was found to be $S = 3/2$ from magnetic susceptibility measurements.[14] The intermediate spin-state may be one reason for the lack of reactivity since six-coordinate thiolate complexes prefer a ground state of $S = 1/2$,[15–18] therefore a spin-state change may be required to bind an additional ligand. This lack of reactivity has been observed with other intermediate-spin ($S = 3/2$) five coordinate thiolate complexes derived from tripodal amines regardless of overall charge.[19] Removal of the methyl group from the backbone to form $[Fe^{III}(S_2{}^{Me2}N^{H}N_2{}^{amide}(Pr,Pr)]^{1-}$ (**11**) (Figure 5.2), will may eliminate two factors that are hindering ligand binding. The complex,

$[Fe^{III}(S_2{}^{Me2}N_3(Pr,Pr)]^+$ (**2**), is in a low-spin state but with the addition of a methyl group on the amine in the backbone, the spin state was found to be in a majority high-spin state with a thermally accessible low-spin state.[20,21] Steric hinderance may be another reason for the lack of reactivity of **8**. Removal of the methyl group from the backbone to form $[Fe^{III}(S_2{}^{Me2}N^{H}N_2{}^{amide}(Pr,Pr)]^{1-}$ (**11**) (Figure 5.2), will decrease the steric hinderance of the opening of the S(2)-Fe-N(2) bond angle to accommodate ligand binding. Since reactivity with dioxygen or oxo-atom donors correlates with the metal ion's ability to bind additional ligands, a synthetic route to potentially tune the spin-state and reduce steric hinderance is investigated.

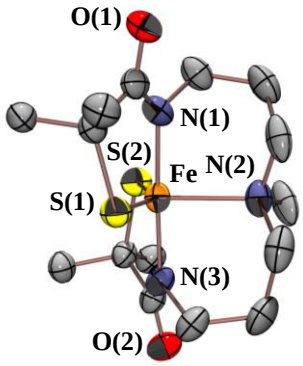

Figure 5.1. Displacement ellipsoid plots of $[Fe^{III}(S_2{}^{Me2}N^{Me}N_2{}^{amide}(Pr,Pr)]^{1-}$ (**8**) with thermal ellipsoids at the 50% probability level. The disorder, cation and hydrogen atoms have been removed for clarity.[14]

Coordinately unsaturated Fe-complexes with bulky anionic ligands may produce biomimetic models capable of stabilizing mononuclear Fe-superoxo and Fe-peroxo intermediates. The novel bis(diisopropylphenyl)aminothiolate) (BDAT) (**12**) ligand was designed to modulate the steric bulk and electronics with the goal to isolate dioxygen derived intermediates. The

proposed $[Fe^{II}(BDAT)]^{1-}$ (**13**) ligand's steric bulk is in the form of isopropyl groups on the amido phenyl rings and aims to inhibit dimerization (Figure 5.2). This approach has seen success with the isopropyl groups in the β-diketiminate ligated copper dioxygen intermediates.[22–25] Additionally coordinately unsaturated metal centers are more Lewis acidic and therefore less likely to cleave the O-O bond thus stabilizing the superoxo or peroxo intermediates.[26] The covalent nature of the Fe-SR bond helps maintain a low coordination number[27,28] and promotes O_2 and $O_2^{\bullet-}$ binding.[29] These important features of **13** will potentially allow for isolation of vital intermediates with intact O-O bonds for the understanding of enzymatic activity.

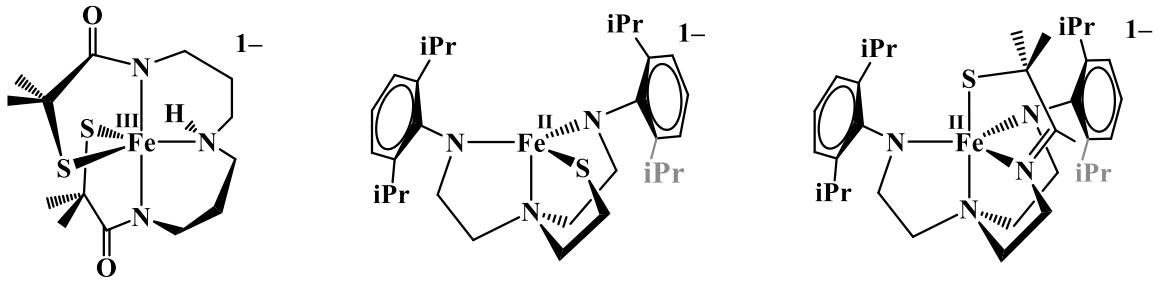

Figure 5.2. Proposed anionic complexes, $[Fe^{III}(S_2{}^{Me2}N^{H}N_2{}^{amide})(Pr,Pr)]^{1-}$ (**11**), $[Fe^{II}(BDAT)]^{1-}$ (**13**) and $[Fe^{II}(S^{Me2}N_4(tren\text{-}dipp_{amide})]^{1-}$ (**14**).

A ligand scaffold designed to isolate a high valent Fe-oxo would also require steric bulk and an electronic rich environment but does not require the low coordination number. For the proposed $[Fe^{II}(S^{Me2}N_4(tren\text{-}dipp_{amide})]^{1-}$ (**14**) complex (Figure 5.2), the same bulky diisopropylphenyl groups can be used hinder dimerization in a five-coordinate ligand. An alkyl-

thiolate can be incorporated using a similar method to a number of complexes used our group including **1** and **2** described above. Anionic environments have been shown to stabilize high valent Fe-oxo complexes with oxidation states of 3+ to 5+.[30–35] The proposed complex **14** incorporates steric bulk and an anionic environment for the goal of isolating a high valent Fe-oxo with a thiolate coordinated, of which there is only one reported example.[6] Described herein is the synthesis of several anionic ligands and progress towards metallation.

5.2 Experimental

General Methods. All manipulations were performed using standard Schlenk techniques or under N_2 atmosphere in a glovebox. Reagents and solvents were purchased from commercial vendors, were of the highest available purity, and were used without further purification unless otherwise noted. Methanol (MeOH) was distilled over calcium hydride and degassed prior to use. Diethyl ether and acetonitrile were purchased from Sigma-Aldrich and purified using solvent purification columns housed in a custom stainless-steel cabinet and dispensed by a stainless steel schlenk-line (GlassContour). The synthesis of *tert*-butyl bis(3-aminopropyl)carbamate (**19**),[36] 2-(2,6-diisopropylphenylamino)ethanol (**24**),[37] 1-(*tert*-butyloxycarbonyl)ethyldiamine (**29**),[38] and 3-methyl-3-mercapto-2-butanone (**31**)[5] were carried out according to published procedures.

^{1}H NMR spectra were obtained on a Bruker AV300 or AV301 spectrometers. Chemical shifts are listed in parts per million and were reported relative to TMS by referencing the residual solvent. Electrospray ionization mass spectroscopy were performed on a Bruker Esquire Liquid Chromograph-Ion Trap mass spectrometer. UV/vis spectra were recorded on a Varian Cary 50 spectrophotometer equipped with a fiber optic cable connected to a “dip” ATR probe (C-

technologies). A custom-built two-neck solution sample holder equipped with a threaded glass connector was sized specifically to fit the "dip" probe.

Synthesis of 2-benzyl-2-methyl propionic acid (18). Adapted from [14] To a stirred solution of ethyl 2- bromo-2-methyl propionate (**16**) (15.0 mL, 102.5 mmol) in EtOH (34.0 mL) was added NaOMe (5.5 g, 102.5 mmol) followed by benzyl mercaptan (**17**) (12.0 mL, 102.2 mmol). After stirring at 90 °C for 3.5 h, NaOH (5.3 g, 133.3 mmol) was added. The solution was filtered, and the solid recovered was washed with the minimum amount of EtOH. The solid was dried under vacuum then dissolved in H_2O (25 mL), and concentrated HCl was added dropwise until the solution reached pH = 2. After filtration, the solid was dried in vacuo overnight to afford **18** (17.3 g, 81.2, 80%) as a white powder. ^{1}H NMR (CDCl3, 301 MHz): δ 7.35-7.32 (m, 5H), 3.93 (s, 2H), 1.60 (s, 6H). ESI-MS calculated for $[C_{11}H_{14}O_2S+ Na]^+$: 233.3, found 233.0.

Synthesis of *N*-(2-benzylthiol-2-methylpropanone)-*N*-[3-(2-benzylthiol-2-methylpropanone) propyl]-*N*-[3-(*tert*-butyloxycarbonyl)]-1,3-propanediamine ($Bn_2S_2^{Me2}NBoc(HN)_2^{amide}$(Pr,Pr)) (20). To a stirred solution of 2-benzyl-2-methyl propionic acid (**18**, 4.664 g, 22.2 mmol) in DCM (20 mL), placed in an ambient temperature H_2O bath, was added thionyl chloride (3.55 mL, 49.0 mmol). After 30 mins, the excess thionyl chloride was removed under vacuum. The crude acid chloride derivative, 2-benzylsulfanyl-2-methyl-propionyl chloride, was used immediately in the next step without further purification.

To a stirred solution of 2-benzyl-sulfanyl-2-methyl propionyl chloride in acetone (25 mL) at ambient temperature was added Et_3N (4.22 mL, 30 mmol) followed by *tert*-butyl bis(3-aminopropyl)carbamate (**19**, 2.31 g, 10.0 mmol). After stirring for 6 hours, saturated aqueous

NH_4Cl (20 mL) was added and solvent removed under vacuum. The remaining solid was dissolved in 20 mL of DI H_2O. The aqueous layer was extracted with Et_2O (3 x 20 mL). The combined organic layers were washed with H_2O and brine (20 mL each), dried over Na_2SO_4, and concentrated *in vacuo* to yield **20** (1.848 g, 3.0 mmol, 30.0%) as a yellow oil. ESI-MS of **20**: expected *m/z* for $C_{33}H_{50}N_3O_4S_2$ = 616.3, found *m/z* = 617.4.

Synthesis of *N*-(2-thiol-2-methylpropanone)-*N*-[3-(2-thiol-2-methylpropanone)propyl]-*N*-[3-(*tert*-butyloxycarbonyl)]-1,3-propanediamine ($(HS^{Me2})_2NBoc(HN)_2^{amide}(Pr,Pr)$) (21) and *N*-(2-thiol-2-methylpropanone)-*N*-[3-(2-thiol-2-methylpropanone)propyl]-1,3-propanediamine hydrochloride $(HS^{Me2})_2NH(HN)_2^{amide}(Pr,Pr)$ hydrochloride (15) . To a stirred solution of liquid ammonia (~50 mL), sodium metal (200 mg) was added to afford an intense blue solution. To this blue solution was added 1 mL aliquots of a solution of **20** (1.848 g, 3.0 mmol) dissolved in diethyl ether (12 mL). Additional sodium was periodically added in small proportions to maintain the deep blue color of the solution. The completion of the reaction was assumed once the solution maintained its deep blue color for more than 30 min. The reaction was quenched with NH_4Cl (200 mg), and the remaining liquid ammonia was evaporated under a stream of N_2. The resulting solid (**19**) was dissolved in MeOH (15 mL), and conc. HCl was then added until the solution reached a pH = 2 and allowed to stir overnight. The solution was concentrated in vacuo, the solid was obtained and redissolved in CH_3CN (15 mL), then filtered and the solvent evaporated under reduced pressure to afford a "light brown glassy paste". Trituration was Et_2O yield **15** (0.643 g, 1.9 mmol, 63%) as a white powder. ESI-MS of **21**: expected *m/z* for $C_{19}H_{37}N_3O_4S_2$ = 435.2, found *m/z* = 434.4. ESI-MS of **15**: expected *m/z* for $C_{14}H_{30}N_3O_2S_2$ = 336.2, found *m/z* = 336.3.

Synthesis of *N*-(2-iodothyl)-2,6-bis(1-methylethyl)-hydrochloride (25). To a stirring solution of triphenylphosphine (11.62 g, 44.33 mmol) in dry methylene chloride (330 mL) was added iodine (11.24 g, 44.33 mmol) and imidazole (3.01g, 44.33 mmol) at 0 ℃. The resulting solution was allowed to stir for 10 mins. A solution of 2-(2,6-diisopropylphenylamino)ethanol **24** in dry methylene chloride (100 mL) was then added to the reaction mixture and allowed to stir for 30 mins. The reaction mixture was then quenched with sat. aqueous $Na_2S_2O_3$ solution (150 mL). The organic layer was separated and washed with brine and then dried over $MgSO_4$. Solvent was removed under reduced pressure. The solid residue was dissolved in a minimal amount of diethyl ether. The insoluble excess triphenylphosphine and by-product triphenylphosphine oxide were filtered off through a Buchner funnel, and the solvent of the filtrate was removed under reduced pressure. This was repeated one additional time. The solid residue was fully dissolved in 20 mL of diethyl ether and 22.15 mL of 2.0 M hydrochloric acid in diethyl ether was added dropwise. This mixture was then allowed to stir for 15 mins. The resultant solid was filtered and washed with diethyl ether, and then dried to obtain a pale yellow crystalline solid (9.99 g, 92 %). ^{1}H NMR (300 MHz, $CDCl_3$) δ 11.2 (br, 2 H), 7.39 (m 1 H), 7.25 (m, 2 H), 3.64-3.83 (m, 4 H), 3.59 (sep, 2 H), 1.33 (d, J = 6.6 Hz, 12 H).

Synthesis of *N*-(2,6-diisopropylphenyl)-*N*-[2-(2,6-diisopropylphenyl)amino]ethyl]-*N*-[2-(phenylthio)ethyl]-1,2-ethanediamine (Bn-BDAT 27). *S*-benzyl-cysteamine hydrochloride **26** (2.07g, 10.15 mmol) was dissolved in 5 M NaOH solution (100 mL) and added dropwise to a stirring solution of **25** (7.47g, 20.3 mmol) dissolved in 5 M NaOH (200 mL) and methanol (100 mL). The resulting mixture was stirred for four days at room temperature. The aqueous solution was then extracted with dichloromethane (2 x 100 mL), washed with brine (1 x 100 mL), and then

dried over Na_2SO_4. Solvent was removed under vacuum to yield a light orange oil (5.24 g, 90%). ^{1}H NMR (300 MHz, $CDCl_3$) δ 7.67 (m, 2 H), 7.49 (m, 3 H), 7.10 (m, 6 H), 3.84 (m, 4 H), 3.71 (s, 2 H), 3.31 (hept, 4 H), 3.05 (m, 4 H), 2.83 (t, *J* = 6.3 Hz, 2 H), 2.53 (t, *J*=6.2 2 H), 1.25 (d, *J*=6.67 Hz, 24 H). ESI-MS: expected *m/z* for $C_{37}H_{55}N_3S$ = 573.41, found *m/z* = 574.8.

Synthesis of *N*-(2,6-diisopropylphenyl)-*N*-[2-(2,6-diisopropylphenyl)amino]ethyl]-*N*-[2-thioethyl]-1,2-ethanediamine (BDAT 12). To a stirred solution of liquid ammonia (50 mL) cooled to -78°C, was added sodium metal (180 mg). The benzyl-protected **27** (2.50 g, 4.36 mmol) was dissolved in dry diethyl ether (~5 mL) added in small aliquots (<0.5 mL). Additional sodium metal was periodically added in small proportions to maintain a deep blue color. The completion of the reaction was assumed once the solution maintained its deep blue color for more than 1 h. Ammonium chloride was added until the solution changed from blue to yellow, thus quenching the sodium. The liquid ammonia was evaporated under a stream of N_2. The diethyl ether was removed under vacuum. A minimal amount of DI H_2O was added, and the solution was acidified with 37% HCl until the reaction reached a pH of 2. Extract the organics with DCM (2 x 20 mL). The organics were then dried with Na_2SO_4 and the volatiles were removed to afford **12** as a clear oil (1.70, 81% yield). ^{1}H NMR (300 MHz, $CDCl_3$) δ 7.67 (m, 2 H), 7.49 (m, 3 H), 7.10 (m, 6 H), 3.84 (m, 4 H), 3.71 (s, 2 H), 3.31 (hept, 4 H), 3.05 (m, 4 H), 2.83 (m, 2 H), 2.53 (t, *J* = 6.2 Hz, 2 H), 1.25 (d, *J* = 6.9 Hz, 24 H). ESI-MS: expected *m/z* for $C_{30}H_{49}N_3S$ = 483.36, found *m/z* = 484.6.

Synthesis of *N*-(2,6-diisopropylphenyl)-*N*-[2-(2,6-diisopropylphenyl)amino]ethyl]-*N*-[2-ethylamino-Boc]-1,2-ethanediamine (30). Mono boc-protected ethylene diamine (NNBoc, **29**) (0.80g, 5.02 mmol) was dissolved in 5 M NaOH solution (100 mL) and added dropwise to a stirring

solution of **25** (3.69 g, 10.04 mmol) dissolved in 5 M NaOH (200 mL) and methanol (100 mL). The resulting mixture was stirred for four days at room temperature. The aqueous solution was then extracted with dichloromethane (2 x 100 mL), washed with brine (1 x 100 mL), and then dried over Na_2SO_4. Solvent was removed under vacuum to yield a clear oil (2.48 g, 87% yield). ^{1}H NMR (300 MHz, $CDCl_3$) δ7.67-7.49 (m, 2 H), 7.06 (m, 4 H), 3.57 (m, 4 H), 3.08 (m, 4 H), 2.79 (m, 4 H), 1.45 (s, 9 H), 1.25 (d, *J*=6.70 Hz, 24 H). ESI-MS: expected *m/z* for $C_{35}H_{58}N_4O_2$ = 566.46, found *m/z* = 567.5.

Synthesis of *N*-(2,6-diisopropylphenyl)-*N*-[2-(2,6-diisopropylphenyl)amino]ethyl]-*N*-[2-ethylamino]-1,2-ethanediamine (N_4(tren-dipp$_{amine}$) (28). Boc-protected **30** (2.46 g, 4.39 mmol) was dissolved in dichloromethane and cooled to 0°C. Excess trifluoroacetic acid (20 mL) was added to the reaction mixture. The stirring solution was allowed to warm to room temperature. The reaction stirred until complete monitored by TLC (~2 h.). Solvent was removed under vacuum. 5 M NaOH was added and the product was extracted with dichloromethane. The product was washed with brine and dried over Na_2SO_4. Solvent was removed under vacuum the resulting clear oil was purified by silica gel column chromatograph (92:8 acetone:methanol) to yield 81%. ^{1}H NMR (300 MHz, $CDCl_3$) δ7.04 (m, 6 H), 3.58 (m, 4 H), 3.42-3.28 (m, 8 H), 3.06 (m, 2 H), 1.24 (d, *J*=6.86, 24H). ESI-MS: expected *m/z* for $C_{30}H_{49}N_4$ = 466.40, found *m/z* = 467.3.

Synthesis of [Fe^{II}($S^{Me2}N_4$(tren-dipp$_{amide}$)]$^{1+}$ (32). Sodium methoxide (0.0.021 g, 0.4 mmol), 3-mercapto-3-methyl-2-butanone (**31**) (0.15 g, 0.4 mmol), and (N_4(tren-dipp$_{amide}$)(**28**) (0.18 g, 0.4 mmol) were combinded and dissolved in MeOH (10 ml) in a drybox. The resulting mixture was allowed to stir at room temperature for another 30 min. This solution was then added dropwise to

a solution of $FeCl_2$ (0.05 g, 0.4 mmol) in 5 ml of MeOH and a stir-bar. This mixture was allowed to stir at room temperature overnight. Sodium hexafluorophosphate (0.07 g, 0.4 mmol) was dissolved in MeOH was added and allowed to stir for an additional day. The reaction mixture was filtered through a bed of celite and the solvent removed under vacuum. The solid was redissolved in a minimal amount of DCM (~4 ml) and layered with pentane (~16 ml). ESI-MS: calculated for $[C_{35}H_{56}FeN_4S+Na]^{2+}$ m/z = 321.7, found *m/z* = 322.3.

5.3 Results and Discussion

5.3.1 *Synthesis of the $(HS^{Me2})_2NH(HN^{amide})_2$(Pr,Pr)•HCl Ligand and Metallation Attempts*

A new synthetic route to make the unmethylated $(HS^{Me2})_2NH(HN^{amide})_2$(Pr,Pr)•HCl (**15**) ligand was pursued starting with the synthesis of *tert*-butyl bis(3-aminopropyl)carbamate (**19**) (Figure 5.3).[39] Selectively protecting a secondary amine is not an arbitrary synthesis. First, the primary amines must be selectively protected, then a Boc-protecting group may be placed on the secondary amine, followed by selective removal of the primary amine protecting groups yielding the desired **16**. Ethyl trifluoroacetate was used as a source of trifluoroacetate which selectively protects primary amines because it forms a salt with the secondary amine (Figure 5.3). This method proved more successful with higher yields (95%) than other methods attempted.[40,41]

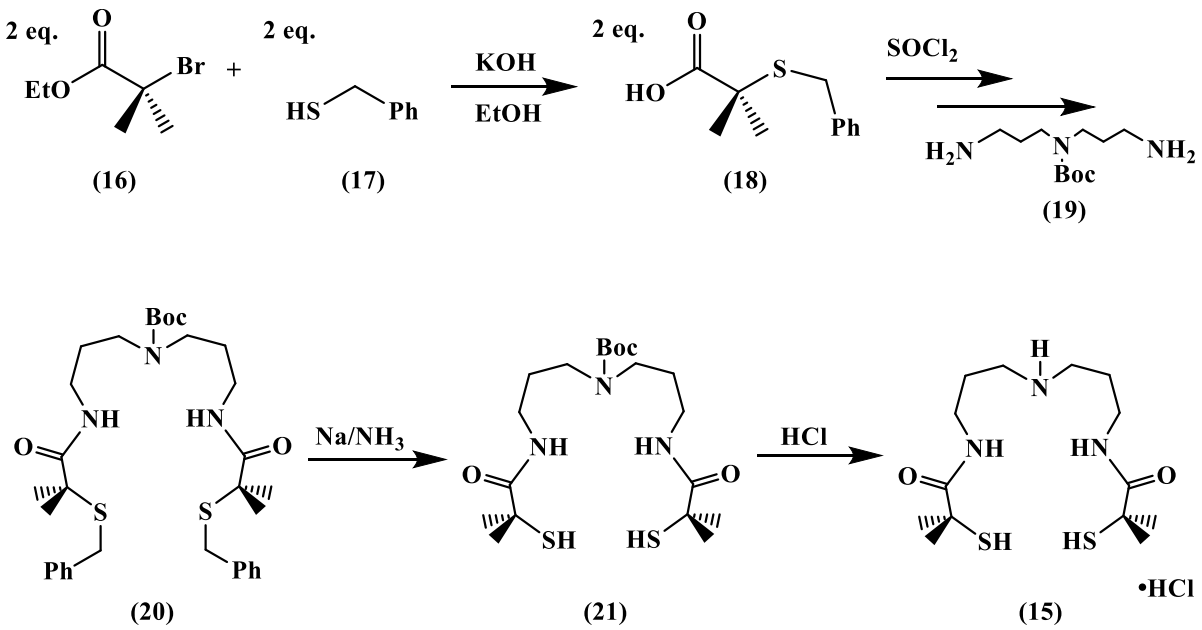

Figure 5.3. Synthetic Route to $(HS^{Me2})_2NH(HN^{amide})_2(Pr,Pr)$•HCl (**15**)

The following alkylation of **17** with two equivalents of 2-benzyl-2-methyl propionic acid (**16**) was based off of the previous ligand synthesis with a few additional considerations.[14] The acid chloride derivative of **18** is generated in situ and used immediately in the alkylation, this requires the use of thionyl chloride. This reagent is capable of removing the Boc-protecting group from the amine backbone. In order to avoid this, solvent and any residual thionyl chloride was removed under vacuum, then acetone was added followed by base (Et_3N) before the addition of **19**. The ^1H NMR and ESI-MS spectra showed that the removal of additional thionyl chloride and the order of addition of the reagents prevented the early removal of the Boc-group which would have resulted in potential mix of over-and under-alkylated species in addition to **19**. Overall the carboxamide ligand without the methyl (**15**) was synthesized, compounds the stepwise removal of protecting groups of **20** to produce **21** then **15** is confirmed by ESI-MS spectra (Figure 5.4).

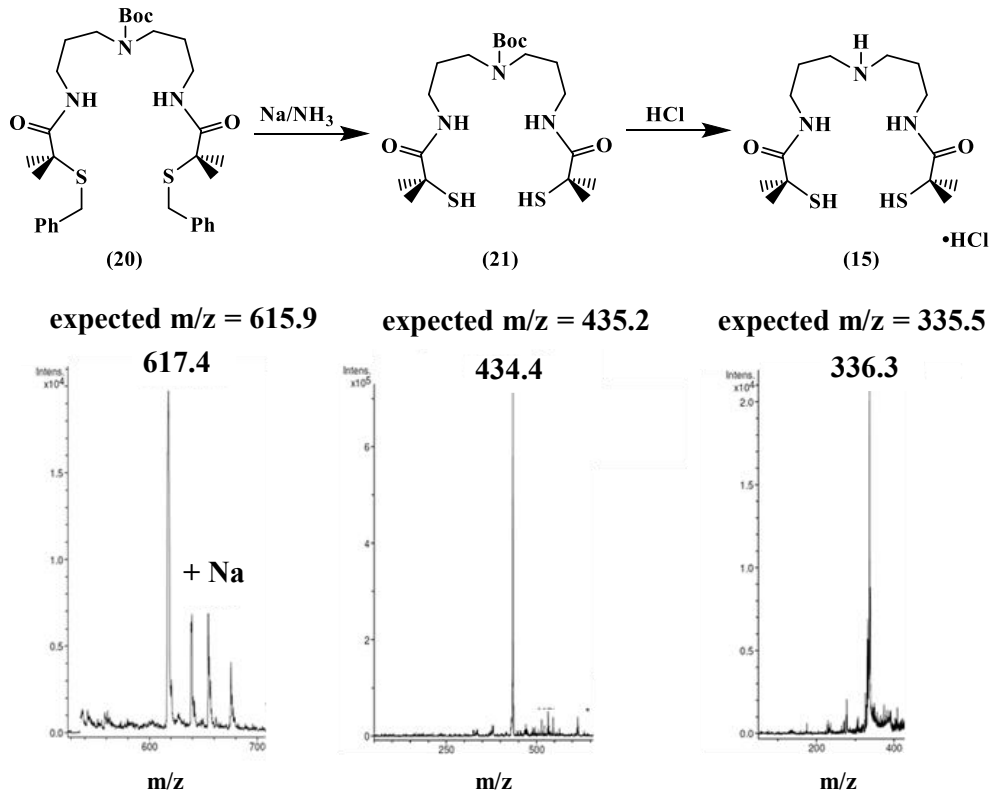

Figure 5.4. The stepwise removal of the protecting grouping on **20** to produce the final product **15**.

Coordination of $(HS^{Me2})_2NH(HN^{amide})_2(Pr,Pr)$•HCl (**15**) to an Fe^{3+} ion has been attempted following the procedure for $[Fe^{III}(S_2{}^{Me2}N^{Me}N_2{}^{amide}(Pr,Pr)]^{1-}$ (**8**).[14] The reaction of $FeCl_3$ and $(S_2{}^{Me2}N^{H}N_2{}^{amide})(Pr,Pr)$ produced a deep blue green reaction mixture similar to the dark green color observed for the formation of **8**. Upon the addition of sodium methoxide, the solution turned a cloudy light brown. This change may be due to methoxide binding and or an auto-reduction producing the Fe^{II} species that have charge transfer bands in the UV instead of visible spectrum. The former may be avoided by using a non-coordinating base such as *N*,*N*-diisopropylethylamine (Hünig's base). No microcrystalline salt of the desired complex **11** has been recovered.

5.3.2 *Synthesis of the BDAT and N_4(tren-dipp$_{amide}$) Ligands and Metallation Attempts*

The synthesis of **12** was accomplished through a four-step procedure (Figure 5.5). Modification to the reported procedure for the synthesis of *N*-(2-iodoethyl)-2,6-diisopropylbenzenaminium chloride **25** by using a commercially available 2.0 M HCl diethyl ether solution, instead of HCl gas, produced increased yields (92%).[37] Diisopropylbenzenaminium chloride **25** is a versatile precursor that is also used in the synthesis of ligand for the target complex, **14.** Alkylation of *S*-benzylcysteamine **26** produced a benzyl protected thiolate **27** (Figure 5.5 & Figure 5.6). The final organic product **12** was isolated as the HCl salt and characterized by ^{1}H NMR and electrospray ionization mass (ESI-MS) spectroscopies (Figure 5.7). The overall yield for this synthetic route is 52%.

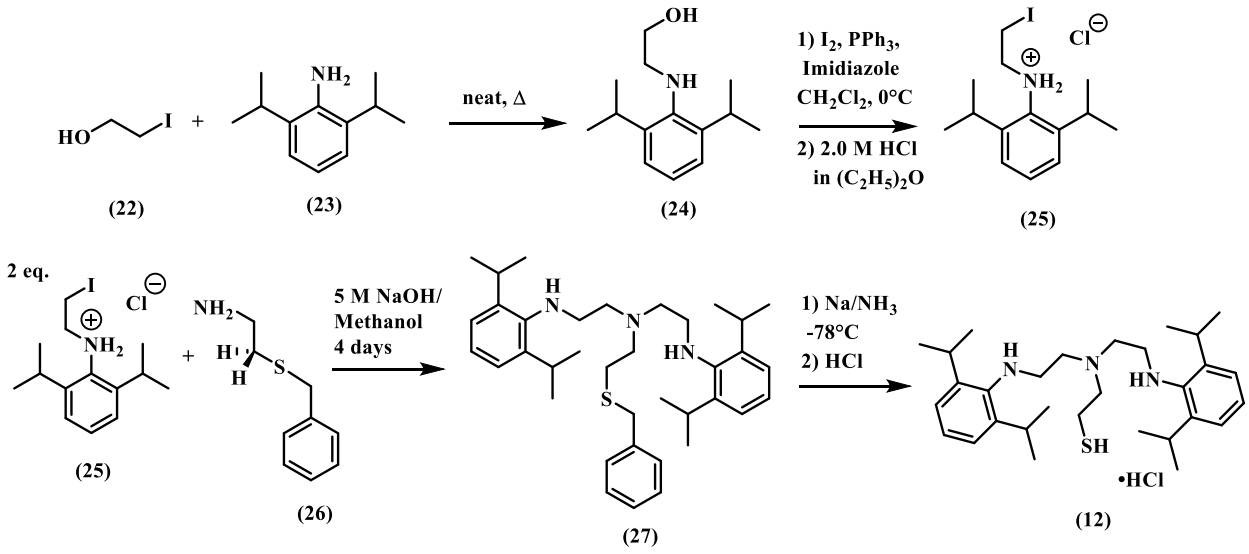

Figure 5.5. Synthetic route to the BDAT ligand (**12**).

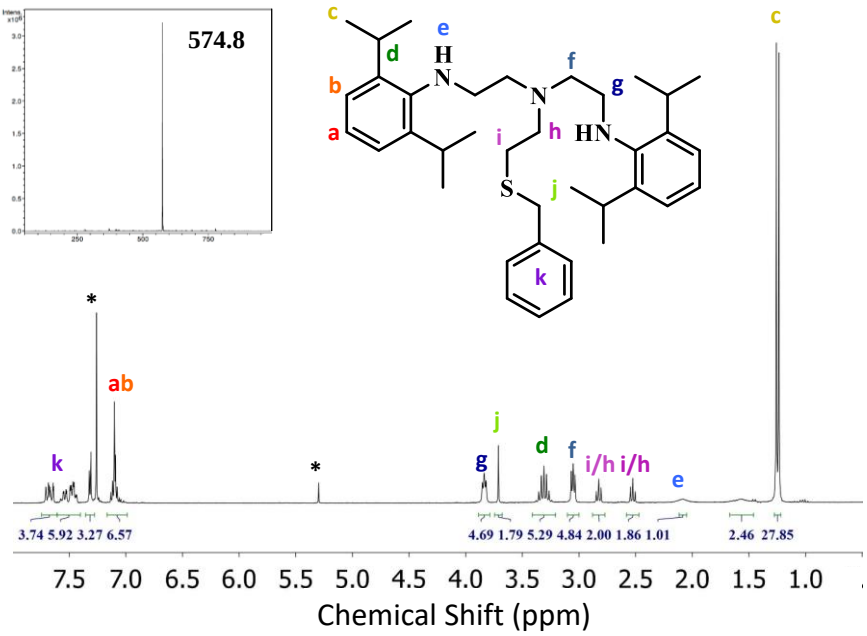

Figure 5.6. ^{1}H NMR spectra and inset ESI-MS (m/z) spectra of BDAT-Bn (**27**). * denote solvent peaks.

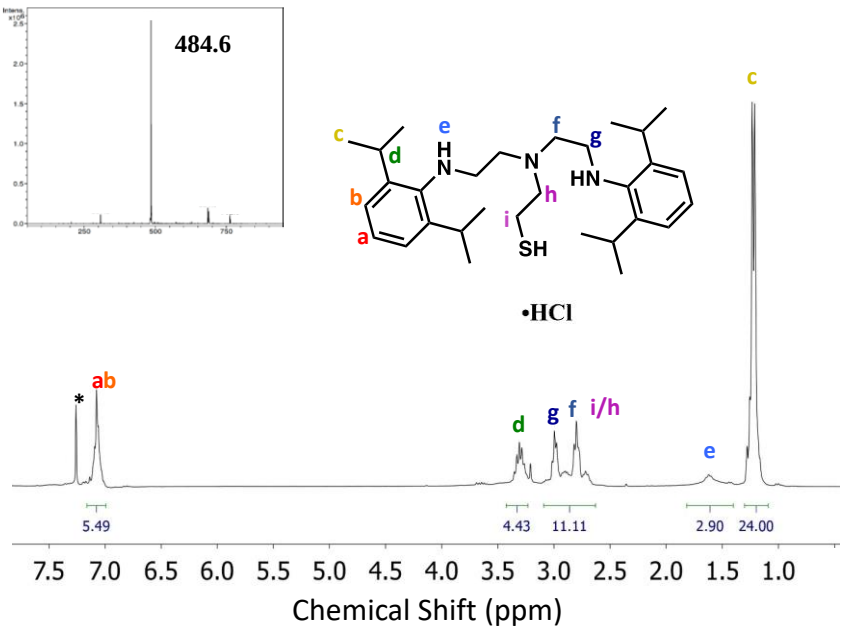

Figure 5.7. ^{1}H NMR spectra and inset ESI-MS (m/z) spectra of BDAT (**12**). * denotes solvent peaks.

The same versatile precursor used to install steric bulk into the BDAT ligand, was implemented in the synthesis of the N_4(tren-dipp$_{amine}$) ligand (**28**). First the singly boc-protected ethyl diamine (**29**) is alkylated with two equivalents of the sterically bulky **25** (Figure 5.8). The boc-protected precursor **31** was produced from an alkylation reaction, followed by deprotection to afford N_4(tren-dipp$_{amine}$) (**28**). A thiolate, 3-methyl-3-mercapto-2-butanone (**32**) is added to the ligand **28** like previous procedures in which the alkyl-thiolate precursor is condensed onto a ligand via a metal-templated Schiff-base condensation. These metalation reactions were only attempted in methanol because the Schiff-base condensation between the ketone and the amine backbone of **28** has been more successful under these conditions for other similar systems.[42,43] No evidence of metalation with Fe^{II}, Mn^{II}, or Co^{II} has been observed with the $S^{Me2}N_4$(tren-dipp$_{amide}$) ligand either, despite the larger possible coordination number that would aid in the stabilization of a metal complex. Isolating anionic Fe^{II}-complexes can be challenging and attempts make the Fe^{III}-complex should be pursued.

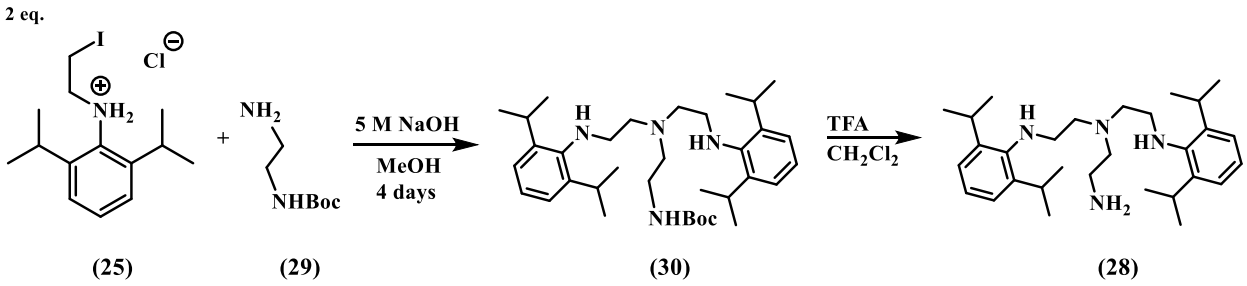

Figure 5.8. Synthetic Route to (N_4(tren-dipp$_{amide}$) (**28**).

5.3.3 *Preliminary Results for the Cationic Derivative, $[Fe^{II}(S^{Me2}N_4$(tren-dipp$_{amide}$)$]^{1+}$ (**32**)*

The BDAT and ($S^{Me2}N_4$(tren-$dipp_{amide}$) both could also be coordinated to Fe^{II} produce cationic complexes. Metallation was first attempted with the ($S^{Me2}N_4$(tren-$dipp_{amide}$) ligand because of its potential to have a higher coordination. This was achieved using a metal-templated Schiff base condensation (Figure 5.9). Evidence for metallation was obtained by a peak in the ESI-MS spectra indicating the 1+ charged **32** was further ionized in the mass spectrometer by the addition of a sodium ion (Figure 5.10). Attempts to isolate solid have been unsuccessful. The methanol solution containing **32** reacts with dioxygen from air to become a deep eggplant purple (λ_{max} = 500 nm) at 25 °C (Figure 5.11). This species decays to a second orange meta-stable species with λ_{max} = 550 nm over the course of 25 minutes (Figure 5.11). Eventually the solution loses all electronic absorption features at room temperature. The observance of two colored species after the addition of oxygen at room temperature is incredibly promising that at lower temperatures these species and potentially others could be isolated and characterized.

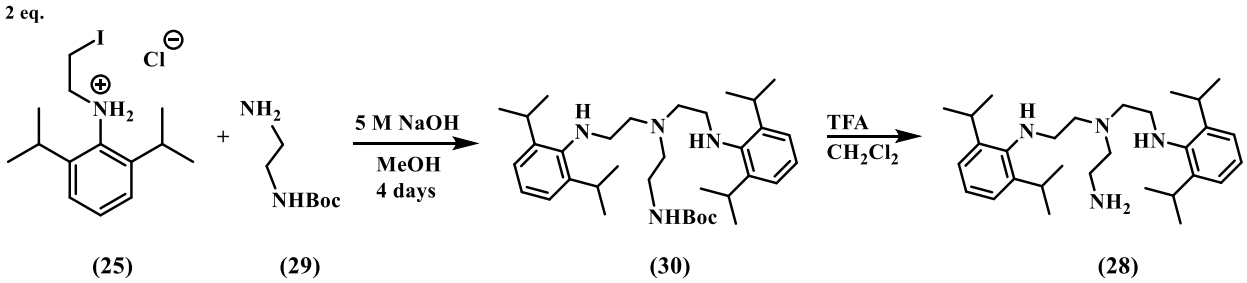

Figure 5.9. Synthetic Route to $[Fe^{II}(S^{Me2}N_4$(tren-dippamide)$]^{1+}$ (**32**)

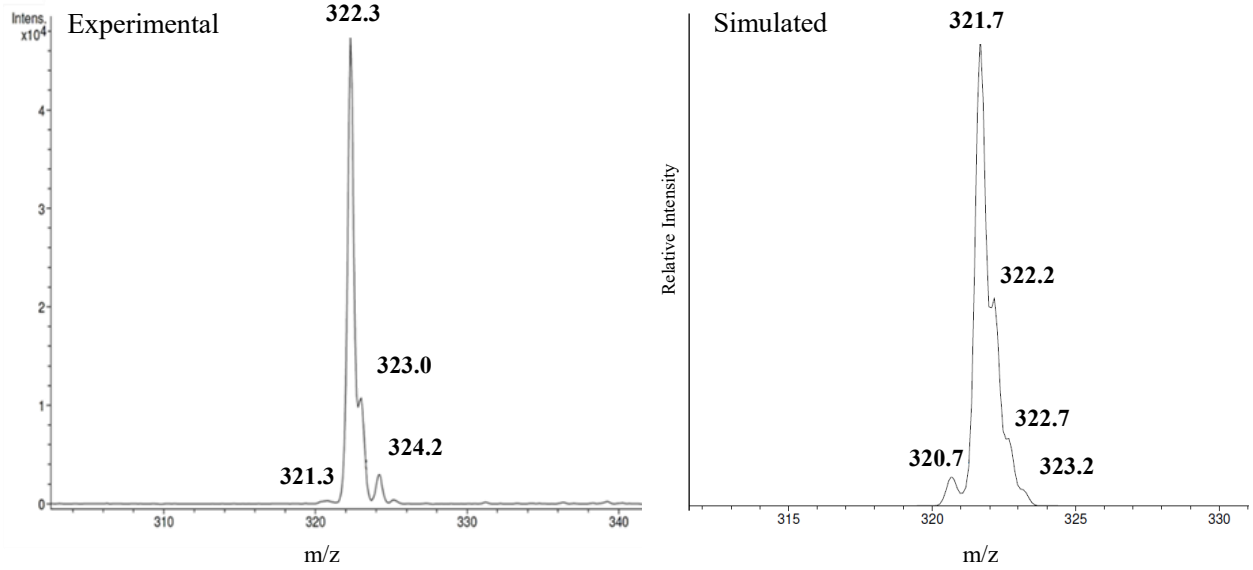

Figure 5.10. ESI-MS spectra of the cationic **32** in the positive with a sodium ion and the calculated spectra for **32** plus a sodium ion.

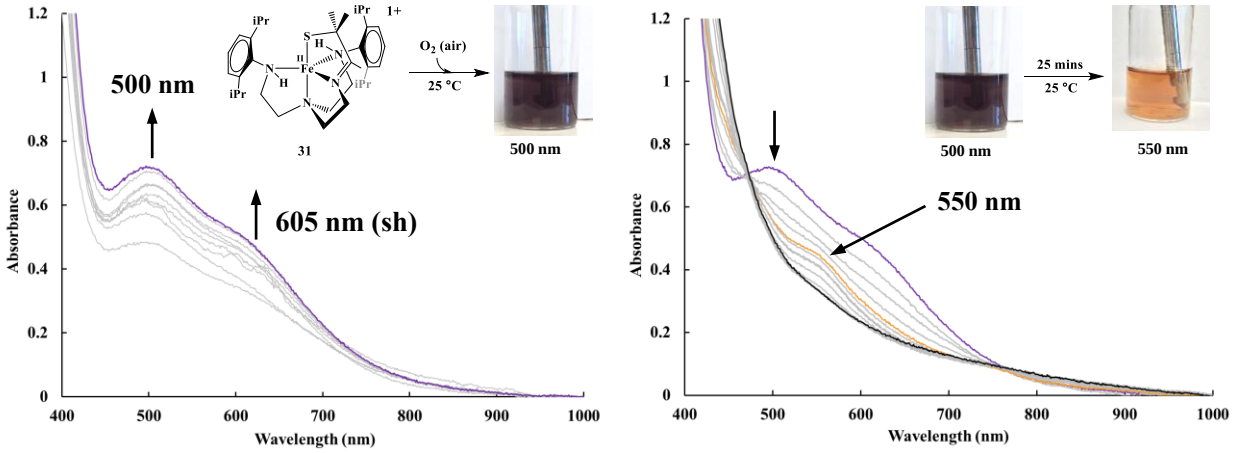

Figure 5.11. Monitoring the electronic absorbance spectra of the reaction of **32** opened to air at 25 °C. Right: The spectra for the first 10 minutes of the reaction. Left: The conversion of the 500 nm species to a species with a should at 550 nm over the course of 25 minutes followed by decay over the course of an additional 25 minutes.

5.4 Conclusion

The design and synthesis of new ligand systems is an integral part of biomimetic modeling since it provides the opportunity to isolate previously unobservable or difficult to access intermediates and to probe the effects of coordination environment on reactivity. The procedures for three new anionic ligands have been established and with minor changes metalation will likely be achieved. The removal of a methyl group from **8** forming **11** may lead to a lower spin-state for the latter and steric bulk of the complex thus possibly allowing a sixth ligand to bind. However, the redox potential is unlikely to be affected by the synthetic change to change and the methylated version has an extremely negative reduction potential (-1.51 V vs SCE)[14] displaying how this ligand is likely to stabilize high valent Fe intermediates. Another five-coordinate anionic complex with a single thiolate, **13**, was proposed to isolate such intermediates, thus far the electronic rich ligand has not been coordinated to an Fe^{II} ion. A more effective strategy may be to synthesis the Fe^{III} complex in the same manner as **8**. Accessing Fe^{V}-oxos would be possible from **14** and **11** using oxo-atom donors. Likewise, **12** may be coordinated to an Fe^{III} ion to form **13** and dioxygen intermediates can be probed through the binding of superoxide and peroxide. With the time intensive task of developing synthetic routes to these complexes completed, metallation with Fe^{III} ions will hopefully yield exciting new opportunities to study the influence of thiolates on dioxygen derived intermediates.

A promising preliminary result is the intense color change the **31** undergoes when exposed to air followed by an additional color change before decaying to a featureless species. This implies there may be multiple intermediates observable at room temperature. Typically, dioxygen derived intermediates with thiolates are only seen at low temperatures.[4,5,44] The steric bulk may be slowing the conversion to the common thermodynamic sink of forming a Fe^{III}_2-μ-oxo complex or slowing

oxidation reactions.[45] While not the initially intended anionic complex, **31** has demonstrated promise as a complex that can stabilize multiple intermediates.

Through the study of many examples of dioxygen derived intermediates spectroscopic and reactivity trends can be established and computational methods can be calibrated. This furthers the understanding of transiently observed intermediates in metalloenzymes helping to explain how they carry out such critical and difficult process under ambient conditions with first row transition metals. This can have a broader impact in design and implementation of biocatalysts and bio-inspired catalysts.

5.5 Reference

(1) Tamanaha, E.; Zhang, B.; Guo, Y.; Chang, W.; Barr, E. W.; Xing, G.; St. Clair, J.; Ye, S.; Neese, F.; Bollinger, J. M.; Krebs, C. Spectroscopic Evidence for the Two C–H-Cleaving Intermediates of Aspergillus Nidulans Isopenicillin N Synthase. *J. Am. Chem. Soc.* **2016**, *138* (28), 8862–8874. DOI: 10.1021/jacs.6b04065.

(2) Tchesnokov, E. P.; Faponle, A. S.; Davies, C. G.; Quesne, M. G.; Turner, R.; Fellner, M.; Souness, R. J.; Wilbanks, S. M.; de Visser, S. P.; Jameson, G. N. L. An Iron–Oxygen Intermediate Formed during the Catalytic Cycle of Cysteine Dioxygenase. *Chem. Commun.* **2016**, *52* (57), 8814–8817. DOI: 10.1039/c6cc03904a.

(3) Fischer, A. A.; Lindeman, S. V.; Fiedler, A. T. A Synthetic Model of the Nonheme Iron–Superoxo Intermediate of Cysteine Dioxygenase. *Chem. Commun.* **2018**, 11344–11347. DOI: 10.1039/C8CC06247A.

(4) Blakely, M. N.; Dedushko, M. A.; Yan Poon, P. C.; Villar-Acevedo, G.; Kovacs, J. A. Formation of a Reactive, Alkyl Thiolate-Ligated Fe III -Superoxo Intermediate Derived

from Dioxygen. *J. Am. Chem. Soc.* **2019**, *141* (5), 1867–1870. DOI: 10.1021/jacs.8b12670.

(5) Shearer, J.; Scarrow, R. C.; Kovacs, J. A. Synthetic Models for the Cysteinate-Ligated Non-Heme Iron Enzyme Superoxide Reductase: Observation and Structural Characterization by XAS of an Fe III −OOH Intermediate. *J. Am. Chem. Soc.* **2002**, *124* (39), 11709–11717. DOI: 10.1021/ja012722b.

(6) Bukowski, M. R.; Koehntop, K. D.; Stubna, A.; Bominaar, E. L.; Halfen, J. A.; Munck, E.; Nam, W.; Que, L. A Thiolate-Ligated Nonheme Oxoiron(IV) Complex Relevant to Cytochrome P450. *Science.* **2005**, *310* (5750), 1000–1002. DOI: 10.1126/science.1119092.

(7) Kitagawa, T.; Dey, A.; Lugo-Mas, P.; Benedict, J. B.; Kaminsky, W.; Solomon, E.; Kovacs, J. A. A Functional Model for the Cysteinate-Ligated Non-Heme Iron Enzyme Superoxide Reductase (SOR). *J. Am. Chem. Soc.* **2006**, *128* (45), 14448–14449. DOI: 10.1021/ja064870d.

(8) Lehnert, N.; Ho, R. Y. N.; Que, L.; Solomon, E. I. Spectroscopic Properties and Electronic Structure of Low-Spin FE(III)-Alkylperoxo Complexes: Homolytic Cleavage of the O-O Bond. *J. Am. Chem. Soc.* **2001**, *123* (34), 8271–8290. DOI: 10.1021/ja010165n.

(9) Brown, C. D.; Neidig, M. L.; Neibergall, M. B.; Lipscomb, J. D.; Solomon, E. I. VTVH-MCD and DFT Studies of Thiolate Bonding to {FeNO}7/ {FeO2}8 Complexes of Isopenicillin N Synthase: Substrate Determination of Oxidase versus Oxygenase Activity in Nonheme Fe Enzymes. *J. Am. Chem. Soc.* **2007**, *129* (23), 7427–7438. DOI: 10.1021/ja071364v.

(10) Green, M. T.; Dawson, J. H.; Gray, H. B. Oxoiron(IV) in Chloroperoxidase Compound II

Is Basic: Implications for P450 Chemistry. *Science.* **2004**, *304* (5677), 1653–1656. DOI: 10.1126/science.1096897.

(11) Rittle, J.; Green, M. T. Cytochrome P450 Compound I: Capture, Characterization, and C-H Bond Activation Kinetics. *Science.* **2010**, *330* (6006), 933–937. DOI: 10.1126/science.1193478.

(12) Denisov, I. G.; Makris, T. M.; Sligar, S. G.; Schlichting, I. Structure and Chemistry of Cytochrome P450. *Chem. Rev.* **2005**, *105* (6), 2253–2277. DOI: 10.1021/cr0307143.

(13) Poon, P. C. Y.; Dedushko, M.; Sun, X.; Yang, G.; Toledo, S.; Hayes, E. C.; Johansen, A.; Rees, J. A.; Stoll, S.; Rybak-Akimova, E.; et al. How Metal Ion Lewis Acidity and Steric Properties Influence the Barrier to Dioxygen Binding, Peroxo O-O Bond Cleavage, and Reactivity. *J. Am. Chem. Soc.* **2019**, *Under Revi*.

(14) Villar-Acevedo, G.; Lugo-Mas, P.; Blakely, M. N.; Rees, J. A.; Ganas, A. S.; Hanada, E. M.; Kaminsky, W.; Kovacs, J. A. Metal-Assisted Oxo Atom Addition to an Fe(III) Thiolate. *J. Am. Chem. Soc.* **2017**, *139* (1), 119–129. DOI: 10.1021/jacs.6b03512.

(15) Shoner, S. C.; Barnhart, D.; Kovacs, J. A. A Model for the Low-Spin, Non-Heme, Thiolate-Ligated Iron Site of Nitrile Hydratase. *Inorg. Chem.* **1995**, *34* (18), 4517–4518. DOI: 10.1021/ic00122a001.

(16) Jackson, H. L.; Shoner, S. C.; Rittenberg, D.; Cowen, J. A.; Lovell, S.; Barnhart, D.; Kovacs, J. A. Probing the Influence of Local Coordination Environment on the Properties of Fe-Type Nitrile Hydratase Model Complexes. *Inorg. Chem.* **2001**, *40* (7), 1646–1653. DOI: 10.1021/ic001271d.

(17) Kovacs, J. A. Synthetic Analogues of Cysteinate-Ligated Non-Heme Iron and Non-Corrinoid Cobalt Enzymes. *Chem. Rev.* **2004**, *104* (2), 825–848. DOI: 10.1021/cr020619e.

(18) Kovacs, J. A.; Brines, L. M. Understanding How the Thiolate Sulfur Contributes to the Function of the Non-Heme Iron Enzyme Superoxide Reductase. *Acc. Chem. Res.* **2007**, *40* (7), 501–509. DOI: 10.1021/ar600059h.

(19) Lugo-Mas, P.; Taylor, W.; Schweitzer, D.; Theisen, R. M.; Xu, L.; Shearer, J.; Swartz, R. D.; Gleaves, M. C.; DiPasquale, A.; Kaminsky, W.; et al. Properties of Square-Pyramidal Alkyl-Thiolate FeIII Complexes, Including an Analogue of the Unmodified Form of Nitrile Hydratase. *Inorg. Chem.* **2008**, *47* (23), 11228–11236. DOI: 10.1021/ic801704n.

(20) Ellison, J. J.; Nienstedt, A.; Shoner, S. C.; Barnhart, D.; Cowen, J. A.; Kovacs, J. A. Reactivity of Five-Coordinate Models for the Thiolate-Ligated Fe Site of Nitrile Hydratase. *J. Am. Chem. Soc.* **1998**, *120* (23), 5691–5700. DOI: 10.1021/ja973129q.

(21) Downing, A. Unpublished Work.

(22) Spencer, D. J. E.; Aboelella, N. W.; Reynolds, A. M.; Holland, P. L.; Tolman, W. B. Beta-Diketiminate Ligand Backbone Structural Effects on Cu(I)/O2 Reactivity: Unique Copper-Superoxo and Bis(Mu-Oxo) Complexes. *J. Am. Chem. Soc.* **2002**, *124* (10), 2108–2109. DOI: 10.1021/ja017820b.

(23) Donoghue, P. J.; Gupta, A. K.; Boyce, D. W.; Cramer, C. J.; Tolman, W. B. An Anionic, Tetragonal Copper(II) Superoxide Complex. *J. Am. Chem. Soc.* **2010**, *132* (45), 15869–15871. DOI: 10.1021/ja106244k.

(24) Neisen, B. D.; Solntsev, P. V.; Halvagar, M. R.; Tolman, W. B. Secondary Sphere Hydrogen Bonding in Monocopper Complexes of Potentially Dinucleating Bis(Carboxamide) Ligands. *Eur. J. Inorg. Chem.* **2015**, *2015* (36), 5856–5863. DOI: 10.1002/ejic.201501060.

(25) Dhar, D.; Yee, G. M.; Tolman, W. B. Effects of Charged Ligand Substituents on the

Properties of the Formally Copper(III)-Hydroxide ([CuOH] 2+) Unit. *Inorg. Chem.* **2018**, *57* (16), 9794–9806. DOI: 10.1021/acs.inorgchem.8b01529.

(26) Coggins, M. K.; Martin-Diaconescu, V.; Debeer, S.; Kovacs, J. A. Correlation between Structural, Spectroscopic, and Reactivity Properties within a Series of Structurally Analogous Metastable Manganese(III)-Alkylperoxo Complexes. *J. Am. Chem. Soc.* **2013**, *135* (11), 4260–4272. DOI: 10.1021/ja308915x.

(27) Brines, L. M.; Villar-Acevedo, G.; Kitagawa, T.; Swartz, R. D.; Lugo-Mas, P.; Kaminsky, W.; Benedict, J. B.; Kovacs, J. A. Comparison of Structurally-Related Alkoxide, Amine, and Thiolate-Ligated MII (M = Fe, Co) Complexes: The Influence of Thiolates on the Properties of Biologically Relevant Metal Complexes. *Inorganica Chim. Acta* **2008**, *361* (4), 1070–1078. DOI: 10.1016/j.ica.2007.07.038.

(28) Brines, L. M.; Shearer, J.; Fender, J. K.; Schweitzer, D.; Shoner, S. C.; Barnhart, D.; Kaminsky, W.; Lovell, S.; Kovacs, J. a. Periodic Trends within a Series of Five-Coordinate Thiolate-Ligated [M II (S Me2 N 4 (Tren))] + (M = Mn, Fe, Co, Ni, Cu, Zn) Complexes, Including a Rare Example of a Stable Cu II −Thiolate. *Inorg. Chem.* **2007**, *46* (22), 9267–9277. DOI: 10.1021/ic701433p.

(29) Kovacs, J. A. Tuning the Relative Stability and Reactivity of Manganese Dioxygen and Peroxo Intermediates via Systematic Ligand Modification. *Acc. Chem. Res.* **2015**, *48* (10), 2744–2753. DOI: 10.1021/acs.accounts.5b00260.

(30) MacBeth, C. E.; Golombek, A. P.; Young, J.; Yang, C.; Kuczera, K.; Hendrich, M. P.; Borovik, A. S. O2 Activation by Nonheme Iron Complexes: A Monomeric Fe(III)-Oxo Complex Derived from O2. *Science.* **2000**, *289* (5481), 938–941. DOI: 10.1126/science.289.5481.938.

(31) Chanda, A.; Shan, X.; Chakrabarti, M.; Ellis, W. C.; Popescu, D. L.; De Oliveira, F. T.; Wang, D.; Que, L.; Collins, T. J.; Münck, E.; et al. (TAML)FeIV=O Complex in Aqueous Solution: Synthesis and Spectroscopic and Computational Characterization. *Inorg. Chem.* **2008**, *47* (9), 3669–3678. DOI: 10.1021/ic7022902.

(32) Popescu, D. L.; Vrabel, M.; Brausam, A.; Madsen, P.; Lente, G.; Fabian, I.; Ryabov, A. D.; Van Eldik, R.; Collins, T. J. Thermodynamic, Electrochemical, High-Pressure Kinetic, and Mechanistic Studies of the Formation of Oxo FeIV-TAML Species in Water. *Inorg. Chem.* **2010**, *49* (24), 11439–11448. DOI: 10.1021/ic1015109.

(33) Lacy, D. C.; Gupta, R.; Stone, K. L.; Greaves, J.; Ziller, J. W.; Hendrich, M. P.; Borovik, A. S. Formation , Structure , and EPR Detection of a High Spin Fe IV s Oxo Species Derived from Either an Fe III s Oxo or Fe III s OH Complex. **2010**, *350* (Iv), 12188–12190. .

(34) Bigi, J. P.; Harman, W. H.; Lassalle-Kaiser, B.; Robles, D. M.; Stich, T. A.; Yano, J.; Britt, R. D.; Chang, C. J. A High-Spin Iron(IV)-Oxo Complex Supported by a Trigonal Nonheme Pyrrolide Platform. *J. Am. Chem. Soc.* **2012**, *134* (3), 1536–1542. DOI: 10.1021/ja207048h.

(35) de Oliveira, F. T.; Chanda, A.; Banerjee, D.; Shan, X.; Mondal, S.; Que, L.; Bominaar, E. L.; Munck, E.; Collins, T. J. Chemical and Spectroscopic Evidence for an FeV-Oxo Complex. *Science.* **2007**, *315* (5813), 835–838. DOI: 10.1126/science.1133417.

(36) Kramer, R. A.; Bröhmer, M. C.; Forkel, N. V.; Bannwarth, W. A New Robust and Versatile Tetradentate Linker for Amides to Be Cleaved under Mild Conditions by Unusual Complexation of the Amide Nitrogen to Cu ++. *European J. Org. Chem.* **2009**, No. 25, 4273–4283. DOI: 10.1002/ejoc.200900291.

(37) Prasad, B. a B.; Gilbertson, S. R. One-Pot Synthesis of Unsymmetrical N-Heterocyclic Carbene Ligands from N -(2-Iodoethyl)Arylamine Salts. *Org. Lett.* **2009**, *11* (16), 3710–3713. DOI: 10.1021/ol901189m.

(38) Coggins, M. K.; Kovacs, J. A. Structural and Spectroscopic Characterization of Metastable Thiolate-Ligated Manganese(III)–Alkylperoxo Species. *J. Am. Chem. Soc.* **2011**, *133* (32), 12470–12473. DOI: 10.1021/ja205520u.

(39) Garrett, S. W.; Davies, O. R.; Milroy, D. A.; Wood, P. J.; Pouton, C. W.; Threadgill, M. D. Synthesis and Characterisation of Polyamine–Poly(Ethylene Glycol) Constructs for DNA Binding and Gene Delivery. *Bioorg. Med. Chem.* **2000**, *8* (7), 1779–1797. DOI: 10.1016/S0968-0896(00)00113-9.

(40) Laduron, F.; Tamborowski, V.; Moens, L.; Horváth, A.; De Smaele, D.; Leurs, S. Efficient and Scalable Method for the Selective Alkylation and Acylation of Secondary Amines in the Presence of Primary Amines. *Org. Process Res. Dev.* **2005**, *9* (1), 102–104. DOI: 10.1021/op049812w.

(41) Kang, S. O.; Day, V. W.; Bowman-James, K. The Influence of Amine Functionalities on Anion Binding in Polyamide-Containing Macrocycles. *Org. Lett.* **2009**, *11* (16), 3654–3657. DOI: 10.1021/ol9014249.

(42) Shearer, J.; Nehring, J.; Lovell, S.; Kaminsky, W.; Kovacs, J. A. Modeling the Reactivity of Superoxide Reducing Metalloenzymes with a Nitrogen and Sulfur Coordinated Iron Complex. *Inorg. Chem.* **2001**, *40* (22), 5483–5484. DOI: 10.1021/ic010221l.

(43) Coggins, M. K.; Toledo, S.; Shaffer, E.; Kaminsky, W.; Shearer, J.; Kovacs, J. A. Characterization and Dioxygen Reactivity of a New Series of Coordinatively Unsaturated Thiolate-Ligated Manganese(II) Complexes. *Inorg. Chem.* **2012**, *51* (12), 6633–6644.

DOI: 10.1021/ic300192q.

(44) Coggins, M. K.; Sun, X.; Kwak, Y.; Solomon, E. I.; Rybak-Akimova, E.; Kovacs, J. A. Characterization of Metastable Intermediates Formed in the Reaction between a Mn(II) Complex and Dioxygen, Including a Crystallographic Structure of a Binuclear Mn(III)-Peroxo Species. *J. Am. Chem. Soc.* **2013**, *135* (15), 5631–5640. DOI: 10.1021/ja311166u.

(45) Theisen, R. M.; Shearer, J.; Kaminsky, W.; Kovacs, J. A. Steric and Electronic Control over the Reactivity of a Thiolate-Ligated Fe(II) Complex with Dioxygen and Superoxide: Reversible μ-Oxo Dimer Formation. *Inorg. Chem.* **2004**, *43* (24), 7682–7690. DOI: 10.1021/ic0491884.

VITA

Maike Nicole Blakely was born in 1991 to parents Kent and Linda Blakely and grew up in Kearney, NE. Maike graduated from Williston Northampton in 2010 and went on to Chatham University to earn a Bachelor of Science degree in Chemistry and a minor in Mathematics in the Fall of 2013. At Chatham University, Maike conducted research on the effect of cadmium concentrations and pH on mature dwarf hydroponic sunflowers' accumulation of cadmium under the guidance of Professor Joseph MacNeil. As an undergraduate, Maike participated in two summer research programs. As part of the 2012 Duquesne University Chemistry URP, she synthesized and characterized a series of 2-D metal-organic compounds under the direction of Professor Jennifer Aitken and Professor Joseph MacNeil. In the fall of 2012, Maike began research in Professor Rosi's laboratory at the University of Pittsburgh. Under the guidance of graduate student mentor Tao Li, she aided in the development of a new method of post-synthetic modification of metal organic frameworks MOFs that resulted in a highly cited publication. The second summer program Maike participated in was the National Nanotechnology Infrastructure Network's REU at the Cornell Nanoscale Science and Technology Center. During her summer in Professor Ober's group, she evaluated three single component molecular glass photoresists selecting the most suitable for future physical vapor deposition studies.

In the fall of 2014, Maike began her graduate research at the University of Washington with Professor Julie Kovacs in the field of bioinorganic chemistry. While at the University of Washington, Maike was awarded the David M. Ritter Endowed Fellowship for Chemistry and later the Joseph Bouknight Endowed Fellowship for Chemistry. After graduating from the University of Washington with her Doctor of Philosophy in Chemistry in the Fall of 2019. Maike plans to

continue research as a postdoctoral scholar at the start of the new year, 2020, at Montana State University with Professor Joan Broderick investigating the mechanism of radical SAM enzymes.